Nano-Bio-Sensing

Sandro Carrara
Editor

Nano-Bio-Sensing

Foreword by Giovanni De Micheli

Springer

Editor
Sandro Carrara
EPFL
Lausanne
Switzerland
sandro.cararra@epfl.ch

ISBN 978-1-4419-6168-6 e-ISBN 978-1-4419-6169-3
DOI 10.1007/978-1-4419-6169-3
Springer New York Dordrecht Heidelberg London

Library of Congress Control Number: 2010938597

© Springer Science+Business Media, LLC 2011
All rights reserved. This work may not be translated or copied in whole or in part without the written permission of the publisher (Springer Science+Business Media, LLC, 233 Spring Street, New York, NY 10013, USA), except for brief excerpts in connection with reviews or scholarly analysis. Use in connection with any form of information storage and retrieval, electronic adaptation, computer software, or by similar or dissimilar methodology now known or hereafter developed is forbidden.
The use in this publication of trade names, trademarks, service marks, and similar terms, even if they are not identified as such, is not to be taken as an expression of opinion as to whether or not they are subject to proprietary rights.

Printed on acid-free paper

Springer is part of Springer Science+Business Media (www.springer.com)

Foreword

Much of our economy and way of living will be affected by nanotechnologies in the decade to come and beyond. Mastering materials at the molecular level and their interaction with living matter opens up unforeseeable horizons. Still much of the potentials of nano-biotechnology is untapped. Although we understand most basic principles of molecular interaction, the transformation of scientific results into robust technologies that can support health care and environment protection has still to take place. In other words, we are at the verge of a technological revolution that will bring to us a multitude of bio-electronic devices that interact with biological systems through intelligent – and possibly distributed – means of computation. The recent strong interest about cyber-physical systems is motivated by this trend.

This book reviews the principles and practice of nano-bio-sensing. It covers extensively the basic principles of interaction of living matters with detectors and the transduction principles. It reviews surface science as well as electrical and optical technologies for bio-sensing. Nano-scale effects, inducing quantum confinement, are specifically addressed along with their benefits, such as the amplification of sensing phenomena, yielding devices with higher sensitivity. Specific importance is given to low-power sensing techniques, as well as nonconventional means for powering the sensors, which may be very useful for implanted biosensors. Moreover, fault-tolerant bio-sensing systems are described. Overall, various physical, chemical, and electrical effects contribute jointly to enable the construction of a new generation of nano-bio-sensors.

The importance of this research field should not be underestimated. The healthcare sector will soon be able to benefit from real-time sensors – *in the body* and *on the body* – that can predict specific pathologies and give the opportunity of preventive treatment. Pharmacology will be positively affected by means of creating rational and personalized drugs that can be tuned to the characteristics of the patient. Nutrition science and practice will benefit from advances in sensors to enable the monitoring of the consumption of nutrients in the right combination and

quantity for the expected effort. Positive impact of these methods can be measured, for example, in the training of sportsmen and in managing the attention span of youths. A combination of electro-sensing technologies can rationalize work and living spaces, enabling better working and living conditions and specifically longer autonomy to the elderly. Similarly, these technologies can be used to monitor the environment, to protect us from infections and pollution, and raise the level of security of individuals and communities. All these important and ethical goals are addressed by some research programs, most notably by the Swiss *nano-tera.ch* initiative which I am leading.

Given the intrinsic scientific merits of nano-bio-sensing and its wide projected impact on society, I believe that this book provides the reader with an important guide through the various technologies. It represents a key reference point for both scientists and engineers.

EPFL Lausanne, 2010 Giovanni De Micheli

Contents

1 Introduction to Nano-Biosensing 1
Sandro Carrara

2 Nano-scale Force Spectroscopy Applied to Biological Samples 23
Sandor Kasas, Charles Roduit, and Giovanni Dietler

3 Surface Nano-patterning of Polymers for Mass-Sensitive Biodetection 45
Adnan Mujahid and Franz L. Dickert

4 Surface Plasmon Resonance on Nanoscale Organic Films 83
Willem M. Albers and Inger Vikholm-Lundin

5 Nanotechnology to Improve Electrochemical Bio-sensing 127
Sandro Carrara

6 Nano-Photonics and Opto-Fluidics on Bio-Sensing 151
Ming C. Wu and Arash Jamshidi

7 Nano-metric Single-Photon Detector for Biochemical Chips 177
Edoardo Charbon and Yuki Maruyama

8 Energy Harvesting for Bio-sensing by Using Carbon Nanotubes 195
Koushik Maharatna, Karim El Shabrawy, and Bashir Al-Hashimi

9 Integrated Nano-Bio-VLSI Approach for Designing Error-Free Biosensors 217
Shantanu Chakrabartty, Evangelyn C. Alocilja, and Yang Liu

Index 241

Contributors

Bashir Al-Hashimi
University of Southampton, Southampton, Hampshire, UK

Willem M. Albers
VTT Technical Research Centre of Finland, Tampere, Finland

Evangelyn C. Alocilja
Michigan State University, East Lansing, MI, USA

Sandro Carrara
EPFL, Lausanne, Switzerland

Shantanu Chakrabartty
Michigan State University, East Lansing, MI, USA

Edoardo Charbon
TU Delft, Delft, The Netherlands

Giovanni De Micheli
EPFL, Lausanne, Switzerland

Franz L. Dickert
University of Vienna, Vienna, Austria

Giovanni Dietler
Laboratoire de Physique de la Matière Vivante, EPFL, Lausanne, Switzerland

Karim El Shabrawy
University of Southampton, Southampton, Hampshire, UK

Arash Jamshidi
University of California, Berkeley, CA, USA

Sandor Kasas
Laboratoire de Physique de la Matière Vivante, EPFL, Lausanne, Switzerland

Yang Liu
University of Michigan, Ann Arbor, MI, USA

Koushik Maharatna
University of Southampton, Southampton, Hampshire, UK

Yuki Maruyama
EPFL, Lausanne, Switzerland

Adnan Mujahid
University of Vienna, Vienna, Austria

Charles Roduit
Laboratoire de Physique de la Matière Vivante, EPFL, Lausanne, Switzerland

Inger Vikholm-Lundin
Technical Research Centre of Finland, Tampere, Finland

Ming C. Wu
University of California, Berkeley, CA, USA

Chapter 1
Introduction to Nano-Biosensing

Sandro Carrara

1.1 Introduction to Nanotechnology

Although Richard Philip Feynman envisaged nanotechnology in his famous lecture held at California Institute of Technology in 1959 [1], modern nanotechnology started when Gerd Binning and Heinrich Rorer invented the scanning tunneling microscope (STM) at the IBM laboratory in Zurich, in the early 1980s [2]. The importance of this invention was immediately recognized and they became Nobel laureates a few years later, in 1986.

The STM is a microscope based on a quantum phenomenon, the tunneling effect, which enables electrons to overcome an energy barrier even if they do not have enough energy. For that, the energy barrier has to be no higher than the electron energy and the barrier width has to be on the scale of tenths of a nanometer. Such a barrier is called a *tunneling barrier*. If an electron sea has a Fermi level below the energy of the tunneling barrier, then the large majority of the electrons do not have enough energy to overcome the barrier. However, a few of them do not have zero quantum probability to overcome the barrier and, thus, a small current flows through the system. This current is called the *tunneling current* and it is usually less than a few nanoamperes. The core of this microscope is a piezoelectric mover that ensures small shifts (with steps below tenths of nanometers) of a conductive tip, which approaches the conductive sample step-by-step until a tunneling current is measured, even if the tip and sample are not in contact. Once the tunneling current has been locked, the piezoelectric mover is driven to obtain a scan over the sample surface, as schematically shown in Fig. 1.1. A feedback system is used to keep the tunneling current constant and an image of the sample surface is acquired from the voltage used to control the feedback. Such an imaging technique is called *microscopy in constant current*.

S. Carrara (✉)
Fac. Informatique et Communications, Labo. Systèmes Intégrés (LSI)
EPFL 1015, Lausanne, Switzerland
e-mail: sandro.carrara@epfl.ch

S. Carrara (ed.), *Nano-Bio-Sensing*,
DOI 10.1007/978-1-4419-6169-3_1, © Springer Science+Business Media, LLC 2011

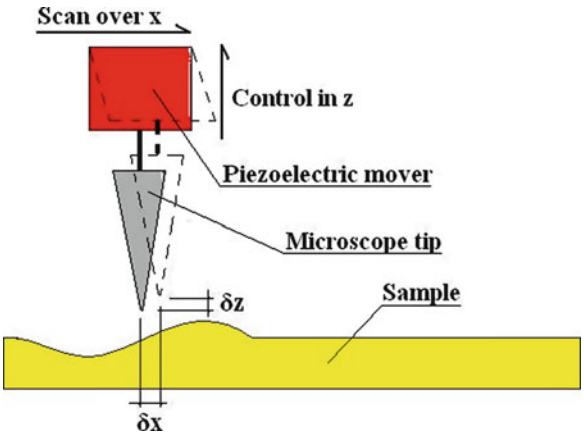

Fig. 1.1 The working principle of a scanning probe microscope, including a tip interacting with the sample and a piezoelectric mover, which scans the sample area for imaging and controls the tip–sample interaction acting on the *z*-position

In a STM, the current is of the order of picoamps, whereas the best piezoelectric mover ensures steps with spatial resolution of the order of picometers. A current control of the order of picoamps provides control of the vertical position of the tip below 1 Å (0.1 nm). So, this microscope enables nanoscale imaging to measure a single gold atom [3] or precise resolution of the interatomic distances in graphite [4]. Of course, if the lateral movement of the microscope tip stops at a sample point, then the application of a high enough tip–sample voltage modifies the sample locally. This allows for sample manipulations at the atomic scale [5].

So, the modern era of nanotechnology was born when technology allowed us to see and manipulate materials at the atomic scale with the invention of the STM.

1.2 Nanoscale Microscopy on Biological Systems

Instead of a current, a more general idea to monitor and control other physical parameters during an image scan over a sample surface led to further inventions in *scanning probe microscopy*. In general, the physical parameters controlled may be the tunneling current, the tip height, the tip–sample interaction forces, or the tip friction on the sample, etc. Each of them leads to a special type of microscopy or to a special operating mode of the microscope. Among the different scanning probe microscopes, the most popular is the *atomic force microscope* (AFM). This is based on the interactions between the tip and the sample and allows measurements of interactions down to 10^{-18} N [6]. In the case of imaging in constant-force mode, the image is once again obtained by the feedback voltage.

The STM, the AFM, and the other scanning probe microscopes may be applied to imaging or investigations of biological samples [7]. With the AFM and the STM,

imaging, sensing, and manipulation are performed at sub-nanometer resolution. Therefore, we are now dealing with proper *nano-biosensing* when we use the STM or the AFM to sense biological samples, such as DNA [8, 9], proteins [9], and cells [10].

Imaging of DNA by using scanning tunneling microscopy of graphite substrates was one of the first applications of scanning probe microscopes to bioimaging. Unfortunately, defects on graphite were found to mimic the image features of the DNA [11]. Therefore, the STM was abandoned in favor of the AFM for imaging of biological molecules [10]. Over the last 15 years, many examples of imaging molecules of biological relevance using the AFM have been published. It is easy to find in the literature good investigations reporting atomic force microscopy of DNA chains [12], antibodies [13], oxidases [14], cytochromes [15, 16], and photosynthetic proteins [17, 18] focused on both single molecular size and crystal structure within the protein film.

More recently, the AFM was applied to sense the single forces of interaction within biological samples. This new emerging field in nano-biosensing has the name force spectroscopy. Carlos Bustamante reported the first example of overstretching of a DNA molecule in 1996 [19]. In the following years, different research groups demonstrated the use of the AFM in force spectroscopy of single molecules. Hermann E. Gaub applied the AFM in force spectroscopy of polysaccharides and synthetic polymers [18]. Bruno Samorì investigated single-protein force spectroscopy, e.g., with angiostatin [20] and fibronectin [21]. Giovanni Dietler and Sandor Kasas proposed stiffness spectroscopy of living cells by using the AFM [22]. Very recently, James Gimzewski demonstrated that cancer cells in an early stage may be recognized by force spectroscopy even when their optical morphology appears to be similar to that of normal cells [23].

In Chap. 2, Sandor Kasas and Giovanni Dietler from EPFL, the Institute of Technology in Lausanne (Switzerland), summarize details of the technique and the most important scientific results obtained in nano-biosensing of DNA, proteins, and cells by using AFM force spectroscopy.

1.3 Nanolayer Made of Organic and Biological Materials

Single molecules of biological relevance are typically on the nanoscale. For example, thiols required for the cell membranes have a size close to 1 nm [24]; a cytochrome may be included in a sphere of 4 nm [25]; an antibody may be included in a box with size below 5 nm [26]. Then, molecular layers built onto a solid substrate with these objects have the right size to obtain nanostructured materials. From this point of view, Irvin Langmuir (Nobel laureate in chemistry in 1932) obtained the very first nanotechnology when in 1917 he provided the first report about the organization of oil films at the air/water interface [27]: this was the first investigation on monolayers obtained with fatty acids.

Three different kinds of molecular films are possible with molecules having an aliphatic chain and a hydrophilic end group. The spreading of such molecules on water produces a monolayer at the air/water interface because the hydrophilic group dips into the water, whereas the aliphatic chain floats on top of the water owing to its hydrophobic character. In the trough, a highly ordered film is obtained on the water surface when the amphiphilic molecules previously dispersed onto the water are compressed by means of moving barriers. These kinds of films are called *Langmuir films*. Once the Langmuir layer has been obtained, there are two ways to transfer the film onto a solid substrate. The substrate may be softly applied to the water and softly removed from the surface. In that manner, the monolayer at the air/water interface is transferred onto the substrate owing to interaction forces established between the hydrophobic tails of the molecules and the substrate surface, as schematically shown in Fig. 1.2a. The films obtained are called *Langmuir–Schaeffer films* in honor of Vincent Schaeffer, an eclectic man who became Langmuir's research assistant in 1932. The other way to transfer Langmuir films onto solid substrates is to dip the vertical substrate into the water and in a gentle manner. In that case, a first monolayer adheres to the substrate surface during dipping, and a second layer adheres to the first one when the substrate is removed from the water, as schematically shown in Fig. 1.2b. The result is a molecular bilayer with the two molecular layers organized in opposite directions with respect to the aliphatic chains. The films obtained are called *Langmuir–Blodgett films* in honor of Katherine Burr Blodgett, who also worked with Irvin Langmuir at General Electric Laboratories, after 1920.

Langmuir–Blodgett and Langmuir–Schaeffer films are also used to obtain multilayers by repeating the transfer of a single monolayer or bilayer. Thus, they are suitable for producing complex films with different functionalities for biosensing.

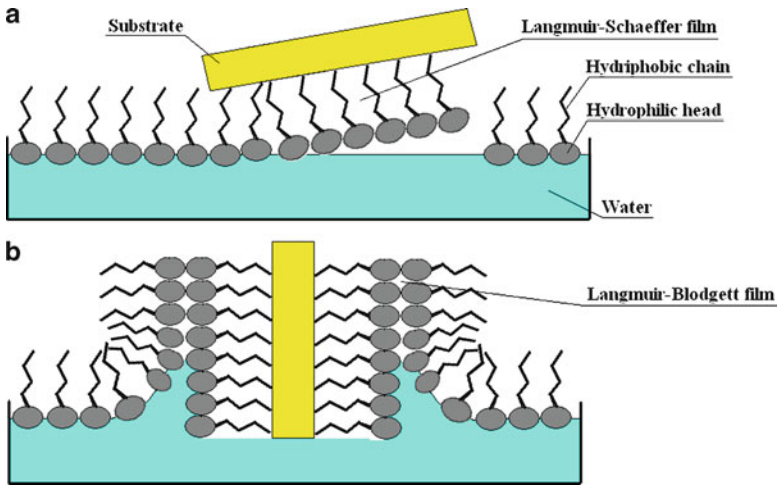

Fig. 1.2 Amphiphilic molecules with hydrophilic head groups and hydrophobic chains at the air/water interface and two methods for obtaining thin films

Although they are usually used with small aliphatic molecules, typically fatty acids, the possibility has been demonstrated to also organize both proteins [28] and polymers [29] in Langmuir–Blodgett or in Langmuir–Schaeffer films, even improving the stability of the molecular structures [30, 31].

Of course, thin films involving more functionality are also obtained by using self-assembly or layer-by-layer deposition. The self-assembly is based on chemical bonds between the layers and the substrate surface. Typically, thiols are self-assembled onto gold or other metals, whereas silane films are formed on silicon. Once the first layer has formed on the substrate surface, the next layers are assembled on the first layer with protocols that use functional groups of the first and the second layers. The repetition of similar chemical anchoring results in a highly organized multilayer with different molecules embedded within the same thin molecular film [32].

Layer-by-layer deposition is based on successive deposition of different molecular layers by using physical adsorption. Typically, a first layer is deposited onto the solid substrate on the basis of the mutual electrostatic attraction between the molecules and the substrate surface. Polar molecules present a positive molecular side chain to a surface that is negatively charged and, then, the molecules adhere to the surface. In a second step, a second molecular layer of a different kind of polar molecule is attached to the first one by using the positively charged side chain of the second molecules. In that way, the second molecules are attracted by the negatively charged side chains present in the first layer. Successive depositions following these steps result in multilayers that may include different kinds of molecules in the same sandwich [33].

The recent literature offers many examples of thin molecular films used for bioelectronics and nano-biosensing. Langmuir–Blodgett films were used by Victor Erokhin [34] for quantum devices. Langmuir–Schaeffer films were used by Frank Würthner and coworkers to study the charge transfer properties of molecular films [35]. Self-assembly was used by us for immunosensors and DNA detectors [36]. Layer-by-layer deposition was used by Reinhard Renneberg for enzyme encapsulation in polymers [37]. Franz Dickert and coworkers used protein crystals for stamping sensing layers [38]. The imprinting and patterning of molecular layer is of crucial importance to define sensing architectures. So, in Chap. 3, Franz Dickert from Vienna University (Austria) presents a valuable overview of the modern techniques of polymer nanopatterning especially dedicated to mass-sensitive biosensing.

1.4 Metallic Nanolayers and Plasmon Resonance

Quantum phenomena become more evident at the nanoscale. Charge quantization appears when electrons are confined within structures with size of the order of a few nanometers. In certain conditions, a Fermi sea confined in a conducting layer with a thickness of a few nanometers may result in coherent Schrödinger waves driving electrons to move as a unique plasmon wave. This phenomenon is observable by using a laser beam with a monochromatic wavelength and varying its incident angle to a

metal surface. Once the incident beam has reached the right angle, the plasmon is switched on and the light reflected by the surface suddenly decreases owing to the loss of the energy needed to push the plasmon. Another way to observe this quantum effect is to fix the angle of incidence and to sweep the frequency of the laser beam until the light reflected suddenly decreases. In both cases, the right incident angle combined with the right beam frequency determines the so-called *plasmon resonance*, which is the beam condition that switches on the electron plasmon within the metal surface.

Theoretical studies have shown that the plasmon resonance conditions are related to properties of the electromagnetic wave at the prism/metal interface [39]. To have a simple understanding of the physical situation, we can think of a simplified ideal situation. When a laser beam is sent, with a certain angle, toward the interface between two light transmitting materials, the incident beam is usually split in two beams: the transmitted and the reflected ones. The angles of these two beams are related to the angle of the incident beam through the Snell equation. Of course, the angle of the transmitted beam may be reduced by varying the angle of the incident beam, depending on the ratio between the refractive indexes of the two materials. Once the so-called *critical angle* for the incident beam has been reached, the transmitted beam has zero emerging angle. This means that the transmitted beam is not transmitted any more but, instead, is now traveling parallel to the interface. We can now introduce a metallic material into this highly simplified model: we can create a similar situation between transparent and conducting materials. The typical situation is that of a glass prism on a gold surface, where a glass/metal interface is obtained. Now, the electromagnetic wave travels parallel to the interface at the critical angle and it affects the electrons in the metal surface. More precise numerical simulations provide a very clear understanding of the electromagnetic field at the interface, called an *evanescent wave*, which typically extends though the interface up to 200 nm [40]. So, the evanescent wave affects electrons in this nanometer-sized region of the metal, creating a plasmon: a coherent electron wave that it is excited by the laser beam incident to the glass/metal interface.

In the case of a glass/gold interface, the incident beam is never transmitted within the metal but is reflected every time. However, the intensity of the reflected beam is highly diminished at the angle that matches the resonance conditions. The resonance conditions depend on the laser frequency, metal nature, and glass refractive index [39]. When the surface plasmon is switched on, part of the incident energy is used to maintain the plasmon. So, the intensity of the reflected beam is suddenly diminished and we can acquire information about the resonance conditions by measuring the intensity of the reflected laser beam. Alternatively, it is possible to fix the incident angle of the primary laser beam, and to vary the frequency of the laser beam. Analogously, the intensity of the reflected beam suddenly decreases once the beam frequency reaches the critical value for the resonance condition.

The quantum phenomenon of surface plasmon resonance was discovered in the 1960s by investigating the interaction of a laser beam with metallic surfaces [41]. Metal/glass interfaces were typically obtained by using a glass prism on metal surfaces. Then, the conditions of the incident laser beam were varied to define the optimal resonance conditions by looking at the reflected beam intensity. In the

first configurations, the prism was used to focus the laser beam onto the surface of a metal in bulk.

The plasmon resonance conditions are so narrow in terms of the optimal angle or frequency that any small variation of the interface conditions results in a large variation of the plasmon and, then, in a large variation in the intensity of the reflected light. For that reason, another configuration was proposed to use the plasmon surface resonance for biosensing purposes: the so-called *Kretschmann configuration* [42]. In this system, a very thin metal layer, typically a 50-nm-thick layer of gold, is used as a support for the electron plasmon. The incident and reflected laser beams are managed by the downside of this layer. The topside of the metal layer is instead used to immobilize probe antibodies and to study the interaction with proteins and antigens by using a microfluidic system. The evanescent wave is affected by the refractive index of the topside of the system because it extends for no more than 200 nm over the glass/metal interface [40]. Then, when the probe molecules interact with target ones, the average refractive index changes. This changes the evanescent wave, which modifies the plasmon and slightly changes the resonance conditions. Therefore, acquisition of the intensity of the reflected beam registers the molecular binding or interaction on the topside in a Kretschmann system, as schematically shown by Fig. 1.3.

The invention of such a nano-biosensor led to the birth of a worldwide company, Biacore (now part of General Electrics Healthcare), that is the worldwide leader in this nano-biosensing technology. With use of its instruments, interactions between monoclonal antibodies and antigens were originally investigated by Robert Karlsson, Anne Michaelsson, and Lars Mattsson [43]. Further investigations by using antibody fragments were performed by Gabrielle Zeder-Lutz [44]. Very specific protein–protein interactions were also improved by developing special molecular precursors based on ethylene glycol monolayer by George Whitesides [45, 46] or based on LipaDEA by Inger Vikholm-Lunding and Martin Albers [47].

In Chap. 4, Inger Vikholm-Lunding and Martin Albers, from a VTT laboratory in Tampere (Finland), summarize the physics of surface plasmon resonance, the

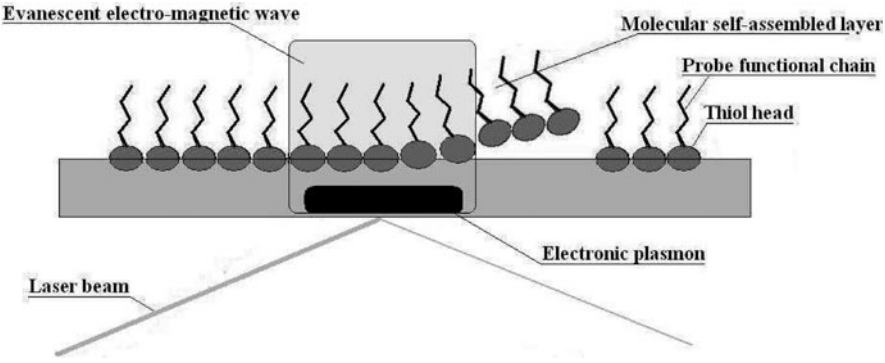

Fig. 1.3 In a small metallic layer, the incident laser beam creates the plasmon, which is affected by molecules in the other side through the evanescent wave

basic principle of the related biosensors, and recent advancements in more reliable surfaces that improve the specificity of molecular recognition.

1.5 Quantum Systems and Electrical Charge Confinement

Nanosized structures made of metals or organic molecules are presented in Chaps. 3 and 4. In both cases, they are nanostructures but they have only one dimension on the nanoscale. As we have seen before, the confinement of the electron sea in a layer with a thickness of only 50 nm results in the appearance of the plasmon resonance. The appearance of the plasmon is due to the quantum nature of the electrons. That means we can try to observe that charge quantization through a direct current measurement. Although the theory of plasmon resonance involves some equations for the current density in the metal surface related to the plasmon [48], it is not reliable to measure directly electron current related to plasmon resonance. However, we can further reduce the layer thickness until the quantum phenomena are so predominant that their effects on the electrical flow through the nanolayer may be measured directly. The ultimate limit of this squeezing would be the single atoms in the conducting layer, which correspond to a metal layer with thickness below 1 nm.

Modern nanotechnology offers a simple method to obtain single-atom-thick and highly oriented crystals of metallic nature: graphene. Graphene has a single atomic layer obtained by mechanical [49] or chemical [50] exfoliation of graphite. The mechanical exfoliation is simply achieved by peeling the graphite, whereas the chemical exfoliation is obtained by using aggressive acids that intercalate between the graphite sheets and cause them to detach from each other. In both cases, the result is a monodispersed suspension of single graphite layers, which are called graphene. Graphene may be cast onto substrate surfaces and then characterized in terms of electrical characteristics. The electrical conductivity on a graphene single sheet is of ambipolar nature [49]. Thus, the intrinsic carrier states in graphene are due to both electrons and holes. It is interesting that even the Schrödinger equation leads to stationary states [51] in the third dimension (that normal to the graphene plane). This means that the electrons confined in the graphene layer have only quantized wavelength in the third dimension. This means we have a quantum well.

In solid-state physics, quantum wells are usually obtained by fabricating a very thin semiconducting layer between two insulating ones [52]. They have thickness on the submicron scale depending on the fabrication techniques. They are usually used for quantum lasers [53] and charge quantization confinement [54]. Usually, the quantum confinement is again measured by means of optical effects. On the other hand, current measurements are directly possible in graphene layers, which have quantum well states [55].

Ideally, graphene sheets may be rolled up to obtain carbon nanotubes. Carbon nanotubes are monoatomically flat tubes with the regular crystal structure of a graphene sheet. They are fabricated by means of arc discharge [56] or chemical vapor deposition [57]. The final product is a set of tubes that may be individual

single-walled tubes or individual multiwalled tubes, depending on the fabrication conditions. They have amazing electrical properties with orders of magnitude improvements in the electrical conductivity [58] and the mean free path [59] of the charge carriers owing to ballistic transport of electrons and holes in their walls. Thus, carrier confinement is also possible in one dimension by using carbon nanotubes because their external radius is typically 2 nm in the case of a single-walled tube. In that case, the electrons are free to move in the tube, remaining confined in its wall [60].

Analogously, an electron may be confined in a quantum region by its injection in a nanosized conducting cube surrounded by insulating material. In such a case, the Schrödinger wavelength is quantized in all three spatial dimensions and pure quantized energy states emerge in the system. So, electrons may be trapped only in steady states in the nanosized cube, whereas any interaction with them shows fully quantized energy. A system that can trap electrical charge carriers at a point is called a quantum dot [61]. Individual small clusters of metallic [62] or semiconducting [63, 64] atoms embedded in insulating materials can produce quantum dots that can work at room temperature. Another possibility is to obtain granular structures by using polysilicon [65]. This results in individual grains separated from each other by tunneling junctions. A further possibility is to embed metal clusters into an insulating material [61]. A third one is to create a monodispersed small metallic cluster in a liquid by stabilizing the metallic cores with alkanethiols [66]. A fourth one is to grow semimetallic nanoclusters within an organic matrix [62]. In all these cases, quantum confinement within the nanostructures obtained has been demonstrated by both electrical and optical characterization.

The electrical properties of graphene, carbon nanotubes, and metallic nanoparticles are highly sensitive to the chemical environment and, then, they are suitable for chemical or biomolecular sensing. Janos Fendler envisaged the used of colloidal nanoparticles for molecular recognition [67]. Smalley applied carbon nanotubes to gas sensing [68]. We obtained improved sensitivity in biosensing using both gold nanoparticles [69] and carbon nanotubes [70]. As we have seen, quantum phenomena take place in these nanosystems and they are directly observable in the electrical properties of the systems. For example, Schönenberger measured direct electron quantum trapping in a metallic nanoparticle in 1992 [62], whereas we observed a similar phenomenon in semiconducting nanoparticles a few years later [63].

In Chap. 5, I summarize the physics of these quantum systems. The electrical properties of quantum wells, wires, and dots are described and their physics is presented. Then, the use of these nanosystems to enhance the properties of electrochemical biosensors is reviewed.

1.6 Molecular Confinement by Optical Nanomanipulation

We have seen that charge confinement is easily investigated by using electromagnetic waves interacting with the confined electrons or holes. This also leads to the development of technologies that use this interaction for nano-biosensing purposes.

The confinement of electrons within 50-nm-thick metal layers leads to applications of plasmon resonance in molecular detection through the interaction of molecules with the evanescent wave of a laser beam and, thus, with the confined electrons. In general, we can say that nanotechnology plays a role in the combination of optics with microfluidics, leading to a new branch of science: integrated optofluidics [71].

Modern optofluidics addresses new functionalities in optical and fluidic systems to develop new methods to manipulate, assemble, pattern, and sense cells or biological molecules in a fluidic environment [72]. The optical laser beam provides new tools for biomanipulation, whereas the fluidic system provides environments similar to native ones for biological systems.

To manipulate objects, highly intense and focused laser beams create gradient forces to trap the objects, as shown in Fig. 1.4. These forces move and trap molecules or cells owing to their electrical charges usually being nonuniformly distributed on the surface [73, 74]. So, gradients focused to a point are used to concentrate cell samples, whereas separation of molecules is obtained thanks to different polarizations in different compounds. Liquid samples are moved along a complex pathway to separate target molecules from interfering ones, to obtain interactions with probe molecules, to mix the complexes obtained with labels, and to obtain the final spots for sensing [75]. Therefore, optical tweezers [76] are a unique tool for nano-biosensing. However, they have some drawbacks owing to their intrinsic physical properties. First, highly intense optical beams might damage the objects, especially in case of soft materials. Moreover, the use of a single laser beams limits manipulations in large-scale as well as high-throughput detection.

Merging electronics with optofluidics offers another tool: optoelectronic tweezers [77, 78]. In this case, charges induced in sample regions of a photoconductive

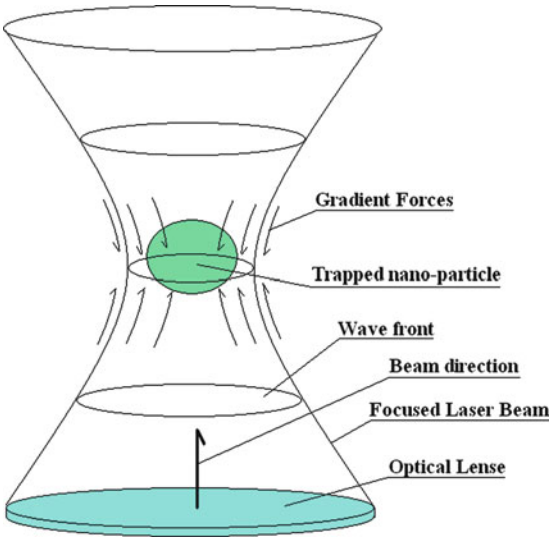

Fig. 1.4 In optical tweezers, gradient forces generated with a focused laser beam trap colloidal nanoparticles at a point

substrate create dielectrophoretic pathways. These charged regions create electrical force gradients that trap biological objects. Once the objects have been trapped, dynamical reconfiguration of the charged regions moves and manipulates the objects along complex pathways [77] even for parallel manipulation [78]. This technique proposes something similar to a "light-induced dielectrophoresis," offering all the advantages of the well-known electrophoresis, which is widely used in biology. An advantage of optoelectronic tweezers is that they use an optical power intensity that is up to 5 orders of magnitudes lower than that required by conventional optical tweezers. Moreover, they are more suitable for large-scale nanomanipulations and high throughput with biological objects. Optical tweezers are also used to permanently assemble molecules in complex structures [79] and this is done at the nanoscale owing to their capability to manipulate single objects at a time.

Very recent years have seen in-depth investigations and extensive developments of optical and optoelectronic tweezers. Different groups have provided exciting results. For example, Yen-Heng Lin and Gwo-Bin Lee demonstrated the feasibility of light-induced concentration and fusion of nanoparticles to assist structure formation by self-assembly [80]. Syoji Ito, Hiroyaki Yoshikawa, and Hiroshi Masuhara obtained photochemical fixation on polymers by optical patterning [81]. Misdy Lee and Philippe Fauchet used photonic crystals for sensing proteins [82]. Ming C. Wu and coworkers invented the NanoPen [83], an innovative technique for dynamic patterning of nanoparticles, and demonstrated its feasibility in cell manipulation.

In Chap. 6, Ming C. Wu from Berkeley University (USA) describes all these exciting findings by introducing the physics of optoelectronic tweezers, and by summarizing the most relevant results published in the field.

1.7 Sensing Biochip Made Using Nanoscale Electronics

In the previous sections, we saw that nano-biosensing is possible by using plasmon resonance, as well as electrochemical detection or atomic force spectroscopy. We have seen that patterning is possible with nanoscale precision both for mass-sensitive as well as for optical biosensing. The very large scale of integration (VLSI) of modern microelectronics offers the possibility to integrate all these nano-biosensing techniques in a single biochip. Modern electronics is able to integrate memory storage with a capacity of more of 200 GB in a single pen drive with a readout speed of up to more than 200 MB per second [84], computation with 147.6×10^9 instructions per second with the novel Core i7 from Intel [85], and a data communication rate of terabits per second in optical fibers [86]. That means there are many opportunities to achieve so-called *distributed diagnostics*. For example, high-throughput DNA detection with a capability similar to that provided by the Affymetrix technology may be replicated onto a silicon biochip that can provide faster and label-free assays with fully electronic readers [87]. This is highly useful to address in-field large screenings of populations. Continuous monitoring of some important metabolites, such as glucose for diabetic patients [88, 89], might be replicated in a fully implantable [90], subcutaneous

biochip [91] providing real-time monitoring and data transmission [92] to open up the human metabolism for remote monitoring. Electrocardiogram acquisition with accuracy similar to that of current hospital instruments was proposed in the form of wearable patches [93] worn under clothes during normal daily life.

For the envisaged new revolution in technology to succeed, modern microelectronics needs to integrate many different functions on the same chip: sample manipulation, biosensing, data acquisition, data elaboration, data verification, data storage, data transmission, energy harvesting. This creates new challenges for system integration design for heterogeneous systems [94]. New biochip heterogeneous systems need to integrate organic molecules onto silicon, including probes (e.g., proteins) and nanostructures (e.g., carbon nanotubes). They need to integrate analog front ends with analog-to-digital converters, microcontrollers with random-access memory and erasable programmable read-only memory (EPROM), radio-frequency transceivers, batteries, large capacitors, and subsystems for energy scavenging.

Each of these chip features requires special efforts to succeed in distributing diagnostics from hospitals to homes. For example, highly packed self-assembled monolayer films with organic molecules with special functions for biosensing purposes have been investigated on gold [95], and now are required for silicon. Analog front ends with very low power consumption [96] are now required for remotely powered biochips. Low-noise front ends [97] are necessary to obtain signals from low-intensity samples. CMOS imagers also integrating a digital signal processing core for image postprocessing [98] are indispensable for real-time acquisition and detail quantification. Of course, the final expected result is solutions that can provide a fully integrated lab-on-chip in systems similar to credit cards [99] or to bring ELISA tests into our hands [100].

In recent years, we have demonstrated improved reliable sensing of DNA and proteins by integrating nanostructured thin-film precursors onto the chip electrodes [32, 36]. Roland Thewes and partners have shown the possibility of fully electronic detection of DNA on a chip [87, 101]. Yuki Maruyama applied CMOS photodetectors to DNA detection on a chip [102], whereas Edoardo Charbon showed the possibility for a large-scale CMOS imager based on *single-photon avalanche diode* lab-on-chip applications [103]. In Chap. 7, Edoardo Charbon and Yuki Maruyama, now both at the Technical Institute of Delft (The Netherlands), summarize the most advanced results in the field of VLSI chips for biosensing by discussing the new 90-nm technology node that nowadays provides higher possible scales of integration.

1.8 Quantized Energy and Its Harvesting

As we saw in the previous section, an innovative biochip needs system integration of biological and organic molecules with silicon substrates, analog front ends with digital memories, and radio-communication transceivers with systems for remote

powering. In general, remote powering [104] and energy scavenging [105] are two key features of the modern biochip to obtain autonomous nodes in distributed diagnostics monitoring. The key role of energy scavenging and remote powering is due to weight constraints for wearable or implantable medical systems. These systems are required to be extremely small and light for their use during normal human daily life. If we want to develop innovative systems for remote monitoring at home of chronic patients and healthy people, then we need to develop systems that can be worn on the skin or implanted under the skin without any pain or any trouble. Patches on the chest for continuous electrocardiogram monitoring [93] should use extremely light and small batteries for the power supply. A subcutaneous implant for measuring glucose in the interstitial tissues should be remotely powered by radio-frequency energy [106]. A similar system for measuring glucose within a blood vessel might recover energy from glucose consumption [107] or from vibrations [108] induced by a fluidic flux.

Energy scavenging or remote powering for autonomous nanosensors and intelligent nodes has been extensively investigated in recent years. Inductive links have been investigated in depth for powering implanted sensors [109]. A system for an inductive link consists of two coils: the primary coil placed on the skin, and a second coil located under the skin. The first generates a variable magnetic field by means of an alternating current flowing through it; the variation of the magnetic flux through the implanted coil generates an electromotive force, in accordance with the Faraday–Neumann–Lenz law. In that way, the energy is transferred from the first to the second coil, and the remote powering is obtained.

Human movements also provide power that we can transform into electrical energy. This energy harvesting is of three different kinds – electromagnetic, electrostatic, and piezoelectric – depending on the method chosen to transduce the kinetic energy. As known, kinetic harvesting by using electromagnetic transducers is used for high-power applications, typically with synchronous machines in power plants. It is also used for powering small biosystems as well as quartz wristwatches such as the Seiko Kinetic [110]. In that case, the watch is able to automatically recharge itself by means of the wrist movements by means of a magnetic rotor.

Body thermal gradients also generate energy [111]. The physical phenomenon used is the Seebeck effect [112]: in the presence of a temperature difference between two different metals or semiconductors, a voltage drop is created across them. The core element of this kind of scavenger is a thermocouple.

A fuel cell is an electrochemical device that generates current through the reaction between two chemical species, one reduced at the anode and the other oxidized at the cathode [113]. The main difference from a classic battery is that the fuel cell can produce energy continuously, as long as the reactants continue to be present. So, an enzymatically catalyzed fuel cell based on the glucose redox reaction might be used for remote powering of a biochip in veins and arteries, where glucose is in sufficient quantity [114].

Alternatively, solar energy is converted into electrical energy by using photovoltaic cells. In the case of miniaturized photovoltaic cells, light and small

systems for energy scavenging from solar light are used for powering biomedical wearable diagnostics tools [115].

Recently, Teresa Meng showed that coils with a size of only 1 mm may be used to remotely power a subcutaneous brain electrode [116]. Sven Kerzenmacher reported the possibility to recover energy from electrochemical transformation of glucose in a fuel cell [114]. Koushik Maharatna and Bashir Al-Hashimi explored structural variability of carbon nanotubes with the aim of developing photovoltaic devices [117]. In Chap. 8, Koushik Maharatna and Bashir Al-Hashimi concentrate on harvesting from solar energy as enhanced by using carbon nanotubes and focus on powering body-worn nanosensors.

1.9 Toward Error-Free and Fault-Tolerant Nano-Biosensing Chips

As we have seen, we can obtain nano-biosensing chips for distributed diagnostics by integrating state-of-the-art technologies in the fields of nanotechnology, biotechnology, and microelectronics. Microelectronics already provides reliable silicon chip production with the technology node at 90 nm and it is now setting the new chip generation at 45 nm. This means a tremendous scale of integration. Biotechnology already provides recombinant DNA sequences and antibodies usable as molecular probes in biosensors for detection specificity. Nanotechnology already offers low-cost methods for producing metallic nanoparticles and carbon nanotubes that help in enhancing detection sensitivity and in lowering detection limits. So, system integration is now possible by merging contributions from different branches of science and technology. However, system integration has to deal with a new challenge to succeed in widely distributed biomedical systems: error-free and fault-tolerant biosensors.

Error-free systems already exist in information and communication theory as well as in microelectronics. In information theory, error detection and correction, or error control, are methods enabling error management to provide reliable data from unreliable noisy channels or communication systems. Noise affects all communication channels and, thus, errors are inevitably added to signals during their transfer from transmitters to receivers. Error detection enables identification of errors in the data received, whereas error correction enables reconstruction of the original transmitted data. Error correction is usually performed in two different ways: the so-called *automatic repeat request* (ARQ) [118] and the *forward error correction* (FEC) [119]. In the ARQ method, a verification-code sequence is added to the data received and the data are transmitted back to the data source with a data-retransmission request. Once the data have been received back, they are checked against the verification code and the data are retransmitted if the check fails. In the FEC method, data redundancy is used to improve information on the data sent. The transmitter adds a verification code to the transmitted data. Once the data have been received, the verification code is used to verify or reconstruct data that are most

likely similar to the original data. Of course, the two methods are often merged to obtain hybrid automatic protocols for error-free data transmission.

Very similar strategies for error correction are often used in flash memory. Flash memory is a nonvolatile memory usually used in memory cards and USB pen drives. It is a specific type of EPROM where data are managed (written and deleted) in blocks. In such a memory, an error-correcting code is written in a few bytes in each memory block. That code is used as a checksum each time data integrity is verified. The idea is to check for errors that might be accidentally introduced during writing, copying, or storing operations. The checksum may be recalculated any time and compared with that stored in the check bytes previously registered in the data block. If the calculated checksum does not match the stored one, the data are corrupted.

Another very important concept introduced in computer science in the 1970s is that of fault-tolerant systems. The fault tolerance is the ability of a system to tolerate faults without stopping its working functions. In 1983, Algirdas Avižienis introduced at the annual International Symposium on Computer Architecture the concept of fault-tolerant system design by introducing the ideas of system pathology, fault detection, and proper recovery algorithms [120]. The fault-tolerance concept was initially considered only for single processors. Nowadays, the concept is largely used also in multicore computing [121], multimachine interactions [122], and network-on-chip [123]. In general, fault tolerance is the ability of a machine to continue operating in the event of failure of one of its components. Of course, the quality of fault-survived working functions depends on how many components fail and how severe the fault events are. But, in any case, the machine has the possibility to remain operating even only partially, which is so important in comparison with a not-fault-tolerant system that goes into total breakdown in the case of a small failure of a single component.

To succeed in distributed diagnostics, present development of nano-biosensing needs to take into account the strategies of fault-tolerant and error-free systems to ensure biochips are robust enough to be used at home by patients and healthy people who may have little knowledge of science and technology. In Chap. 9, Yang Liu and Shantanu Chakrabartty present the new concept of error-free biosensors and describe new lines of development toward robust and reliable nano-biosensing VLSI chips.

1.10 Conclusion

In this first chapter, we have seen different aspects of nano-biosensing. New detection methods are offered by nanotechnology for unexpected scales of sensitivity. Atomic force spectroscopy enables detection of piconewton forces on samples scanned with picometer resolution. Surface plasmon resonance allows molecular detection of very few nanomoles in protein–protein interactions. Mass-sensitive biodetection can also extend to the range to sub-nanomoles. In addition, optical

tweezers enable manipulation in a liquid at the level of a single cell and a single molecule, even allowing nanopattering of the substrate surface. Electrochemical sensing offers fully electronic readers for biosensing, with the possibility to directly integrate silicon chips, organic nanoenhancers, and molecular probes. With the 90-nm technology node fully operating now and the newly envisaged technology node at 45 nm, modern VLSI electronics provide a previously impossible scale of integration and new ideas for energy harvesting and the development of error-free biochips will lead to a monitoring nano-biosensing chip that is autonomous, robust, and reliable enough for daily use at home or in the field.

Scientific and technical details making it possible that distributed diagnostics might became a reality in the next 10–15 years are presented and discussed in the next pages of this book.

References

1. J. Devreese, Sensing the importance of nanosensors: Feynman's visionary 1959 Christmas lecture, Somnologie – Schlafforschung und Schlafmedizin 11/4 (2007) 268.
2. M.R. Mozafari, A review of scanning probe microscopy investigations of liposome–DNA complexes, Journal of Liposome Research 15/1 (2005) 93.
3. C.E.D. Chidsey, D.N. Loiacono, T. Sleator, S. Nakahara, STM study of the surface morphology of gold on mica, Surface Science 200/1 (1988) 45.
4. S. Carrara, P. Facci, C. Nicolini, More information on the calibration of scanning stylus microscopes by two-dimensional fast Fourier-transform analysis, Review of Scientific Instruments 65/9 (1994) 2860.
5. E.S. Snow, Fabrication of silicon nanostructures with a scanning tunneling microscope, Applied Physics Letters 63/6 (1993) 749.
6. G. Binnig, C.F. Quate, C. Gerber, Atomic force microscope, Physical Review Letters 56/9 (1986) 930.
7. A. Engel, C.-A. Schoenenberger, D.J. Müller, High resolution imaging of native biological sample surfaces using scanning probe microscopy, Current Opinion in Structural Biology 7/2 (1997) 279.
8. D.D. Dunlap, R. García, E. Schabtach, C. Bustamante, Masking generates contiguous segments of metal-coated and bare DNA for scanning tunneling microscope imaging, Proceedings of the National Academy of Sciences of the United States of America 90/16 (1993) 7652.
9. R. Garcia, Imaging of metal-coated biological samples by scanning tunneling microscopy, Ultramicroscopy 27/4 (1989) 367.
10. L. Haggerty, STM and AFM in biotechnology, Biotechnology Progress 9/1 (1993) 1.
11. W.M. Heckl, Applications of atomic force microscopy to structural characterization of organic thin films, Ultramicroscopy 42 (1992) 1073.
12. K. Yoshikawa, Nucleation and growth in single DNA molecules, Journal of the American Chemical Society 118/4 (1996) 929.
13. L. Yang, AFM and impedance spectroscopy characterization of the immobilization of antibodies on indium–tin oxide electrode through self-assembled monolayer of epoxysilane and their capture of *Escherichia coli* O157: H7, Biosensors and Bioelectronics 20/7 (2005) 1407.
14. M. Quinto, A molecular resolution AFM study of gold-adsorbed glucose oxidase as influenced by enzyme concentration, Journal of Electroanalytical Chemistry 448/1 (1998) 51.

15. K. Nakano, T. Yoshitake, Y. Yamashita, E. Bowden, Cytochrome c self-assembly on alkanethiol monolayer electrodes as characterized by AFM, IR, QCM, and direct electrochemistry, Langmuir 23/11 (2007) 6270.
16. M.B. Faletto, Cytochrome P3–450 cDNA encodes aflatoxin B1–4-hydroxylase, Journal of Biological Chemistry 263/25 (1988) 12187.
17. I. Lee, Biomolecular electronics: vectorial arrays of photosynthetic reaction centers, Physical Review Letters 79/17 (1997) 3294.
18. M. Rief, Single molecule force spectroscopy on polysaccharides by atomic force microscopy, Science 275/5304 (1997) 1295.
19. S.B. Smith, Overstretching B-DNA: the elastic response of individual double-stranded and single-stranded DNA molecules, Science 271/5250 (1996) 795.
20. B. Yasser, S. Bruno, G. Binning, Domain walls on graphite mimic DNA, Angewandte Chemie International Edition (2002) 1546.
21. Y. Bustanji, C.A. Arciola, M. Conti, E. Mandello, L. Montanaro, B. Samorí, Dynamics of the interaction between a fibronectin molecule and a living bacterium under mechanical force, Proceedings of the National Academy of Sciences of the United States of America 100/23 (2003) 13292.
22. A. Yersin, Elastic properties of the cell surface and trafficking of single AMPA receptors in living hippocampal neurons, Biophysical Journal 92/12 (2007) 4482.
23. S.E. Cross, J. Tondre, R. Wong, J.Y. Rao, J.K. Gimzewski, AFM-based analysis of human metastatic cancer cells, Nanotechnology 19/38 (2008) 384003.
24. J. Spinke, Molecular recognition at self-assembled monolayers: the construction of multicomponent multilayers, Langmuir 9/7 (1993) 1821.
25. O.I. Kiselyova, AFM study of membrane proteins, cytochrome P450 2B4, and NADPH-cytochrome P450 reductase and their complex formation, Archives of Biochemistry and Biophysics 371/1 (1999) 1.
26. A. Raab, Antibody recognition imaging by force microscopy, Nature Biotechnology 17 (1999) 902.
27. I. Langmuir, The constitution and fundamental properties of solids and liquids. II. Liquids, Journal of the American Chemical Society 39 (1917) 1848.
28. K. Noda, N.A. Zorin, C. Nakamura, M. Miyake, I.N. Gogotov, Langmuir–Blodgett film of hydrogenase for electrochemical hydrogen production, Thin Solid Films 327 (1998) 639.
29. T.J. Reece, S. Ducharme, A.V. Sorokin, M. Poulsen, Nonvolatile memory element based on a ferroelectric polymer Langmuir–Blodgett film, Applied Physics Letters 82/1 (2003) 142.
30. V.E.C. Nicolini, F. Antolini, P. Catasti, P. Facci Thermal stability of protein secondary structure in Langmuir–Blodgett films, Biochimica et Biophysica Acta 1158/3 (1993).
31. F. Antolini, S. Paddeu, C. Nicolini, Heat stable Langmuir–Blodgett film of glutathione-S-transferase, Langmuir 11/7 (1995) 2719.
32. S. Carrara, V. Bhalla, C. Stagni, L. Benini, A. Ferretti, F. Valle, A. Gallotta, B. Riccò, B. Samorì, Label-free cancer markers detection by capacitance biochip, Sensors and Actuators B: Chemical 136/1 (2009) 163.
33. Y. Lvov, K. Ariga, I. Ichinose, T. Kunitake, Assembly of multicomponent protein films by means of electrostatic layer-by-layer adsorption, Journal of the American Chemical Society 117/22 (1995) 6117.
34. S.C.V. Erokhin, H. Amenitch, S. Bernstorff, C. Nicolini, Semiconductor nanoparticles for quantum devices, Nanotechnology 9 (1998) 158.
35. A. Tolkki, E. Vuorimaa, V. Chukharev, H. Lemmetyinen, P. Ihalainen, J. Peltonen, V. Dehm, F. Wuürthner, Langmuir−Schaeffer films from a π−π stacking perylenediimide dye: organization and charge transfer properties, Langmuir 26/9 (2009) 6630.
36. S. Carrara, L. Benini, V. Bhalla, C. Stagni, A. Ferretti, A. Cavallini, B. Riccò, B. Samorì, New insights for using self-assembly materials to improve the detection stability in label-free DNA-chip and immuno-sensors, Biosensors and Bioelectronics 24/12 (2009) 3425.

37. F. Caruso, Enzyme encapsulation in layer-by-layer engineered polymer multilayer capsules, Langmuir 16/4 (2000) 1485.
38. O. Hayden, R. Bindeus, C. Haderspöck, K.-J. Mann, B. Wirl, F.L. Dickert, Mass-sensitive detection of cells, viruses and enzymes with artificial receptors, Sensors and Actuators B: Chemical 91/1–3 (2003) 316.
39. K. Kurihara, Theoretical understanding of an absorption-based surface plasmon resonance sensor based on Kretchmann's theory, Analytical Chemistry 74/3 (2002) 696.
40. P. Schuck, Kinetics of ligand binding to receptor immobilized in a polymer matrix, as detected with an evanescent wave biosensor. I. A computer simulation of the influence of mass transport, Biophysical Journal 70/3 (1996) 1230.
41. E. Kretschmann, H. Raether, Radiative decay of nonradiative surface plasmons excited by light (surface plasma waves excitation by light and decay into photons applied to nonradiative modes) Zeitschrift für Naturforschung 23A (1968) 2135.
42. A. Hatta, Y. Chiba, W. Suëtaka, Infrared absorption study of adsorbed species at metal/water interface by use of the Kretschmann configuration, Surface Science 158/1–3 (1985) 616.
43. R. Karlsson, A. Michaelsson, L. Mattsson, Kinetic analysis of monoclonal antibody–antigen interactions with a new biosensor based analytical system, Journal of Immunological Methods 145/1–2 (1991) 229.
44. G. Zeder-Lutz, R. Wenger, M.H.V. Van Regenmortel, D. Altschuh, Interaction of cyclosporin A with an Fab fragment or cyclophilin affinity measurements and time-dependent changes in binding, FEBS Letters 326/1–3 (1993) 153.
45. M. Mrksich, G.M. Whitesides, Poly(ethylene glycol), American Chemical Society, Washington, 1997, p. 361.
46. R.G. Chapman, E. Ostuni, S. Takayama, R.E. Holmlin, L. Yan, G.M. Whitesides, Surveying for surfaces that resist the adsorption of proteins, Journal of the American Chemical Society 122/34 (2000) 8303.
47. K. Tappura, I. Vikholm-Lundin, W.M. Albers, Lipoate-based imprinted self-assembled molecular thin films for biosensor applications, Biosensors and Bioelectronics 22/6 (2007) 912.
48. F. Flores, F. García-Moliner, Model-independent theory of surface plasmons, Solid State Communications 11/9 (1972) 1295.
49. K.S. Novoselov, A.K. Geim, S.V. Morozov, D. Jiang, Y. Zhang, S.V. Dubonos, I.V.Grigorieva, A.A. Firsov, Electric field effect in atomically thin carbon films, Science 306/5696 (2004) 666.
50. Y. Hernandez, V. Nicolosi, M. Lotya, F.M. Blighe, Z. Sun, S. De, I.T. McGovern, B. Holland, M. Byrne, Y.K. Gun'Ko, J.J. Boland, P. Niraj, G. Duesberg, S. Krishnamurthy, R. Goodhue, J. Hutchison, V. Scardaci, A.C. Ferrari, J.N. Coleman, High-yield production of graphene by liquid-phase exfoliation of graphite, Nature Nanotechnology 3/9 (2008) 563.
51. M.I. Katsnelson, Graphene: carbon in two dimensions, Materials Today 10/1–2 20.
52. R. Dingle, C.H. Henry, U.S. Patent #3982207, issued September 21, 1976, Quantum Effects in Heterostructure Lasers, filed March 7, 1975.
53. A.A. Belyanin, F. Capasso, V.V. Kocharovsky, V.V. Kocharovsky, M.O. Scully, Infrared generation in low-dimensional semiconductor heterostructures via quantum coherence, Physical Review A 63/5 (2001) 053803.
54. F.F. So, S.R. Forrest, Evidence for exciton confinement in crystalline organic multiple quantum wells, Physical Review Letters 66/20 (1991) 2649.
55. F. Patthey, W.D. Schneider, Layer-by-layer-resolved quantum-well states in ultrathin silver islands on graphite: a photoemission study, Physical Review B 50/23 (1994) 17560.
56. C. Journet, Large-scale production of single-walled carbon nanotubes by the electric-arc technique, Nature 388/6644 (1997) 756.
57. L.F. Sun, J.M. Mao, Z.W. Pan, B.H. Chang, W.Y. Zhou, G. Wang, L.X. Qian, S.S. Xie, Growth of straight nanotubes with a cobalt–nickel catalyst by chemical vapor deposition, Applied Physics Letters 74/5 (1999) 644.

58. T.W. Ebbesen, H.J. Lezec, H. Hiura, J.W. Bennett, H.F. Ghaemi, T. Thio, Electrical conductivity of individual carbon nanotubes, Nature 382/6586 (1996) 54.
59. C.T. White, Carbon nanotubes as long ballistic conductors, Nature 393/6682 (1998) 240.
60. S.J. Tans, M.H. Devoret, H. Dai, A. Thess, RE. Smalley, LJ Geerligs, Individual single-wall carbon nanotubes as quantum wires, Nature 386/6624 (1997) 474.
61. D.V. Averin, A.N. Korotkov, K.K. Likharev, Theory of single-electron charging of quantum wells and dots, Physical Review B 44/12 (1991) 6199.
62. C. Schonenberger, H. Van Houten, H.C. Donkersloot, A.M.T. Van Der Putten, Single-electron tunneling up to room temperature, Physica Scripta T45 (1992).
63. V.E.P. Facci, S. Carrara, C. Nicolini, Room-temperature single-electron junction, Proceedings of the National Academy of Sciences of the United States of America 93/20 (1996) 10556.
64. L. Zhuang, L. Guo, S.Y. Chou, Silicon single-electron quantum-dot transistor switch operating at room temperature, Applied Physics Letters 72/10 (1998) 1205.
65. D.M. Pooley, Fabrication and electron transport in multilayer silicon-insulator-silicon nanopillars, Journal of Vacuum Science and Technology 17/6 (1999) 3235.
66. K.V. Sarathy, P.J. Thomas, G.U. Kulkarni, C.N.R. Rao, Superlattices of metal and metal−semiconductor quantum dots obtained by layer-by-layer deposition of nanoparticle arrays, Journal of Physical Chemistry B 103/3 (1999) 399.
67. J.H. Fendler, Self-assembled nanostructured materials, Chemistry of Materials 8/8 (1996) 1616.
68. J. Kong, N.R. Franklin, C. Zhou, M.G. Chapline, S. Peng, K. Cho, H. Dai, Nanotube molecular wires as chemical sensors, Science 287/5453 (2000) 622.
69. V.V. Shumyantseva, S. Carrara, V. Bavastrello, D. Jason Riley, T.V. Bulko, K.G. Skryabin, A.I. Archakov, C. Nicolini, Direct electron transfer between cytochrome P450scc and gold nanoparticles on screen-printed rhodium–graphite electrodes, Biosensors and Bioelectronics 21/1 (2005) 217.
70. S. Carrara, V.V. Shumyantseva, A.I. Archakov, B. Samorì, Screen-printed electrodes based on carbon nanotubes and cytochrome P450scc for highly sensitive cholesterol biosensors, Biosensors and Bioelectronics 24/1 (2008) 148.
71. C. Monat, P. Domachuk, B.J. Eggleton, Integrated optofluidics: a new river of light, Nature Photonics 1/2 (2007) 106.
72. A. Ashkin, J.M. Dziedzic, Optical trapping and manipulation of viruses and bacteria, Science 235/4795 (1987) 1517.
73. L. Novotny, R.X. Bian, X.S. Xie, Theory of nanometric optical tweezers, Physical Review Letters 79/4 (1997) 645.
74. A. Ashkin, Optical trapping and manipulation of neutral particles using lasers, Proceedings of the National Academy of Sciences of the United States of America 94/10 (1997) 4853.
75. J.T. Blakely, R. Gordan, D. Sinton, Flow-dependent optofluidic particle trapping and circulation, Lab on a Chip 8/8 (2008) 1350.
76. S.M. Block, L.S.B. Goldstein, B.J. Schnapp, Bead movement by single kinesin molecules studied with optical tweezers, Nature 348/6299 (1990) 348.
77. P.Y. Chiou, A.T. Ohta, M.C. Wu, Massively parallel manipulation of single cells and microparticles using optical images, Nature 436/7049 (2005) 370.
78. A.O.P.Y. Chiou, M.C. Wu, A novel optoelectronic tweezer using light induced dielectrophoresis, Optical MEMS, 2003 IEEE/LEOS International Conference on (2003) 8.
79. J.A. Rogers, Optoelectronic tweezers: organizing nanowires, Nature Photonics 2/2 (2008) 69.
80. Y.-H. Lin, G.-B. Lee, An optically induced cell lysis device using dielectrophoresis, Applied Physics Letters 94/3 (2009) 033901.
81. S. Ito, H. Yoshikawa, H. Masuhara, Optical patterning and photochemical fixation of polymer nanoparticles on glass substrates, Applied Physics Letters 78/17 (2001) 2566.
82. M. Lee, P.M. Fauchet, Two-dimensional silicon photonic crystal based biosensing platform for protein detection, Optics Express 15/8 (2007) 4530.

83. A. Jamshidi, S.L. Neale, K. Yu, P.J. Pauzauskie, P.J. Schuck, J.K. Valley, H.-Y. Hsu, A.T. Ohta, M.C. Wu, NanoPen: dynamic, low-power, and light-actuated patterning of nanoparticles, Nano Letters 9/8 (2009) 2921.
84. E.S.S. Park, J.Y. Shin, S. Maeng, J. Lee, Exploiting internal parallelism of flash-based SSDs, IEEE Computer Architecture Letters 9/1 (2010) 9.
85. X.X.Y. Pan, S. Solanki, X. Liang, R. Bin Adrian Tanjung, C. Tan, T.-C. Chong, Fast CGH computation using S-LUT on GPU, Optics Express 17/21 (2009) 18543.
86. A.K. Hasegawa, Y. Kodama, Signal transmission by optical solitons in monomode fiber, Proceedings of the IEEE 69/9 (1981) 1145.
87. C. Stagni, C. Guiducci, L. Benini, B. Ricco, S. Carrara, C. Paulus, M. Schienle, R. Thewes, A fully electronic label-free DNA sensor chip, IEEE Sensors Journal 7/4 (2007) 577.
88. A. Poscia, M. Mascini, D. Moscone, M. Luzzana, G. Caramenti, P. Cremonesi, F. Valgimigli, C. Bongiovanni, M. Varalli, A microdialysis technique for continuous subcutaneous glucose monitoring in diabetic patients (part 1), Biosensors and Bioelectronics 18/7 (2003) 891.
89. M. Varalli, G. Marelli, A. Maran, S. Bistoni, M. Luzzana, P. Cremonesi, G. Caramenti, F. Valgimigli, A. Poscia, A microdialysis technique for continuous subcutaneous glucose monitoring in diabetic patients (part 2), Biosensors and Bioelectronics 18/7 (2003) 899.
90. G.E. Perlin, A.M. Sodagar, K.D. Wise, Neural recording front-end designs for fully implantable neuroscience applications and neural prosthetic microsystems, Conference Proceedings – IEEE Engineering in Medicine and Biology Society 1 (2006) 2982.
91. B. Yu, N. Long, Y. Moussy, F. Moussy, A long-term flexible minimally-invasive implantable glucose biosensor based on an epoxy-enhanced polyurethane membrane, Biosensors and Bioelectronics 21/12 (2006) 2275.
92. P. Valdastri, S. Rossi, A. Menciassi, V. Lionetti, F. Bernini, F.A. Recchia, P. Dario, An implantable ZigBee ready telemetric platform for in vivo monitoring of physiological parameters, Sensors and Actuators A: Physical 142/1 (2008) 369.
93. L.Y.J. Yoo, S. Lee, H. Kim, H.J. Yoo, A wearable ECG acquisition system with compact planar-fashionable circuit board based shirt, IEEE Transactions on Information Technology in Biomedicine 13/6 (2009) 897.
94. G.D. Micheli, An outlook on design technologies for future integrated systems, IEEE Transactions on Computer-Aided Design of Integrated Circuits and Systems 28 (2009) 777.
95. S. Carrara, V. Bhalla, C. Stagni, B. Samorì, Nanoscale film structure related to capacitive effects in ethylene-glycol monolayers, Surface Science 603/13 (2009) L75.
96. M.H.M. Zhang, M.A. Huque, M.A. Adeeb, A low power sensor signal processing circuit for implantable biosensor applications, Smart Materials and Structures 16/2 (2007) 525.
97. M. Mollazadeh, K. Murari, G. Cauwenberghs, N. Thakor, Micropower CMOS integrated low-noise amplification, filtering, and digitization of multimodal neuropotentials, IEEE Transactions on Biomedical Circuits and Systems 3/1 (2009) 1.
98. F. Xu, J.-J. Zeng, Y.-L. Zhang, Design of a DSP-based CMOS imaging system for embedded computer vision, IEEE Conference on Cybernetics and Intelligent Systems, (2008) 430.
99. Siemens, The quick lab system, http://www.siemens.com/innovation/en/publikationen/publications_pof/pof_fall_2004/sensors_articles/biosensors.htm.
100. P. Grosso, S. Carrara, C. Stagni, L. Benini, Cancer marker detection in human serum with a point-of-care low-cost system, Sensors and Actuators B: Chemical 147/2 (2010) 475.
101. R.T.K. Chakrabarty, Guest editors' introduction: biochips and integrated biosensor platforms, IEEE Design and Test of Computers 24/1 (2007) 8.
102. Y. Maruyama, S. Terao, K. Sawada, Label free CMOS DNA image sensor based on the charge transfer technique, Biosensors and Bioelectronics 24/10 (2009) 3108.
103. E. Charbon, Towards large scale CMOS single-photon detector arrays for lab-on-chip applications, Journal of Physics. D, Applied Physics 41/9 (2008) 094010.

104. K.F.G. Park, C.R. Farrar, T. Rosing, M.D. Todd, Powering wireless SHM sensor nodes through energy harvesting, Springer, New York doi:10.1007/978-0-387-76464-1_19 (2008).
105. C. Mathúna, Energy scavenging for long-term deployable wireless sensor networks, Talanta 75/3 (2008) 613.
106. J. Wang, In vivo glucose monitoring: towards 'sense and Act' feedback-loop individualized medical systems, Talanta 75/3 (2008) 636.
107. F. Sato, M. Togo, M.K. Islam, T. Matsue, J. Kosuge, N. Fukasaku, S. Kurosawa, M. Nishizawa, Enzyme-based glucose fuel cell using vitamin K3-immobilized polymer as an electron mediator, Electrochemistry Communications 7/7 (2005) 643.
108. C. Serre, Vibrational energy scavenging with Si technology electromagnetic inertial micro-generators, Microsystem Technologies 13/11–12 (2007) 1655.
109. M. Sawan, Multicoils-based inductive links dedicated to power up implantable medical devices: modeling, design and experimental results, Biomedical Microdevices 11/5 (2009) 1059.
110. Seiko http://www.seikowatches.com/.
111. L.M. Goncalves, Thermoelectric micro converters for cooling and energy-scavenging systems, Journal of Micromechanics and Microengineering 18/6 (2008) 064008.
112. M. Ujihara, Thermal energy harvesting device using ferromagnetic materials, Applied Physics Letters 91/9 (2007) 093508.
113. F.A. De Bruijn, D. Bruijn, Review: durability and degradation issues of PEM fuel cell components, Fuel Cells 8/1 (2008) 3.
114. S. Kerzenmacher, J. Ducrée, R. Zengerle, F. von Stetten, Energy harvesting by implantable abiotically catalyzed glucose fuel cells, Journal of Power Sources 182/1 (2008) 1.
115. Z. Chen, 980-nm laser-driven photovoltaic cells based on rare-earth up-converting phosphors for biomedical applications, Advanced Functional Materials 19/23 (2009) 3815.
116. C.K.Z. Zumsteg, S. O'Driscoll, G. Santhanam, R. Ahmed, K. Shenoy, T. Meng, Power feasibility of implantable digital spike sorting circuits for neural prosthetic systems, IEEE Transactions on Neural Systems and Rehabilitation Engineering 13 (2005) 272.
117. K.M.K. El-Shabrawy, B. Al-Hashimi, Exploiting SWCNT structural variability towards the development of a photovoltaic device, International Symposium on Integrated Circuit, ISIC 2009, conference proceeding p. 248.
118. Y.M. Abdelmalek, New optical random access code-division multiple-access protocol with stop-and-wait automatic repeat request, Optical Engineering 46/6 (2007) 065007.
119. V.J. Hernandez, A 320-Gb/s capacity (32-user× 10 Gb/s) SPECTS O-CDMA network testbed with enhanced spectral efficiency through forward error correction, Journal of Light-wave Technology 25/1 (2007) 79.
120. A. Avižienis, Framework for a taxonomy of fault-tolerance attributes in computer systems, Proceedings of the 10th annual international symposium on computer architecture Stockholm, Sweden (1983) 16.
121. N. Aggarwal, Configurable isolation: building high availability systems with commodity multi-core processors, Proceedings of the 34th annual international symposium on Computer architecture – ISCA 07 ISCA 07, 2007.
122. M.B.E. Ball, Event-B Patterns for specifying fault-tolerance in multi-agent interaction chapter in Methods, models and tools for fault tolerance 5454, Springer, New York (2009) 104.
123. R.S.S. Tamhankar, A. Pullini, F. Angiolini, L. Benini, G. De Micheli, Timing-error-tolerant network-on-chip design methodology, IEEE Transactions on Computer-Aided Design of Integrated Circuits and Systems 26/7 (2007) 1297.

Chapter 2
Nano-scale Force Spectroscopy Applied to Biological Samples

Sandor Kasas, Charles Roduit, and Giovanni Dietler

2.1 Introduction

The term force spectroscopy (FS), being widely used and somewhat broadly applied in the scientific community, can convey a rather misleading impression. In the framework of the present article, its use will be confined to the technique where measurements are made to study the behavior of a molecule or a system that is subjected to stretching or torsional forces. The number of published studies relating to this topic has notably increased during the recent years, a trend that reflects technical advancements in the means of manipulating single atoms or single molecules. FS is performed by applying a controlled pulling force to the molecule or system of interest. The force may be exerted optically [1], with magnetic tweezers [2], by the application of biomembrane force probes of hydrodynamic drag [3], via the mediation of fibers [4], or by the use of an atomic force microscope (AFM) [5]. The latter technique is the most commonly applied option. Consequently, this review will report mainly on AFM experiments. Similarly, since the vast majority of force-spectroscopy studies nowadays involve biological systems, these will be dealt in most detail.

Biological entities, from single proteins to whole organisms, are continuously exposed to mechanical stress. Consequently, numerous force-resisting structures have been developed during the course of evolution. The physical principles that underlie the mechanical functions of proteins are still a subject of intensive investigation. Fortunately, FS now offers us an opportunity of exploring and understanding the molecular basis of the different solutions that have been selected by evolution. AFM-based FS permits an exploration of biological assemblies on different scales. This review article will open with a short introduction to the forces that act on the molecular scale and this will be followed by a brief description of the

S. Kasas (✉)
Laboratoire de Physique de la Matière Vivante, EPFL, CH-1015 Lausanne, Switzerland
e-mail: sandor.kasas@epfl.ch

S. Carrara (ed.), *Nano-Bio-Sensing*,
DOI 10.1007/978-1-4419-6169-3_2, © Springer Science+Business Media, LLC 2011

instrument and its working principles. Finally, FS experiments that have been conducted using systems of increasing complexities from single-molecule stretching to protein–plasmalemma interactions will be described.

2.2 Forces on the Molecular Scale

The smallest forces that act on a molecule are of entropic origin and are generated by thermal agitation. They represent the work that has to be undertaken to fully stretch a polymeric molecule without deforming its chemical bonds. This polymeric molecule spontaneously adopts a randomly coiled configuration, which maximizes its configurational entropy. These forces are rather weak and typically involve energies in the order of k_BT, where k_B is the Boltzman constant and T is the absolute temperature. Bond lengths in the order of a nanometer are typically implicated, and the resulting forces lie in the pN-range.

Noncovalent-interaction forces are stronger than the entropic ones and usually involve van der Waals, hydrogen, or ionic bonding. A single noncovalent interaction can be in the order of 10–100 pN. These are typically the forces that are needed to break most of the receptor–ligand bonds encountered in biology and to deform the internal structure of a molecule (e.g., secondary, tertiary, or quaternary structure of a protein).

Covalent bonds are the strongest forces encountered on the molecular scale, and they have a magnitude of approximately 1 nN. To deflect a typical AFM cantilever by 1 nm, a force of 60 pN must be applied to its end. Hence, depending upon the sensitivity of the instrument, all of the aforementioned forces lie within the measurable range of an AFM.

2.3 The Atomic Force Microscope

The AFM was invented in 1986 [6] for the imaging of samples, and it soon became popular among biologists. The reason thereof lies in the instrument's potential to "observe", with an unprecedented vertical and lateral resolution, biological systems that are immersed in a fluid (viz., under near-physiological conditions). The working principle of the instrument can be summarized as follows. A very sharp tip, which is fixed to the end of a cantilever, scans the sample. During the scanning, the interaction forces between the atoms of the sample and the atoms of the tip-end bend the cantilever. The vertical deflection of the cantilever is computationally correlated with the x and the y-coordinates of the tip to yield the three-dimensional topography of the sample. The tip and the cantilever are composed of silicon or silicon nitride and are available in different sizes and shapes and with different spring constants. Typically, the tips are pyramidal in shape with a base length of about 5 μm and an apical radial curvature of less than 15 nm. Cantilevers can have either a triangular or a rectangular form, with the longest-side lengths ranging from maximally 200 μm

down to 3 μm. Cantilevers with the smallest dimensions are used for high-speed AFM imaging. The vertical position of the tip is detected by a laser beam, which is reflected off the end of the cantilever. The beam terminates on a multi-segment photodiode (2 or 4 components), which converts the light intensity into a current. Variations in the illumination of the different segments of the photodiode are used by the controlling computer to calculate the tip's position along the *z*-axis. In most instruments, sample scanning beneath the tip is achieved using piezo electric crystals, which deforms in a predictable manner when exposed to a certain voltage. The scanning process can be achieved by different means. In some microscopes, the sample is moved in the *x*, *y*, and *z*-directions beneath an immobile tip. Instruments that are used for the observation of large samples and that are designed to be mounted above an inverted optical microscope are usually equipped with a tip that can be moved above an immobile sample. A combination of these two options has recently become available on the market: the sample is moved in the *x* and the *y*-directions, while the tip is displaced only along the *z*-axis. This configuration maximizes the scanning size and the displacement of the tip in the *z*-direction.

The feature that renders the instrument particularly interesting for biological applications is its capacity to operate equally well within vacuum, air, or fluid. By virtue of special injection systems, near-atomic resolution can be preserved even during the course of fluid exchange within the imaging chamber [7] (Fig. 2.1).

As aforementioned, the AFM was originally developed to map the topography of nonconducting samples. However, since 1992, the instrument has been shown to be capable of probing also the mechanical properties of a sample, or its affinity for

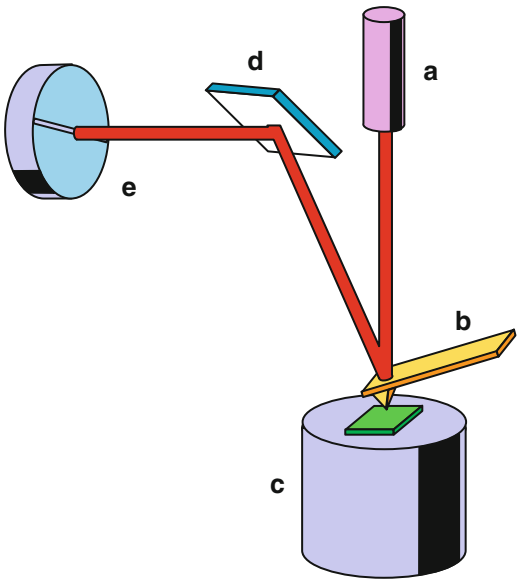

Fig. 2.1 The principal components of an AFM: (1) laser diode, (2) cantilever and tip, (3) piezo and sample (*green*), (4) mirror, (5) photodiode

tip-attached molecules. This type of measurement is achieved by recording and analyzing the so-called force–distance (FD) curves. These curves represent the deformation of the cantilever during its approach toward and its withdrawal from the sample. The mechanical properties of the sample are explored by pushing the tip into the sample, which causes its indentation, and recording the deformation of the cantilever during the process. If the sample is hard, the tip will not penetrate it, and the in-contact region of the FD curve will be a straight line with a slope of 45°. If the sample is soft, the tip will penetrate it, and the in-contact region of the FD curve will be flatter and of a more complex shape, which, in ideal cases, can be fitted to the Hertz model. This model predicts the shape of the FD curve for a sample that is flat, of infinite dimensions, isotropic, and homogeneous. For this mathematical modeling, the shape of the tip and the spring constant of the cantilever must be known. A comprehensive review of the factors that influence the shape of FD curves has been published by Cappella [8].

The affinity between the tip (or between any chemical species attached to it) and the sample can be deduced by careful examination of the retraction part of the FD curve. After making contact with the sample, the tip retracts, and if no link connects it to the sample, the cantilever recovers its resting position as soon the tip leaves the surface. However, if the tip (or the chemical species that coats it) interacts with the sample due to the existence of a strong attractive force or to the establishment of a molecular link between the tip and the sample, the cantilever is first deflected downwards. However, as soon as the retraction force of the cantilever exceeds the rupturing point of the newly formed bond, the cantilever recovers its resting position, which is maintained until the end of the FD curve.

If one knows the spring constant of the cantilever (viz., the constant that relates the deflection of the cantilever to the restoring force that it generates) and its deformation at the moment when the unbinding event occurs, then it is possible to calculate the force that is required to detach the tip from the surface or to break the bond between the tip-attached molecules and those on the surface of the sample (Fig. 2.2).

FD curves can be successively recorded all over the sample to yield a force–volume (FV) image. To this end, an FD curve is recorded for each pixel that composes the image. This type of imaging is extremely rich in information: a single FV file can furnish data respecting the topography of the sample, its stiffness as a function of depth, the position of a molecule of interest at its surface, and the interaction force between this molecule and those attached to the tip.

The potential of the AFM has been greatly exploited in recent years to gain an insight into numerous molecular phenomena in the fields of biology and biophysics, such as protein folding and ligand–receptor affinity. In the following sections, some of the domains in which the analysis of FD curves has significantly contributed to our understanding of the bio-nano world will be reviewed. Several other fields of investigation, which have been less successful to date, but are likely to benefit from future developments in nanotechnology, are also mentioned.

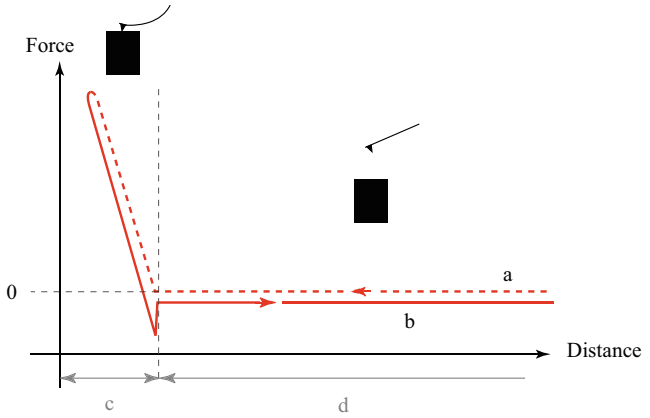

Fig. 2.2 Graph depicting the four relevant sections of a typical force–distance (FD) curve: (a) extension, (b) retraction, (c) in contact, (d) off-contact region

2.4 Unzipping and Stretching of DNA Molecules

Because of its profound importance to life, DNA has been more intensively studied than any other polymeric molecule. In living cells, certain proteins and drugs exert forces that can unzip and stretch DNA molecules. The development of instruments that permit the application of forces at a molecular level offers a unique opportunity of mimicking these physiological and pharmacological interactions. An understanding of the way in which proteins can exert DNA-deforming forces is of paramount importance in the fields of molecular biology, pharmacology, and polymer sciences. Furthermore, in recent years, several applications of DNA have been identified in the field of nanotechnology. These include its use as a molecular handle in single-molecule experiments [9], as a building block for the self-assembly of nanostructures [10], and as a base material for computing [11]. Hence, this field would also benefit from an improved knowledge of the physical properties of DNA.

Experiments that have been conducted to disclose the properties of DNA by applying forces to it can be essentially divided into two categories: those that pull the molecule along its axis, and those that unzip the molecule by pulling its two strands apart.

A study of the force-induced separation of double-stranded DNA is an important step toward understanding the processes of transcription and replication. The approach has been proposed as an alternative to the existing sequencing methods, since a sensitive force probe, such as optical tweezers [12] or an AFM [13], can accurately detect the binding strength between complementary base-pairs during the unzipping process. Krautbauer et al. used the AFM to sequence short DNA molecules with a resolution of 10 base-pairs. In these experiments, complementary molecules of single-stranded DNA were chemically attached to the AFM tip and to the substrate by their 5′ and 3′ ends, respectively. As the tip approached the substrate, complementary single strands came into

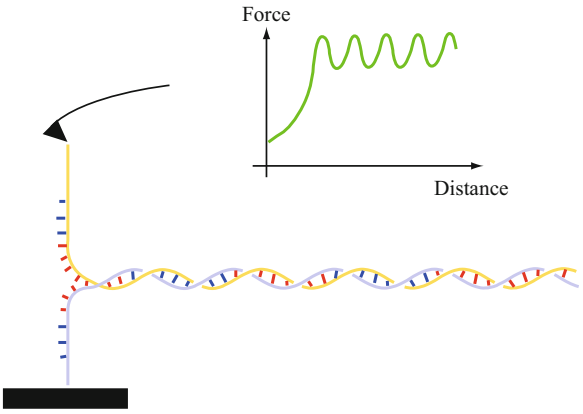

Fig. 2.3 Unzipping of complementary DNA oligonucleotides in the AFM (adapted from [13])

contact and double-stranded DNA was formed. As the tip was retracted from the substrate, the newly formed double strand was opened in a zipper-like fashion. The DNA sequence consisted of repeating blocks of 10 pure GC and 10 pure AT base-pairs. Since base-pairs of AT and GC are characterized by different pairing free energies (3.2 kT for AT and 5.2 kT for GC), the unzipping forces for the AT and the GC blocks should differ by approximately 5–10 pN over a stretch of about 20–25 nm. The experimental data confirmed this theoretical prediction (Fig. 2.3).

However, this technique suffers from the serious limitation that an ever-increasing amount of flexible, single-stranded DNA is created between the tip and the unzipping site. The stiffness of the single-stranded DNA thus rapidly dominates the FD curve, dramatically reducing the resolution of the instrument.

The stretching of double-stranded DNA along its axis can afford an insight into the stability and the phase transitions of the molecule. DNA is known to exist in different conformations, the B-form being the most common in living cells. However, if a force of about 65 pN is applied to the molecule, its contour length increases by a factor of 1.7, with the result that the B-form is converted into an over-stretched s-configuration [14–16].

Depending on which extremities of the DNA molecule are being pulled, the helical configuration is either conserved (if both 5′ ends are pulled) or transformed into a ladder-like structure. By using an AFM to stretch different double-stranded DNA molecules, the B- to S-transition has been shown to depend upon the specific base-pairing in the double helix.

2.5 The Unfolding of Single Proteins

Proteins play a major role in all biological systems. Several of their functions are more or less directly related to their static structure and/or to their dynamics. Among the structural functions of proteins, conservation of the three-dimensional

shapes of cells and cellular rigidity via the cytoskeleton involving actin, tubulin, or intermediate filaments are the most obvious examples. Important dynamic functions include muscular contraction, vesicular transport in neuronal cells, and mechano-transduction in the inner ear. These functions are achieved by virtue of the particular molecular assemblies that permit proteins to resist deformation or to change their conformation under the influence of mechanical or chemical stimuli. Unveiling the subtle arrangements that underlie these functions is necessary to understand how biological systems operate and the reasons for their failure.

Knowledge about the atomic structure of a protein cannot throw any light on the constituents that are important for its mechanical properties. This information can be obtained only by applying a load to the protein and monitoring its pattern of deformation. Such experiments can be conducted using various tools, such as optical and magnetic tweezers. These devices can apply forces in the range of 1–100 pN to a single molecule. However, a survey of 7,500 proteins in a coarse-grained molecular-dynamics model has revealed that the unfolding forces lie between 0 and 350 pN [17]. The AFM operates precisely in this range of forces and is therefore the ideal (or at least a most appropriate) tool to monitor the behavior of proteins under force regimes that can unfold them completely and measure their changes in length at an Angstrom-level of resolution. Table 2.1 compares the specificities of various measurements made using optical tweezers, magnetic tweezers, and the AFM.

In a typical protein-unfolding experiment with the AFM, one end of the protein of interest is first attached to AFM tip of the instrument, and the other end is fixed to the substrate. Numerous techniques are available for anchoring the proteins to the AFM tip and to the substrate, a comprehensive overview of which has been published by Bizzarri and Cannistraro [18]. The measurement begins at the onset of tip retraction, which stretches the suspended segment of the protein. During its deflection downward, the cantilever applies a force to the protein, which is proportional to its vertical deflection. The first source of resistance to the extension is an entropic force, which tends to cause coiling up of the protein to maximize its disorder. Extension of the molecule reduces its entropy and produces a restoring force that bends the cantilever downwards. Knowing the spring constant of the cantilever, its deformation can be calibrated and translated into force.

Table 2.1 Comparison of the different specificities of single-molecule manipulation techniques (adapted from [50])

	Optical tweezers	Magnetic tweezers	AFM
Length scale	0.1–1,000 nm	10–10,000 nm	1–10,000 nm
Time scale	10^{-4}–10^{3} s	10^{-3}–10^{5} s	10^{-3}–10^{2} s
Force range	0.1–100 pN	0.005–20 pN	5–10,000 pN
Spatial resolution	0.1 nm	10 nm	0.5 nm
Limitations	Photo damage	Difficult to manipulate single molecules	Random-attachment geometries

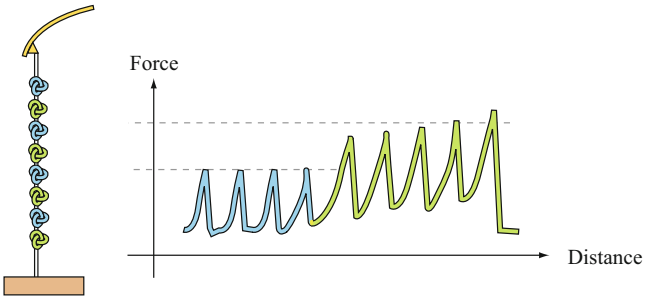

Fig. 2.4 Successive unfolding of the different domains of a heterodimeric polyprotein. The domains (depicted in *green* and *blue*) unfold according to their mechanical stability, irrespective of their order in the polyprotein (adapted from [49])

A further extension of the protein may cause an unfolding of some of its segments and an increase in its effective length. A sudden increase in the length of the protein causes a drop in the force acting on the cantilever and its return to the resting position. If the tip retraction continues and the protein contains other segments that can unfold, the process is repeated unless the protein breaks or detaches from the surface or the tip.

Figure 2.4 shows the saw-tooth extension curve of a polyprotein that is composed of four I27 and four I28 modules of human cardiac titin. The FD curve exhibits two levels of unfolding forces. Unfolding of the less stable I27 domains occurs at a force of approximately 200 pN and that of the more stable I28 ones at about 300 pN.

This technique can be used to study the unfolding of not only the single proteins but also the natural or synthesized polyproteins. In the latter situations, the technique permits an unambiguous identification of the parts of the polyprotein that are unfolding. Since an increase in the signal-to-noise ratio is possible, the amino acids can also be resolved. Furthermore, the technique renders possible an accurate module sizing of both the folded and the unfolded domains.

It is for this reason that the AFM is, nowadays, used to conduct force-spectroscopy experiments with heteropolyprotein constructs. An example of such an assembly is depicted in Fig. 2.5.

The first part of the construct embraces the protein of interest, while the second consists of identical, well-characterized domains, which serve as spacers and fingerprint the assembly (Ig/Fn domains in this specific case). The FD curve that is generated is depicted in the lower half of Fig. 2.5. The interpretation of FD curves is by no means a trivial undertaking and deserves a brief explanation.

2.5.1 Structural Basis for the Resistance to Unfolding

As aforementioned, when the force applied by the cantilever to the protein exceeds the entropic forces, then the naturally unfolded part of the protein can be assumed to

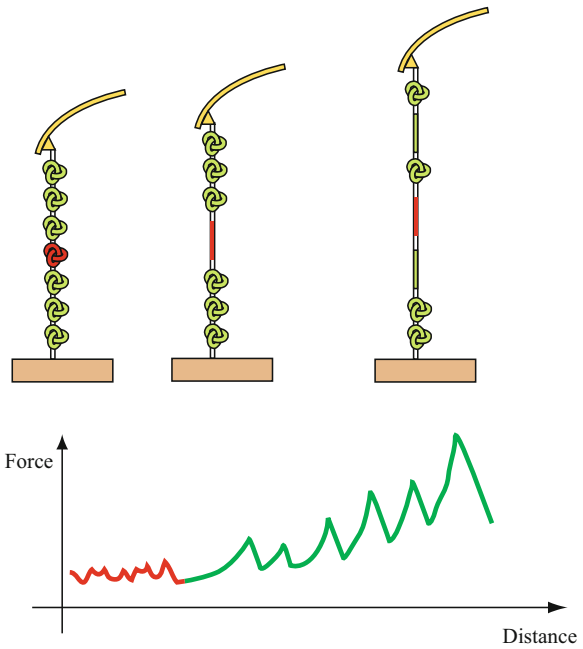

Fig. 2.5 The illustrated protein construct consists of five spacer domains (*blue*), which serves to fingerprint and furnish the domain of interest (*red*). The five evenly spaced contour-length increments, in *green*, are generated during the unfolding of the spacer domains, whereas the initial *red* path is generated by the domain of interest (adapted from [52])

be completely stretched. A characteristic unfolding then ensues, which leads to a sudden increase in the contour length of the protein and to a sharp drop in the acting force. The entropic elasticity of the unfolded portion of the protein can be formally described by different models, such as the freely jointed chain model [3], the freely rotating chain model [19], or the worm-like chain model [20]. The latter model is more widely implemented than any other option in the AFM community. It predicts that the stretch force (F) is related to the relative extension of the chain (x/L):

$$F(x) = \frac{kT}{A}\left(\frac{1}{4\left(1-\frac{x}{L}\right)^2} - \frac{1}{4} + \frac{x}{L}\right),$$

where A is the persistence length, which measures the chain's bending rigidity, k is the Boltzmann constant, T is the absolute temperature, x is the extension, and L is the contour length of the polyprotein. The contour length (L) increases after each unfolding event by an increment that equals the contour length in one of the folded domains.

Molecular-dynamics simulations reveal that the resistance of a protein to a force is determined principally by the topology of the molecule. Beta-sheets, in

which the hydrogen bonds are simultaneously loaded in a shear-geometry, appear to be more resistant to an externally applied force than the alpha-chains or mixtures of alpha-chains and beta-sheets [21]. However, recent studies have shown that even the load-resistance of beta-sheets is context-dependent and reflects other parts of the protein. It should also be borne in mind that rupture forces and extension lengths follow a distribution curve and that experimental parameters such as temperature [22] or the nature of the solvent [23] can influence the behavior of a protein. Pulling speed is also an important consideration in this type of measurement, and an increase in this parameter will give rise to an increase in the unfolding force [24]. This phenomenon will be discussed more fully later in this article, but a brief explanation is warranted here. An increase in the external force that is applied to a protein lowers the activation barrier between the folded and the unfolded states within the time-span of the experiment. Consequently, the thermal fluctuations exceed the unfolding barrier. The dependence of the unfolding forces on the force-loading rate can be used to estimate the unfolding rate constant, which represents the time that a domain needs to unfold spontaneously (i.e., in the absence of an external force). The unfolding rate constant can be calculated using Bell's model:

$$\alpha(F) = \alpha_{o}\exp\left(\frac{F\Delta x}{kT}\right),$$

where α_o represents the unfolding rate in the absence of an external force, F the applied force, and $\Delta x$the distance to the unfolding transition state.

The unfolding probability of a protein pulled at a constant speed can be calculated using Monte-Carlo simulations. These simulations reveal that unfolding must be viewed as a stochastic process in which the unfolding probability is close to zero in the absence of an external force and increases with an increase in the applied force level to a maximum (100%) at F_{max} (the magnitude of which depends upon the pulling speed).

2.5.2 *Influence of Pulling Geometry on Force-Spectroscopy Measurements*

So far, we have assumed polyproteins to be pulled in a direction that is perpendicular to the surface of the substrate. But this may not always be the case, and it has thus been considered worthwhile to estimate the measuring error that would arise if the polyproteins were to be stretched at a different angle. Surprisingly, simple trigonometric calculations of this kind [25] have disclosed the error to be less than 1%.

However, this kind of error should not be confused with the errors that arise by varying the direction of the externally applied force relative to the orientation of

the polyprotein. Changes in this parameter can give rise to a much broader margin of error [26].

2.5.3 *Force-Ramp and Force-Clamp Measurements*

Thus far, we have considered only constant-velocity measurements, which involve pulling the protein at a constant speed until each of the various domains has unfolded. On the one hand, this type of measurement furnishes precise information relating to the end-to-end length of the polyprotein and to the positions of the different barriers. On the other hand, force ramping [27] and force clamping [28] involve feed-back loops to control the force that is applied to the molecule, thereby permitting an easier determination of the folding and the unfolding rates.

In force-clamp spectroscopy, the polyprotein is held at a constant stretching force. When a module of the protein unfolds, the global length increases and the force (viz., the deflection of the cantilever) drops to zero. Since the feed-back loop in this mode is programmed to keep the force constant, the tip moves rapidly upward until the polyprotein is again stretched at the programmed force. This cycle is repeated until each of the modules has unfolded or until the protein detaches from the surface or the tip. One of the advantages of this technique is that it permits a straightforward determination of the unfolding probability by fitting a single exponential to the length versus time curve (Fig. 2.6).

In force-ramp spectroscopy, a linearly increasing force is applied to the polyprotein by raising the tip at a predetermined, constant speed. When a module

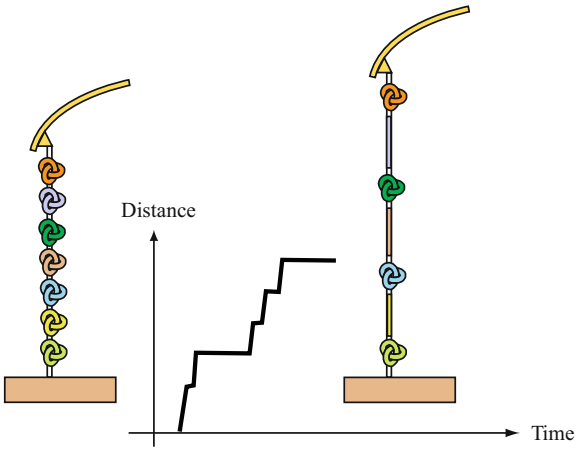

Fig. 2.6 Graph depicting a typical force-clamp measurement. The trace follows a characteristically staircase course, which reflects the stepwise unfolding of a single polyprotein (adapted from [37])

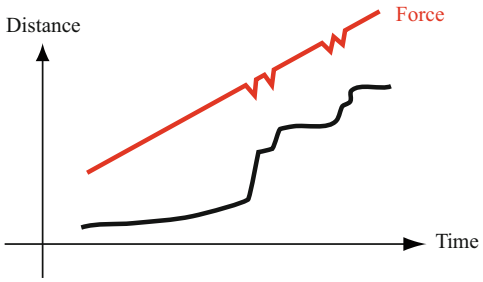

Fig. 2.7 Graph depicting a typical force-ramp measurement during the unfolding of a polyprotein (adapted from [37])

of the polyprotein unfolds, the retraction force drops to zero and the feed-back loop raises the tip rapidly until the force of the cantilever reaches the previous value. The linearly increasing force is then once again applied until another unfolding event occurs. The advantage of this technique is that it directly measures the unfolding probability as a function of the force that is applied to the protein (Fig. 2.7).

2.5.4 Refolding Studies

Force-clamp spectroscopy also permits monitoring of protein refolding at the single-molecule level. In experiments of this kind, the protein is first unfolded at a high force and then quenched at a lower one to permit refolding. Different types of protein such as ubiquitin [29], titin [30], and titin-like molecules [31] have been studied this way. Data gleaned from such experiments have revealed the different phases of the refolding process.

2.5.5 The Unfolding of Titin

To date, the AFM has been used to probe the force-spectroscopic characteristics of more than 50 different proteins. Notable examples include tenascin [32], spectrin [33], ubiquitin [34], and fibrinogen [35]. However, no protein has been more thoroughly investigated than titin. This circumstance is readily accounted for by the fact that titin is the largest known naturally occurring protein. It was also the first molecule to be investigated in FS by AFM [36]. Titin occurs within skeletal and cardiac muscle, radiating from the *z*-line to the center of a sarcomere. Its function can be likened to a spring that is charged to recoil the extended muscle fibers. The bulk of its mass is represented by an assemblage of globular domains, each of which is composed of immunoglobulin and fibronectin-type-III-like folds, and which are connected by elastin-like units.

Although several AFM studies have been performed using isolated molecules of native titin, most of the experiments have been conducted on recombinant, region-specific constructs. A comprehensive review of these investigations has been published by Linke and Grutzner (2008) [37].

2.6 Measurement of Protein–Ligand Interactions

Protein–ligand interactions play a central role in biological processes. Recent developments in the AFM now render possible a direct quantification of the range and magnitude of the interactive forces operating between proteins and their ligands. Hitherto, interactions of this kind were essentially described in terms of the binding equilibrium, whereas now, they can be explored kinetically. This kinetic information is not only necessary to elucidate the molecular mechanism of the interaction, but is also important for the design of pharmacological agents.

Kinetic parameters that characterize protein–ligand interactions can be derived from FD curves. To understand the rationale of this methodology, one has to consider protein–ligand interaction as a molecular association with a limited lifetime. Even if no force is applied to pull the components of the complex apart, a spontaneous dissociation will be ultimately effected by thermal fluctuations. If the duration of the measurement exceeds the lifetime of the complex, then no unbinding event will occur. But if a constant stretching force is applied to the complex, its lifetime will be shortened, and it will dissociate more rapidly than it would in the absence of the force. The application of a force to the complex lowers its energy barrier, as depicted in Fig. 2.8.

The interaction force between a protein and its ligand depends greatly upon the manner in which the external force is applied during the course of an experiment, or, more precisely, upon the load rate, which is defined as the product of cantilever stiffness and pulling speed. Lowering of the loading rate results in lowering of the

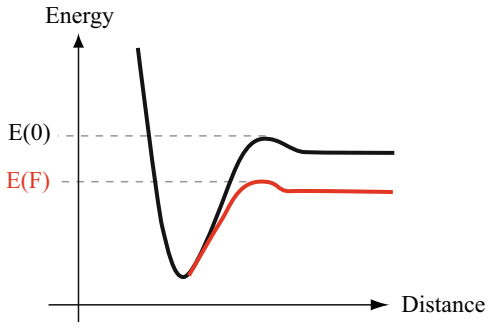

Fig. 2.8 Graph depicting the energy barrier for the dissociation of a protein–ligand complex in the absence (*black line*) or presence (*red line*) of an externally applied force (adapted from [39])

interaction force. However, monitoring of unbinding force as a function of the loading rate is not in itself a useful measurement. Nevertheless, this information can be used to derive more meaningful thermodynamic and kinetic parameters, such as the kinetic off-rate (K_{off}), which affords an insight into the formation of bonds, their strength, and relaxation times. The kinetic off-rate is defined as:

$$K_{off}(F) = K_{off}(0)^{\left(\frac{Fx}{kT}\right)},$$

where k is the Boltzmann constant, T is the absolute temperature, and kT is the thermal energy.

In practice, K_{off} is estimated by a first-order extrapolation of unbinding-force measurements that are recorded at different loading rates, since the unbinding force is usually linearly correlated with the logarithm of the loading rate.

If more than one barrier is involved, and if we assume that all barriers lie along a single one-dimensional escape path, then the curve follows a continuous sequence of linear regimes, as depicted in Fig. 2.9.

Using the AFM, loading rates ranging from 10 to 100 nN/s can be applied. Outside this range, hydrodynamic instabilities arise. The plotting of unbinding force against the logarithm of the loading rate permits an estimation of the dissociation rate at zero force [38].

The different steps that must be undertaken to estimate the K_{off} of a protein and ligand pair are represented in Fig. 2.10. Initially, the protein is attached to the tip and the ligand to the substrate (A), several thousand consecutive FD curves are then recorded at different loading rates (B). The unbinding events must be identified on the FD curves, and the corresponding unbinding force must be calculated. For each loading rate, a histogram is then constructed in which unbinding events is represented as a function of the force (C). These data are fitted to a Gaussian or Lorentzian curve to derive the value of the unbinding force for the protein–ligand pair. Finally, the logarithms of the most probable unbinding-forces values are plotted against the corresponding loading rate (D). The linear extrapolation of this curve gives the K_{off}-value.

Numerous protein–ligand unbinding experiments have been conducted in the AFM and a comprehensive review of this topic has been published by Lee et al.

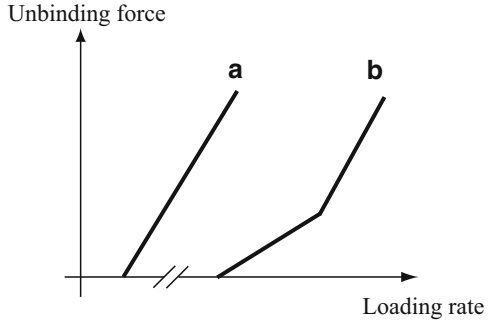

Fig. 2.9 Graphs depicting the relationship between the unbinding force and the logarithm of the loading rate for a molecule with a single energy barrier (**a**), and for one with two such barriers (**b**) barriers (adapted from [39])

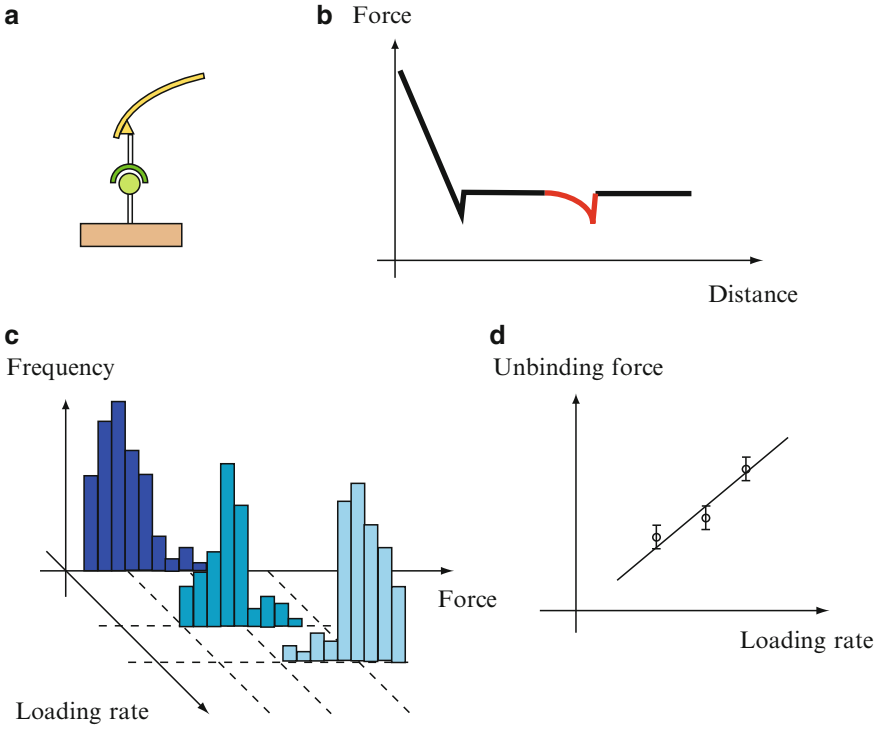

Fig. 2.10 Sequence of steps involved in deriving the K_{off}-value for a protein–ligand complex form measurements in the AFM (adapted from [39, 51])

(2007) [39]. One such study that is worth singling out here relates to the SNARE complex [40], which plays an important role in neurotransmission. It participates in the docking of neurotransmitter-filled vesicles and their fusion with presynaptic membranes. In the reported AFM experiments, the physiological system was simulated by anchoring some of the proteins onto the tip and several others onto the substrate. The interaction forces and the K_{offs}-values for the different proteins pairs that comprise the SNARE complex were calculated. Using these data, an estimate was made of the number of complexes that is required to securely attach a vesicle to the presynaptic membrane. The experimental set-up was also used to follow on-line the tetanus-toxin-induced disruption of the SNARE complex.

2.7 Stretching of Single Polysaccharides in the AFM

Polysaccharides have diverse and important functions in nature. They serve as building blocks in the construction of mechanically strong structures, as energy-storage molecules, and as recognition and signaling intermediates. To gain an

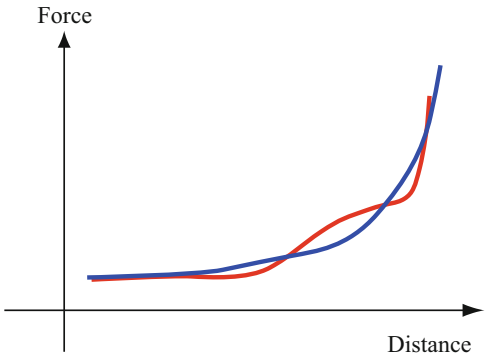

Fig. 2.11 Elasticity fingerprints of two linear polysaccharides (adapted from [43])

insight into the functional diversity of these molecules, it is necessary to analyze their structures. The primary structure of all polysaccharides comprises an arrangement of monosaccharides along the polymer chain. This mode of organization gives rise to a degree of structural diversity that is reputedly three orders of magnitude greater than is possible in proteins. Moreover, since the primary structure of polysaccharides is not encoded in genetic material, evolutionary changes therein cannot be effected as rapidly as with proteins.

Since 1997, AFM has been used to probe the elastic properties of single polysaccharide chains [41]. In the first experiments of this kind, chains of carboxymethylated dextran were mechanically stretched with a view to record the conformational changes in the C5–C6 bond of the glucose unit. Among the published studies, one in particular is worthy of mention here. It involved an attempt to identify the composition of polysaccharide samples by mechanically stretching individual, fluid-suspended molecules [42]. The FD curves that were collected during the course of these experiments differed according to the different shapes of the various length-normalized polysaccharides and could be used as fingerprints to identify single molecules (Fig. 2.11).

For reviews of investigations in which the AFM has been used to characterize the elastic properties of polysaccharides, the interested reader is referred to the publications of Sletmoen et al. [43] and Abu-Lail and Camesano [44].

2.8 Extraction of Surface Molecules

The methodology that is used to unfold single proteins can also be applied to extract proteins from the plasma membranes of living cells. In such experiments, the AFM tip is coated with covalent cross-linkers against the extracellular domains of the membrane proteins. When the tip approaches the cell, covalent bonds are formed

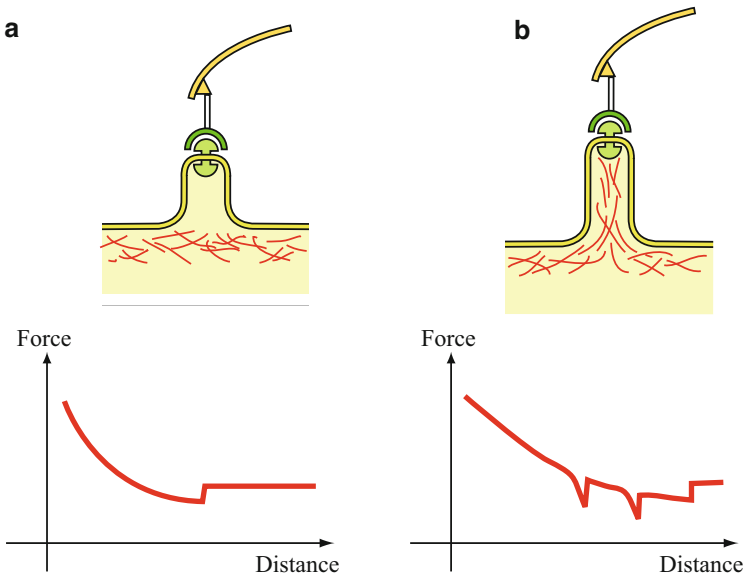

Fig. 2.12 Extraction of a plasmalemmal protein from a living cell, using the AFM (adapted from [53])

between the tip and the membrane proteins, and the maximal downward deflection of the cantilever during its retraction path yields information respecting the extraction force. Such experiments were conducted for the first time by Ikai and Afrin in 2002 [45]. The extraction force lay most frequently in the range of 400–600 pN, with little dependency on the loading rate. However, it should be borne in mind that to extract a protein from the plasmalemma of a living cell, first it is necessary to disrupt the hydrophobic bonds between the intramembranous portion of the protein and the surrounding phospholipids, and then to pull out its intracytoplasmic domain, which usually has a larger diameter than the intramembranous segment. Finally, it is necessary to rupture the noncovalent interactions between the cytoplasmic domain of the protein and submembranous components, such as the cytoskeleton as depicted on Fig. 2.12b.

2.9 Mapping of Surface-Membrane Molecules in Living Cells

If the AFM is programmed in such a way that the tip (or sample) is moved in the *xy*-plane after the acquisition of each set of FD curves, then it is possible to scan the surface of the sample and to map the distribution of individual receptors with a nanometric-scale resolution. The topography of the sample is resolved by

displaying the position of the tip as it contacts the sample (viz., by recording the point at which the cantilever begins the upward deflection that follows the tip-sample contact): such an image is depicted for a nerve cell in Fig. 2.13. During the retraction part of the FD curve, specific unbinding events can be topographically located. Typically, 16 × 16 or 32 × 32 FD curves are recorded for an area of a given size, and are then analyzed to extract information relating to parameters such as the tip-sample contact position and the location of binding–unbinding events between the functionalized tip and the surface receptors in the sample. This recognition imaging mode of the AFM has been successfully applied to erythrocytes and osteoblasts, as well as to vascular endothelial, ovary, and yeast cells. A comprehensive review of this topic has been published by Muller et al. [46].

Single-molecule mapping has been applied to reveal the distribution of fibronectin-attachment proteins (FAPs) on the surface of mycobacteria [47]. These proteins play an important role in the adhesion of bacteria and promote their binding to fibronectin within the extracellular matrix of the host. If FAPs were found to be homogenously distributed over the surface of the bacterium under "physiological" conditions, then a dramatic change in this situation could be induced by the application of an antibiotic.

A similar methodology has also been used to localize glycosylphosphatidylinositol (GPI)-anchored proteins within the neurolemma of hippocampal neurons [48]. Although GPI-proteins are known to partition preferentially into cholesterol-rich micro domains, their mechanical properties and sizes are still under debate. By analyzing the in-contact region of FD curves, Roduit et al. were able to evaluate the mechanical properties of the cell membrane as well as the sizes and the stiffnesses of the microdomains. The image found in Fig. 2.13 simultaneously displays the topography of an axon, its variations in surface stiffness (coded in false colors), and the locations of GPI-anchored proteins.

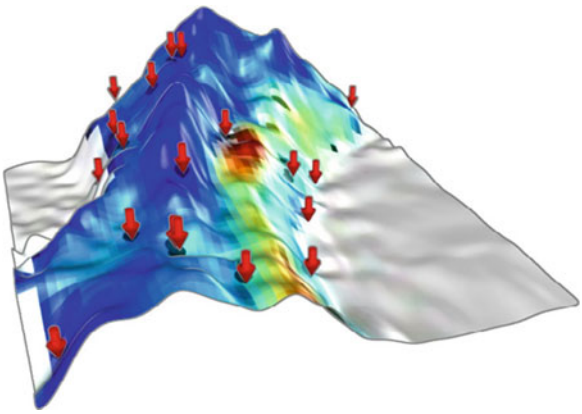

Fig. 2.13 AFM image of an axon, revealing its surface topography, variations in its surface stiffness (coded in *false colors*), and the locations of GPI-anchored neurolemmal proteins (*red arrows*)

2.10 Conclusion

In this article, the applications of the AFM to biologically relevant questions are briefly described. Biologically relevant systems that have been studied range from the single-molecule level to the cellular scale. The tool permits the investigation of the mechanical and elastic properties of proteins and of the kinetics of their interactions with ligands. By these means, it is now becoming possible to gain a truer insight into the relationships existing between biological activity and the physical properties of living matter.

References

1. Ashkin, A. (1980) Applications of laser-radiation pressure. Science 210: 1081–1088.
2. Amblard, F., B. Yurke, A. Pargellis, et al. (1996) A magnetic manipulator for studying local rheology and micromechanical properties of biological systems. Review of Scientific Instruments 67: 818–827.
3. Smith, S. B., L. Finzi and C. Bustamante (1992) Direct mechanical measurements of the elasticity of single DNA-molecules by using magnetic-beads. Science 258: 1122–1126.
4. Ishijima, A., T. Doi, K. Sakurada, et al. (1991) Sub-piconewton force fluctuations of actomyosin in vitro. Nature 352: 301–306.
5. Florin, E. L., V. T. Moy and H. E. Gaub (1994) Adhesion forces between individual ligand-receptorpairs. Science 264: 415–417.
6. Binnig, G., C. F. Quate and C. Gerber (1986) Atomic force microscopy. Physical Review Letters 56: 930–933.
7. Kasas, S., L. Alonso, P. Jacquet, et al. (2010) Microcontroller-driven fluid-injection system for atomic force microscopy. Review of Scientific Instruments 81.
8. Cappella, B. and G. Dietler (1999) Force-distance curves by atomic force microscopy. Surface Science Reports 34: 1–104.
9. EssevazRoulet, B., U. Bockelmann and F. Heslot (1997) Mechanical separation of the complementary strands of DNA. Proceedings of the National Academy of Sciences of the United States of America 94: 11935–11940.
10. Yan, H., S. H. Park, G. Finkelstein, et al. (2003) DNA-templated self-assembly of protein arrays and highly conductive nanowires. Science 301: 1882–1884.
11. Liu, Q. H., L. M. Wang, A. G. Frutos, et al. (2000) DNA computing on surfaces. Nature 403: 175–179.
12. Rief, M., H. Clausen-Schaumann and H. E. Gaub (1999) Sequence-dependent mechanics of single DNA molecules. Nature Structural Biology 6: 346–349.
13. Krautbauer, R., M. Rief and H. E. Gaub (2003) Unzipping DNA oligomers. Nano Letters 3: 493–496.
14. Cluzel, P., A. Lebrun, C. Heller, et al. (1996) DNA: an extensible molecule. Science 271: 792–794.
15. Smith, S.B., Y. Cui, and C. Bustamante (1996) Overstretching B-DNA: the elastic response of individual double-stranded and single-stranded DNA molecules. Science 271: 795-799.
16. Cocco, S., J. Yan, J. Léger, D. Chatenay and J.F. Marko (2004) Overstretching and force-driven strand separation of double-helix DNA. Phys. Rev. E 70: 011910.
17. Sulkowska, J. I. and M. Cieplak (2007) Mechanical stretching of proteins – a theoretical survey of the Protein Data Bank. Journal of Physics-Condensed Matter 19.

18. Bizzarri, A. R. and S. Cannistraro (2009) Atomic force spectroscopy in biological complex formation: strategies and perspectives. Journal of Physical Chemistry B 113: 16449–16464.
19. Livadaru, L., R. R. Netz and H. J. Kreuzer (2003) Stretching response of discrete semiflexible polymers. Macromolecules 36: 3732–3744.
20. Bustamante, C., J. F. Marko, E. D. Siggia, et al. (1994) Entropic elasticity of lambda-phage DNA. Science 265: 1599–1600.
21. West, D. K., D. J. Brockwell, P. D. Olmsted, et al. (2006) Mechanical resistance of proteins explained using simple molecular models. Biophysical Journal 90: 287–297.
22. Schlierf, M. and M. Rief (2005) Temperature softening of a protein in single-molecule experiments. Journal of Molecular Biology 354: 497–503.
23. Dougan, L., G. Feng, H. Lu, et al. (2008) Solvent molecules bridge the mechanical unfolding transition state of a protein. Proceedings of the National Academy of Sciences of the United States of America 105: 3185–3190.
24. Evans, E. and K. Ritchie (1997) Dynamic strength of molecular adhesion bonds. Biophysical Journal 72: 1541–1555.
25. Carrion-Vazquez, M., P. E. Marszalek, A. F. Oberhauser, et al. (1999) Atomic force microscopy captures length phenotypes in single proteins. Proceedings of the National Academy of Sciences of the United States of America 96: 11288–11292.
26. Brockwell, D. J., E. Paci, R. C. Zinober, et al. (2003) Pulling geometry defines the mechanical resistance of a beta-sheet protein. Nature Structural Biology 10: 731–737.
27. Marszalek, P. E., H. B. Li, A. F. Oberhauser, et al. (2002) Chair-boat transitions in single polysaccharide molecules observed with force-ramp AFM. Proceedings of the National Academy of Sciences of the United States of America 99: 4278–4283.
28. Oberhauser, A. F., P. K. Hansma, M. Carrion-Vazquez, et al. (2001) Stepwise unfolding of titin under force-clamp atomic force microscopy. Proceedings of the National Academy of Sciences of the United States of America 98: 468–472.
29. Fernandez, J. M. and H. B. Li (2004) Force-clamp spectroscopy monitors the folding trajectory of a single protein. Science 303: 1674–1678.
30. Garcia-Manyes, S., J. Brujic, C. L. Badilla, et al. (2007) Force-clamp spectroscopy of single-protein monomers reveals the individual unfolding and folding pathways of I27 and ubiquitin. Biophysical Journal 93: 2436–2446.
31. Bullard, B., T. Garcia, V. Benes, et al. (2006) The molecular elasticity of the insect flight muscle proteins projectin and kettin. Proceedings of the National Academy of Sciences of the United States of America 103: 4451–4456.
32. Cao, Y. and H. B. Li (2006) Single molecule force spectroscopy reveals a weakly populated microstate of the FnIII domains of tenascin. Journal of Molecular Biology 361: 372–381.
33. Rief, M., J. Pascual, M. Saraste, et al. (1999) Single molecule force spectroscopy of spectrin repeats: low unfolding forces in helix bundles. Journal of Molecular Biology 286: 553–561.
34. Brujic, J., R. I. Z. Hermans, S. Garcia-Manyes, et al. (2007) Dwell-time distribution analysis of polyprotein unfolding using force-clamp spectroscopy. Biophysical Journal 92: 2896–2903.
35. Brown, A. E. X., R. I. Litvinov, D. E. Discher, et al. (2007) Forced unfolding of coiled-coils in fibrinogen by single-molecule AFM. Biophysical Journal 92: L39–L41.
36. Rief, M., M. Gautel, F. Oesterhelt, et al. (1997) Reversible unfolding of individual titin immunoglobulin domains by AFM. Science 276: 1109–1112.
37. Linke, W. A. and A. Grutzner (2008) Pulling single molecules of titin by AFM – recent advances and physiological implications. Pflugers Archiv-European Journal of Physiology 456: 101–115.
38. Schwesinger, F., R. Ros, T. Strunz, et al. (2000) Unbinding forces of single antibody-antigen complexes correlate with their thermal dissociation rates. Proceedings of the National Academy of Sciences of the United States of America 97: 9972–9977.
39. Lee, C. K., Y. M. Wang, L. S. Huang, et al. (2007) Atomic force microscopy: determination of unbinding force, off rate and energy barrier for protein-ligand interaction. Micron 38: 446–461.

40. Yersin, A., H. Hirling, P. Steiner, et al. (2003) Interactions between synaptic vesicle fusion proteins explored by atomic force microscopy. Proceedings of the National Academy of Sciences of the United States of America 100: 8736–8741.
41. Rief, M., F. Oesterhelt, B. Heymann, et al. (1997) Single molecule force spectroscopy on polysaccharides by atomic force microscopy. Science 275: 1295–1297.
42. Marszalek, P. E., H. B. Li and J. M. Fernandez (2001) Fingerprinting polysaccharides with single-molecule atomic force microscopy. Nature Biotechnology 19: 258–262.
43. Sletmoen, M., G. Maurstad, P. Sikorski, et al. (2003) Characterisation of bacterial polysaccharides: steps towards single-molecular studies. Carbohydrate Research 338: 2459–2475.
44. Abu-Lail, N. I. and T. A. Camesano (2003) Polysaccharide properties probed with atomic force microscopy. Journal of Microscopy-Oxford 212: 217–238.
45. Ikai, A., R. Afrin, A. Itoh, et al. (2002) Force measurements for membrane protein manipulation. Colloids and Surfaces B-Biointerfaces 23: 165–171.
46. Muller, D. J., M. Krieg, D. Alsteens, et al. (2009) New frontiers in atomic force microscopy: analyzing interactions from single-molecules to cells. Current Opinion in Biotechnology 20: 4–13.
47. Verbelen, C. and Y. F. Dufrene (2009) Direct measurement of Mycobacterium–fibronectin interactions. Integrative Biology 1: 296–300.
48. Roduit, C., G. van der Goot, P. de Los Rios, et al. (2008) Elastic Membrane Heterogeneity of Living Cells Revealed by Stiff Nanoscale Membrane Domains. Biophysical Journal 94: 1521–1532.
49. Carrion-Vazquez, M., A. F. Oberhauser, T. E. Fisher, et al. (2000) Mechanical design of proteins-studied by single-molecule force spectroscopy and protein engineering. Progress in Biophysics and Molecular Biology 74: 63–91.
50. Greenleaf, W. J., M. T. Woodside and S. M. Block (2007) High-resolution, single-molecule measurements of biomolecular motion. Annual Review of Biophysics and Biomolecular Structure 36: 171–190.
51. Ikai, A. and R. Afrin (2003) Toward mechanical manipulations of cell membranes and membrane proteins using an atomic force microscope – an invited review. Cell Biochemistry and Biophysics 39: 257–277.
52. Puchner, E. M. and H. E. Gaub (2009) Force and function: probing proteins with AFM-based force spectroscopy. Current Opinion in Structural Biology 19: 605–614.
53. Afrin, R. and A. Ikai (2006) Force profiles of protein pulling with or without cytoskeletal links studied by AFM. Biochemical and Biophysical Research Communications 348: 238–244.

Chapter 3
Surface Nano-patterning of Polymers for Mass-Sensitive Biodetection

Adnan Mujahid and Franz L. Dickert

Abbreviations

AIDS	Acquired immune deficiency syndrome
AFM	Atomic force microscopy
BLV	Bovine leukemia virus
BAW	Bulk acoustic wave
BG	Blood group
BSA	Bovine serum albumin
DVB	Divinyl benzene
ELISA	Enzyme-linked immuno sorbent assay
ESA	Electrostatic self assembly
FBAR	Film bulk acoustic resonators
FMDV	Foot and mouth disease viruses
HPLC	High performance liquid chromatography
HRV	Human rhinovirus
HSA	Human serum albumin
HRP	Horseradish peroxidase
IAA	Indole-3-acetic acid
IBA	Indole-3-butyric acid
IET	Indole-3-ethanol
LBL	Layer-by-layer
MAA	meth acrylic acid

F.L. Dickert (✉)
Department of Analytical Chemistry, University of Vienna, Waehringer Strasse 38, A-1090 Vienna, Austria
e-mail: franz.dickert@univie.ac.at

S. Carrara (ed.), *Nano-Bio-Sensing*,
DOI 10.1007/978-1-4419-6169-3_3, © Springer Science+Business Media, LLC 2011

MIP	Molecular imprinted polymer
PET	Poly ethylene terephthalate
PCR	Polymerized chain reaction
QCM	Quartz crystal microbalance
RBC	Red blood cells
SAW	Surface acoustic wave
STW	Shear transverse wave
SAM	Self-assembled monolayers
SEM	Scanning electron microscopy
SPR	Surface plasmon resonance
SARS	Severe acute respiratory syndrome
TMV	Tobacco mosaic virus

3.1 Introduction

Detection of biological species such as enzymes, microorganisms, proteins, DNA, etc., has gained substantial importance in various fields, which include health care, industrial and environmental analysis, and biotechnology and process control. Currently, most of the detection systems used to monitor binding of biological molecules on sensor surface need some fluorescent or enzymatic labeling. This labeling step charges additional cost and time to the bioanalysis. The other concerned problem regarding this type of analysis is that, in some cases, the labeling reagent itself interferes with the analyte molecule, which then leads to false measurements. This makes the analysis more complex and less reliable. Considering the cost, time consumption, and reliability of the measuring system, this strategy has some disadvantages in monitoring the binding of biological species at the surfaces.

There is a growing interest in designing modern bio-recognition systems because of the rapid developments in this field. To obtain the desired information about the analyte molecule with certain degree of confidence, we have to develop suitable sensitive, selective, fast, inexpensive, and label-free detection systems. This problem needs to be addressed mainly in two parts: The first part is associated with the design of selective antibody surfaces that are capable of interacting only specifically with analyte molecules in complex matrices; and the second part is related with the design of transducer that can generate signals more sensitively for very low concentrations of analytes. Mergence of these two strategies can produce innovative detection systems, which can perform monitoring of different bioanalytes with appropriate selectivity and sensitivity.

Molecular imprinted polymers (MIPs) along with acoustic or mass-sensitive devices provide a highly favorable route to carry out various types of bioanalysis. Although there are some other surface structuring techniques that have some

applications in mass-sensitive biodetections, molecular imprinting has high repute in this regard. The imprinted polymers are of rigid and robustness nature, which is not damaged by exposing them into extreme conditions, and, in contrast, acoustic devices give a direct change in frequency corresponding to the bounded mass on their surface. Such detection systems have gained substantial importance during the last decade because of their widespread applications in different fields such as degradation analysis, compost monitoring, enantio-selective sensors, and environmental monitoring. To understand how to design highly selective surfaces for bioanalytes and for their detection by mass-sensitive devices, one should follow the concept of molecular imprinting along with other surface crafting schemes and fundamental principles of acoustic devices. In this chapter, coming sections will focus on these issues and discuss their potential applications in bioanalytics.

3.2 Surface Structuring Strategies

3.2.1 Natural Antibodies: A Direct Tool for Biodetection

Crafting of innovative materials for selective detection of different species is clearly a key assignment in bioanalytics, and especially their surface structuring is even more a challenging task at micro and nanoscale. The issue can be resolved by considering natural antibodies [1] as a direct tool for monitoring immunochemical reactions for detection purposes. One of the major advantages of this scheme is that natural antibodies provide sufficient degree of specificity for desired target molecule in complex mixtures. These materials can be immobilized on an appropriate transducer and be used to design biosensors [2, 3]. A very recent example of this strategy has been explained in a review article in which a thin layer of enzymes is immobilized on an electrochemical probe. This sort of detection systems has shown good results regarding sensitivity and selectivity. The major drawback of this technique is the lack of ruggedness and long-term stability of the designed surface, which limits their applications while crafting materials that can face severe conditions and retain their properties for longer period of time. The other concerned problem regarding these materials is that the interaction between antibody and antigen is usually very strong, which significantly reduces the reversibility and thus restricts their reuse.

3.2.2 Layer-By-Layer Approach

One of the modern trends in material designing to synthesize very thin films of layer heights ranging from one micrometer to several nanometers is set by the layer-by-layer (LBL) or electrostatic self assembly (ESA) methods. It was first introduced by Decher

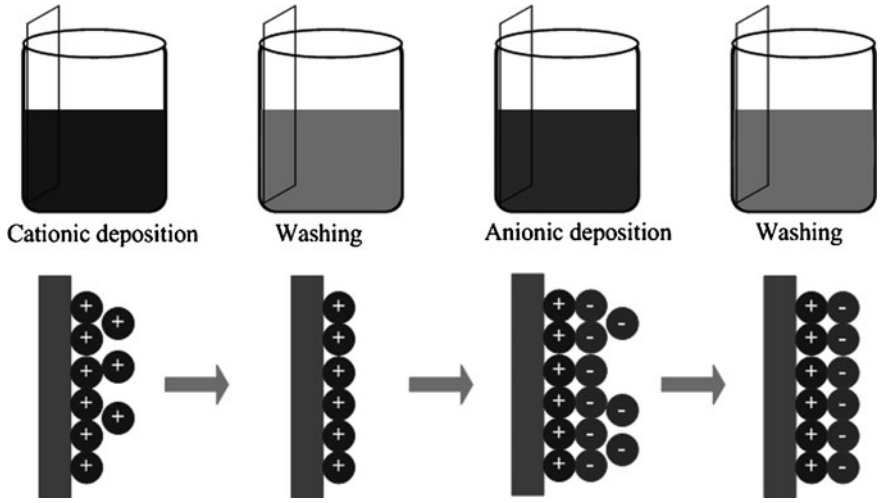

Fig. 3.1 Layer-by-layer assembling method

et al. [4] in 1992 during the synthesis of controlled thin films [5]. The synthetic procedure for developing LBL assembly is relatively easy and convenient. A schematic diagram for the preparation of LBL thin films is shown in Fig. 3.1.

This is a four-step procedure as shown in the figure, which is continuously repeated until the required numbers of layers are generated. This technique is quite new but still promising to craft the different materials to get the desired properties such as chemical, mechanical, thermal, and biocompatibility having sufficient degree of roughness. The synthesized LBL assemblies are of robust nature, which can effectively perform in severing conditions. The stimulating feature about these materials is that the layer-to-layer attractions are not restricted to electrostatic forces but assemblies can also be formed by hydrogen bonding [6], covalent bonding [7, 8], and some hydrophobic interactions [9, 10] as well. LBL assembly methods are very advantageous to organize the surface structures at nanometer scale and to incorporate the desired biomolecules. The versatility of this strategy enables us to launch any kind of charge species such as proteins [11–14], polypeptides [15], DNA [16], viruses [17], antibodies [18], and various other biological compounds in thin films preparation. The introduction of different biological species in LBL assembly generates very sensitive biological receptors having tunable selectivity. The induced functionalities in thin films truly favor the production of biorecognition materials. These materials can also be patterned by fabricating different components such as nanoparticles [19], nanotubes [20], and some other nanoplates [21–22]. This is of course of great interest in designing the biorecognition [23] of thin films at nanoscale [24], which can be deposited on a suitable transducer to conduct various bioanalyses.

Besides many significant advantages of LBL technique, there are certain limitations. The major drawback of this method is that it requires quite a long deposition

time of layer formation, which makes synthetic procedure too lengthy. Moreover, very high concentrations of deposition reactants are needed in order to coat appropriate layer material. Certain LBL assembly formation steps are very complex, which needs special masking and is time consuming. Although the binding of LBL receptors are of selective nature, sometime it is nonspecific due to exposition of the whole substrate surface to reactant solutions.

The practical examples of LBL assemblies in mass-sensitive biodetection applications are still infancy but, nevertheless, talented enough to meet the challenges of modern bioanalytics.

3.2.3 Host–Guest Interactions

Supramolecular chemistry provides an alternative synthetic route to design these materials, according to the technical needs. In these artificial materials, intramolecular and intermolecular noncovalent forces operate between the analyte and the host molecule. This strategy has been proven to be very successful in generating selective recognition systems for biomolecules [25]. It has solved the problem of reversibility and reusability when compared with the natural antibodies. The major drawback of this scheme is that the synthetic procedure is complicated and relatively time consuming. It is also a tedious task to find out the optimal interaction conditions between host and guest molecule. Therefore, to design an optimal recognitions system with minimum effort and technical expertise, we have to consider other strategies.

3.2.4 Molecular Imprinting: A Novel Approach for Developing Surface Recognition

The problem can be solved by introducing artificial recognition layers modified according to the shape and size of bioanalyte. These artificial recognition materials offer considerable flexibility in terms of tailoring the interaction sites in polymer surfaces. MIPs [26] promise to solve all the concerned problems and meet the desired needs in designing of novel materials. The most exciting aspect of molecular imprinting is that it provides molecular recognition to polymer matrix, which generates selectivity for very similar class of biomolecules. This technique was first discovered by the groups of Kiefer [27] and Wulff [28] independently in 1972, during the synthesis of organic polymers. Initial applications of molecular imprinting were found in separation processes and since after that the scope of this technique was extended to other fields such as chemical and biosensors [29], artificial biorecognition surfaces, and artificial synthetic antibodies.

3.2.4.1 Principle of Molecular Imprinting

The principle of molecular imprinting can be better understood from the following example in Fig. 3.2 where the model compound as template (i.e., usually analyte molecule) is introduced in polymer mixture along with monomers and cross linker. The required degree of polymerization is achieved by carefully controlling reaction conditions. During polymerization reaction, the polymer chains are self organized around the template compound, which are fixed at the end of reaction. The template or analyte molecules are finally removed from polymer matrix by heating or washing methods, which leaves behind geometrically adapted cavities for analyte reinclusion.

Generally imprinting procedure can be accomplished as a three-step process: the first step is the prearrangement of template, monomer, and cross linker; second is the engulfing of polymer chains around template; and the third is the extraction of the template molecules. In fact imprinted polymer possesses the memory of removed analyte molecule and can recognize and extract it selectively from a complex mixture of closely related compounds. The geometrical shape, size, and configuration of cavities can be improved for optimal template interaction by modifying the reaction conditions [30, 31] such as pressure, temperature, amount of cross linker and monomer to template proportion [32]. The amount of cross linker is very important as the higher degree of cross linking ensures the generation of cavities of very fine shape for optimal selectivity. Some post-imprinting modifications can also be employed to further improve the cavities shapes for reinclusion. The basic

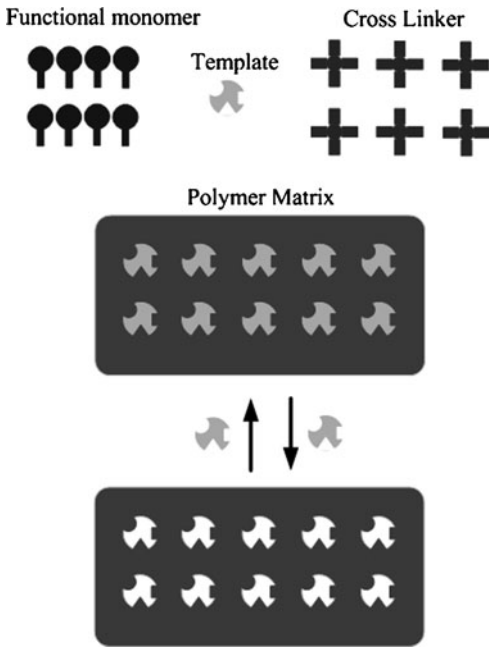

Fig. 3.2 Principle of molecular imprinting

requirements to conduct imprinting process are the high cross linking of polymer and the noninterfering nature of template with polymer matrix. Molecular imprinting can be classified into two types, according to the interaction of monomers with template molecules (i.e., covalent and noncovalent imprinting).

3.2.4.2 Noncovalent and Covalent Molecular Imprinting

Noncovalent imprinting was first introduced by Mosbach [33], where the template molecules develop affinity with function groups of monomer through noncovalent associations such as hydrogen boding, dipole–dipole interactions, Van der Waals forces, etc. prior to polymerization. The removal of template molecules takes place very fast as it does not require any bond rupture. This is a fast and straightforward way to design recognition materials for different detection purposes or developing chemical sensors. The only requirement for this process as earlier mentioned is that the template should not interfere with polymer, so there are no more restrictions for analyte size and shape. The only drawback of this technique is that it cannot be applied to those template molecules that do not have any functional group to interact with polymer system, which limits the construction of binding sites for analyte interactions. This problem is solved by later technique in which the model compound is covalently linked with polymer chain. After polymerization, the template molecules are removed by bond rupturing between template and polymer. The imprinted polymer can rebind the analyte molecules reversibly, and the selectivity is achieved by reactive groups in polymer matrix. Covalent imprinting is no doubt a practical method to various templates not having functional group but is limited due to the small number of useful applications of reversible covalent bonding.

A hybrid imprinting technique was developed by Whitecombe [34] in 1995 in which template molecule is covalently bonded to polymer matrix, whereas after its removal reversible and noncovalent interactions takes place. Tepper [35] has adopted a different imprinting approach in which the polymerization was carried out on transducer surface in solid phase rather than in solution form in the presence of alkaline vapors that contribute to generate imprinted sites for analyte reinclusion.

The sensitivity achieved by MIPs is accessed by number of imprinting sites available for analyte interactions (i.e., more the imprinted sites available higher will be the sensitivity). Nanoporous polymers possess more imprinted sites when compared with microporous polymers. The other important aspect regarding the sensitivity is the distribution of imprinted sites in polymer layer prior to use for detection purposes. The size of analyte molecules governs the imprinting strategy whether *bulk imprinting* [36] or *surface imprinting* is suitable [37]. In bulk imprinting (as shown in Fig. 3.2), the template molecule is added along with monomer and cross linker at the start of reaction and after polymerization is removed. This strategy is useful for relatively smaller analyte molecules having molecular mass <500 g mol^{-1} but while considering the larger analytes such as biomolecules, the bulk imprinting is not always complimentary. Although number of interaction sites in bulk imprinting are high

in comparison with surface imprinting, keeping in mind the larger size of biomolecules, incomplete reversibility, relatively longer diffusion pathways, and longer time for measurement make their detection highly unfavorable. Therefore, for larger biomolecules, surface imprinting, as shown in Fig. 3.3, is proposed where template molecules are directly imprinted on the prepolymerized surface by stamping method [38] with a little force. Thus, the patterned polymer surface possesses the dimensions from one to several hundred nanometers that can exclusively extract target molecule from the complex mixture.

Molecular imprinting provides a straightforward, versatile, and unproblematic way to synthesize selective coating materials for the detection of various biospecies. The most beneficial aspect of this scheme is that it is not limited to a certain class of compounds unlike the natural antibodies detection systems. The other significant feature of these materials is that they exhibit long-term stability and do not undergo degradation over the course of time, which makes use of these materials for extended period of time. Reversibility of surface imprinted materials makes reusable these materials for several analyses, which reduces the cost. The synthetic route of imprinting procedure is relatively easy as compared to the scheme followed for host–guest interactions such as in the case of cyclodextrines, paracyclophanes, and calixarenes. Considering the versatility in synthetic approach, ruggedness of designed imprinted material to severe conditions, flexibility regarding choice of analyte, and long-term stability make these materials superior for rapid, inexpensive, and selective detections of various bioanalytes over other strategies.

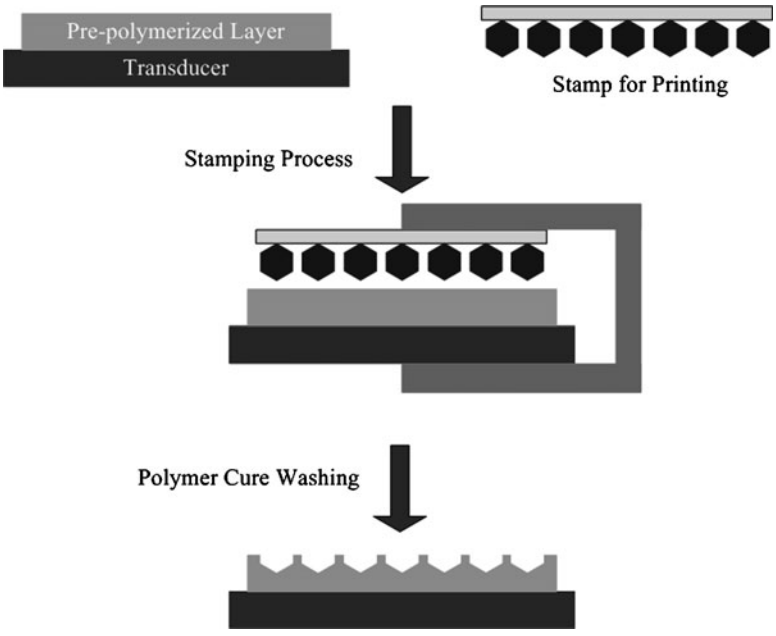

Fig. 3.3 Surface imprinting strategy by using analyte stamping

In order to make use of surface strategies for the detection of biospecies, first we have to understand the fundamental principles involved in transducers (i.e., acoustic or mass-sensitive devices). There are different types of these devices, which are employed in different working environments, according to their specific job to get desired information with minimum error. Thus, it is very important to select a right device for the dedicated task. In the coming section, we will focus on the basic principles of these devices and their operating modes in diverse mediums to get an optimized detection signal of different analytes.

3.3 Basic Principle and Theory of Mass-Sensitive Transducers

The fundamental principle involved in acoustic or mass-sensitive devices can be explained by piezoelectric effect, which was first discovered in 1880 [39] by two brothers Pierre Curie and Jacques Curie, in some crystalline materials such as quartz, rockchille salt, and ceramic. They had observed that if stress is applied on such crystalline materials in certain dimensions, it separates the negative and positive charges from their center creating a dipole, which leads to the generation of electrical voltage. The same is true if we apply an electrical voltage to such materials, it causes mechanical deformation in their shape. Former phenomenon is called piezoelectric effect, while the later one is known as inverse piezoelectric effect. The common examples of such materials that possess piezoelectric character are cane sugar, Rochelle salt, berlinite ($AlPO_4$), and quartz, which are natural materials, while synthetic examples are gallium orthophosphate ($GaPO_4$), langasite ($La_3Ga_5SiO_{14}$), and lithium tantalate ($LiTaO_3$). The selection of these materials depends upon their application in a typical medium and working environment: for example, gallium orthophosphate has high temperature coefficient than quartz and can be employed in working environment having temperature up to 900°C.

Quartz crystals are well-known acoustic device, which are widely used as mass-sensitive transducers for different sensing purposes. They are capable of measuring the mass changes in nanogram range. To have the desired properties of piezoelectric material, the crystal plate is cut at a specific angle, which is AT-cut (35° 15′) and BT-cut (49°). The AT-cut quartz is very famous and most frequently used as mass-sensitive transducer, as it has remarkable temperature and frequency properties.

Acoustic devices are considered as mass-sensitive devices because when a certain mass is loaded on an oscillating device, there is a corresponding change in the frequency of these devices. This phenomenon was first reported by Sauerbrey in 1959 [40] in his famous article. Sauerbrey has developed a relationship of frequency change in acoustic resonators upon mass deposition considering all the physical parameters of crystal material. The relationship is best described by the following equation.

$$\Delta f = -f_0^2 \frac{2}{A_{cr}\left(\rho_m C_q\right)^{\frac{1}{2}}} \Delta m,$$

In this relationship, the symbols represent the following:

Δf is the frequency change,
f_o is the resonant frequency,
Δm is the change in mass,
A_{cr} is the active piezoelectric area of quartz (usually electrode area),
C_q is the shear modulus of quartz crystal, and
ρ_m is the density of quartz.

This equation clearly indicates that the frequency change is directly related to the mass load on the surface of substrate. This equation is designed for typical gas phase environment. If we shift from gaseous phase to liquid phase, the equation is modified as described, considering the certain physical parameters associated with liquids such as viscosity and density.

The other important information revealed from Sauerbrey equation is that the frequency change also depends upon the square of fundamental resonance frequency of device. It means by doubling the fundamental frequency of the device, the frequency change would be four times. This is very important in the design of device because extremely low concentrations of analyte can be determined by simply selecting a device of highest available frequency.

The frequency of a piezoelectric material is mainly determined by its thickness. The characteristic frequency of these materials is given by the following relationship.

$$f = \frac{C}{2d}.$$

In this relation, $\boldsymbol{C}$ is the velocity of sound in the material and d is the thickness of the sheet. The quartz sheet undergoes resonance oscillations when connected with circuit oscillator, where an electrical and mechanical oscillation comes close to the fundamental frequency of quartz. An equivalence circuit for quartz resonator is designed to understand the oscillation phenomena and to calculate the quality factor (Q) of oscillations or dissipation (D) (i.e., mass accumulation on quartz surface and visco elastic behavior of deposited polymer). This equivalence circuit is shown in Fig. 3.4.

The oscillations of resonating quartz having two electrodes can be compared with this circuit in such a way that L stands for deposited mass, C shows elastic behavior, R represents the damping loss, and C_o shows the capacity between two electrodes. The impedance is calculated by taking the ratio of applied electrical voltage and the current flowing through it. This value of impedance gives information about the quality of oscillations and explain about visco elastic nature of deposited layer on quartz surface. The different resonating modes of a 10 MHz quartz wafer (i.e., serial resonance and parallel resonance) can be compared with this circuit along with the phase shift. Generally, acoustic devices can be classified

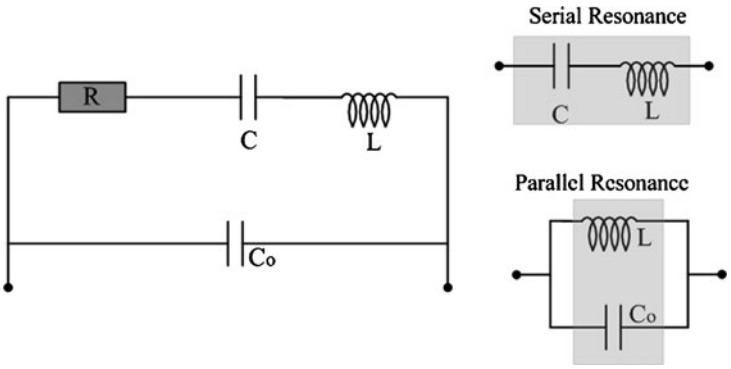

Fig. 3.4 Equivalent circuit to QCM resonator

in two main types depending upon the nature of wave propagation mode (i.e., bulk acoustic wave (BAW) devices as discussed earlier and surface acoustic wave (SAW) devices, which is explained later).

3.3.1 Surface Acoustic Wave Resonators

As from the name, it is obvious these are the devices in which oscillation phenomena is related to the surface of the material. Rayleigh [41] had discovered the phenomena of surface waves and explained their propagation mode in 1885, since then they are known Rayleigh waves. SAWs have both components shear vertical and shear horizontal, which can couple with the surface of substrate and propagate in a nondispersive manner. The coupling of these components determines the velocity and amplitude of the waves that travel along the surface, and hence, make these devices a useful tool for mass sensing purposes. A typical setup for SAW resonator has been shown in Fig. 3.5. SAW devices are typically made of ST-cut quartz crystal on which comb-shaped electrodes are generated by lift off process. The distance between these comb-shaped electrodes determines the wavelength, which leads to a distinct resonance frequency of SAW devices. Although the maximum frequency achieved for SAW devices is 2.5 GHz, the analytically reported frequency for chemical sensors is about 1 GHz [42]. Such a high resonating frequency of these devices make themselves exceptionally valuable for detecting very low mass of analytes (e.g., for 430 MHz device mass changes up to 1 pg can be detected).

Apart from their successful sensor applications at higher frequencies, there are some limitations about their use in liquid phase. SAW resonators are influenced by the viscosity of surrounding liquid, which increases the damping of device significantly such that it becomes almost impossible to conduct measurements in liquid phase.

This problem can be solved by introducing shear transverse wave (STW) resonators [43, 44]. STW resonators are made of lithium tantalate ($LiTaO_3$) in contrast to SAW devices, which are made of quartz substrate. The high dielectric

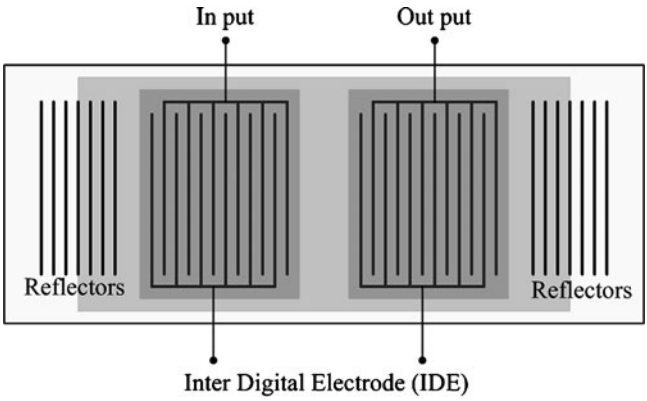

Fig. 3.5 A typical design of SAW device

constant of $LiTaO_3$ (i.e., (40)) is somehow similar to that of water, which is (80). This makes the STW devices operational in highly polar mediums avoiding any short circuiting. The other modification made in these devices is that the ST-cutting angle of crystal material is rotated in such a way that it demonstrates a complete shear horizontal wave that dissipates a very small amount of energy when subjected to liquid phase analysis. STW devices have established themselves a highly useful tool for various analysis particularly where the analyte concentration is too low to generate a reasonable signal.

3.4 Mass-Sensitive Detection of Bioanalytes by Tailored Surfaces

Different surface modifications techniques for the sensitive and selective detection of various biospecies have already been discussed including natural antibodies, host–guest biointeractions, LBL strategy, and surface imprinting. Among them, surface imprinting seems to be very attractive to get the desired specificity especially for bioanalytes. On the other hand, the basic principle and theory of mass-sensitive transducers have also been explained in previous section. The next headings will focus on the combination of surface modification techniques along with mass-sensitive transducers to design suitable biodetection systems.

3.4.1 Microorganisms Recognition System

Microorganisms have key role in almost every field of human life and particularly toward the environment. The microbial activities have significant applications in different areas such as genetic engineering, food processing, photo synthesis,

biotechnology, bioremediation, and many more. Besides the numerous useful applications of microorganisms, there are some serious threats to health as some of them are source of infectious diseases. Classical methods for the analysis of dangerous microorganisms require very long time, which restricts the rapid determination. It is the beauty of molecular imprinting that design sophisticated sensitive surfaces for the quick detection of different microorganisms such as yeast, bacteria, different blood groups, viruses, and others. Some examples of mass-sensitive detection of unicellular and multicellular species have been discussed further.

3.4.1.1 Yeast Cells Detection

Yeast [45] are very important microorganisms that have several applications in biotechnology, among them fermentation of sugar is the most widely known. Basically, these are unicellular eukaryotic microbes having the length from 1 to 9 μm and diameter of 1–5 μm. Production of different wines through fermentation process, bread baking, and synthesis of ethanol at industrial scale are the well-established applications of yeasts. *Saccharomyces cerevisiae* [46] are the most widely used yeast species that have been extensively examined in microbiology laboratories because they are considered as the model microorganism [47] in the development of useful biosensors and to study certain biological phenomena. In different microbiology laboratories and other production plants, their growth in cultured medium is controlled at defined conditions. The growth and reproduction of yeast cells largely depends upon the composition of prepared medium, humidity, and temperature that demands constant surveillance. It has been noted that during the phase of production, concentrations of different reactants are changing with the passage of time that makes the mixture more complex. Already established methods for the monitoring of yeast cells in different production processes are based on indirect measurements or some labeling techniques. The online monitoring in fermentation plants at larger scale has always been of fundamental importance for process control. This can be achieved by employing mass-sensitive transducers such as quartz crystal microbalances (QCM) having patterned coatings on them for selective detection of yeast cells.

Highly sensitive and selective coatings can be prepared by surface imprinting strategy, which has already been explained. The selection of polymer for surface imprinting is also very important as the cavities generated by yeast imprints should retain the structural characteristics in terms of size and dimension after the interaction of analytes with surface. Polyurethane is a robust polymer that has been used widely for imprinting purposes. This polymer is synthesized using higher ratios of cross linker at defined reaction conditions. The image of *S. cerevisiae* is casted on polymer layer by pressing glass stamp to make highly packed and flat imprinted surface. The QCM measurement performed at suitable conditions on such surface shows remarkable sensor effect. While considering cross sensitive, it has been noticed that designed imprinted polymer surface shows highest frequency shift for the target molecule when compared with other similar yeast strands [48] as shown in Fig. 3.6.

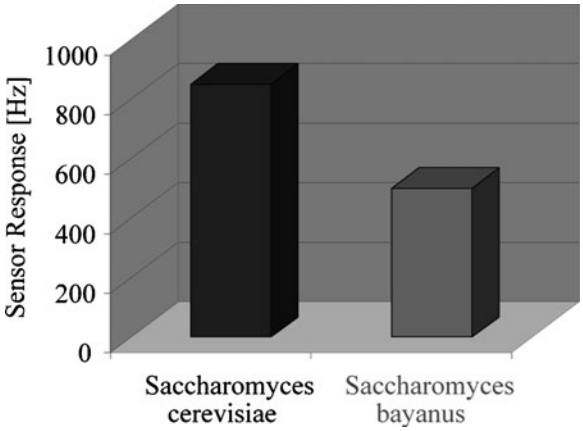

Fig. 3.6 Cross sensitivity measurements on *Saccharomyces cerevisiae* imprinted polyurethane surface to an analogous yeast strad (i.e., *Saccharomyces bayanus*), adapted from [48]

Fig. 3.7 AFM image of yeast imprints on polyurethane surface

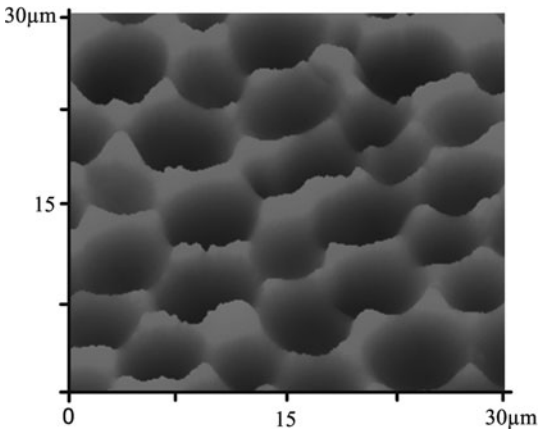

Although some of them have a size smaller than the cavity, they still do not have much impression on the same surface, which indicates the selective nature of the imprinted polymer. This reveals that the surface structure is patterned down to molecular/nanolevel, whereas the cavity shape and whole dimensions are optimized to the target analyte. An AFM image of imprinted surfaces has been shown in Fig. 3.7.

This measurement scheme does not stop here but it further investigates to monitor the growth stages [49] of yeast cells in order to study the cell behavior, which is of great interest in different pharmaceutical industrial applications, drug release, and many other biological processes. Especially in food processing industries, molecularly imprinted polyurethane surfaces of suitable layer heights can be used to inspect the changes taking place in surroundings such as concentration of nutrients,

humidity effect, and variable pH. This is indeed a significant achievement by biomimetic surfaces when realizing the concept of process control [49] for online monitoring purposes. Recent developments shows that individual growth stages of yeast cells can also be monitored simultaneously by employing a multichannel QCM [50] following the similar synthetic strategy.

In comparison with classical methods for yeast detections, surface imprinted polymers along with mass-sensitive transducers are highly favorable in many regards. As already stated that classical methods are focused on indirect measuring techniques that are not much reliable in complex matrix where different chemical and physical parameters are varying continuously. The side-by-side selective detection of yeast cells at different growth stages is made possible by surface modified coatings on QCMs, but other methods lack this advance feature, and thus cannot be applied for online monitoring. Mass-sensitive devices having tailor-made surfaces have established themselves as promising tool to study cell properties and behavior in various biotechnology applications.

3.4.1.2 Bacterial Detection with Synthetic Receptors

The detection of different pathogenic bacteria is of great concern in microbiology and modern clinical analysis owing to the public health and safety. The contamination of harmful microbes in drinking water and food can lead to severe diseases. For example, *Escherichia coli (E. coli)* are gram-negative pathogenic [51] bacteria, which causes contamination in food and beverages. Although not all of *E. coli* are toxic for human beings, still some of them are a potential hazard to public health. Among the dangerous species, *E. coli* O157:H7 is the most fatal one, which can cause severe diseases such as diarrhea, kidney failure, and even death in certain cases. In the United States, there are about 20,000 cases [52] related to different diseases spread by *E. coli* annually. Therefore, accurate, quick, cost-effective, and direct determination methods are needed in order to meet the requirements of environmental monitoring and other diagnostic purposes. The development of such detection systems are highly desirable in various industrial applications particularly related to food stuff [53]. Already established methods for bacterial detection are related to culturing, microscopy, and some other biochemical test. These methods are unfit for rapid analysis and particularly inappropriate for screening purposes, where prompt decision has to be made. The latest technology such as DNA chips has solved this problem to make faster analysis and reach toward conclusion. For a very sensitive and sophisticated detection of *E. coli*, polymerized chain reaction (PCR) [54, 55] technique is also very useful. Mass-sensitive devices such as QCM [56, 57] and surface plasmon resonance (SPR) [58] are also used for the characterization of PCR products. These detection methods are time consuming and not widely adoptable because of the high expertise required for handling. Some other sensing schemes based on electrochemical impedance [59, 60], chemiluminescence [61], SPR [62–64], and optical absorbance spectroscopy [65] are also reported in literature for *E. coli* O157:H7 detection. The direct

use of mass-sensitive devices as transducer for *E. coli* detection [66, 67] is not very general but still good enough to give a direct change in the frequency corresponding to the binding mass of analyte.

The idea of using functionalized surfaces with acoustic or mass-sensitive devices seems to be promising for developing a sensitive, selective, rapid, and relatively inexpensive detection system. In literature, there are different surface techniques that have been used with mass-sensitive transducers for detection of different types of bacteria. During the last decade, different groups tried to develop various biosensors based on natural antibodies for the detection of *E. coli* using different transducers. Most of them had applied specific antibodies immobilized on gold electrode of piezoelectric device such as quartz crystal microbalance. The strategy is very attractive in terms of getting selectivity as natural antibodies specifically bound to particular bacteria with sufficient sensitivity. Zhihong [68] has developed interestingly an unusual strategy for mass-sensitive bacterial detection. He has exploited the carbohydrates and protein recognition interactions for a very sensitive and specific *E. coli* detection. This method is not purely synthetic but in fact a hybrid approach by designing suitable mannose surfaces for a rigid and strong binding of *E. coli*. It has been noticed that the detection of *E. coli* on lectin modified mannose surface has much higher sensitivity about 10^4 times better than mannose alone detection. This in terms of sensitivity is quite good as it improves the detection limit. As the binding of bacteria is strong that does not increase damping drastically, which is good for smooth QCM measurements without too much loss. The sensor specificity was also characterized by exposing different electrodes coated with different chemical layers to known concentration (i.e., 7.5×10^7 cells/mL of *E. coli* W1485). The frequency shift for different layers, that is, lectin-modified mannose layer (A) and recombinant antibody (210E scFv-cys-) treated electrode QCM surface (B) was determined. The control antigen test was also conducted by adding *Staphylococcus aureus* (C), and the results have been shown in Fig. 3.8. The lectin-modified sensor layer exhibits highest sensor response

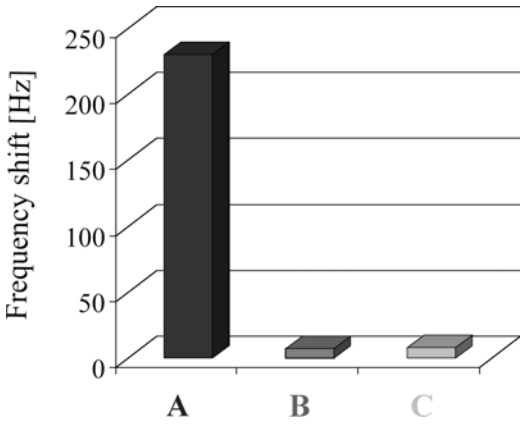

Fig. 3.8 Evaluation of sensor specificity by exposing three different layer materials coated on gold electrodes a solution of *E. coli* W1485 (adapted from [68])

for *E. coli* W1485 in comparison with other layer and control antigen, which indicates the enhanced sensor specificity.

Recently, a new strategy has been introduced where gold nanoparticles [69] are immobilized on thiol modified QCM electrode to develop piezoelectric sensor for real time detection of *E. coli* O157:H7 detection.

The main problem is related to the low stability of antibodies deposited on the transducer surface. These antibodies cannot perform for a longer period of time as they tend to deteriorate with the passage of time and so cannot be stored for long-term use. Some antibody coatings are good for sensing purpose but most of them are of a flexible nature that can cause severe damping during mass-sensitive measurements, which leads to an unreliable data both in terms of qualitatively and quantitatively. Moreover, some natural antibodies once bound to microorganisms then afterward they are reluctant to release them, which reduce the reversibility of mass-sensitive measurements. The solution of these problems can be made by following a different approach in which artificial recognition materials are used. Surface imprinted layers can be used as artificial antibodies [70] for bacterial detection more effectively when compared with natural antibodies. Polyurethane layers that are robust and rigid in nature have been utilized for surface imprinting of *E. coli*. The imprinting is done on prepolymerized surface of polyurethane with a suitable stamp made of densely packed cells. The AFM image of *E. coli* imprinted polyurethane surface has been shown in Fig. 3.9. These layers coated on QCM exhibit significant sensor response to *E. coli*. Although there was anti-Sauerbrey effect, the reported sensitivity and the reversibility of the measurement is quite good for *E. coli* detection. Surface studies of imprinted polyurethane layers reveal that excess of phenolic groups hindered the covalent linkage with polymer surface. This indeed is very useful to improve the imprinting effects for bacteria sensing and to develop a completely reversible detection system.

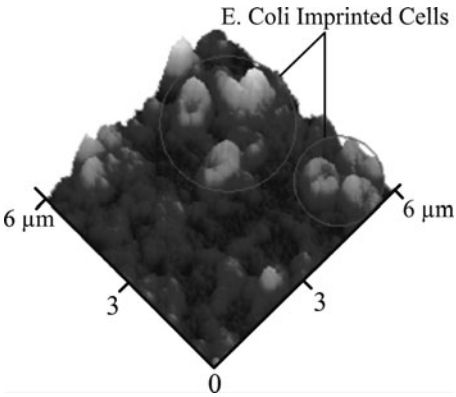

Fig. 3.9 *E. coli* imprinting on surface imprinted polymer surface

3.4.1.3 Virus Sensing by Nano-structured Polymer Surfaces

Molecular imprinting has introduced a new aspect in material science for designing sensor surfaces for exceptionally small entities. This becomes highly useful for the recognition of viruses, which have size in the range of some 100 nm. Their extremely small size makes their detection virtually impossible on normal optical devices. Viruses have serious health effects on human life as they can cause various diseases such as common cold, influenza, chicken pox, and some severe ones are acquired immune deficiency syndrome (AIDS), severe acute respiratory syndrome (SARS), hepatitis, etc. Enzyme-linked immuno sorbent assay (ELISA) [71] and PCR [72] are highly adopted methods for determining the exact stage of viral disease but their cost is too high and they need highly trained personnel to operate. Some inexpensive strips are available in the market for screening purposes for hepatitis C virus and HIV detection [73] in blood. This screening technology is of low cost and gives quick results, which are very suitable for rapid detection but these strips are limited to certain viruses and not generally available for a broad variety. At the moment, there are not much rapid and online analysis methods available for the viral detection, which have low cost, easily operable, and can be applied to a wider range of these species. This is a highly demanding task in which one has to make quick decisions about fatal viral diseases and reach a conclusion as some viral diseases are incurable and require immediate diagnosis. So, express detection systems need to be developed for fast and accurate analysis of viruses that have relatively low cost.

Tobacco mosaic virus (TMV) is the first discovered species of this class, which has the potential to damage the leaves of different plants particularly of tobacco. The structure of TMV [74] is surprisingly rigid and it can survive in a very broad range of pH 3.5–9.0 and can tolerate the temperature up to 90°C. AFM picture shows that TMV rods arrange themselves linearly over designed surface. It has been reported that the immobilization of TMV should be done on nonpolar surfaces, which prevent any structural distortion due to virus surface interaction [75] (Fig. 3.10).

Surface imprinted polyacrylic [76] acid has been applied successfully for casting TMV image. Mass-sensitive measurement performed on 10 MHz QCM shows excellent response for imprinted channel, whereas nonimprinted exhibits very small effect, which is due to unspecific binding. The frequency shift for MIP and NIP has been demonstrated in Fig. 3.11. The surface modified polyurethane layers [74] offer better sensitivity for TMV than polyacrylic acid, which is very valuable to detect lower concentrations and ultimately avoid production losses.

Although TMV have not been considered widely as a model for designing virus sensitive layers, still it has found some important functions in other areas. An exciting application of TMV imprints has been reported by Kenz et al. [77] in which they have used this virus as template to generate highly selective nano-structured inorganic matrices for binding metal ions. This not only offers a true nano pattering of surfaces but also induces recognition properties to design functionalized materials.

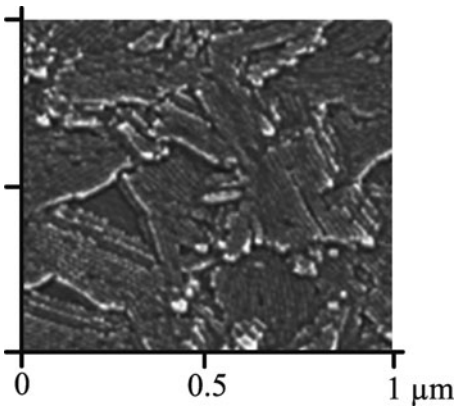

Fig. 3.10 AFM image of TMV aggregation on mica surface

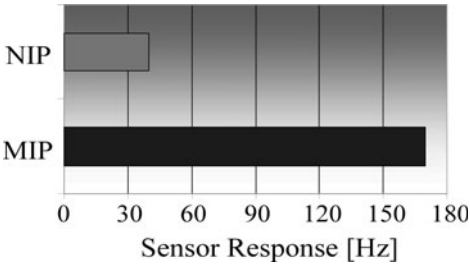

Fig. 3.11 Sensor response of TMV imprinted and nonimprinted polymer layers, respectively (adapted from [76])

Similarly, another interesting example of TMV imprints has been reported by Bolisay et al. [78] in which they have used this virus to improve the binding affinities for itself against the other non-target virus. Although the detection was not made on acoustic devices, still this synthetic approach is useful to avoid nonspecific binding and is a step toward improving imprinting factor for TMV. Surface pattering can also be used to differentiate the different viruses of same group (e.g., human rhinovirus, HRV), which is an infectious virus that causes common cold. This class of virus has a very small diameter of about 18 nm but has a length of 300 nm for surface patterning of polymers. The study [79] has been conducted on different types of rhinoviruses (i.e., HRV1A, HRV2, and HRV14) to examine cross sensitivity. The reported results in Table 3.1 show that polymer surface imprinted with one specie prefer to bind selectively the very same virus over the others. In other words, HRV1A imprinted polymer surface exhibit comparatively higher frequency shift for HRV1A than the others.

This demonstrates that imprinted structure of polymer surface is competent enough to recognize the target virus among similar species at nanometer scale. The imprinting of HRV along with other viruses of same class and their selective detection on QCM is a model example of intragroup selectivity.

Table 3.1 Comparison of relative sensor responses of various HRV imprinted polymers toward similar species (adapted from [79])

		Relative sensor effect [%]		
Imprinted HRV	virus	HRV1A	HRV2	HRV14
HRV1A		100	15	17
HRV2		20	100	19
HRV14		44	37	100

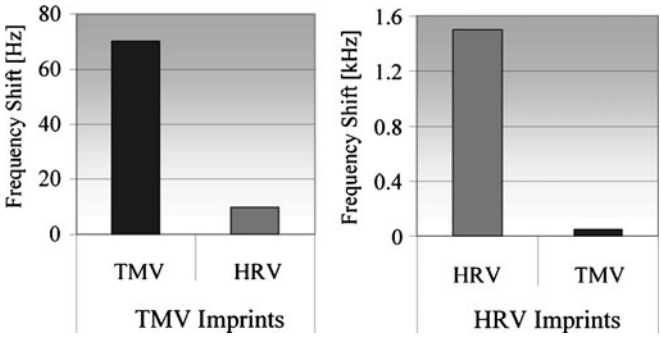

Fig. 3.12 Differential measurements conducted on TMV and HRV imprinted polymer surfaces and the respective frequency shift has been compared (adapted from [75])

The study can also be extended to attain intergroup selectivity pattern among different classes of viruses. Suitable imprinting procedures can also be employed to distinguish between two different groups of viruses, using acoustic devices. The detection system [74] has been designed for selectively determining TMV and HRV in controlled conditions. These viruses have entirely different structural dimensions, for example, TMV has cylindrical shape whereas HRV is found mostly in icosahedral form. Mass-sensitive measurements performed on premeditated polymer surfaces show excellent selectivity pattern as shown in Fig. 3.12 for the respective imprinted virus.

This detection scheme is very useful as it gives rapid results about different virus species including cross sensitivity studies in comparison with other modern techniques such as PCR. Recently, an outstanding advancement has been made in this regard where a suitable MIP chip [80] is designed for continuous monitoring of viral contamination. This development has introduced an innovative sensor platform for screening diverse biological complex mixtures and for micro total analysis system (μTAS).

These artificial receptors [79] are used to design more selective matrices for different pico viruses (i.e., HRV, foot and mouth disease viruses, FMDV). Although FMDV rarely infects humans however, it has strong impact on animals which is dangerous for agriculture industry and livestock. Molecular imprinting promise to achieve desired intergroup selectivity between HRV and FMDV. Mass-sensitive measurements performed on HRV stamped polyurethane layers

demonstrate substantial frequency change for the imprinted picovirus, whereas the same surface shows very little effect for FMDV.

One interesting strategy has been developed in which the whole analyte is not used as a template for the detection of biological analytes. This strategy is named as epitope approach [81] in which a certain protein sequence is used as template that acts as antigen for the detection of target microorganism. The method is somewhat inspired from natural antibodies where only a small part of antigen interacts (e.g., instead of whole protein molecule only amino acid sequence is detected). Although there are not too many applications of this approach in literature for biological detection, still this scheme can be introduced where practically whole structure cannot be used as a template. One successful example of this strategy is reported in Dengue virus [82] detection, which is an infectious pathogen virus that has been a serious threat to human life. A similar approach as epitope has been used to design biological sensor for bovine leukemia virus [83] (BLV).

The overall studies conducted on surface imprinted polymers along with mass-sensitive devices for viral detection open a new dimension for rapid, inexpensive, selective, and precise analysis methods, which is not provided by other analytical tools.

3.4.2 Protein Imprinting and Their Mass-Sensitive Detection

Proteins are highly significant macromolecules that possess very complex structure, and their selective recognition is also very important in biochemistry. Molecular imprinting has widely adopted technique to generate suitable polymer systems for protein sensing. In recent years, a number of review articles are presented for the imprinting of proteins [84–90] in which different strategies such as bulk imprinting, surface imprinting, epitope approach, and hydro gels are used. The protein imprinted surfaces are characterized by different techniques such as AFM and scanning electron microscopy (SEM). The images obtained from these methods reveal that the artificially imprinted protein materials have nano-patterned structures that possess specificity for template protein, which can be confirmed by other methods. It has been noted that the imprinted surface retains the utmost amount of that protein molecules, which were being used as model template while the nonspecific binding were very less when exposed to other protein solutions.

Despite the numerous applications of molecular imprinting for proteins and other macromolecules, their detection by mass-sensitive devices is not fully explored. Zahang et al. [91] has reported the piezoelectric detection of proteins using molecularly imprinted self-assembled thin films. They have selected human serum albumin (HSA) (i.e., a major plasma protein taken from urine) as a template and used silane sol-gel layers for imprinting. The inherent features of sol-gel technology provide a better platform for successful imprinting of biomolecules without modifying their original functionality. The imprinted sol-gel films were examined by SEM to observe the conductivity difference between coated and uncoated quartz crystal gold electrode. They have found that the impedance of coated electrode increases with increasing

layer height. Authors have also studied the other parameters such as temperature, effect of different salts and solvents on binding capacity, and concentration effect to develop an optimize detection system for HAS. The thin sol-gel films have shown suitable selectivity pattern in the presence of bovine serum albumin (BSA), horseradish peroxidase (HRP), and trypsin. The detection procedure of HAS was not fully directly based on mass change by quartz crystal, but rather based on electrochemical impedance, which is good enough for selective protein detection.

Surface imprinted polymers [92] are very effective for selective recognition of different proteins induction for crystallization. An example of such approach has been reported where methacrylic acid along with divinyl benzene (DVB) was polymerized at suitable conditions, and crystallized lysozyme was stamped for surface imprinting. Mass-sensitive measurements conducted on dual electrode QCM show that the imprinted channel shows significant frequency shift, while the nonimprinted channel remain unaffected. The growing of lysozyme crystals on imprinted polymer surface have been demonstrated by AFM image shown in Fig. 3.13.

Another very interesting example of trypsin imprinting [93] and its detection on QCM has been reported where template has been used in three different forms: amorphous, crystalline, and solubilized. Although the surface imprinting is possible with all three template models, experimental results suggest that the solubilized form of trypsin is highly appreciable concerning sensitivity point of view. These data obtained by exposing a set of different concentrations to three differently imprinted forms of trypsin have been presented in Table 3.2.

Trypsin imprinted surface was exposed to different other enzymes such as lysozyme and pepsin, and their relative mass change is noted. An excellent selectivity pattern is observed where the mass change is higher for trypsin than that for lysozyme and pepsin. This scheme was extended for lysozyme imprinting, and then a differential measurement was carried out for trypsin and lysozyme. It was evident from QCM results that surfaces imprinted with lysozyme and trypsin exhibit higher frequency response toward their original imprints in the presence of other (Fig. 3.14).

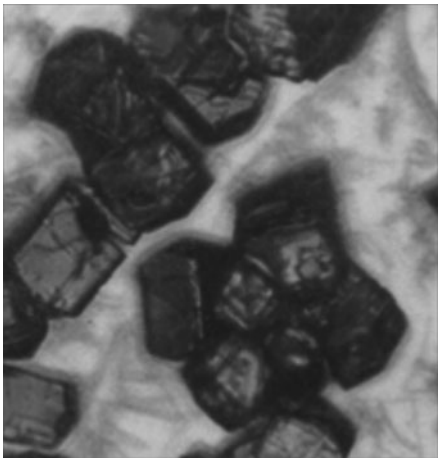

Fig. 3.13 AFM image of lysozyme crystallization on MIP surface

Table 3.2 Comparison of three differently imprinted polymer surfaces by calculating respective frequency shifts on various concentrations (adapted from [93])

	Sensor response [Hz] for three different template forms of trypsin		
Concentration of trypsin (μg/mL)	Lypophilized form	Crystalline form	Solubilzed form
100	60	90	310
500	80	180	400
1,000	170	250	550
2,000	275	300	850

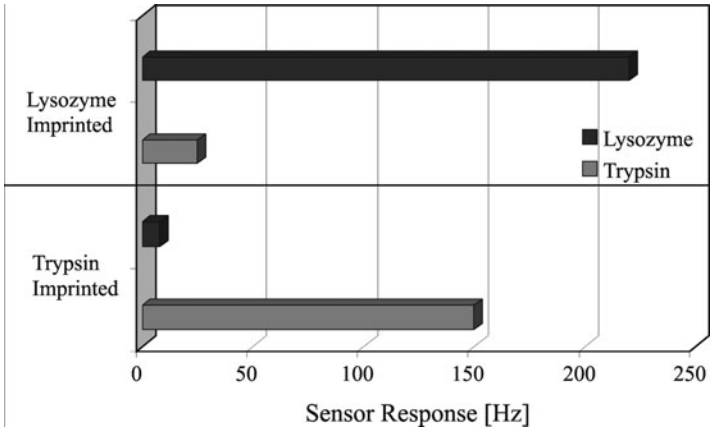

Fig. 3.14 Cross sensitivity comparison by differential mass-sensitive measurements on trypsin and lysozyme imprinted surfaces (adapted from [93])

In all the mass-sensitive measurements, the response of nonimprinted channel was almost negligible to different enzymes. The effect of pH on trypsin detection was also monitored by performing the measurement in different conditions. The frequency shift for trypsin imprinted surface was calculated for three different pH values, 5, 7, and 9.2 and found to be highest at a pH value 7. This could be explained in a way that the varying conformations of enzymes and the columbic interactions between surface and analyte seriously distort the imprinted surface structure. The most remarkable feature of this sensing technique is that the detection limit of 100 ng/mL can be achieved.

Nicholas et al. [94] has also reported protein imprinting and their very sensitive and specific detection by QCM. A very interesting approach about protein imprinting has been presented by John Rick and Tse-Chuan Chou in which they have used single and double protein molecules and observed protein–protein interactions [95] by mass-sensitive devices. They have used lysozyme and cytochrome *c* as individual templates

and together in different molar ratios for imprinting using poly-aminophenylboronic acid as a monomer. Experimental results have revealed that the lysozyme imprinted layer shows fairly selective binding of the own template, while cytochrome *c* imprinted layer does not exhibit recognition properties. Regarding the double imprinted protein structure, both species were used as templates in different molar ratios and their response toward different proteins was monitored. It has been found that when lysozyme and cytochrome *c* were used in equal molar ratios for imprinting, the layer has shown maximum frequency change for the imprinted proteins. These observations provide a new route for multiple imprinting procedures for studying the interactions between same biomolecules on quartz surface.

3.4.3 Artificial Receptors for Erythrocytes

Erythrocytes are basically red blood cells (RBC) that have hemoglobin and act as transporter for oxygen in blood. Erythrocytes are very flexible cells shaped like disks, having a diameter of approximately 7 μm, and a thickness of 2 μm. In previous examples, we already have knowledge of molecular imprinting for generating sensitive and selective materials for recognizing various microorganisms including bacteria and viruses. As erythrocytes have four different blood groups,A, B, O, and AB, for which molecular imprinting [96] can be handy to generate selective polymer layers capable of recognizing the respective blood group. The three blood groups, A, B, and AB, are recognized by the antigen on their surfaces and composed of oligosaccharides having six sugar molecules excluding blood group O, which has one less. The difference between blood group A and B is by only sixth sugar molecule at terminal position, whereas in the case of A, it is N-acteyl-D-galactosamine, and D-galactoside for blood group B. Molecular imprinting provides a straightforward approach to design suitable recognition materials for the detection of different blood groups on acoustic resonators. The blood groups A, B, AB, and O can be used as template model for imprinting on highly cross linked polyurethane layer. Typical polyurethane is composed of diphenyl diisocyanate as monomer, whereas bis phenol A and phloroglucinol are used as cross linkers. These cross linkers have excess of hydroxyl groups that play a very important role in imprinting as they offer suitable hydrogen bonding to the sugars present on blood group surface. Although the geometrical shapes of all these blood groups are almost identical, the predefined interaction of cells through hydrogen bonds with polyurethane surface offers suitable recognition. AFM image of imprinted erythrocytes on polymer surface have been shown in Fig. 3.15.

Different blood groups A, B, AB, and O have been used as templates [97] for surface imprinting by stamping method. The modified polyurethane surface was exposed to equal concentrations of different blood group samples. Mass-sensitive measurements reveal that the polyurethane surface imprinted with certain blood group (BG) shows utmost mass loads, particularly for BG that was used as template

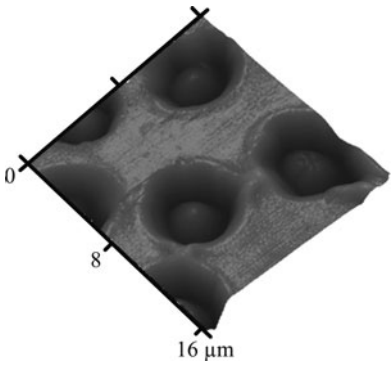

Fig. 3.15 AFM image of erythrocytes imprints

Table 3.3 Relative sensor response of different BG imprinted polymers by differential QCM measurements (adapted from [97])

Imprinted blood groups (BG)	Relative sensor effect [%]			
	BG A	BG B	BG AB	BG O
BG A	100	37	62	57
BG B	45	100	50	70
BG AB	85	70	100	40
BG O	65	85	29	100

in surface imprinting procedures. Generally, in each case, the relative sensor response of a polyurethane layer is highest for its own template. These data obtained from mass-sensitive measurements have been presented in Table 3.3.

These findings show that these studies can be extended to real-life samples. Despite the fact that the structural dimensions of erythrocytes are in micrometer range, the recognition of antigens present on their interface ensures the nano structuring pattern on polymer surface.

The conventional methods for blood group detection are based on chemical reactions with specific antigens that form precipitates, whereas the latest methods give a change in the reflectance of laser beam when the surface is exposed to the samples. On the other hand, molecular imprinting in combination with mass-sensitive devices offers much cheaper and rapid detection scheme for different blood group samples.

MIPs can be designed in a more sophisticated way to differentiate the subblood groups (i.e., A1 and A2) by mass-sensitive transducers. Recently [98], polyvinyl pyrrolidone has successfully been used for surface imprinting of A1 and A2 and were put under mass-sensitive measurements. Experimental results showed that the MIP layer gives larger signal for that subgroup, which was used for imprinting. For example, the mass effect for A1 imprinted layer is higher by a factor of approximately three when compared with A2 (Fig. 3.16).

The results obtained from mass-sensitive measurements show remarkable selectivity as they have similar geometrical dimensions and belong to the same ABO

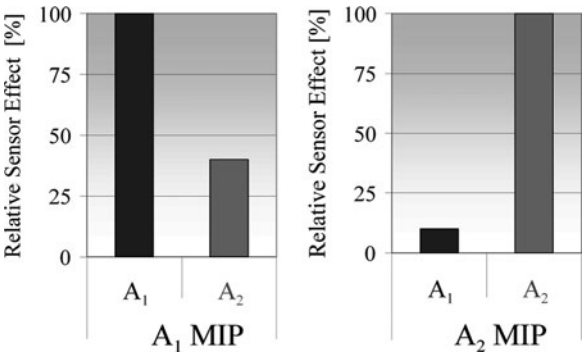

Fig. 3.16 Comparison of relative sensor responses of A1 and A2 imprinted polymers (adapted from [98])

system. They differ from each other by the amount of antigen density on their surface as in the case of A1 it is 0.81–1.17 $\times$ 10^6 A-antigens and for A2 it is 2.4–2.9 $\times$ 10^5. It is the beauty of molecular imprinting that provides patterned surfaces for selective incorporation of antigens. This study also reveals that MIP surfaces does not interact with analyte partially but shows affiliation with the whole cell to get complete information about surface density. These results are very appreciable and provide a complete understanding about the interactions of whole cell with modified polyvinyl pyrrolidone surfaces.

A slightly different synthetic strategy has been proposed for monitoring [99] of different blood groups and immunohematological reactions, using mass-sensitive devices (i.e., QCM) as transducers.

3.4.4 Hormones Detection

Hormones are basically chemical envoys in the body that carry the commands from one part to the other and are released by body cells in response to certain metabolic reactions. The excess or deficiency of any hormone in the body is called hormone disorder, which can lead to severe problems in functioning of cells. Different hormones in human body can be detected by examining blood, urine, and saliva samples, according to the desired hormone test. Among different hormones, insulin is very important, which takes the glucose from blood and stocks it up as glycogen in the liver and other cells and does not allow the use of body fat as energy resource. The disorder of insulin can cause serious diseases to the body such as diabetes, insulinoma, and others. In market, synthetic insulin can be produced for diabetic patients by fermentation process governed by yeast and bacteria. So, the detection of insulin is very important not only in human body to control metabolic reactions but also highly desirable in commercial point of view. The application of artificial materials for mass-sensitive detection of insulin and other hormones is very rare. The versatility of

surface imprinting makes promise to design suitable sensor materials for insulin detection [100] with a broad concentration range. Highly cross-linked polyurethane was prepared and coated on suitable mass-sensitive transducer (i.e., QCM) having 10 MHz fundamental resonance frequency. As mentioned already, solution phase stamping procedure was followed for imprinting of insulin on polyurethane surface. A series of different concentration solutions of insulin ranging from 1 μg/mL to 7 mg/mL has been exposed to imprinted channel and corresponding frequency change was monitored. It has been observed that the sensor response for different insulin solutions was linear for such a broad range, which suggests that this system can be used for quantitative determination of insulin in pharmaceutical formulations (i.e., 40 IU or 100 IU). IU stands for international unit for pharmacology activity that is 35 μg/mL of insulin.

Interestingly, different experiments have shown that the sensor response for insulin does not depend upon the layer height of the polymer on quartz, which is very surprising while considering surface imprinted layers. The sensor signal was reversible and reproducible for several measurements performed on different layer heights of polyurethane.

The temperature effect on insulin has also been monitored to examine its behavior by performing mass-sensitive measurements at different temperatures (i.e., 25, 40, 60, and 95°C). At all these temperatures, same concentration of insulin (i.e., 1 mg/mL) was used for analysis. It has been observed that the frequency shift is highest for that measurement, which was conducted at 25°C and then gradually decreases until at 95°C where it is lowest. Although the concentrations are same, the effect is different at different temperatures. This is probably due to the denaturing of insulin in which the structural features and functionality is lost, which ultimately cuts down the surface interactions between the analyte and the polymer layer. It signifies that by selecting proper storage temperature, the shelf life of insulin drugs can be enhanced. These findings are very significant for monitoring the quality of insulin products in pharmaceutical industry (Fig. 3.17).

Another strategy has also been proposed by Satish et al. [101], where a sandwich layer material has been crafted and coated on QCM for insulin detection. They

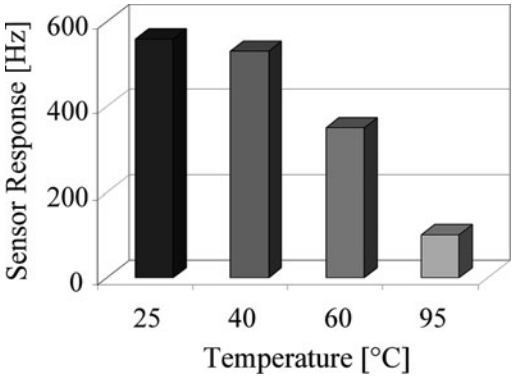

Fig. 3.17 Temperature effect on insulin sensor (adapted from [100])

have sandwiched an antigen between two specific antibodies and used it as sensing element. The lower antibody layer is deposited on quartz surface, while the upper antibody layer is used for insulin recognition and in between these layers an antigen is pressed. This layer material is exposed to different insulin concentrations and corresponding frequency shifts were noted. Although the lowest detection limit was achieved (i.e., 1 ng/mL), the sensor signal does not remain linear after 10 μg/mL of insulin, which is not favorable for commercial use. The effect of temperature on mass-sensitive measurement has not been discussed. The synthetic scheme is also very complex for layer structuring that requires relatively more care, and more importantly low stability of natural antibodies restrict their use for long-term analysis.

Catecholamine is a very important class of hormones, which acts as neurotransmitters in the body and is released in response to certain psychological reactions. Major catecholamines are dopamine, norepinephrine, and epinephrine, which are excreted in urine. Disorder in this hormone can lead to serious complications in the central nervous system. The detection of these hormones can be made by fluorescent technique and other methods such as ion exchange chromatography and high performance liquid chromatorgraphy (HPLC), where different catecholamines are isolated and characterized from urine samples. Suitable sensor materials can be generated through molecular imprinting for selective detection of catecholamines in a complex urine solution. Tzong et al. [102] designed such materials by imprinting dopamine and developed a suitable sensor system using QCM as transducer. Authors have synthesized dopamine MIP powder and examined their binding properties at different pH values by HPLC studies. Dopamine MIP films were also generated by following a different reaction route and the effect of pH was also monitored on rebinding capacity of these films. These studies reveal that dopamine imprinted film preferably binds dopamine when compared with norepinephrine and epinephrine. Similarly other catecholamine imprinted films (i.e., norepinephrine and epinephrine) specifically bind the original imprint molecule as shown in Table 3.4. Dopamine MIP layer coated on 9 MHz quartz exhibits maximum frequency shift for dopamine itself, while for norepinephrine and epinephrine it is negligible. The results are summarized in Table 3.4. These studies are valuable and encouraging in designing a suitable detection model for catecholamines.

MIPs with acoustic devices have also been employed for detection of plant hormones, for example, indole-3-acetic acid (IAA) plays a vital role in plant development. Akimitsu and Toshifumi [103] had designed molecularly imprinted

Table 3.4 Summarized results of different MIP hormones to monitor the rebinding quantity on from analyte solutions (adapted from [102])

	Rebinding quantity of analyte solutions [μ mol]		
MIP hormones	Dopamine	Norepinephrine	Epinephrine
Dopamine	0.17	0.05	0.03
Norepinephrine	0.01	0.08	0.02
Epinephrine	0.01	0.02	0.05

meth acrylic acid (MAA) polymer for selective recognition of IAA, using 9 MHz QCM to perform mass-sensitive measurement. A series of different concentrations of IAA ranging from 10 to 200 nM has been used on imprinted and the nonimprinted QCM. The change in the frequency is linear in the defined range upon mass loading of IAA. This experiment was performed on three different QCMs to observe the relative variation in the frequency shifts on same concentrations of IAA. The reported results show a coefficient of variation for three different sensors 5.3%, 6.1%, and 8.8%, respectively, which means that there is no significant difference in their performance. This is an evidence for a sensor system to generate reproducible results. The selectivity of this sensor has also been monitored by performing measurements with indole-3-butyric acid (IBA), indole, and indole-3-ethanol (IET) of same concentrations. Sensor results clearly demonstrate that the frequency change for IAA is maximum, while for IBA, indole, and IET, the response is quite low, which shows the selective nature of designed sensor material. The reason of highly selective nature of imprinted MAA polymer is could be due to the suitable electrostatic interactions between *N*,*N*-dimethylamino group from monomer to carboxylic group of IAA (Fig. 3.18).

Synthetic receptors derived from molecular imprinting possess desired degree of selectivity in comparison with other schemes. In combination with mass-sensitive devices, molecular imprinting is very advantageous for developing suitable sensor systems for hormones detection. Despite of the fact that MIP applications for hormones detection are very few but still promising to replace conventional methods for their detection.

3.4.5 Bilirubin Detection by Synthetic Receptors

Molecularly imprinted polymers have been proved very effective for bilirubin detection via mass-sensitive devices. Bilirubin is a yellow color waste material

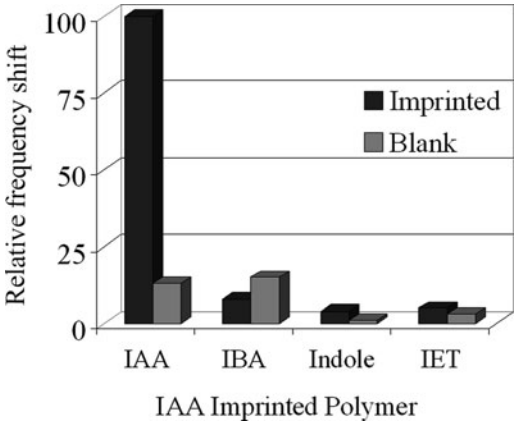

Fig. 3.18 Relative frequency shifts for other similar hormones on IAA imprinted polymer surface (adapted from [103])

that is produced from the breakdown of hemoglobin molecules of RBC. Bilirubin tests are often conducted to examine its production and excretion from body, which ultimately refers to the working of the liver cells. Elevated amounts of bilirubin in the body indicate the improper functioning of liver, which causes hepatic diseases and in severe cases permanent damage to the brain or even results in death [104]. Various voltammetric [105] and flourometric [106] methods have been reported for bilirubin analysis with substantial sensitivity. Conventional method for bilirubin detection is based on dizao reaction, where azobilirubin is produced by the condensation reaction of diazotized sulfanilic with bilirubin.

Authors [107] have successfully prepared bilirubin imprinted polymer, using 4-vinyl pyrrolidone as functional monomer along with DVB as cross linker. The polymerization reaction was initiated by benzophenone and carried out under UV light. The surface of gold electrodes on QCM is properly cleaned and is modified by treating it with thiols before coating MIP layer. Different topographical images of the coated film had been recorded by SEM that exhibit a uniform surface structure of bilirubin MIP. Mass-sensitive measurements performed on 9 MHz QCM exhibit suitable sensor response for defined amounts of bilirubin samples. The effect of pH on bilirubin detection was also examined by performing mass-sensitive measurements at different pH values ranging from 5.4 to 11.5. It has been found that at higher pH value (i.e., 11.5), the frequency shift is also higher. The bilirubin MIP surface was exposed to a set of different concentrations (i.e.) from 0.45 to 11.0 mg/dL of bilirubin and found that the sensor response is linear in this range. Biliverdin, which is a similar compound to bilirubin, was selected as a model to examine the selectivity of bilirubin MIP. The sensor signal for bilirubin is much higher when compared with biliverdin, which shows that bilirubin imprinted surface preferably binds the own template compared with other analogous species.

MIP coated on QCM has proven itself as an effective tool for clinical analysis of bilirubin, which offers a reliable, simple, and fairly cheap detection system in comparison with other methods.

3.4.6 Miscellaneous Examples

Molecular imprinting approach can also be extended for another very important class of materials (i.e., nanoparticles) to generate more sophisticated surfaces for sensing principles. Kristina et al. [108] prepared imprinted nanoparticles and introduced them in to a thin poly ethylene terephthalate (PET) layer coated on quartz wafer. The AFM study of imprinted nanoparticles shows a fine and uniform distribution that has potential to recognize pair (*R*)- and (*S*)-propranolol in aqueous buffer. Propranolol is a nonselective beta blocker drug that is very useful for hypertension treatment. The imprinted nanoparticles show a definite degree of chiral selectivity for enantiomeric pair of (*R*)- and (*S*)- propranolol. This indeed is a positive step toward designing enantiomeric biosensor materials and can only be achieved by careful controlling of the morphology of nanoparticles.

The applications of molecular imprinting with mass-sensitive devices such as QCM are very limited for DNA identification. Recently, a new biosensor has been designed for DNA recognition [109], based on molecularly imprinted polymers coated on QCM. Authors had synthesized thymine-MIP by using methacryloylamido, adenine, thymine (MA-Ade-thymine) as functional monomer along with EDMA as cross linker with AIBN initiator. The nonimprinted polymer was prepared in a similar fashion excluding thymine. They had modified the gold electrode surface of QCM before coating thymine-MIP layer. The surface of bare electrode, thiol-treated gold surface, and thymine layer was characterized by AFM on wave mode. MIP generates very suitable tailor-made cavities for thymine interactions through hydrogen bonding with functional groups of polymer. Mass-sensitive measurements performed on imprinted and nonimprinted channels exhibit a substantial difference in frequency shifts for a defined concentration range. The selectivity of MIP layer was also examined by calculating the sensor response for same concentrations of thymine, uracil, poly(dT) (ssDNA), and poly(U) (ssRNA). The sensor signal for thymine at all concentration points was higher in comparison with others.

Some other strategies are also reported where instead of a synthetic polymer, gold nanoparticles act as sensing material [110] for mass-sensitive detection of DNA molecules. Although these materials are very rarely used for biorecognition, they have very good sensitivity (e.g., 10^{-14} M and 10^{-16} mol/L). Another more advanced design has been reported [111] where 3×3 QCM matrix is assembled on which specific antibody is coated for DNA sensing. This detection mechanism is very attractive as it provides a suitable platform for online monitoring of various biological analytes. Colloidal gold nanoparticles have also been reported [112] to improve the gold-coated QCM surface. These gold particles possess high surface area and enhanced interaction sites that exhibit appreciable sensor signal for target DNA strands. Despite the fact that these schemes do not hold any modified polymer interface on quartz surface, they are good enough for designing DNA sensing systems.

The LBL technique also contributes to the detection of various bioanalytes but along with mass-sensitive devices, their applications are relatively limited. A LBL assembling of liposomes and protein membrane [113] was made on QCM surface for biological recognition. The sensitive layer was characterized by AFM and put under detection of nonylphenols where it had showed satisfactory results in low ppm concentration range. Some other examples are also reported where LBL films with QCM have proven very handy for sensitive detection of DNA strains. A very exciting example of dengue virus detection has been reported using LBL hybridized gold nanoparticles [114] as sensing element. These modified nanoparticles provide high sensitivity through QCM for the detection of dengue virus. In comparison with other polymer surfaces, nanoparticles provide more binding sites that has affinity for target analyte. SEM images give a clear picture of LBL assembling of gold nano particles on quartz surface. The modified oligonucleotide gold particles are not only sensitive for viral detection but also very specific for target specie. Along with mass-sensitive devices, they have proven themselves to be very successful for diagnostic purposes in real blood samples of dengue viral infections. Almost

more than hundred countries had suffered from this virus and very high rate of causalities have been reported in different regions. Such detection methods are very encouraging in developing more effective systems that are low cost and suitable for online surveillance.

Multi-sensor strategy is very exciting and innovative regarding the detection of diverse bioanalytes on a single platform. In this way, we would be able to immobilize different MIP on a single QCM that would be competent to bind specifically target analytes. One such approach has already been mentioned.

3.5 Conclusion and Future Outlook

Considering the material designing for biosensors, molecular imprinting has shown potential for recognition of various bioanalytes including microorganisms such as yeast, bacteria, viruses, and others such as proteins, enzymes, erythrocytes, etc. The tailor-made structures of imprinted polymers provide enhanced selectivity for target analyte molecules at nanometer scale where the size, shape, and dimensions of imprinted cavities are optimized for a desired biomolecule. The most significant aspect is that molecular imprinting is virtually applicable to almost all biological species unless template does not chemically react with polymer matrix. The synthetic procedure of imprinting is much more convenient when compare with other methods that are more complex, time consuming, and relatively need expansive chemical reagents. As we have learnt from the previous study that surface imprinted polymers have very broad spectrum for biosensors when compared with other material crafting technique. Unlike natural antibodies, MIPs bind analyte molecules reversibly through weak attraction forces and thus makes reusability of these materials that can be used for several analysis. The other material designing strategies such as natural antibodies, LBL, and host–guest interactions have some contributions in developing biorecognition materials but not exploited for commercial use of biosensors. The other part of biosensors concerning transducers is accomplished by acoustic or mass-sensitive devices such as QCM, which furnishes high sensitivity to designed biosensors. These devices are capable of sensing the mass of analyte in nanogram or even in picogram range (i.e., SAW devices, which are very valuable while dealing with extremely low concentrations).

The sensitive and precise detection of different bioanalytes can be enhanced in two ways: first, optimizing the synthetic procedures for imprinting, and second by tuning mass-sensitive devices for achieving best possible sensitivity. The first part of sensor design deals with imprinting technique where the analyte interactions with MIP surface need to be made better adjusting monomer cross linker ratio, establishing proper reaction conditions such as favorable solvent, temperature, and heating time. The careful monitoring of different reaction parameters not only provides maximum binding sites but also constructs template-oriented cavities for selective detection. Another very important aspect (i.e., response time) can be

improved by controlling the surface structures of MIPs so that the analyte molecule readily be attached or detached without consuming much time. These modifications in synthetic receptors enhance the sensitivity and permit only target analyte to be bounded specifically with MIP surface. Concerning the reusability of the sensor materials, the template MIP interaction should be entirely reversible that can only be achieved by developing noncovalent interface.

The other part is concerned with the design of transducers. At the moment, QCMs having frequency 5–20 MHz are used widely as mass-sensitive transducers. The fundamental resonance frequency depends on thickness of quartz sheet, which is a key parameter to amplify the mass sensing capabilities of acoustic devices. The sensitivity can be made better by producing more thin QCMs, which is not feasible from a mechanical point of view as these devices would turn out to be very fragile. This restricts the use of acoustic devices to extend the detection limits of acoustic biosensors. An alternative can be used to overcome this deficiency of acoustic resonators by introducing film bulk acoustic resonators (FBAR). These devices operate in the GHz range, which is higher by a factor of 10^3 than typical QCM resonance frequency. They not only offer enhanced sensitivity but also exhibit fine linearity, small and compact size, and less damping loss in viscoelastic medium.

The overall objective of this study is to demonstrate patterned polymer surfaces for selective recognition of different bioanalytes through acoustic resonators, thus providing a suitable, economic detection system to improve public health and ensure a safe environment.

Acknowledgments I thank Higher Education Commission (HEC) of Pakistan for providing funding for my PhD studies.

References

1. Caruso F, Rodda E, Furlong DN (1996) Orientational aspects of antibody immobilization and immunological activity on quartz crystal microbalance electrodes. J Colloid Interface Sci 178:104–115
2. Steinem C, Janshoff A (2007) Piezoelectric sensors (Springer Series on Chemical Sensors and Biosensors. Springer, Berlin
3. Lee S, Stubbs DD, Cairney J et al (2005) Rapid detection of bacterial spores using a quartz crystal microbalance (QCM) immunoassay. IEEE Sens J 5:737–743
4. Decher G, Hong JD, Schmitt J (1992) Buildup of ultrathin multilayer films by a self-assembly process: III. Consecutively alternating adsorption of anionic and cationic polyelectrolytes on charged surfaces. Thin Solid Films 210:831–835
5. Decher G (1997) Fuzzy nanoassemblies: toward layered polymeric multi composites. Science 277:1232–1237
6. Stockton WB, Rubner MF (1995) Molecular layer processing of polyaniline via the use of hydrogen bonding interactions. Mater Res Soc Symp Proc 369:587–592
7. Brynda E, Houska M (1996) Multiple alternating molecular layers of albumin and heparin on solid surfaces of medical devices. J Colloid Interface Sci 183:18–25

8. Sun J, Wu T, Sun Y et al (1998) Fabrication of a covalently attached multilayer via photolysis of layer-by-layer self-assembled films containing diazo-resins. Chem Commun 1853–1854
9. Kotov NA (1999) Layer-by-layer self-assembly: the contribution of hydrophobic interactions. Nanostruct Mater 12:789–796
10. Lojou E, Bianco P (2004) Buildup of polyelectrolyte-protein multilayer assemblies on gold electrodes. Role of the hydrophobic effect. Langmuir 20:748–755
11. Hong JD, Lowack K, Schmitt J et al (1993) Layer-by-layer deposited multilayer assemblies of polyelectrolytes and proteins: from ultrathin films to protein arrays. Prog Colloid Polym Sci 93:98–102
12. Lvov Y, Ariga K, Kunitake T (1996) Layer-by-layer assembly of alternate protein/polyion ultrathin films. Chem Lett 12:2323–2326
13. Kong W, Zhang X, Gao ML et al (1994) A new kind of immobilized enzyme multilayer based on cationic and anionic interaction. Macromol Rapid Commun 15:405–409
14. Lvov Y, Ariga K, Ichinose I et al (1995) Assembly of multicomponent protein films by means of electrostatic layer-by-layer adsorption. J Am Chem Soc 117:6117–6123
15. Boulmedais F, Ball V, Schwinte P et al (2003) Buildup of exponentially growing multilayer polypeptide films with internal secondary structure. Langmuir 19:440–445
16. Lvov Y, Decher G, Sukhorukov G (1993) Assembly of thin films by means of successive deposition of alternate layers of DNA and poly(allylamine). Macromolecules 26:5396–5399
17. Yoo PJ, Nam KT, Qi J et al (2006) Spontaneous assembly of viruses on multilayered polymer surfaces. Nat Mater 5:234–240
18. Caruso F, Niikura K, Furlong DN et al (1997) Assembly of alternating polyelectrolyte and protein multilayer films for immunosensing. Langmuir 13:3427–3433
19. Kotov NA, Dekany I, Fendler JH (1995) Layer-by-layer self-assembly of polyelectrolyte-semiconductor nanoparticle composite films. J Phys Chem 99:13065–13069
20. Jiang C, Ko H, Tsukruk VV (2005) Strain-sensitive Raman modes of carbon nanotubes in deflecting freely suspended nanomembranes. Adv Mater 17:2127–2131
21. Keller SW, Kim HN, Mallouk TE (1994) Layer-by-Layer assembly of intercalation compounds and heterostructures on surfaces: toward molecular "Beaker" epitaxy. J Am Chem Soc 116:8817–8818
22. Kleinfeld ER, Ferguson GS (1994) Stepwise formation of multilayered nanostructural films from macromolecular precursors. Science 265:370–373
23. Anzai J-I, Kobayashi Y, Nakamura N (1999) Layer-by-layer construction of multilayer thin films composed of avidin and biotin-labeled poly(amine)s. Langmuir 15:221–226
24. Koktysh DS, Liang X, Yun BG et al (2002) Biomaterials by design: layer-by-layer assembled ion-selective and biocompatible films of TiO_2 nanoshells for neurochemical monitoring. Adv Funct Mater 12:255–265
25. Fiammengo R, Crego-Calama M, Reinhoudt DN (2001) Synthetic self-assembled models with biomimetic functions. Curr Opin Chem Biol 5:660–673
26. Sellergren B (ed) (2001) Molecularly imprinted polymers – techniques and instrumentation in analytical chemistry, vol. 23, 1st edn. Elsevier, Amsterdam
27. Kiefer HC, Congdon WI, Scarpa IS et al (1972) Catalytic accelerations of 1012-fold by an enzyme-like synthetic polymer. Proc Natl Acad Sci U S A 69:2155–2159
28. Wulff G, Sarhan A (1972) The use of polymers with enzyme-analogous structures for the resolution of racemates. Angew Chem Int Ed 11:341
29. Karsten H, Mosbach K (2000) Molecularly imprinted polymers and their use in biomimetic sensors. Chem Rev 100:2495–2504
30. Piletsky SA, Piletska EV, Karim K et al (2002) Polymer cookery: influence of polymerization conditions on the performance of molecularly imprinted polymers. Macromolecules 35:7499–7504

31. Piletsky SA, Guerreiro A, Piletska EV et al (2004) Polymer cookery. 2. Influence of polymerization pressure and polymer swelling on the performance of molecularly imprinted polymers. Macromolecules 37:5018–5022
32. Andersson HS, Karlsson JG, Piletsky SA et al (1999) Study of the nature of recognition in molecularly imprinted polymers II. Influence of monomer-template ratio and sample load on retention and selectivity. J Chromatogr A 848:39–49
33. Mosbach K (1994) Molecular imprinting. Trends Biochem Sci 19:9–14
34. Whitecombe MJ, Rodriguez E, Villar P et al (1995) A new method for the introduction of recognition site functionality into polymers prepared by molecular imprinting: synthesis and characterization of polymeric receptors for cholesterol. J Am Chem Soc 117:7105–7111
35. Pestov D, Levit N, Maniscalco V et al (2004) Molecular imprinting using monomers with solid-state polymerization. Anal Chim Acta 504:31–35
36. Defreese JL, Katz A (2005) Synthesis of a confined class of chiral organic catalysts via bulk imprinting of silica. Chem Mater 17:6503–6506
37. Hayden O, Haderspock C, Krassnig S et al (2006) Surface imprinting strategies for the detection of trypsin. Analyst 131:1044–1050
38. Hayden O, Bindeus R, Dickert FL (2003) Combining atomic force microscope and quartz crystal microbalance studies for cell detection. Meas Sci Technol 14:1876–1881
39. Curie J, Curie P (1880) Développement, par pression, de l'électricité polaire dans les cristaux hémièdres à faces inclinées. C R Acad Bulg Sci 91:294–295
40. Sauerbrey G (1959) Verwendung von schwingquarzen zur wangung dunner schichten und zur mikrowagung. Z Phys 155:206–222
41. Rayleigh L (1885) On waves propagated along the plane surface of an elastic solid. Proc Lond Math Soc s1–17:4–11
42. Dickert FL, Forth P, Bulst WE et al (1998) SAW devices – sensitivity enhancement in going from 80 MHz to 1 GHz. Sens Actuators B 46:120–125
43. Tom-Moy M, Baer RL, Spira-Solomon D et al (1995) Atrazine measurements using surface transverse wave devices. Anal Chem 67:1510–1516
44. Briot JB, Ballandras S, Bigler E, Martin G (1997) Gravimetric sensitivity of transverse waves trapped by metal gratings on thin quartz plates. IEEE Symp. Freq. Cont.:207-212
45. Barnett JA (2003) Beginnings of microbiology and biochemistry: the contribution of yeast research. Microbiology 149:557–567
46. Ostergaard S, Olsson L, Nielsen J (2000) Metabolic engineering of *Saccharomyces cerevisiae*. Microbiol Mol Biol Rev 64:34–50
47. Baronian KHR (2004) The use of yeast and moulds as sensing elements in biosensors. Biosens Bioelectron 19:953–962
48. Hayden O, Dickert FL (2001) Selective microorganism detection with cell surface imprinted polymers. Adv Mater 13:1480–1483
49. Seidler K, Lieberzeit, PA, Dickert FL (2009) Application of yeast imprinting in biotechnology and process control. Analyst 134:361–366
50. Seidler K, Polreichova M, Lieberzeit PA et al (2009) Biomimetic yeast cell typing – application of QCMs. Sensors 9:8146–8157
51. Rangel JM, Sparling PH, Crowe C et al (2005) Epidemiology of *Escherichia coli* O157:H7 outbreaks, United States, 1982–2002. Emerg Infect Dis 11:603–609
52. Maule A (1997) In: Kay D, Fricker C (eds) Coliforms and *E. coli*: problem or solution? The Royal Society of Chemistry, Cambridge, UK
53. Tuttle J, Gomez T, Doyle M P et al (1999) Lessons from a large outbreak of *Escherichia coli* O157:H7 infections: Insights into the infectious dose and method of widespread contamination of hamburger patties. Epidemiol Infect 122:185–192
54. Cui S, Schroeder CM, Zhang DY et al (2003) Rapid sample preparation method for PCR-based detection of *Escherichia coli* O157:H7 in ground beef. J Appl Microbiol 95:129–134
55. Fode-Vaughan KA, Maki JS, Benson JA et al (2003) Direct PCR detection of *Escherichia coli* O157:H7. Lett Appl Microbiol 37:239–243

56. Fawcett NC, Evans JA, Craven R.D et al (1997) Polymers for use on bulk acoustic wave DNA hybridization biosensors. Polym Mater Sci Eng 76:461–462
57. Deisingh AK, Thompson M (2001) Sequences of *E. coli* O157:H7 detected by a PCR-acoustic wave sensor combination. Analyst 126:2153–2158
58. Kai E, Ikebukuro K, Hoshina S et al (2000) Detection of PCR products of *E. coli* O157:H7 in human stool samples using surface plasmon resonance. FEMS Immunol Med Microbiol 29:283–288
59. Ruan C, Yang L, Li Y (2002) Immunobiosensor chips for detection of E. coli O157:H7 using electrochemical impedance spectroscopy. Anal Chem 7:4814–4820
60. Zhang D, Chen S, Qin L et al (2005) The novel immunobiosensors for detection of *Escherichia coli* O157:H7 using electrochemical impedance spectroscopy. Conf Proc IEEE Eng Med Biol Soc 7:7111–7113
61. Liu Y, Ye J, Li Y (2003) Rapid detection of *E. coli* O157:H7 in ground beef, chicken carcass, and lettuce samples using an immunomagnetic chemiluminescence fiber optic biosensor. J Food Prot 66:512–517
62. Berqwerff AA, Knapen FV (2006) Surface plasmon resonance biosensors for detection of pathogenic microorganisms: Strategies to secure food and environmental safety. J AOAC Int 89:826–831
63. Taylor AD, Ladd J, Yu et al (2006) Quantitative and simultaneous detection of four foodborne bacterial pathogens with a multi-channel SPR sensor. Biosens Bioelectron 22:752–758
64. Subramanian A, Irudayaraj J, Ryan T (2006) A mixed self-assembled monolayer-based surface plasmon immunosensor for detection of *E. coli* O157:H7. Biosens Bioelectron 21:998–1006
65. Liu Y, Li Y (2001) An antibody-immobilized capillary column as a bioseparator/ bioreactor for detection of *E. coli* O157:H7 with absorbance measurement. Anal Chem 73:5180–5183
66. Su XL, Li Y (2004) A self-assembled monolayer-based piezoelectric immunosensorfor rapid detection of *Escherichia coli* O157:H7. Biosens Bioelectron 19:563–574
67. Howe E, Harding G (2000) A comparison of protocols for the optimisation of detection of bacteria using a surface acoustic wave (SAW) biosensor. Biosens Bioelectron 15:641–649
68. Zhihong S, Mingchuan H, Caide X et al (2007) Nonlabeled quartz crystal microbalance biosensor for bacterial detection using carbohydrate and lectin recognitions. Anal Chem 79:2312–2319
69. Wang LJ, Wei QS, Wu CS et al (2008) The *Escherichia coli* O157:H7 DNA detection on a gold nanoparticle-enhanced piezoelectric biosensor. Chin Sci Bull 53:1175–1184
70. Dickert FL, Hayden O, Lieberzeit PA et al (2003) Borderline applications of QCM-devices: synthetic antibodies for analytes in both nm- and μm-dimensions. Sens Actuators B 95:20–24
71. Young PR, Hilditch PA, Bletchly C et al (2000) An antigen capture enzyme-linked immunosorbent assay reveals high levels of the dengue virus protein NS1 in the sera of infected patients. J Clin Microbiol 38:1053–1057
72. Shi L, Chen Q, Norling LA et al (2004) Real time quantitative PCR as a method to evaluate xenotropic murine leukemia virus removal during pharmaceutical protein purification. Biotechnol Bioeng 87:884–896
73. Branson BM (2000) Rapid tests for HIV antibody. AIDS Rev 2:76–83
74. Hayden O, Lieberzeit PA, Blaas D et al (2006) Artificial antibodies for bioanalyte detection – sensing viruses and proteins. Adv Funct Mater 16:1269–1278
75. Knez M, Sumser MP, Bittner AM et al (2004) Binding the tobacco mosaic virus to inorganic surfaces. Langmuir 20:441–447
76. Dickert FL, Hayden O, Lieberzeit PA et al. (2003) Nano- and micro-structuring of sensor materials – from molecule to cell detection. Synth Met 138:65–69
77. Knez M, Sumser M, Bittner AM et al (2004) Spatially selective nucleation of metal clusters on the tobacco mosaic virus. Adv Funct Mater 14:116–124

78. Bolisay LD, Culver JN, Kofinas P (2007) Optimization of virus imprinting methods to improve selectivity and reduce nonspecific binding. Biomacromolecules 8:3893–3899
79. Jenik M, Schirhagl R, Schirk C et al (2009) Sensing picornaviruses using molecular imprinting techniques on a quartz crystal microbalance. Anal Chem 81:5320–5326
80. Birnbaumer GM, Lieberzeit PA, Richter L et al (2009) Detection of viruses with molecularly imprinted polymers integrated on a microfluidic biochip using contact-less dielectric microsensors. Lab Chip 9:3549–3556
81. Rachkov A, Minoura N (2001) Towards molecularly imprinted polymers selective to peptides and proteins. The epitope approach. Biochim Biophys Acta 1544:255–266
82. Tai DF, Lin CY, Wu TZ et al (2005) Recognition of dengue virus protein using epitope-mediated molecularly imprinted film. Anal Chem 77:5140–5143
83. Ramanaviciene A, Ramanavicius A (2004) Molecularly imprinted polypyrrole-based synthetic receptor for direct detection of bovine leukemia virus glycoproteins. Biosens Bioelectron 20:1076–1082
84. Ge Yi, Turner APF (2008) Too large to fit? Recent developments in macromolecular imprinting. Trends Biotechnol 26:218–224
85. Turner NW, Jeans CW, Brain KR et al (2006) From 3D to 2D: a review of the molecular imprinting of proteins. Biotechnol Prog 22:1474–1489
86. Bossi A, Bonini F, Turner APF et al (2007) Molecularly imprinted polymers for the recognition of proteins: the state of the art. Biosens Bioelectron 22:1131–1137
87. Janiak D, Kofinas P (2007) Molecular imprinting of peptides and proteins in aqueous media. Anal Bioanal Chem 389:399–404
88. Hansen DE (2007) Recent developments in the molecular imprinting of proteins. Biomaterials 28:4178–91
89. Byrne ME, Park K, Peppas NA (2002) Molecular imprinting within hydrogels. Adv Drug Delivery Rev 54:149–161
90. Hillberg AL, Tabrizian M (2008) Biomolecule imprinting: developments in mimicking dynamic natural recognition systems. ITBM-RBM 29:89–104
91. Zhang Z, Long Y, Nie L et al (2006) Molecularly imprinted thin film self-assembled on piezoelectric quartz crystal surface by the sol–gel process for protein recognition. Biosens Bioelectron 21:1244–1251
92. Hayden O, Bindeus R, Haderspock C et al (2003) Mass-sensitive detection of cells, viruses and enzymes with artificial receptors. Sens Actuators B 91:316–319
93. Hayden O, Haderspock C, Krassnig S et al (2006) Surface imprinting strategies for the detection of trypsin. Analyst 131:1044–1050
94. Turner NW, Wright BE, Hlady V et al (2007) Formation of protein molecular imprints within Langmuir monolayers: a quartz crystal microbalance study. J Colloid Interface Sci 308:71–80
95. Rick J, Chou TC (2005) Imprinting unique motifs formed from protein–protein associations. Anal Chim Acta 542:26–31
96. Dickert FL, Lieberzeit PA, Miarecka SG et al (2004) Synthetic receptors for chemical sensors – subnano- and micrometer patterning by imprinting techniques. Biosens Bioelectron 20:1040–1044
97. Hayden O, Mann KJ, Krassnig S et al (2006) Biomimetic ABO blood-group typing. Angew Chem Int Ed 45:2626–2629
98. Seifner A, Lieberzeit PA, Jungbauerb C et al (2009) Synthetic receptors for selectively detecting erythrocyte ABO subgroups. Anal Chim Acta 651:215–219
99. Zuccato A, Facci P, Alessandrini A (2008) Rapid monitoring system for blood groups and immunohematological reaction detection. United States patent US 2008/0160600 A1
100. Lieberzeit PA, Afzal A, Podlipna D et al (2007) Printing materials in micro- and nano-scale: Systems for process control. Sens Actuators B 126:153–158

101. Saha S, Raje M, Suri CR (2002) Sandwich microgravimetric immunoassay: sensitive and specific detection of low molecular weight analytes using piezoelectric quartz crystal. Biotechnol Lett 24:711–716
102. Ling TR, Syu YZ, Tasi YC et al (2005) Size-selective recognition of catecholamines by molecular imprinting on silica–alumina gel. Biosens Bioelectron 21:901–907
103. Kugimiya A, Takeuchi T (1999) Molecularly imprinted polymer-coated quartz crystal microbalance for detection of biological hormone. Electroanalysis 11:1158–1160
104. Cotler SJ, Taylor SL, Gretch DR et al (2000) Hyperbilirubinemia and cholestatic liver injury in hepatitis C-infected liver transplant recipients. Am J Gastroenterol 95:753–759
105. Doumas BT, Perry FB, Jendrezjczac B et al (1987) Measurement of direct bilirubin by use of bilirubin oxidase. Clin Chem 33:1349–1353
106. Wu N, Hovath WJ, Huie CW (1992) Light emission from bilirubin using the peroxyoxalate chemiluminescence reaction. Anal Chim Acta 269:99–107
107. Wu AH, Syu MJ (2006) Synthesis of bilirubin imprinted polymer thin film for the continuous detection of bilirubin in an MIP/QCM/FIA system. Biosens Bioelectron 21:2345–2353
108. Reimhulta K, Yoshimatsub K, Risvedenb K et al (2008) Characterization of QCM sensor surfaces coated with molecularly imprinted nanoparticles. Biosens Bioelectron 23:1908–1914
109. Diltemiza SE, Hüra D, Ersöza A et al (2009) Designing of MIP based QCM sensor having thymine recognition sites based on biomimicking DNA approach. Biosens Bioelectron 25:599–603
110. Zhao1 HQ, Lin L, Li1 JR et al (2001) DNA biosensor with high sensitivity amplified by gold nanoparticles. J Nanopart Res 3:321–323
111. Huang GS, Wang MT, Hong MY (2006) A versatile QCM matrix system for online and high-throughput bio-sensing. Analyst 131:382–387
112. Liu T, Tang J, Jiang L (2004) The enhancement effect of gold nanoparticles as a surface modifier on DNA sensor sensitivity. Biochem Biophys Res Commun 313:3–7
113. Nakane Y, Kubo I (2009) Layer-by-layer of liposomes and membrane protein as a recognition element of biosensor. Thin Solid Films 518:678–681
114. Chen SH, Chuang YC, Yi-Chen Lu et al (2009) A method of layer-by-layer gold nanoparticle hybridization in a quartz crystal microbalance DNA sensing system used to detect dengue virus. Nanotechnology 20:215501 (10pp)

Chapter 4
Surface Plasmon Resonance on Nanoscale Organic Films

Willem M. Albers and Inger Vikholm-Lundin

4.1 Introduction

Surface plasmon resonance (SPR) has been known since the pioneering work by Kretschman, Reather, and Ritchie in the late 1960s, who demonstrated the possibility for excitation of electrons at the interface of a dielectric and conductive (metallic) surface by polarized light or by using a metallic diffraction grating, and this was soon applied to determination of optical constants of metals [1–23]. The first monograph on SPR appeared in 1988 [4]. The application of SPR to gas and biochemical sensing was first reported by Nylander et al. in 1982 [5], and recently a few handbooks have appeared, which cover most theory and applications of SPR [6–78].

The biosensing capabilities of SPR are based on the fact that thin layers of biomolecules, monolayers, or sub-monolayers strongly attenuate the surface plasmon excitation conditions, which can be measured as a change in the resonance angle or wavelength. The strong optical absorbance of metallic nanoparticles, particularly that of gold colloids, has been known for a long time, and colored gold colloids have been used for glass staining in the medieval times. However, it was Michael Faraday, who first made a systematic study of the synthesis and optical properties of colloidal gold [9], and Mie, who devised theoretical models for the scattering behavior of gold colloids [10]. Nowadays, gold colloids are abundantly used in biochemical assays by virtue of the localized surface plasmon resonance (LSPR) phenomenon [11, 12]. LSPR produces a strong absorbance, which is not only dependent on the optical constants of the metal and the dimensions and shape of the particle, but also sensitive to changes in the medium close to the particle.

W.M. Albers (✉)
VTT Technical Research Centre of Finland, Microtechnologies and Sensors, Molecular Sensors, 1300, FIN-33101 Tampere, Finland
e-mail: martin.albers@vtt.fi

S. Carrara (ed.), *Nano-Bio-Sensing*,
DOI 10.1007/978-1-4419-6169-3_4, © Springer Science+Business Media, LLC 2011

The present chapter will briefly introduce the basics of SPR sensing, and review some novel strategies for immobilization of biomolecules for sensing purposes, as presented in recent literature.

4.2 Theory of Surface Plasmons

Plasmons are quasi-particles/waves associated with the collective oscillations of the free electron gas in a metal. Plasmons can be excited with photons of a polarized light beam at the interface of a dielectric medium, giving rise to *surface plasmons*. They can be observed by a strong absorbance of a well-collimated p-polarized light beam that impinges upon a metal surface at a certain incident angle at a certain wavelength. Calculations on surface plasmons make use of the complex number nature of the refractive index ($\hat{n}$) of metals [13, 15], which are intrinsically related to the material constants, which are χ, the extinction coefficient[1]; ε, the dielectric constant; σ, the conductivity; and μ, the permeability, according to:

$$\hat{n} = n + ik = n(1 + i\kappa) = \sqrt{\mu\hat{\varepsilon}}, \tag{4.1}$$

$$\hat{\varepsilon} = \varepsilon + \mathrm{i}\varepsilon\text{'} \tag{4.2}$$

$$\varepsilon\text{'} = 4\pi\sigma/\omega, \tag{4.3}$$

$$\chi = 4\pi\kappa/\lambda, \tag{4.4}$$

where n is the real part of the refractive index, and k is the imaginary part of the refractive index (also called the damping factor)[2], and κ is a derivative form of k called the attenuation index. The theoretical formulae for describing surface plasmons lies in solving the Maxwell equations for stratified optical layer systems, such as the one schematically shown in Fig. 4.1b. The resonance condition occurs at a critical angle (θ_c), and it has been shown that this angle can be calculated via the wave-matching equation:

$$\frac{\omega}{c}\sqrt{\varepsilon_0}\sin(\theta_c) = \frac{\omega}{c}\sqrt{\frac{\varepsilon_1\varepsilon_2}{\varepsilon_1 + \varepsilon_2}}. \tag{4.5}$$

[1] The extinction (E) of a thin film is calculated by the usual relation: $E = \chi.d = -\ln(T) = -\ln(I/I_0)$, where I_0 is the intensity of the incident beam and I that of the transmitted light, T being the transmittance of the film.

[2] In the ellipsometric literature, the convention $\hat{n} = n - \mathrm{j}k$, is often used, but then the k-values are expressed as negative numbers.

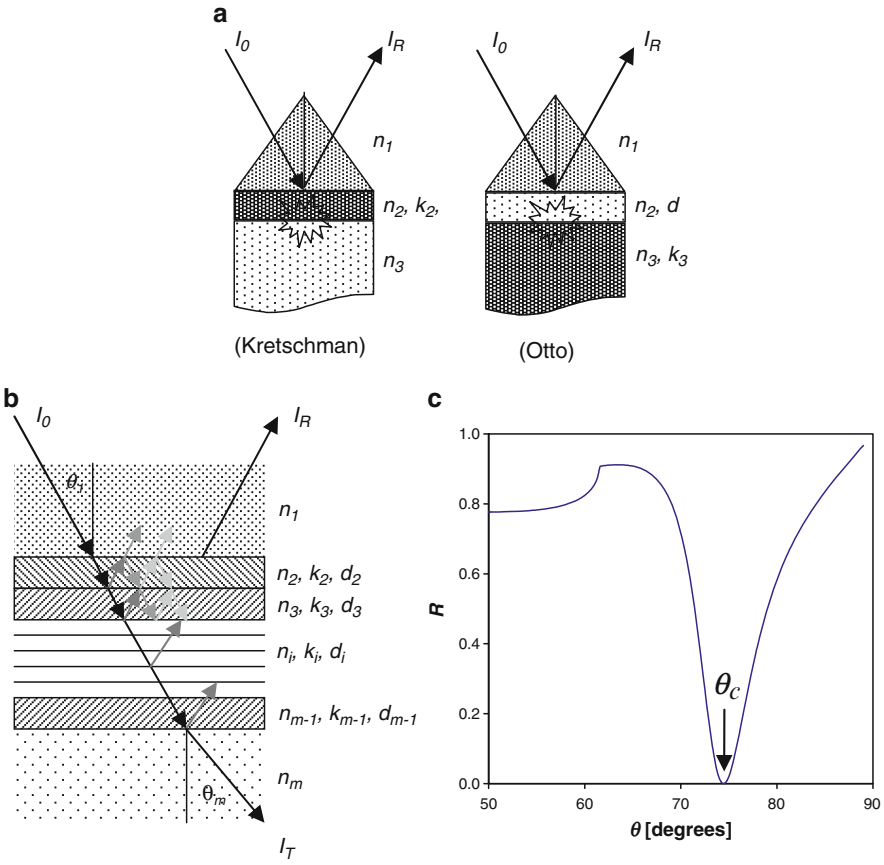

Fig. 4.1 (**a**) Configuration for excitation of surface plasmons according to Kretschman [1] or Otto [14]. The incident p-polarized light is reflected by total internal reflection in a dense dielectric medium of refractive index n_1, typically glass (the inner medium). In the Kretschmann configuration, surface plasmons are generated in a thin metal layer with complex refractive index n_2+i.k_2 and thickness d, having on the opposite site a semi-infinite dielectric medium with refractive index n_3 (the outer medium). In the Otto-configuration, the plasmons are generated over a thin layer of less dense dielectric material ($n_2 < n_1$), such that total internal reflection occurs, and in which the evanescent field of the impinging light is absorbed in a semi-infinite metal layer with complex refractive index n_3+ i.k_3. (**b**) Layer structure used in calculation of reflectance and transmittance of p-polarised light in m media with m-2 thin layers. The incident p-polarized light (with intensity I_0) enters under angle θ_1, and is partly transmitted (intensity I_T), partly reflected (I_R) and partly absorbed in the film. (**c**) Surface plasmons can be observed as a strong decrease in the intensity of the reflected light (I_R) either as a function of wavelength (λ) or incident angle (θ), here a typical optical reflection curve for a 50 nm gold film with BK-7 glass as the inner medium and water as the outer medium at 652.6 nm, where surface plasmon resonance (SPR) occurs at the angle θ_c

For modeling of SPR experiments, it is generally useful to have an expression that relates the reflection or transmittance to the wavelength and incident angle, taking as input the d, n, and k-values of each layer. A general solution can be found by using the Jones or the Müller matrix formulation of optical components with polarized light, depending on whether the optical system contains anisotropic components [15]. In the domain of biochemical sensing, one can deal with the more simple model of isotropic layers with the Jones calculus, in which polarized light beams are represented by 2×1 vectors, and the optical elements (interfaces and layers) by 2×2 *scattering matrices*. The reflectance (or transmittance) of the layer system (Fig. 4.1b) can be calculated by building a 2×2 scattering matrix $\mathbf{S}$ for the layer system, according to:

$$S = \begin{pmatrix} S_{11} & S_{12} \\ S_{21} & S_{22} \end{pmatrix} = \prod_{i=1}^{m-2} (\mathbf{I}_{\mathrm{i}} \mathbf{L}_{i+1}) \mathbf{I}_{m-1} \tag{4.6}$$

where m is the number of *media*, of which the first medium and the mth medium should be semi-infinite and not adsorbing ($k = 0$), $\mathbf{I}_{\mathrm{i}}$ is the scattering matrix for reflection and transmission at the interface of medium i and medium $i+1$, and $\mathbf{L}_{\mathrm{i}+1}$ is the Jones matrix for absorbance in layer $i+1$. The explicit form of these matrices is given in Appendix A. The matrix elements S_{11} and S_{12} are used for calculating the reflectance, R, or the transmittance, T, according to:

$$R = |S_{21}/S_{11}|^2, \tag{4.7a}$$

$$T = 1/|S_{11}|^2. \tag{4.7b}$$

This formalism enables quite accurate modeling of the SPR phenomena for most types of layer systems encountered in biochemical studies [16]. For various calculation examples, we can refer the reader to the study of Salamon et al. [17] and the recent review of Homola [18]. The sensitivity and, more importantly, reliability of SPR detection is due to the inherent stability of the optical constants of gold. The n and k values of gold have been compiled by various investigators over a large range of wavelengths, and some of the literature values are plotted in Fig. 4.2a for n and Fig. 4.2b for k in the UV to near-IR region along with the values measured with spectrometric ellipsometry of gold samples used in our work, which are closest to the values reported by Theye [19]. It can be observed that the real part of the refractive index steeply drops in the range of 470–610 nm, and that the damping factor grows steadily at wavelengths larger than 500 nm.

The values for the optical constants of gold n and k allow a priori assessment of the optimal film thickness (d_{Au}) as well as the angular detection sensitivity ($\mathrm{d}\theta/\mathrm{d}n$) of SPR as a function of wavelength, and some characteristic curves are plotted in Fig. 4.2c for d_{Au} (the thickness of the gold layer) and 4.2d for $\mathrm{d}\theta/\mathrm{d}n$, in the case for pure water as the outer medium. It can be noticed that in the region where both k and n values of gold are lowest (in the region around 600 nm), the shift in resonance angle due to refractive

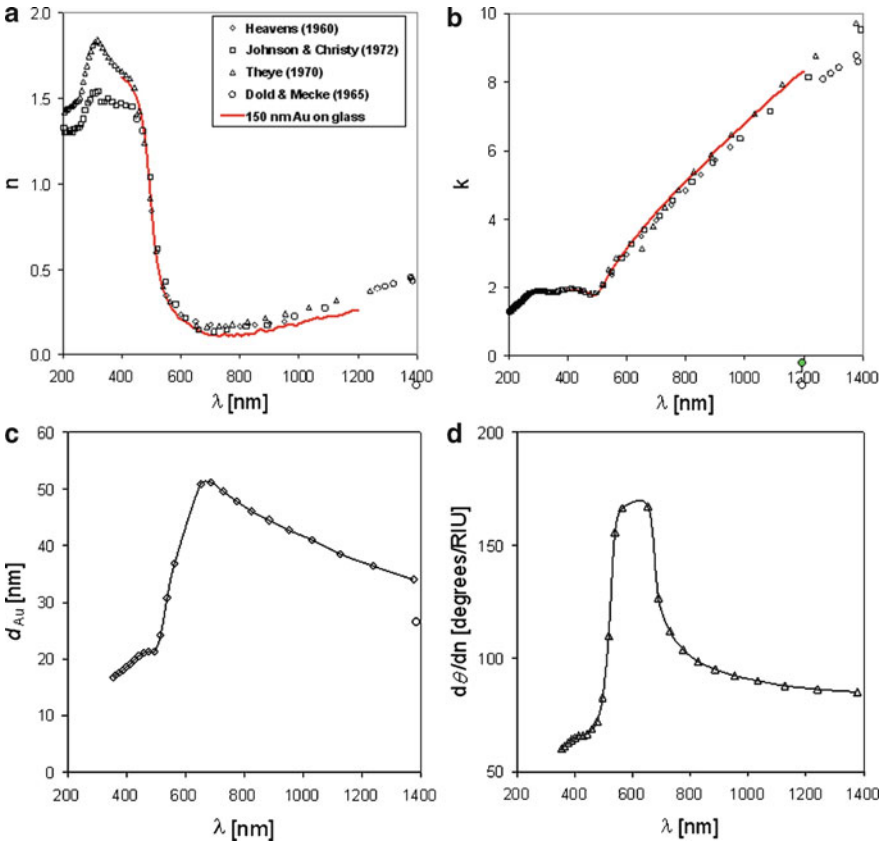

Fig. 4.2 (**a**) Real part and (**b**) imaginary part of the refractive index as a function of wavelength of pure gold as reported in the literature (data points) [19–21] and as measured for a 150 nm gold film on glass with spectrometric ellipsometry (line). (**c**) Optimal thickness of gold for SPR with BK-7 glass as the inner medium and pure water as the outer medium, based on the literature values of the refractive index of gold [19], and dispersion relation-derived values for the refractive index for water [22] and BK-7 glass [23]. (**d**) Angular detection sensitivity calculated from the data of Fig. 4a-c according to formula 4.6 under the same conditions as (**c**), defined as the change in resonance angle with change in refractive index in the outer medium (water)

index changes in the outer medium is largest. In practical measurements, the detection sensitivity is also dependent on the sharpness of the resonance peak ($W½$). Although the width of the resonance peak is dependent on the surface roughness, calculations prospect that its value is relatively large at wavelengths below 500 nm (±25 degrees), but sharply drops above 500 nm. Above 650 nm, the $W½$ is already lesser than 5 degrees, and at wavelengths above 950 nm even lesser than 1 degree. As the resonance angle itself becomes lesser at wavelengths above 700 nm, measuring in the near-IR affords an increase in sensitivity and dynamic range, despite the lower angular sensitivity [24].

4.3 Density and Refractive Index of Biomolecular Thin Films

Another essential parameter in optical biosensing is the refractive index increment of absorbing biomolecules, dn/dc:

$$\frac{\mathrm{d}n}{\mathrm{d}c} = \frac{n_\mathrm{p} - n_\mathrm{m}}{C_\mathrm{p}}, \tag{4.8a}$$

where n_p is the refractive index of a solution of biomolecule p with concentration C_p, and n_m is the refractive index of the medium in which the adsorbent is diluted. The surface density (Γ) is given according to the equation of the Gibbs surface excess as:

$$\Gamma = C_\mathrm{p} d_\mathrm{p}, \tag{4.8b}$$

where d_p is the thickness of the adsorbed molecular layer, and C_p is the concentration of the protein in the layer. Combining the above equations, and eliminating C_p gives the "de Feiter"-equation that relates the surface density to the refractive index increment, the refractive index change and the layer thickness [25]:

$$\Gamma_\mathrm{p} = \frac{(n_\mathrm{p} - n_\mathrm{m}) d_\mathrm{p}}{dn/dc}. \tag{4.8c}$$

Although the differences in the refractive index of the medium (n_m) are generally small, the differences of dn/dc of biomolecules in different buffers may vary significantly, as illustrated in Table 4.1 for various proteins. Moreover, the refractive index increment depends on the measurement wavelength: generally lower refractive indices are found with increasing wavelength. The differences are usually smaller than the other experimental errors, and a refractive index increment of 0.182 for proteins with a molecular weight >20 kDa is generally

Table 4.1 Literature values for refractive index increments of proteins in various solvents

Protein	Solvent	dn/dc	Light source	Ref
Ovalbumin	Water	0.180	White	[25]
BSA	Water	0.187	White	[25]
BSA	PBS	0.166–0.169	632.8	[27]
Pig IgG	PBS	0.168–0.170	632.8	[27]
Mouse IgG	PBS	0.175	632.8	[27]
Lysozyme	Water	0.186	White	[25]
Lysozyme	Water	0.153	632.8	[28]
Lysozyme	10 mM NH_4HCO_3	0.260	632.8	[28]
Lysozyme	10 mM $NaSCN^+$10 mM HEPES	0.272	632.8	[28]
Lysozyme	10 mM $NaCl^+$10 mM HEPES	0.188	632.8	[28]
Lysozyme	100 mM $NaCl^+$10 mM HEPES	0.186	632.8	[28]

applied [26]. Still, the inference of exact thickness and refractive index of protein layers is not straightforward, as the degree of hydration varies in protein layers introducing variation of C_p.

To determine the thickness and refractive index of biomolecular thin films separately, ellipsometric measurements are needed [29] or measurements on waveguides where TM and TE modes can be simultaneously monitored [30]. An even better method is to use more than one method, such as the combination of optical and QCM techniques [26]. With SPR, the thickness and refractive index of an adsorbed protein layer may be assessed by measurements at different wavelengths or by measuring the layer in two media of different refractive index, for instance air and buffer. It logically follows from (4.8c) that in two different media two hyperbolic curves $n_p = \Delta_{m1}/d_p + n_{m1}$ and $n_p = \Delta_{m2}/d_p + n_{m2}$ may be formulated, where ($\Delta = \Gamma \cdot dn/dc$). The factors Δ_{m1} and Δ_{m2} can be directly obtained from SPR curve

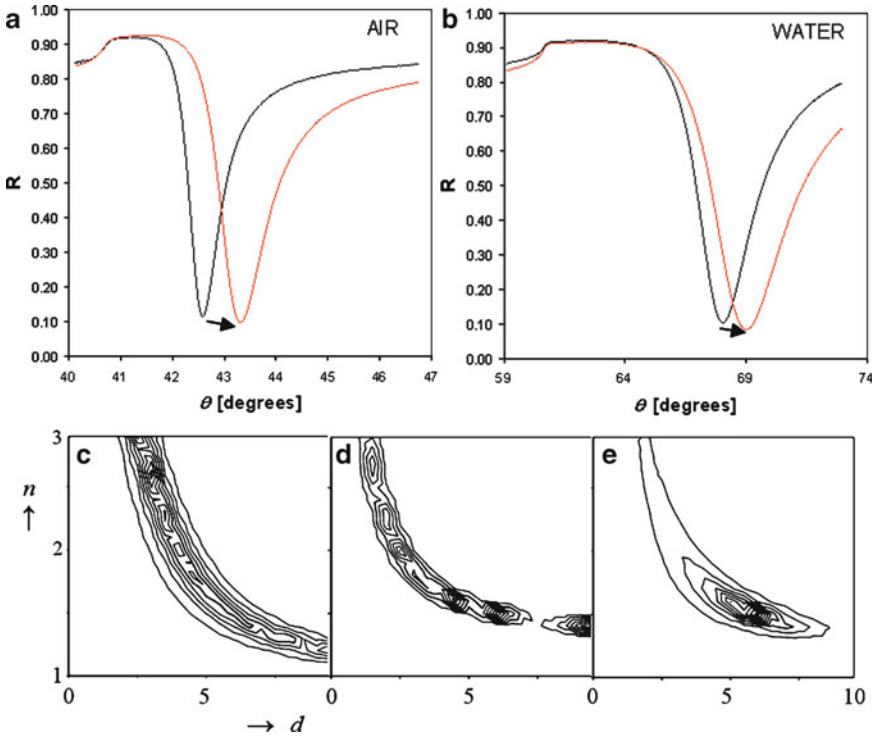

Fig. 4.3 Determination of the n and d of a silicon oxynitride film depositied on gold by fitting of experimental SPR data in air (**a**) and water (**b**). These data were obtained with the SPR-Navi instrument (BioNavis Oy, Tampere, Finland). Results were obtained from modeling of the shift induced by the silicon oxynitride layer (from the *left* to the *right* curve). The goodness of fit to the experimental curves was separately mapped in *n-d* space to air (**c**) and water (**d**), and t fitted for air and water simultaneously (**e**). The refractive index of water was 1.3335, and the optical constants of the gold film were: $d = 47.4$ nm, $n = 0.28$, $k = 4.2$

fitting, while n_{m1} and n_{m1} are usually known. The two hyperbolae may intercept at a certain point, which yields a unique solution for d_p and n_p.

An example of the 2-media method is given in Fig. 4.3, where the SPR spectra of a silicon oxynitride layer deposited on gold is displayed as measured in air (Fig. 4.3a) and water (Fig. 4.3b). This layer gives a significant shift in SPR resonance angle for illustrative purposes. When fitting these data with theoretical SPR curves, according to the theory presented earlier, the goodness of fit to the experimental curves can be mapped to thickness and refractive index of the layers separately in air (Fig. 4.3c) and water (Fig. 4.3d), which results in two hyperbolic sets of solutions in *n-d* space. When the goodness of fit is plotted to the combined set of data (Fig. 4.3e), a solution can be found for the SiO_2-layer: $n = 1.62$ and $d = 6.25$ nm. The thickness was in good agreement with the one found by AFM (6.29 nm), and the refractive index lies between that of silicon dioxide (1.456) and silicon nitride (2.03). In the same way, the refractive index of a BSA layer adsorbed onto gold was found to be 1.48 with an average thickness of 3.3 nm. This also corresponds to the values found in the literature [29]. Thus, it can be stated that fitting of whole SPR curves has the great advantage of more elaborate characterization with relatively simple means [16, 31].

4.4 Properties and Applications of Gold Colloids

Despite the long history of noble metal colloids, there has been undiminished interest in their development, particularly for bioanalytical applications [32]. At present, interesting new nanostructures, usually of gold, have been constructed with high application potential in bioanalytical sensors [12], such as nanocone [33] or nanohole arrays [34]. The present paragraph, however, will focus only on the use of conventional gold nanoparticles.

Gold colloids are generally formed by reduction of a gold salt (such as $HAuCl_4$) with a mild reducing agent in very dilute solution (e.g., with citrate [35, 36] or ascorbate [37]). The reducing agent, or its oxidized form, functions as a capping agent to stabilize the particles in solution, and controls the size distribution, which can be extremely narrow, as evidenced from the fact that recently even X-ray crystallographic data and the precise structure was published of monodisperse gold colloids capped with p-mercaptobenzoic acid [38]. A narrow size distribution is attained only when very clean glassware is used, free of particles, which may act as interferences in the nucleation process. For obtaining gold colloids of the standard size of 20–50 nm, citrate reduction is generally sufficient, but for the production of smaller particles, the method reported by Slot and Geuze can be recommended, which relies on using tannic acid as an additional capping agent with citrate in the reduction solution [39]. Another method for preparation of the small-sized gold nanoparticles has been described by Brust, in a highly cited research paper, which comprises the reduction of $HAuCl_4$ with $NaBH_4$ in a two-phase system in the presence of thiols as capping agents [40]. For the preparation of

larger particles (up to 150 nm), the citrate reduction can be used, but at sizes above 30 nm, the particles tend to become elliptical, and therefore a seeding method has been devised, in which spherical particles of larger size are grown around small seed particles by slow reduction of gold ions by slow addition of a diluted solution of reducing agent, such as ascorbate [37].

Although the size and shape of nanoparticles is generally determined by transmission electron microscopy, UV/VIS spectra can be used to obtain preliminary estimates of the size and concentration of nanoparticles in aqueous solutions. The electro-optical properties of gold nanoparticles can be described by Mie theory, in which the total extinction cross-section due to absorption and scattering is formulated as the sum of all electro-magnetic multipole oscillations [41]. Theoretical spectra have been calculated for a large range of metallic nanoparticles [42]. In case of nanoparticles, with a size of the particle smaller than the excitation wavelength, the following simplified relation was derived [41, 43]:

$$\sigma_{\text{ext}}(\lambda) = \frac{3\pi^2 d^3 \varepsilon_{\text{m}}^{3/2}}{\lambda} \frac{\varepsilon'(\lambda)}{[\varepsilon(\lambda) + 2\varepsilon_{\text{m}}]^2 + \varepsilon\prime(\lambda)^2}, \tag{4.9a}$$

where $\sigma_{\text{ext}}(\lambda)$ is the extinction cross-section (in nm^2), d is the particle diameter, λ is the wavelength, $\varepsilon(\lambda)$ is the real part, and $\varepsilon'(\lambda)$ is the imaginary part of the dielectric constant of gold (see further equation), with ε_{m} being the dielectric constant of the medium. The absorbance can then be calculated from the extinction cross-section as:

$$E(\lambda) = N \cdot \sigma_{\text{ext}}(\lambda) \cdot l, \tag{4.9b}$$

where N is the number density of particles, and l is the path length (in matching units of nm).

The theoretical absorption spectrum of a 20 nm gold nanoparticle suspension in pure water is given in Fig. 4.4, using the known optical constants of gold and water (from [19]) and compare it with a commercial preparation. As can be observed, the theoretical resonance peak in the spectrum is narrower and has a slightly lower resonance wavelength ($\lambda_{\text{max}} = 515$ nm) compared with a real particle preparation ($\lambda_{\text{max}} = 521$ nm). The small blue-shift can be easily explained by the circumstance that the real particle is coated with a thin organic layer, and is not dispersed in pure water, while the slightly broader peak is the logical effect of a small particle size distribution, which is 17–23 nm. Recently, Haiss et al. and Klebtsov have evaluated more accurate formulae for calculation of the absorption maximum (λ_{max}) and concentration of gold colloid preparations [44, 45], claiming an error level of about 3–5%.

In Fig. 4.5, the calibration curves for λ_{max} are compared with some literature values of gold colloids, together with the λ_{max}-values of three commercial gold colloid preparations. Despite the accurate relations by Haiss and Khlebtsov, the Mie theory has the main drawback that calculations are based on macroscopic parameters (optical constants of particle and medium), and they do not easily allow incorporation of microscopic parameters. It can thus be observed that the real absorption values may significantly deviate from the theoretical models.

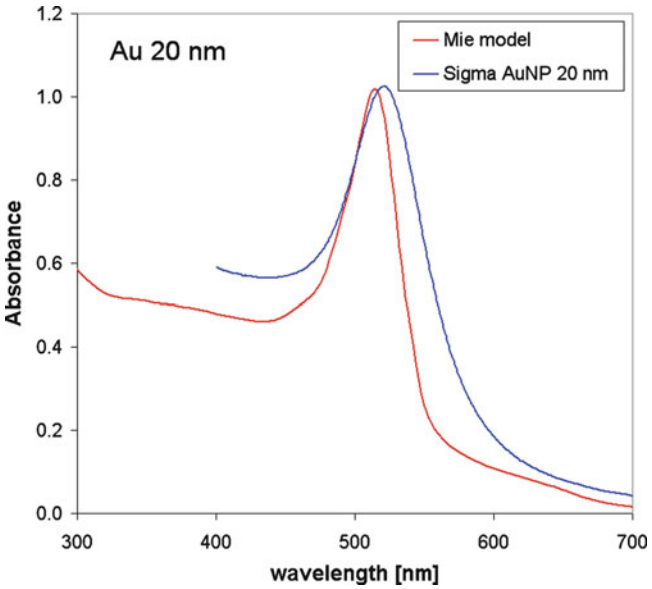

Fig. 4.4 Absorption maximum of 20 nm gold colloid in pure water, as estimated with the Mie equation, using known optical constants of gold and water, and experimental curve of a commercial 20 nm particle from Sigma-Aldrich

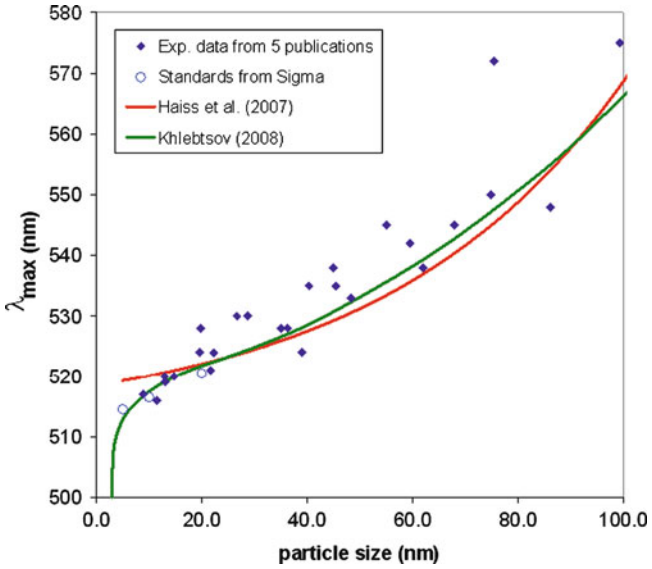

Fig. 4.5 Absorption maximum dependence of regular gold colloids on size. These data were plotted from tabulated data in the publications of Haiss [44] and Khlebtsov [45]. These data are compared with values of well-characterized gold particles from 5 publications (*diamonds*), and with three gold colloids that are commercially available from Sigma-Aldrich, of nominal size 5, 10, and 20 nm (Cat. Nr.: G-1402, G-1527, and G-1652, respectively)

In practical applications, the first important asset of gold nanoparticles is the fact that when they are dispersed in solution, they are extremely sensitive indicators of biomolecular binding reactions *by themselves*: adsorption of even small molecules onto the surface of a gold nanoparticle, when it has the optimal size of 40–80 nm, will induce a measureable shift of the resonance wavelength to higher wavelengths. Thus, antibody-coated gold colloids have been used in clinical analyzers as homogeneous immunoassay reagents for a variety of analytes, including hCG [46] and small drug molecules as theophiline or digoxin [43]. Besides sensitivity for adsorption reactions, also the coagulation of gold particles strongly shifts the absorption maximum, and this effect too has been used in homogeneous immunoassays, although the nonspecific interactions seem to be larger when working with blood or serum samples [47]. Another important advantage of gold colloids is that they can be used as a label in various optical sensing systems. Gold colloids have been widely used in immunochromatographic test strips [48], but lately also in combination with SPR detection [49]. This latter asset will be further discussed.

4.5 Modeling of Biomolecular Interactions

The modeling and fitting of kinetic and equilibrium binding data had very much flourished since the Biacore instrument was launched in the early 1990s, through which kinetic studies of unlabeled biomolecules became feasible for a broad research community [50, 51]. It proved to be a superior alternative to affinity chromatographic techniques for determination of binding constants [52][3], and the systems have by now been extensively benchmarked [53–56]. Although ready software has been implemented by Biacore for kinetic analysis, which can be expanded to the study of more complicated systems [57, 58], correct use of the equipment and fitting methods seems to be rare [59]. Thus, it is useful to review the elementary theory, and for a more comprehensive description refer the reader to some recent reviews on SPR [7, 60] and protein chemistry [61].

4.5.1 Determination of Binding Constants from Equilibrium Data

The collection and interpretation of equilibrium data is more facile than kinetic experiments, because it is slightly less prone to interference due to temperature fluctuation and inadequate mass transport [80]. The usual procedure comprises acquisition of the equilibrium binding level as a function of concentration of the analyte for a particular (immobilized) ligand, preferably using many data points and a broad concentration range, spanning many orders of magnitude. This yields a

[3] With the use of hydrogel layers on the gold surface, the SPR method is close to affinity chromatography in which the adsorption and desorption can be monitored directly, instead of monitoring the analyte released from the surface with a down-stream detector.

binding isotherm, which can be fitted to an appropriate model. In solution, and in the most ideal case, the binding model is a normal one-to-one reaction, as illustrated in (4.5) for ligand A and analyte B combining to give complex AB, according to:

$$\mathrm{A} + \mathrm{B} \rightleftarrows \mathrm{AB} \qquad K_\mathrm{A} = \frac{1}{K_\mathrm{D}} = \frac{[\mathrm{AB}]}{[\mathrm{A}] \cdot [\mathrm{B}]} \qquad [\mathrm{AB}] = \frac{Q_\mathrm{A} \cdot K_\mathrm{A} \cdot [\mathrm{B}]}{1 + K_\mathrm{A} \cdot [\mathrm{B}]}, \tag{4.10a}$$

where square brackets indicate the concentration (in mol/L), K_A is the (homogeneous) affinity constant (in L/mol), K_D is the dissociation constant (in mol/L), and Q_A is the total amount of A (which is [A]+[AB], also called the binding capacity). On a surface, however, these equations are different with respect to units: both species A and AB need to be surface concentrations (Γ_A and Γ_AB) and we have to formulate a heterogeneous (or apparent) affinity constant K'_A:

$$\mathrm{A} + \mathrm{B} \rightleftarrows \mathrm{AB} \qquad K'_\mathrm{A} = \frac{1}{K'_\mathrm{A}} = \frac{\Gamma_\mathrm{AB}}{\Gamma_\mathrm{A} \cdot [\mathrm{B}]} \qquad \Gamma_{AB} = \frac{Q_\mathrm{A} \cdot K'_\mathrm{A} \cdot [\mathrm{B}]}{1 + K'_\mathrm{A} \cdot [\mathrm{B}]}, \tag{4.10b}$$

where Q_A is Γ_A+ Γ_AB. In many instances, it is practical to refer to the fractional surface coverage θ:

$$\Gamma_\mathrm{AB} = Q_\mathrm{A} \cdot \theta, \quad \text{where} \quad \theta = \frac{K'_\mathrm{A} \cdot [\mathrm{B}]}{1 + K'_\mathrm{A} \cdot [\mathrm{B}]}. \tag{4.10c}$$

Although the heterogeneous affinity constant has the same units (L/mol) as the homogeneous affinity constant, this difference in dimension of the reaction system should be kept in mind, and the value of K'_A is not necessarily the same as that of the K_A, although in an experiment it may seem to be so. The use of hydrogel layers, however, circumvents the surface concentration problem and with the Dextran matrix, it was found that binding constants frequently correspond to the values in solution (see Chap. 6 in [7]). The ideal binding is easily disturbed by binding *heterogeneity* (the affinity constant shows a distribution of values instead of a single value) and *cooperativity* of binding (one analyte can bind to more than one ligand on the surface). Both phenomena can be incorporated in the equation of the binding isotherm by introducing *binding exponent* η:

$$\Gamma_\mathrm{AB} = \frac{Q_\mathrm{A} \cdot \left(K'_\mathrm{A} \cdot [\mathrm{B}]\right)^\eta}{1 + \left(K'_\mathrm{A} \cdot [\mathrm{B}]\right)^\eta}. \tag{4.10d}$$

This equation is known as the Sips (or Langmuir-Freundlich) isotherm [62–64]. In the ideal case, the binding exponent will be 1, but heterogeneity will decrease it, while cooperativity will increase the exponent. There is also the possibility that there are distinct classes of binding affinities, in which case the Sips isotherm can be expanded for N distinct sites as:

$$\Gamma_{AB} = \sum_{i=1}^{N} [Q_{Ai} \cdot \theta_i], \quad \text{where} \quad \theta_i = \frac{\left(K'_{Ai} \cdot [B]\right)^{\eta_i}}{1 + \left(K'_{Ai} \cdot [B]\right)^{\eta_i}}. \tag{4.10e}$$

When very accurate binding data can be obtained over a wide range of concentrations, it is possible to calculate affinity distributions within a certain interval of binding affinities according to:

$$\theta(x) = \int_{K_{A1}}^{K_{A2}} \frac{f(K_A) \cdot K_A x}{1 + K_A x} \mathrm{d}(K), \tag{4.10f}$$

where $f(K_A)$ is a frequency distribution of binding affinities in the interval K_{A1} to K_{A2}, (or, more usually, $f(U)$, the distribution function of the free binding energy, with $U = \log(K) = \Delta G^*/RT$). The distribution function $f(K_A)$ can be a series of Gaussians or a decay function [65]. For fitting these distributions, a large spectrum of numerical methods and programs have been developed, such as CONTIN [66] and some methods even use Fourier transforms. Some of the numerical fitting routines have been compared by Koopal and Vos [67].

With polyclonal antibodies both heterogeneity and cooperativity effects can be readily observed. Figure 4.6 gives a typical isotherm of human IgG (h-IgG) binding to a polyclonal antibody, which is immobilized within a polymer matrix on a gold surface. Fitting of the experimental data was significantly improved by applying a dual-site Sips isotherm instead of a single-site isotherm. In this example, a specific binding reaction with high affinity was separated from the nonspecific binding with a much lower affinity.

Still, for successful fitting to binding distributions, these data have to be very precise, because the error level influences the results very strongly [68]. Generally, the difference between the fitted data and the experimental data is evaluated by *chi-square fitting*, in which the deviation from the model (χ) is expressed as [69]:

$$\chi^2 = \sum_{i=1}^{n} \left(\frac{y_i - Y(x_i, a)}{\sigma_i} \right)^2, \tag{4.11}$$

where $Y(x_i,a)$ is the fitted value of data point (x_i,y_i) with a measured standard deviation of σ_i, n is the number of data points, and a is a linear array of p parameters to be estimated. In cases where the standard deviation of each measured data point is unknown, an average standard deviation can be calculated according to:

$$\sigma^2 = \frac{\sum_{i=1}^{n} (y_i - Y(x_i, a))^2}{n - p} \tag{4.12}$$

where $n-p$ is the number of degrees of freedom of the data set. This illustrates the desirability of data sets with a sufficient amount of data points, and limitation

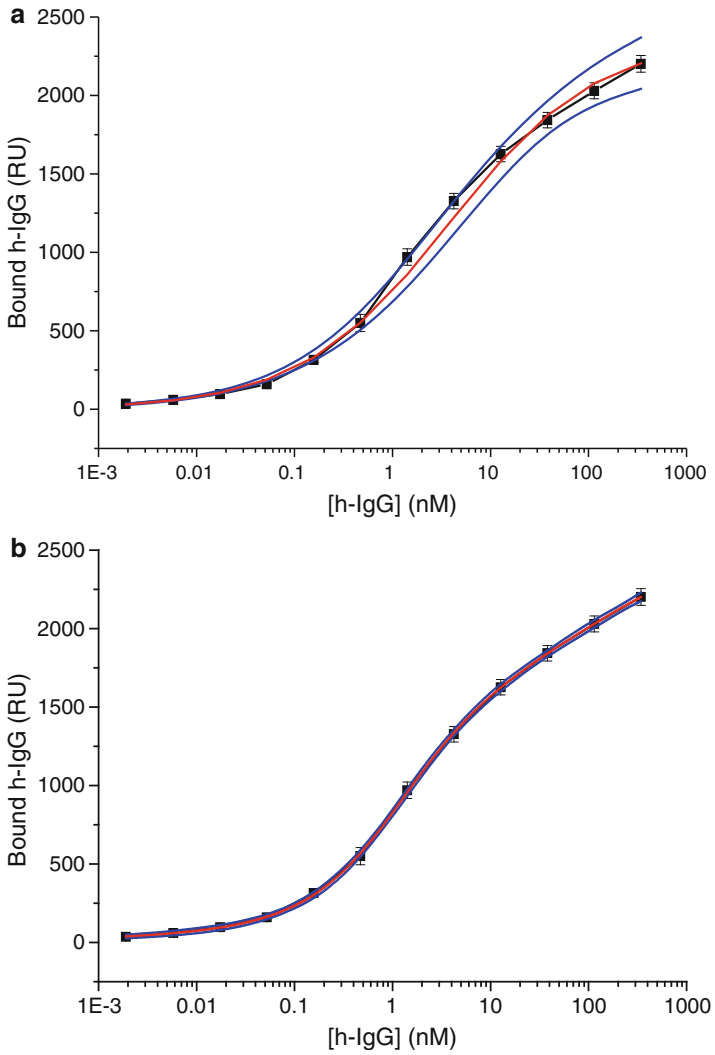

Fig. 4.6 Binding of human IgG binding to polyclonal anti-human IgG, and fitted (**a**) to single-site heterogeneous binding model and (**b**) to the two-site heterogeneous binding model. The fit is given with the 95% confidence intervals. The estimated parameters for the single site model were: $K_A = 0.26 \pm 0.03$ nM^{-1}, $Q = 2370 \pm 50$ RU and $\eta = 0.57 \pm 0.01$ ($r^2 = 0.99514$), while for the dual site binding model they were: $Q_1 = 1{,}160 \pm 260$, $K_{A1} = 0.9 \pm 0.1$ nM^{-1}, $\eta_1 = 1.0 \pm 0.1$, $Q_2 = 1{,}724 \pm 220$, $K_{A2} = 0.01 \pm 0.02$ nM^{-1}, $\eta_2 = 0.35 \pm 0.06$ ($r^2 = 0.99989$)

of the amount of parameters to the smallest number possible. It is obviously not possible to fit data with 4 data points to a function with 5 parameters, and it is not useful to fit the same data to a function with 4 parameters, although a distinct solution might be found that passes *exactly* through the 4 data points.

The Sips-isotherm is quite useful because cooperativity and heterogeneity can be represented by a single parameter (η). When fitting fractional surface coverage, the function only has two parameters per distinct site. With a distribution function, however, the amount of parameters will become quickly larger, because for each Gaussian there are three parameters, amplitude, width, and position, and incorporation of cooperativity of binding will yield an extra parameter. It is thus preferred that $n>>p$, and this is more readily achieved with time-dependent kinetic data.

4.5.2 Determination of Rate Constants from Kinetic Data

According to the laws of *mass action*, the rate of a reaction at time point t, $\upsilon(t)$, depends on the concentration of the reactants and a rate constant k. For the bimolecular reaction A + B → AB, the *association* rate, $v_a(t)$, is:

$$v_a(t) = k_a \cdot [A] \cdot [B] \tag{4.13a}$$

with k_a being the rate constant of the association reaction, and [A] and [B] denoting the (molar) concentration of A and B. The reaction rate is the change of concentration of reactants in time:

$$v_a(t) = d[AB]/dt = -d[A]/dt = -d[B]/dt = dx/dt. \tag{4.13b}$$

The molar progression of the reaction, x, can be found by integrating υ_a with respect to time. For the irreversible reaction A + B → AB, the rate equation can be written as a differential equation of the form:

$$\frac{dx}{dt} = k_a(a-x)(b-x), \tag{4.13c}$$

where a and b are shorthand notations for the initial concentrations of A and B. With initial conditions $x(0) = 0$, this equation can be integrated to give:

$$(a-b)k_a t = \ln\frac{b(a-x)}{a(b-x)} \quad \text{or} \tag{4.13d}$$

$$x(t) = ab(1 - e^{(a-b)k_a t})/(b - ae^{(a-b)k_a t}),$$

which is very suitable for the fitting of irreversible reactions or calculation of initial rates. However, for the reversible bimolecular reaction A + B ⇄ AB, the system becomes more complicated because a dissociation rate and a rate constant need to be introduced:

$$v_d(t) = k_d \cdot [AB]. \tag{4.14a}$$

The forward reaction is a second-order reaction (i.e., having two reactants), while the reverse reaction is a first-order reaction (i.e., having one reactant). The differential equation then takes the form:

$$\frac{dx}{dt} = k_a(a - x)(b - x) - k_d x. \tag{4.14b}$$

When $a>>x$ (x does not deplete the concentration of A, as is a prerequisite for manageable kinetic studies)[4], this equation can be solved [also with $x(0) = 0$] as:

$$x(t) = \frac{k_a ab}{k_a a + k_d}(1 - e^{-(k_a a + k_d)t}). \tag{4.14c}$$

At increasing time, the reaction will thus progress to the equilibrium concentration, where:

$$x_{eq} = \frac{K'_A \cdot a \cdot b}{1 + K'_A \cdot a} \tag{4.14d}$$

with $k_a/k_d = K'_A$, which corresponds to (4.10a). It can also be seen that for each concentration of species A used in the assay, the observed rate constant can be defined as:

$$k_{obs} = k_a a + k_d. \tag{4.14e}$$

Hence, the rate constants can be determined by plotting the observed rate against a, yielding a straight line with slope k_a and intercept k_d. These rate constants are related to the temperature through the frequency factor A and the activation energy E^*, according to the well-known Arrhenius-equation[5]:

$$k = A \cdot e^{(-E^*/RT)}. \tag{4.15}$$

Thus, by measurement of reaction rate constants at a range of temperatures, the basic parameters A and E^* may also be determined.

[4] In fact, with surface concentrations for x and b, the term $(a-x)$ may not be directly used, because a is in mol/L and b in mol/dm^2. Thus, a condition of depletion of a should be checked (see Chap. 5 of [7] for a mathematical evaluation).

[5] Svante Arrhenius (1859–1927) was a Swedish scientist, and one of the founders of the science of physical chemistry: originally he was a physicist, but he is often regarded as a chemist. The Arrhenius equation he developed based on the work by J. H. van't Hoff. He was also the first to develop a theory of the greenhouse effect caused by carbon dioxide.

An important parameter, occurring frequently in adsorption/desorption systems at surfaces is the rate of transport of reactant species from the bulk of the solution to the surface:

$$v_t(t) = k_t \cdot ([A^*] \quad [A]), \tag{4.16a}$$

where k_t is a rate constant related to diffusion, [A*] is the concentration of species A in solution and [A] the concentration of A at the stagnant surface layer. When there is a steady-state condition, [$\upsilon_t(t)$ does not change in time], it can be shown that k_t depends on the diffusion layer thickness d and the diffusion constant of A, D_A, through:

$$k_t = D_A/d. \tag{4.16b}$$

The thickness of this ("Nernstian") diffusion layer depends on the degree of convection, and the diffusion constant depends on the size of the molecule and the temperature. In kinetic measurements, the transfer rate may become smaller than the reaction rate of mass action, in which case a diffusion step must be added to the reaction scheme. Some reaction schemes and rate equations used for frequently occurring biochemical reactions are listed in Appendix B. Using similar rules, sets of differential equations can be constructed for more complicated systems with a larger number of reactions and species. In such cases, one generally needs to solve a larger system of differential equations. This is generally performed numerically, and nowadays it can be readily achieved with commercial software packages [70, 71]. An example of a strongly diffusion-limited binding and dissociation reaction is added to Fig. App. B.1, illustrating the effects of limited mass transfer by an increased linearization of the initial response and a slack reverse reaction.

In practical measurements, there are limitations to the values for reactions rates, and Fig. 4.7 presents a plot of the working ranges of the forward and reverse reaction rate constants encountered in a one-to-one biomolecular binding system, mainly attainable with the Biacore systems [72, 73].

As mentioned earlier, kinetic data yield larger and more precise sets of data, and this gives possibilities for determination of kinetic rate constants and elucidation of reaction mechanisms in a more reliable way, and, for instance, 2-D contour plots of rate constants can even be obtained for inhomogeneous systems [74]. However, as with equilibrium data, the evaluation of kinetic data requires the acquisition of binding at a broad range of analyte concentrations. This generally means that the ligand should be stably immobilized, and that many measurement cycles are needed, comprising binding of the analyte at a preset concentration, followed by regeneration of the surface with a suitable solution for the next binding cycle [57].

There are, however, situations where regeneration is not possible either due to instability of the immobilized ligand or due to the formation of a too tight complex that cannot be disrupted with any suitable reagent. In these cases, it is favorable to

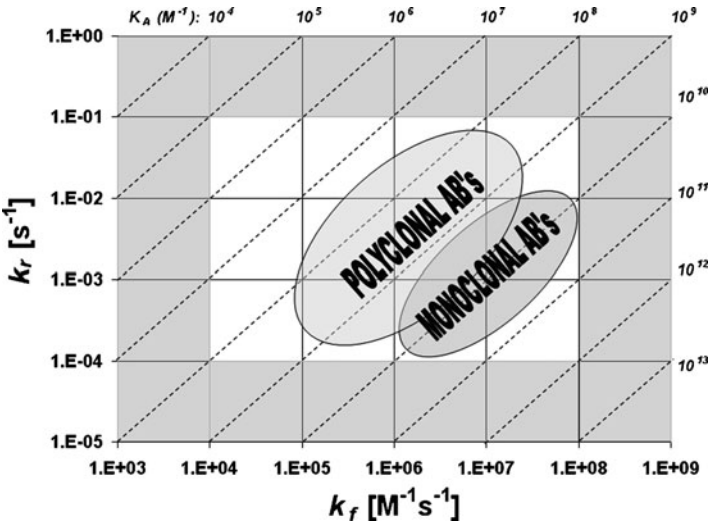

Fig. 4.7 Binding regimes of polyclonal and monoclonal antibodies for forward (k_f) and reverse (k_r) reaction rate constants, and affinity constants (K_A). The usual range of values found for monoclonal and polyclonal antibodies are also indicated

carry out a series of injections at widely spaced concentrations of the analyte (e.g., 1:3 dilutions) without regeneration, but taking into account the changes in analyte concentration as well as the changing capacity of the sensor chip. For this purpose, the CLAMP-routine has been developed [71, 75]. In all cases, however, the preparation of good data for kinetic fitting is a major concern [76, 77]. Not only the experimental parameters need to be carefully controlled, but also, in most cases, it is necessary to check for anomalies, for example, *step functions* due to bulk effects (incompatibility between the injected buffer and desorption buffer solutions) as well as *adsorption/desorption effects of the matrix*. Thus, subtracting data from a reference surface or subtracting blank injections (or both) is strongly recommended [77].

Examples of high-quality and inferior data have been given in an extensive scan of the optical biosensor literature of the year 2008 by Rich and Myszka [59]. The most important caveat was that any model suggested by the fitting results has to be *verified*. If a model fits the data very well, and it *suggests*, for example, that there may be limited mass transport, then this has to be verified by setting up an experiment at different flow rates, such that one can see the k_t increasing with flow rate. If the fit suggests that there may be a conformational change of the formed complex, then experiments have to be conducted with varying contact time, showing that the overall dissociation rate becomes smaller with increasing contact time. If the model suggests that there is a bivalent analyte, this can be checked by decreasing the surface density of the ligand, which should reduce or eliminate the bivalency.

4.6 Antibody-Based Sensing

SPR-based sensing has mostly focussed on antibody/antigen, protein/ligand, and protein/protein interactions. In this section, we refer mainly to the antibody/antigen interaction as the basis for an immunosensor to be used in clinical diagnostic applications. There are some demands that have to be fulfilled before one can speak of an immunosensor: according to the more strict IUPAC definition of biosensors in general, the response must be *real-time*, and there must be *reversibility* [78]. The irreversibility of most immunologic reactions, however, easily leads to incompatibility with this definition, because of the need for *regeneration*. In this case, the word *immunoprobes* was deemed more appropriate [79].

Already in 1987, Mark Eddowes formulated the basic kinetic limitations that are likely to pose fundamental limitations to the operation of immunosensors in clinical applications [80] and to some degree these limitations still hold. First, with equilibrium binding experiments, a lower detection limit was envisaged in the order of nanomolar or slightly below, mainly depending on the sensitivity of the detection method and the affinity constant.[6] Second, for kinetic measurements, mass transport and slow dissociation rates were deemed a serious limitation to the detection sensitivity. Third, from a point of view of interferences, the non-discriminatory nature of the detection method was expected to give rise to intractable non-specific binding problems. It is particularly the Biacore systems that have addressed these problems. First, the instruments utilise a microfluidic system with extremely small flow cell volumes that enable high mass transfer rates even at low volumetric flow rates. Second, they contain a highly optimised SPR detector that is able to follow angular shifts down to 10^{-5} degree (0.1 RU) [81]. The latter problem of nonspecific binding was solved by the use of the dextran matrix, which has quite low non-specific binding, while allowing high capacity binding of ligands with various chemistries [82, 83].

There still remain large hurdles to adopt the SPR sensing method to the study of real samples for diagnostics applications. New expectations have been raised through the use of protein array techniques, which allows novel referencing schemes (see Chap. 10 in [7] and [84–87]). In many cases, however, the sensitivity needs to be increased and the non-specific binding is more drastically suppressed, and the key role is evidently to be played by the immobilisation method. Besides non-specific binding of proteins of high abundance, there are very many types of specific cross-reactions possible with other parts of the antibody that are involved in triggering functions for the innate immunosystem (e.g., complement), and also those reactions have to be suppressed [88]. For instance, by embedding the antibody into a repellent matrix, whereby only the antigen-binding site will be exposed to the solution, the cross-reactive flanks may become shielded from such binding interactions.

[6] A recent scan of the literature readily reveals that most studies with direct detection using SPR instrumentation move in the low nanomolar range [18].

4.6.1 Immobilisation Issues

Although the direct adsorption of antibodies onto polystyrene and nitrocellulose surfaces is still universally used in clinical diagnostic applications, a great variety of alternative methods have been described in the literature for the immobilisation of biomolecules, mainly antibodies and oligonucleotides [89–91]. Within the repertoire of general methods, such as physical adsorption, entrapment, and covalent binding, the methods for immobilization of antibodies have generally focussed on covalent binding by the site-directed approach [92]. Covalent linking of antibodies to Dextran matrices has been used most regularly because of the commercial availability and the advantages mentioned earlier [83, 93, 94]. The dextran matrix allows very high surface loadings to be applied (up to 16 kRU, corresponding to 16 ng/mm^2 for the CM5 chip [95, 96], and even higher for the CM7 chip [97]), which has advantages for the detection of small molecular weight analytes [53, 98–101]. On the other hand, in protein–protein interaction studies, antibody loadings have usually been kept in the range of 1,000–2,500 RU, because of increased steric hindrance [102]. In the scientific literature, various new matrices for immobilisation have been reported, such as modified cellulose [103], synthetic polymers [104, 105], and sol-gel matrices [91]. It seems reasonable that many polymers that are used in biochromatography and electrophoresis, such as Sephadex, Sephacryl, or various acrylamide polymers, could be used as immobilisation matrices in optical biosensors. Also, histidine tags [106], biotin/(strept)avidin [64, 107, 108], self-assembled thin films [109, 110], or lipid bilayers [111, 112] have been much used for immobilisation. For obtaining biomolecular layers with a higher degree of orientation, intermediate linking molecules have also been used, such as the Fc-receptors Protein A [113], protein G [114, 115], and new, more effective constructs, such as protein LA [116] and protein LG [117].

Systematic studies of orientational effects of unfragmented antibody molecules are relatively rare, but Vijayendran and Leckband have reported interesting work on the binding of a fluorescent TNT analogue to anti-TNT [64]. Using equilibrium data fitting to the Sips isotherm, highly variable binding parameters were found with a range of immobilisation methods, and the binding parameters were compared with that of the antibody in solution. The results are summarised in Table 4.2 and Fig. 4.8. As can be observed from Table 4.2, the highest affinity constant (K_A) was obtained in solution, in which case the binding exponent (η) was very close to unity. Random immobilisation via an amine-reactive silane layer resulted in a very low binding exponent ($\eta < 0.1$), which is an undesired situation. The linking via the carbohydrate groups in the Fc-domain of the antibody, however, readily improved the results.

The most optimal binding was obtained when the antibody was attached via the carbohydrate region to streptavidin via biotin, attaching also the streptavidin via biotin to the surface. It is also observed in Table 4.2 that the affinity constant of the immobilised systems is in the most optimal case significantly lower than the affinity in solution.

Table 4.2 Affinity constants and binding exponents and for an anti-TNT antibody binding to a Cy5-analog of TNT as a function of various immobilization schemes in fluorescence measurements, tabulated from [64]

Immobilisation scheme	K_A (M^{-1})	$K_A/K^0{}_A$ (%)	η
No immobilization (solution binding)	3.50×10^8 ($=\boldsymbol{K}^0{}_A$)	100	0.98
Random via NH_2	0.70×10^8	20	0.07
Oriented via carbohydrate	0.63×10^8	18	0.90
Oriented via Protein G	0.061×10^8	1.7	0.78
Oriented via Streptavidin bound to NH_2	0.076×10^8	2.2	0.79
Oriented via Streptavidin bound via biotin	0.71×10^8	20	0.98

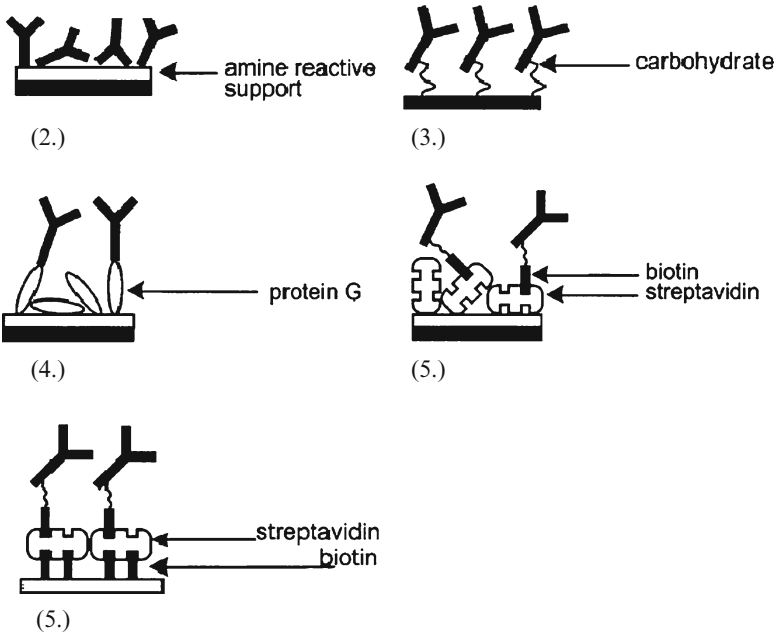

Fig. 4.8 Illustration of the various immobilisation methods summarised in Table 4.2 used for an anti-TNT antibody, from [64] with permission

In most of the studies on *site-oriented* or *site-directed* immobilisation, the use of antibody fragments has been strongly emphasized, particularly *Fab'-fragments*, which have two thiol groups in the residual hinge region opposite to the antigen-binding site [118, 119]. When antibodies are covalently coupled to self-assembled layers (SALs) or Langmuir-Blodgett (LB) films via these thiol groups, high specific activity of antibodies can be attained (>70%), but the total surface densities remain relatively small [109, 111, 119].

The adsorptions of antibodies directly onto gold surfaces have not been regarded expedient because of conformational re-arrangements, unfavorable orientation, and

desorption of the protein or even complete denaturation [120]. However, O'Brien et al. have shown that Fab′-fragments with terminal thiol groups can be directly self-assembled with high density onto gold, giving rise to a high epitope density for antibody binding [121]. Since gold is the surface of choice in many optical or electronic sensing devices, such as SPR, QCM, etc., there is a great demand for direct immobilisation methodology onto gold. The maximisation of the amount of binding sites and vicinity of the molecules to the sensing surface is still very important, particularly in those devices where the penetration depth is lesser than that in SPR [122].

It has recently been demonstrated in our own studies that Fab′ fragments can be directly self-assembled onto hydrophilic gold in high density with good preservation of activity for the antigen, and very much improved sensitivity and possibility for regeneration of the Fab′-fragments were obtained by employing a non-ionic hydrophilic polymer ("pTHMMAA") as a blocking agent, which effectively fills up the residual empty space between the antibody molecules [123–127]. The pTHMMAA polymers were synthesized from Tris-(hydroxymethyl)methylacrylamide by thermal polymerisation with an initiator conjugated to α-lipoic acid via a *N*-methyl-aminoethanol [124] or a diaminopropane linker [123] (Scheme 4.1, structures 1 and 2, respectively). These polymers can intercalate between the antibody molecules and bind through the lipoate moiety to the gold surface. The immobilization principle is illustrated in Fig. 4.9 for a polyclonal antibody, and its fragments, against human IgG (h-IgG).

When Fab′-fragments of anti-h-IgG were directly coupled to gold, there was a threefold increase in response on binding of antigen when compared with that of a layer composed of $F(ab')_2$-fragments, which indicates a strong increase in orientation. In a study with the infection marker CRP, it was shown that a considerably lower degree of non-specific binding could be attained in serum samples when the pTHMMAA polymer was used as a blocking agent [126].

4.6.2 Enhancement of the Sensitivity

There are many cases where direct detection of biomolecules by optical methods is hampered by sensitivity limitations due to a very small refractive index increment, low clinical concentrations, or limited molecular weight (or combinations of these). In these instances, it is possible to enhance the sensitivity considerably by using gold nanoparticles (AuNPs) in either competitive or sandwich assay formats [49, 128]. As discussed briefly earlier, the signal amplification of AuNPs is, additionally to the high density and high mass of the particles, related to the electronic coupling between surface plasmon waves and localized surface plasmons. Thus, besides latex particles, dyes, and liposomes, which all have been previously employed for amplification of the optical response [129, 130], gold labels have yielded the most significant advantages [18], including the fact that the amplification factor can be tuned by the size and shape of the nanoparticles [131–133]. In sandwich assays, the

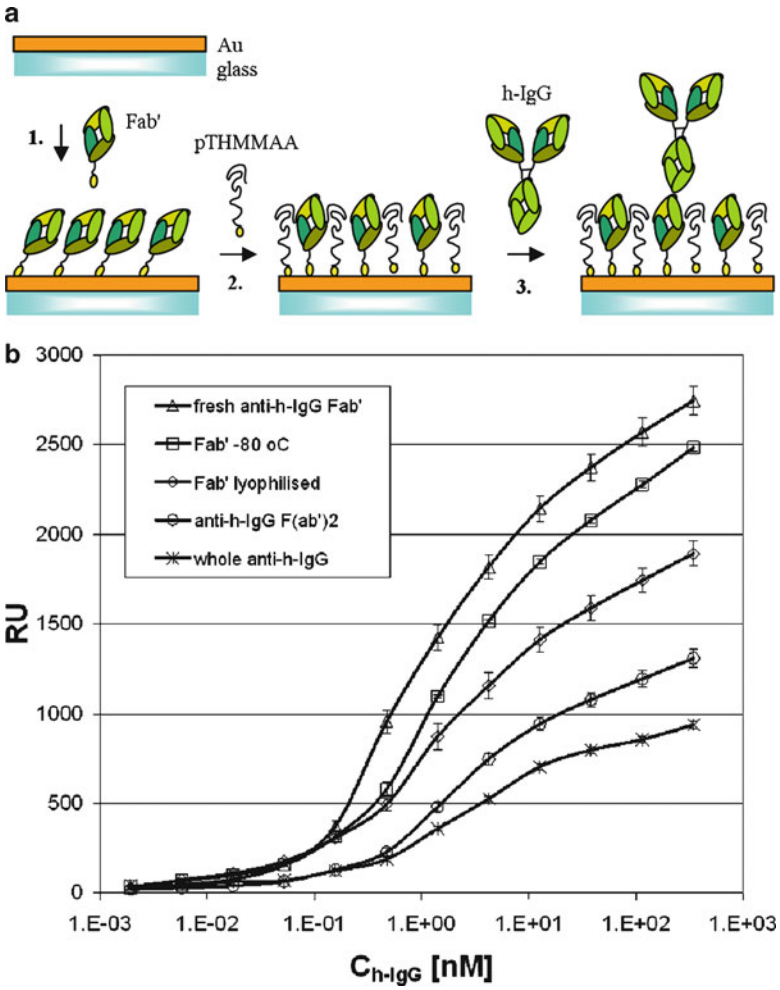

Fig. 4.9 (**a**) Cartoon showing (1) the adsorption of anti-h-IgG Fab′-fragments, followed by (2) "blocking" with pTHMMAA polymer and (3) the binding of the antigen h-IgG to the Fab′-fragments. The Fab′-fragments become embedded in the polymer, which stabilizes the layer and shields the surface from nonspecific interactions. (**b**) Equilibrium binding curves for various preparations of the antibody, and fitted to the two-site Sips isotherm. Highest activity was observed for freshly prepared Fab′-fragments, with a minor effect for preservation of the Fab′-fragments at −80°C. Lyophilisation of the Fab′-fragment nearly halved the response, while use of $F(ab')_2$-fragments and use of the whole antibody, gave less than 50% of the optimal activity

antigen is first bound to an immobilized (capture) antibody, and then a second, labeled antibody is bound to another site of the antigen. Thus, in addition to a higher response, the assay is also more selective [132, 133]. Alternatively, a competitive interaction scheme can increase the detection sensitivity when a labeled molecule bound to the sensing surface is displaced by a small molecule that cannot be easily

detected directly [134, 135]. A few examples will be shown from the literature and from our own work that illustrate this approach.

As a first example, the recent study of Besselink et al. on the detection of prostate-specific antigen (PSA) illustrates the use of various sandwich assay formats [136]. In this study, the amplification efficiency of two types of labels (AuNPs and latex particles) on two types of surfaces (gel-modified surface and flat surface) was investigated, and it was found that the lowest detection limit for PSA could be obtained with the AuNPs on a planar surface: 0.6 ng/mL (Fig. 4.10). Even better detection limits have been found for similar systems [137], and this readily demonstrates the utility of AuNPs in clinical diagnostics tests (e.g., for point-of-care devices), since the amplification allows measurements to be made at much lower concentrations.

In our own studies, we investigated the applicability of the pTHMMAA polymers to intercalate between Fab′-fragments also on AuNPs, with the purpose to increase the stability of the particles, because it was observed that pTHMMAA polymers effectively inhibit flocculation of AuNPs [138]. Figure 4.11 presents a comparison between direct and amplified detection of an SPR-based assay for a model antigen, human IgG (h-IgG) [139].

An antibody (or its $F(ab')_2$-fragment) was immobilized on a gold surface by embedding in a repellent polymer layer of pTHMMAA (Scheme 4.1, structure 2), and the direct binding of the h-IgG measured. Hereafter, a gold label, with

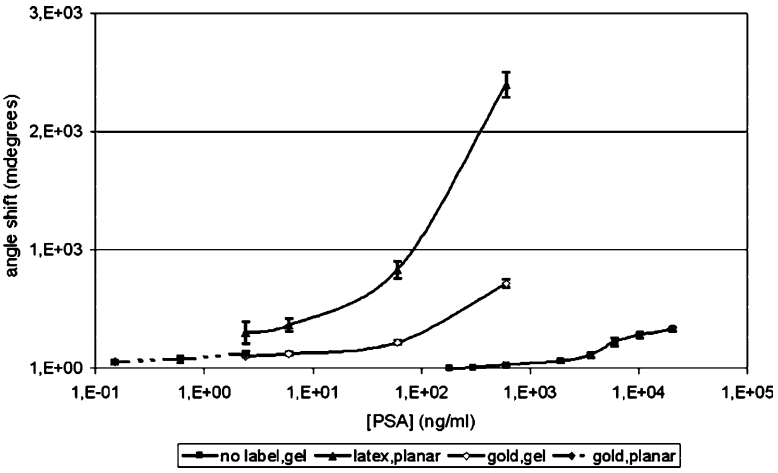

Fig. 4.10 Measurements of the angular shift as a function of PSA concentration, in various assay configurations (from [136] with permission). Measurements without label (on a gel-type surface) gave a response at concentrations between 0.3 and 34 μg/mL, with maximum response of 400 mdegrees (≈4,000 RU). On the same surface, the amplification by gold particles gave a response between 2.4 and 600 ng/mL PSA, with a maximum response of 700 mdegrees. On a planar surface, the maximum response for the gold particles was slightly higher: 900 mdegrees, in a working range of 0.6–600 ng/mL. For the latex particles, the response was even much higher: on both type of surfaces the maximum response was 2,500 mdegrees, in the working range 2.4–600 ng/mL

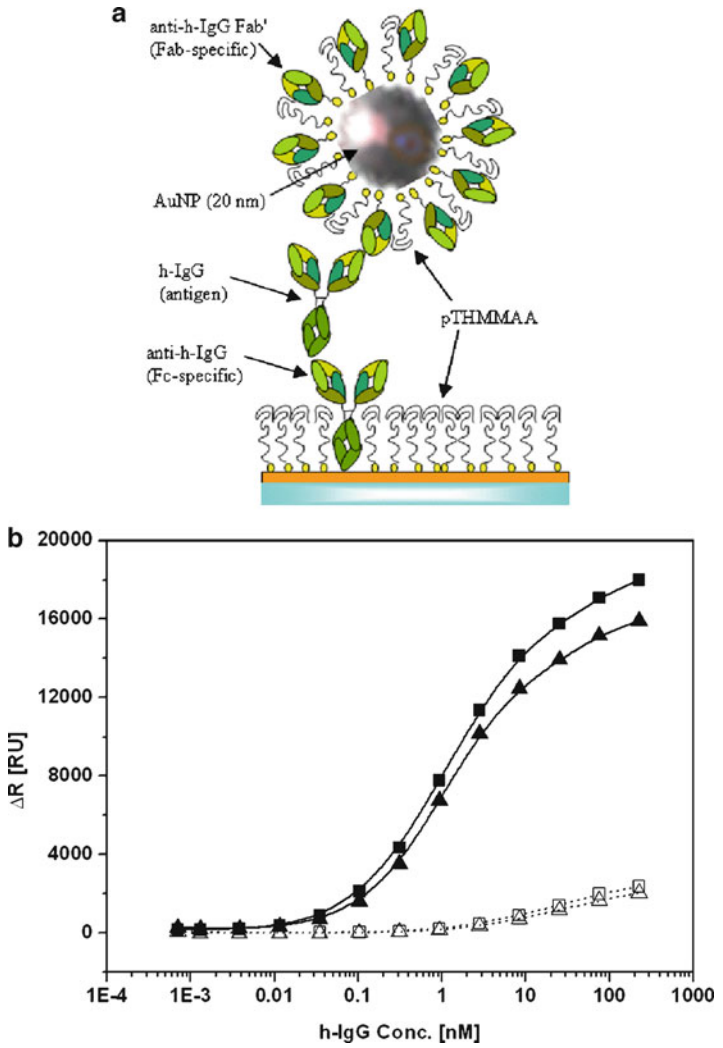

Fig. 4.11 (**a**) Structure of the sandwich assay on gold in SPR-based detection. The capture antibody, "anti-h-IgG (Fc), was a whole IgG or F(ab′)$_2$-fragment specific to the Fc-domian of human IgG, while the gold label was modified with Fab′-fragments specific for the Fab domains of human IgG (anti-h-IgG Fab′). Both antibodies used in the assay were embedded in the pTHMMAA polymer to reduce nonspecific binding effects. (**b**) Response curves for direct binding of human IgG (*open symbols*) and subsequent binding of the gold label (*closed symbols*): (*filled triangle*) for whole IgG antibody on the surface, (*filled square*) for F(ab′)$_2$-fragment on the surface

specificity for a different site of human IgG, was allowed to form a sandwich (Fig. 4.11a). When the binding with h-IgG and label was studied over a broad concentration range, it could be observed that already at very low concentrations, the gold label afforded a large amplification (>100×). The splitting of the capture

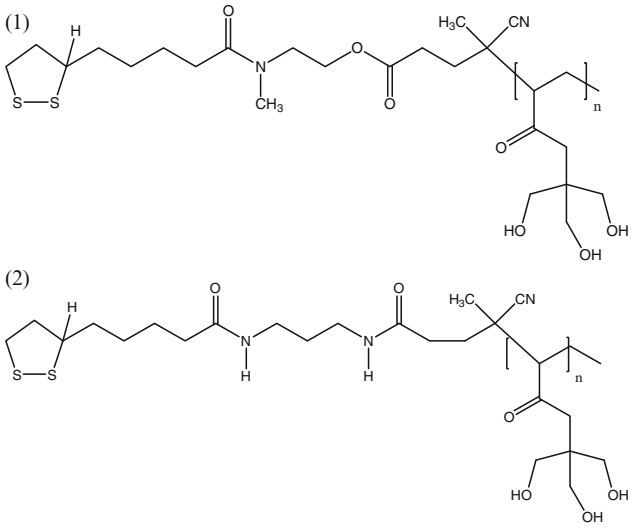

Scheme 4.1 Structure of the two types of pTHMMAA molecules used as a repellent polymer and blocking agent in immobilisation of Fab′-fragments on gold

antibody to $F(ab')_2$ gave a minor increase in both of the direct and amplified response, which indicated that still some increase of packing of the particles could be achieved.

Thus, the use of the pTHMMAA polymers as a blocking and stabilizing agent is one of the examples of surface design in which a rather facile single or dual-step surface modification technique was able to give superior results with a variety of model systems, and was applicable for planar gold surfaces and gold nano-particles alike.

4.7 DNA-Based Sensing

DNA hybridisation tests still heavily rely on fluorescent probes in most of the recently developed microarray-based systems. The sensitivity is high due to low background noise, but costly reagents and time-consuming labeling procedures need to be used [140]. Recently, many new studies have been conducted on the real-time detection of interactions of nucleic acids with other nucleic acids [141–143], with proteins or small molecules [144], while much new work with aptamers is underway [145].

With SPR detection, a portable, commercially available SPREETA™ sensor proved to be suitable for detection of DNA hybridisation between surface immobilised thiol-modified probes both with synthetic oligonucleotides and PCR-amplified real samples, and the system could be used for detection of gene mutations

[146–149]. Recently, SPR imaging has been employed for multiplexed real-time monitoring of the hybridisation reaction of unlabeled oligonucleotide targets to oligonucleotide probes immobilised in a 196-spot array. Biotinylated probes were attached to extravidin and streptavidin coupled to layers of 11-mercaptoundecanoic acid-poly(ethylenimine) and 11-mercaptoundecanol-carboxylated dextran, respectively [148, 149]. There are, however, still many improvements possible for immobilisation of DNA probes.

The conventional immobilisation method for oligonucleotides comprises coupling of biotinylated single-stranded DNA oligonucleotide probes (biotin-ssDNA) to a layer of streptavidin, in which the streptavidin is immobilized by various methods, such as covalent linking to carboxylated dextran [150–152]. DNA has been attached to a variety of surfaces by adsorption [153], copolymerization [154], or complexation [155], but most methods use covalent binding [156–161]. Methods for covalent attachment include self-assembly of thiol-modified oligos, as further discussed later, or silanisation [162].

Thiol-modified oligos are expected to spontaneously assemble onto the gold surface in a similar manner as conventional ligands for self-assembly, although the interaction of DNA bases directly with gold cannot be ignored [163]. Surface hybridisation depends strongly on the length of the probe, its density, surface orientation, and target sequence [159, 164]. Single-stranded DNA (ssDNA) has usually been self-assembled in mixed monolayers with mercaptohexanol to reduce nonspecific binding (NSB) of interfering nucleic acids or proteins from the sample solution and improve the attachment of the probes to the surface [159, 160–165]. The most usual probes to be immobilised on gold are thiol-modified single-stranded DNA probes (SH-ssDNA) and disulfide-modified probes with a dimethoxytrityl group (DMT-S-S-ssDNA), typically about 15–30 base pairs long. The immobilisation step comprises simply adsorbing the probes onto the gold surface for many hours, although 10–15 min has proven to be a sufficient time for reaching saturation coverage for both thiol- and disulfide-modified probes. The layer is then typically posttreated with 6-mercapto-1-hexanol for 10–15 min.

In our own studies, we have initially utilised the polymer pTHMMAA (Scheme 4.1, structure **1**) to fill up the remaining space between the ssDNA probes [166], and lately also short hydroxy-alkyl-substituted lipoamides have been successfully used for the same purpose [167, 168].

With shorter DNA probes, (16–18 mer), the surface density of nucleic acid layers was twice ($2.4 \pm 0.2 \times 10^{13}$ probes/cm^2) in comparison with the longer probes (25–27 mer). Hybridization of single-stranded polymerase chain reaction (PCR) amplified products with a length above 300 base pairs produced only a very low degree of hybridization. However, for amplicons with about 100 base pairs, the response was high (Fig. 4.12). The surface coverage was comparable with that of complementary ssDNA binding (3.0×10^{12} strands/cm^2).

Efficient immobilisation of 15-mer SH-ssDNA probes was attained on gold with these shorter compounds, which are likely to induce less steric hindrance in hybridisation reactions at surfaces than the longer polymer chains of pTHMMAA. However, both the short lipoamides and the pTHMMAA

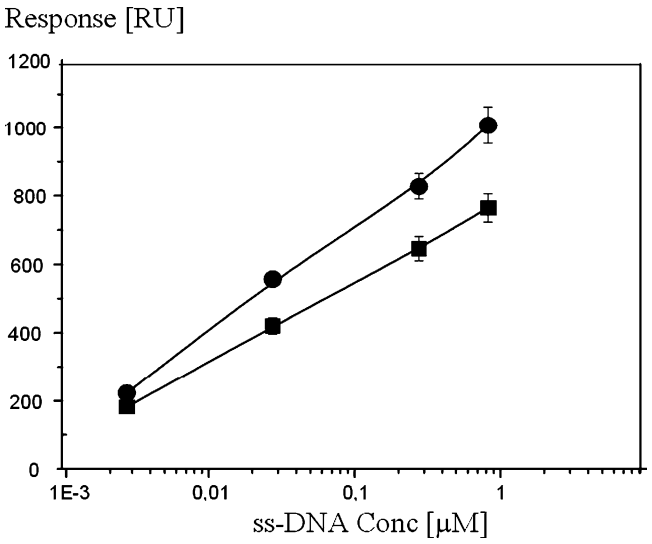

Fig. 4.12 Hybridisation of ssDNA 100 base pairs long amplicons to monolayers of SH-ssDNA (*filled circle*) and DMT-S-S-ssDNA (*filled square*), both posttreated with Lipa-DEA as measured with Biacore 3000. The layers were tested for nonspecific binding of BSA and noncomplementary binding of DNA [168]

polymer infer very low non-specific binding and can be stably attached onto the gold surface through the disulphide of the lipoate moiety as earlier demonstrated for the antibody fragments.

4.8 AFM Studies of Immobilised Biomolecules

In recent years, a large body of atomic force microscopy (AFM) images has been compiled of biomolecules on surfaces [169–171], and AFM is more and more used in imaging of the surfaces of cells [172, 173]. In this paragraph, we will very briefly present some images of immunoglobulin (IgG) and DNA molecules attached to sensing surfaces, as they are of complementary importance to the subjects presented in this chapter.

With AFM, various measurement modes and methods can be readily applied to obtain high-resolution images related to topographical, charge, softness, and other parameters of the biomolecular layer [169]. The first high-resolution pictures of antibody molecules were obtained from cryogenic samples of IgG on mica surfaces, and they revealed the typical Y-shaped subdomain structure [174]. AFM tips modified with single-walled carbon nanotubes (SWCNTs) have enabled the first high-resolution images of IgG molecules to be acquired at room temperature, in which also the typical *Fc-Fab* substructure could be clearly discerned [175–177].

Molecules were imaged in ambient air on a mica surface in *tapping mode*, although in this mode it has also been shown that the quality of the images of antibody molecules may readily decrease upon repeated scanning [178]. More recently, it has been shown that the typical domain structure of IgG molecules can be resolved in *non-contact* mode, using standard silicon tips [179, 180]. By using well-desiccated samples and controlling the cantilever drive frequency and set-point amplitude to optimal values within the non-contact regime, the Fc and Fab subunits could be readily resolved when the molecule has the appropriate orientation on the surface (Fig. 4.13). The AFM results can be validated by comparing the AFM images with X-ray crystallography data from the protein data bank.

Especially, the presence of a water layer on hydrophilic mica has been found to be an inhibiting factor for obtaining sufficient imaging contrast, which was a consequence of capillary neck-formation between tip and surface [181]. Thus, desiccation of samples to remove surface bound water layers yields reproducible imaging of the IgG substructure [182]. The desiccation approach facilitated higher resolution than previously achieved: down to 25 kDa [180].

In the case of dense monolayers, it will be clear that the features of individual molecules may easily be lost. However, it has been possible to visualise the

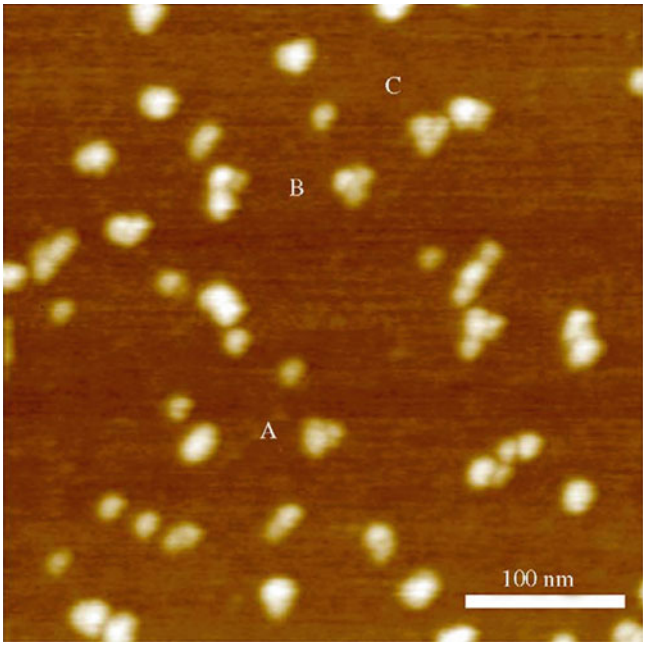

Fig. 4.13 Non-contact-mode AFM image of IgG on a mica surface. The images were taken in ambient laboratory conditions (relative humidity 30–40%). As can be observed, the IgG molecules have a rather randomised orientation on the surface, but the molecules marked A, B, and C have an orientation where the AFM tip can resolve the three 50 kDa subunits, obtained from [180] with permission

immunoreaction between human IgG, and Fab′-fragments, in which the Fab′-fragments were bound to lipid monolayers. In these layers, the density of the Fab′-fragments was still sufficiently low to discern both individual and clusters of bound biomolecules [111]. Figure 4.14a shows AFM images, acquired in tapping mode in air, of a monolayer composed of three components: the lipid DPPC, a lipid linker DPPE-EMS (carrying a maleimide functional group for binding to free thiol groups of the antibody), and cholesterol. The layer had globular structures of about 3–7 nm height, which were likely micelles or half-micelles.

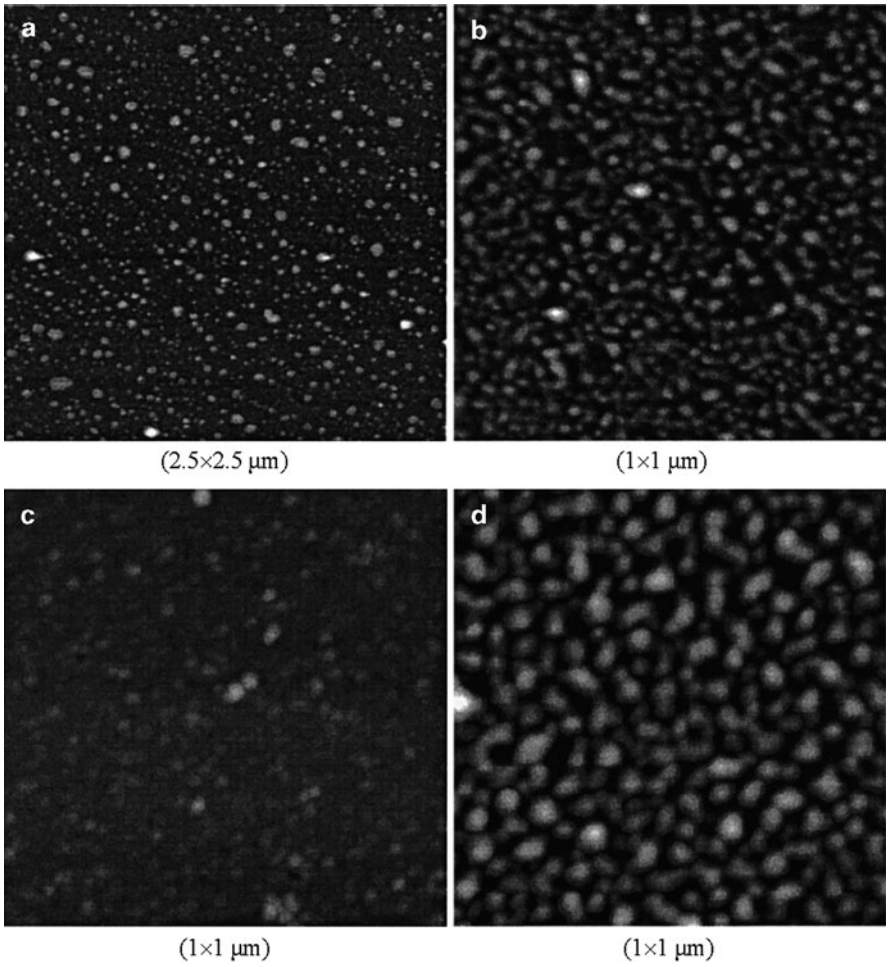

Fig. 4.14 Tapping-mode AFM image of Fab′-fragments bound to a mixed monolayer of lipid, linker lipid and cholesterol, studied on octadecyl-trichlorosilane-modified silicon slides. (**a**) The mixed lipid monolayer without Fab′-fragments, (**b**) after reaction with Fab′-fragments at a concentration of 50 μg/mL, (**c**) after blocking with 100 μg/mL BSA, and (**d**) after reaction with 100 μg/mL human IgG, obtained from [111] with permission

Figure 4.14b shows the same layer, at slightly larger magnification, after binding of Fab′-fragments, which gave slightly increased amount of similar-sized domain structures. The addition of BSA (Fig. 4.14c) produced a much smoother surface, with occasional holes of 1.5–5 nm depth. Finally, the reaction with human IgG produced detached globular structures slightly larger in size compared with the Fab′-fragments (Fig. 4.14d), with a characteristic height of 8–12 nm, typical for slightly tilted IgG molecules. The study revealed that the composition of the lipid layer greatly influenced the orientation of the antibody fragments, and that the nonspecific binding was increased when using cholesterol in the layer.

Oligonucleotides, particularly long dsDNA strands, can be readily imaged by various AFM methods (see Chap. 4 in [169]). However, studies of DNA probes on actual sensing surfaces under various conditions are still rare. Lallemand et al. have preliminarily studied ssDNA probes with noncontact mode AFM, in which model ssDNA strands with a length of 12 and 25 bases were attached via a terminal amine group to silanized and HNS-ester activated silicon wafers [183]. There was a clear growth of globular structures observed with a characteristic height of 11 nm for the shorter and 23–25 nm for the longer ssDNA probes. A surface density of $1.75–2.25 \times 10^{11}$ molecules/cm^{-2} was measured for the probes, which compared favorably with the results of radiochemical measurements. Hybridisation of a complementory amplicon (1,500 base pairs long) was also visualized, in which a single strand of the target could be seen lying onto the "bed" of ssDNA probes (Fig. 4.15) [162].

As a final issue, high-speed AFM has been recently developed for studying dynamic biomolecular processes, with which frame rates larger than 10 s^{-1} could be accomplished [184]. Studies have been made on movement of actin filaments on Myosin V, and GroES binding to GroEL, while also the movement of defect points

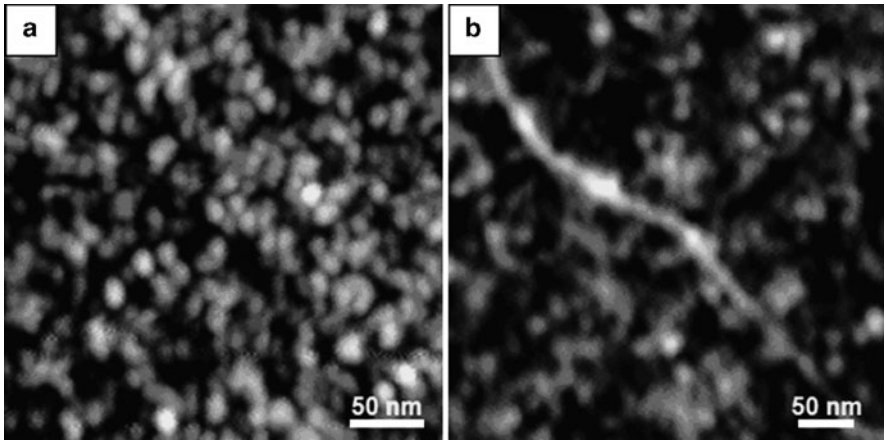

Fig. 4.15 Non-contact-mode AFM image of (**a**) ssDNA probes (25-mer) on silicon, showing as isolated islands (**b**) after hybridisation with complementary 1,500 base pair amplicon, obtained from [162] with permission

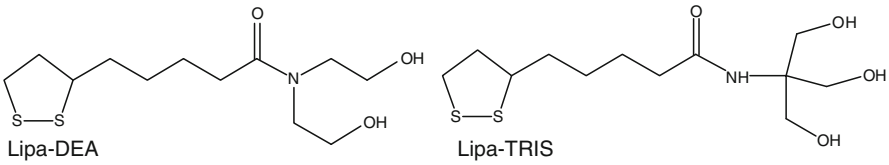

Scheme 4.2 Structure of two types of lipoate derivatives for intercalation with DNA probes on gold surfaces, Lipa-DEA and Lipa-TRIS [168]

in two-dimensional crystals of streptavidin has been visualised. Thus, it seems likely that also immunological reactions can be followed by AFM in real time in the near future.

4.9 Outlook

As evidenced by a recent monograph on the subject [8], there are still many opportunities for surface designing in bioscience and nanotechnology applications. Stimuli-responsive polymer brushes are one class of compounds, where still much interesting work can be done, while the repertoire of silanes and lipoate derivatives, for tailoring inorganic surfaces by self-assembly, is still far from exhausted. We have demonstrated that various short self-assembling molecules, as well as hydrophilic polymers are very useful in improving biosensor characteristics, particularly with respect to suppression of non-specific binding and increase in the stability of molecular layers. Some lipoate derivatives have even enabled the construction of synthetic receptors by surface imprinting [185].

As there are many reported studies on the immobilisation of biomolecules, it is impractical to give a complete overview in this limited space. In the end, much will depend on the particulars related to the price, material, surface area, and penetration depth of the final sensor system. However, for diagnostic purposes, the set of demands on immobilization becomes in many aspects very stringent, particularly when endeavoring direct detection in clinical samples without labels [186]. One possibility for increase in selectivity and sensitivity is to take advantage of the penetration depth of the sensing phenomenon (i.e., to adapt the effective thickness of the sensing layer to the penetration depth). It is generally favorable to reduce the penetration depth, such that less interference will occur from the bulk solution. With evanescent wave methods, the sensing layer can be up to 500-nm thick, but with high frequency resonators, the penetration depth may be much smaller, in the region of a few tens of nanometers [187].

Acknowledgments Financial support from VTT Technical Research Centre, the EU, and TEKES in various projects is gratefully acknowledged. We also express thanks to Risto Ahorinta, of ORC, Tampere University of technology, for some ellipsometric measurements reported in this chapter.

Appendix A

The Jones matrix $\mathbf{I}_\mathrm{i}$ for reflection/transmission at an interface between layer i and $i+1$ is based on the Fresnell reflection/transmission coefficients r_i and t_i, according to:

$$\mathrm{I}_i = \left(\frac{1}{t_i}\right)\begin{pmatrix} 1 & r_i \\ r_i & 1 \end{pmatrix},$$

where in the case of p-polarized light, the coefficients are:

$$r_i = \frac{\hat{n}_{i+1}c_i - \hat{n}_i c_{i+1}}{\hat{n}_{i+1}c_i + \hat{n}_i c_{i+1}} \text{and } t_i = \frac{2\hat{n}_i c_i}{\hat{n}_{i+1}c_i + \hat{n}_i c_{i+1}}$$

in the case of s-polarised light, the coefficients are:

$$r_i = \frac{\hat{n}_i c_i - \hat{n}_{i+1}c_{i+1}}{\hat{n}_i c_i + \hat{n}_{i+1}c_{i+1}} \text{and } t_i = \frac{2\hat{n}_i c_i}{\hat{n}_i c_i + \hat{n}_{i+1}c_{i+1}}.$$

The Jones matrix $\mathbf{L}_i$ for the light absorption in layer i takes the form, according to the Lambert-Beer law as:

$$\mathrm{L}_i = \begin{pmatrix} \mathrm{e}^{-i\beta_i} & 0 \\ 0 & \mathrm{e}^{i\beta_i} \end{pmatrix} \text{with } \beta_\mathrm{i} = \frac{2\pi}{\lambda}\mathrm{d_i}\hat{n}_i c_i$$

(when using the convention $\hat{n} = n{+}ik$) *where* $c_i = \cos(\theta_i) = \sqrt{1 - \frac{\hat{n}_1^2}{\hat{n}_i^2}\sin^2(\theta_1)}$.

Appendix B

Reaction Schemes and rate equations for the most frequently used binding systems, from [57] in modified form.

One-to-one reaction

$$\mathbf{A} + \mathbf{B} \rightleftarrows \mathbf{AB}$$

$$\mathrm{d}R/\mathrm{d}t = k_\mathrm{a} \cdot [\mathrm{A}] \cdot (R_\mathrm{max} - R) - k_\mathrm{d} \cdot R$$

One-to-one reaction with mass transfer

$$\mathbf{A}^* \rightleftarrows \mathbf{A} \qquad \mathbf{A} + \mathbf{B} \rightleftarrows \mathbf{AB}$$

$$\mathrm{d}[\mathrm{A}]/\mathrm{d}t = k_\mathrm{t} \cdot ([\mathrm{A}^*] - [\mathrm{A}]) - k_\mathrm{a} \cdot [\mathrm{A}] \cdot (R_\mathrm{max} - R) + k_\mathrm{d} \cdot R$$

$$\mathrm{d}R/\mathrm{d}t = k_\mathrm{a} \cdot [\mathrm{A}] \cdot (R_\mathrm{max} - R) - k_\mathrm{d} \cdot R$$

One-to-two reaction (bivalent analyte)

$$\mathbf{A} + \mathbf{B} \rightleftarrows \mathbf{AB} \quad \mathbf{A} + \mathbf{AB} \rightleftarrows \mathbf{A_2B}$$

$$\mathrm{d}R_1/\mathrm{d}t = k_\mathrm{a1} \cdot [\mathrm{A}] \cdot (R_\mathrm{max} - R_1 - R_2) - k_\mathrm{d1} \cdot R_1 - k_\mathrm{a2} \cdot [\mathrm{A}] \cdot R_1 + k_\mathrm{d2} \cdot R_2$$

$$\mathrm{d}R_2/\mathrm{d}t = k_\mathrm{a2} \cdot [\mathrm{A}] \cdot R_1 - k_\mathrm{d2} \cdot R_2$$

Two-state reaction

$$\mathbf{A} + \mathbf{B} \rightleftarrows \mathbf{AB} \quad \mathbf{AB} \rightleftarrows \mathbf{AB},$$

$$\mathrm{d}R_1/\mathrm{d}t = k_\mathrm{a1} \cdot [\mathrm{A}] \cdot (R_\mathrm{max} - R_1 - R_2) - k_\mathrm{d1} \cdot R_1 - k_\mathrm{a2} \cdot R_1 + k_\mathrm{d2} \cdot R_2$$

$$\mathrm{d}R_2/\mathrm{d}t = k_\mathrm{a2} \cdot R_1 - k_\mathrm{d2} \cdot R_2$$

Competing analyte

$$\mathbf{A} + \mathbf{B} \rightleftarrows \mathbf{AB} \quad \mathbf{C} + \mathbf{B} \rightleftarrows \mathbf{CB}$$

$$\mathrm{d}R_1/\mathrm{d}t = k_\mathrm{a1} \cdot [\mathrm{A}] \cdot (R_\mathrm{max} - R_1 - p \cdot R_2) - k_\mathrm{d1} \cdot R_1$$

$$\mathrm{d}R_2/\mathrm{d}t = k_\mathrm{a2} \cdot [\mathrm{C}] \cdot (R_\mathrm{max}/p - R_1/p - R_2) - k_\mathrm{d2} \cdot R_2,$$

where A and C are the analyte species involved in the reaction, with square brackets indicating their concentration at the surface, and A* denoting species A in the bulk of the solution. B is the immobilized species, and AB, CB, AB', and A_2B are the complexes formed at the surface, with R, R_1, and R_2 are the responses of the bound species, and R_max is the maximum response of species B. The parameter p is a correction factor, for example, to account for difference in molecular weight between species A and C. k is the rate constant, with a and d indicating the forward (association) and reverse (dissociation) reaction, and indices 1 and 2 indicating the equation

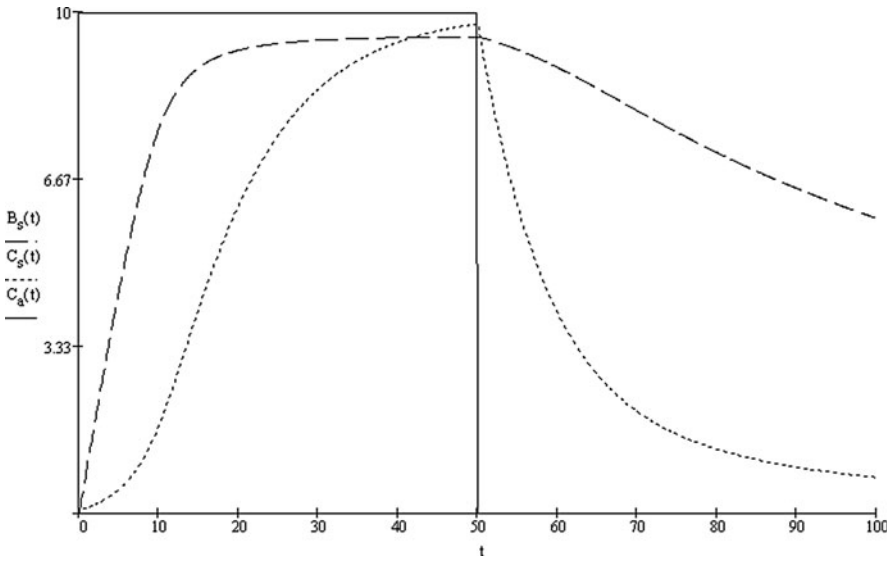

References

1. Kretschmann E (1968) Radioactive decay of non radiative surface plasmons excited by light. Z. Naturforsch A 23a:2135–2136
2. Ritchie R H, Arakawa E T, Cowan J J, Hamm R N (1968) Surface-plasmon resonance effect in grating diffraction. Phys. Rev. Lett. 21:1530–1533
3. Kretschmann E (1971) The determination of the optical constants of metals by excitation of surface plasmons. Z. Phys. A 241:313–324
4. Raether H (1988) Surface Plasmons. Springer-Verlag, Berlin
5. Nylander C, Lundstrom I, Liedberg B (1983) Surface plasmon resonance for gas detection and biosensing. Sens. Actuators 4:299–304
6. Homola J (2006) Surface Plasmon Resonance Based Sensors. Springer-Verlag Heidelberg
7. Schasfoort R B M, Tudos A J (2004) Handbook of Surface Plasmon Resonance. RSC Publishing, Cambridge
8. Förch R, Schönherr H, Jenkins A T A (Eds) (2009) Surface Design: Applications in Bioscience and Nanotechnology. VCH/Wiley, Weinheim
9. Faraday M (1857) Experimental relations of gold (and other metals) to light. Phil. Trans. R. Soc. Lond. 147:145–181
10. Mie G (1908) Beiträge zur Optik trüber Medien, speziell kolloidaler Metallösungen. Ann. Phys. 4:377–445
11. Hutter E, Fendler J H (2004) Exploitation of localized surface plasmon resonance. Adv. Mater. 16:1685–1706
12. Stewart M E, Anderton C R, Thompson L B, Maria J, Gray S K, Rogers J A, Nuzzo R G (2008) Nanostructured plasmonic sensors. Chem. Rev. 108:494–521
13. Born M, Wolf E (1987) Principles of Optics. Pergamon Press, Oxford
14. Otto A (1968) Excitation of non-radiative surface plasma waves in silver by the method of frustrated total reflection. Z. Phys. 216:398–410
15. Azzam R M A, Bashara N M (1987) Ellipsometry and Polarised Light. Elsevier, Amsterdam
16. Sadowski J W, Korhonen I K J, Peltonen J P K (1995) Characterisation of thin films and their structures in surface plasmon resonance measurements. Opt. Eng. 34:2581–2586

17. Salamon Z, Macleod H A, Tollin G (1997) Surface plasmon resonance spectroscopy as a tool for investigating the biochemical and biophysical properties of membrane protein systems. Part I. & 2. Biochim. Biophys. Acta 1331:117–129, 131–152
18. Homola J (2008) Surface plasmon resonance sensors for detection of chemical and biological species. Chem. Rev. 108:462–493
19. Theye M L (1970) Investigation of the optical properties of Au by means of thin semitransparent films. Phys. Rev. B 2:3060–3078
20. Dold B, Mecke R (1965) Optische Eigenschaften von Edelmetallen, Übergangsmetallen und deren Legierungen im Infrarot (1. Teil). Optik 22:435–446
21. Heavens O S (1960) Optical properties of thin films. Rep. Prog. Phys. 23:1–675
22. Schiebener P, Straub J, Levelt-Sengers, J M H, Gallagher J S (1990) Refractive index of water and steam as function of wavelength, temperature and density. J. Phys. Chem. Ref. Data 19:677
23. Ghosh G (1997) Sellmeier coefficients and dispersion of thermo-optic coefficients for some optical glasses. Appl. Opt. 36:1540–1546
24. Nelson B P, Frutos A G, Brockman J M, Corn R M (1999) Near-infrared surface plasmon resonance measurements of ultrathin films. 1. Angle shift and SPR imaging experiments. Anal. Chem. 71:3928–3934
25. De Feijter J A, Benjamins J, Veer F A (1978) Ellipsometry as a tool to study the adsorption behavior of synthetic and biopolymers at the air-water interface. Biopolymers 17:1759–1772
26. Vörös J (2004) The density and refractive index of adsorbing protein layers. Biophys. J. 87:553–561
27. Qian R L, Mhatre R, Krull I S (1997) Characterization of antigen-antibody complexes by size-exclusion chromatography coupled with low-angle light-scattering photometry and viscometry. J. Chromatogr. A 787:101–109
28. Ball V, Ramsden J J (1998) Buffer dependence of refractive index increments. Biopolymers 46:489–492
29. Arwin H (1986) Optical properties of thin layers of bovine serum albumin, γ-globulin, and hemoglobin. Appl. Spectrosc. 40:313–318
30. Oudshoorn R C G, Kooyman R P H, Greve J (1996) Refractive index and layer thickness of on adsorbing protein as reporters of monolayer formation. Thin Solid Films 284–285:836–840
31. Sadowski J W, Lekkala J, Vikholm I (1991) Biosensors based on surface plasmons excited in non-noble metals. Biosens. Bioelectron. 6:439–444
32. Mayer C, Schalkhammer T (2005) Bioanalytical sensing using noble metal colloids. Top. Fluoresc. Spectrosc. 8:135–195
33. Kontio J M, Husu H, Simonen J, Huttunen M J, Tommila J, Pessa M, Kauranen M (2009) Source nanoimprint fabrication of gold nanocones with ∼10 nm tips for enhanced optical interactions. Opt. Lett. 34:1979–1981
34. Dahlin A, Zäch M, Rindzevicius T, Käll M, Sutherland D S, Höök F (2005) Localized surface plasmon resonance sensing of lipid-membrane-mediated biorecognition events. J. Am. Chem. Soc. 127:5043–5048
35. Turkevich J, Stevenson P C, Hillier J A (1951) Study of the nucleation and growth processes in the synthesis of colloidal gold. Discuss. Faraday. Soc. 11:55–75
36. Frens G (1973) Controlled nucleation for the regulation of the particle size in monodisperse gold suspension. Nat. Phys. Sci. 241:20–21
37. Jana N R, Gearheart L, Murphy C J (2001) Evidence for seed-mediated nucleation in the chemical reduction of gold salts to gold nanoparticles. Chem. Mater. 13:2313–2322
38. Jadzinsky P D, Calero G, Ackerson C J, Bushnell, D A, Kornberg, R D (2007) Structure of a thiol monolayer-protected gold nanoparticle at 1.1 Å resolution. Science 318:430–433
39. Slot J W, Geuze H J (1985) A new method for preparing gold probes for multiple-labelling cytochemistry. Eur. J. Cell. Biol. 38:87–93

40. Brust M, Walker M, Bethell D, Schiffrin D J, Whyman R (1994) Synthesis of thiol-derivatised gold nanoparticles in a two-phase liquid–liquid system. J. Chem. Soc. Chem. Commun. 94:801
41. Link S L, El-Sayed M A (1999) Size and temperature dependence of the plasmon adsorption of colloidal gold nanoparticles. J. Phys. Chem. 103:4212–4217
42. Creighton J A, Eadon D G (1991) Ultraviolet-visible absorption spectra of the colloidal metallic elements. J. Chem. Soc. Faraday Trans. 87:3881–3891
43. Englebienne P, Van Hoonacker A, Verhas M (2003) Surface plasmon resonance: principles, methods and applications in biomedical sciences. Spectroscopy 17:255–273
44. Haiss W, Thanh N T K, Aveyard J, Fernig D G (2007) Determination of size and concentration of gold nanoparticles from UV-Vis spectra. Anal. Chem. 79:4215–4221
45. Khlebtsov N G (2008) Determination of size and concentration of gold nano-particles from extinction spectra. Anal. Chem. 80:6620–6625
46. Englebienne P (1998) Use of colloidal gold surface plasmon resonance peak shift to infer affinity constants from the interactions between protein antigens and antibodies specific for single or multiple epitopes. Analyst 123:1599–1603
47. Gribnau T C J, Leuvering J H W, van Hell H (1986) Particle-labelled immunoassays: a review. J. Chrom. B 376:175–189
48. Brooks D E, Devine D V, Harris P C, Harris J E, Miller M E, Olal A D, Spiller L J, Xie Z C (1999) RAMP™: a rapid, quantitative whole blood immunochromatographic platform for point-of-care testing. Clin. Chem. 45:1676–1678
49. Lyon L A, Musick M D, Natan M J (1998) Colloidal Au-enhanced surface plasmon resonance immunosensing. Anal. Chem. 70:5177–5183
50. Liedberg B, Nylander C, Lundström I (1995) Biosensing with surface plasmon resonance – how it all started. Biosens. Bioelectron. 10:i–ix
51. McDonnell J M (2001) Surface plasmon resonance: towards an understanding of the mechanisms of biological molecular recognition. Curr. Opin. Chem. Biol. 5:572–577
52. Arnold F H, Schofield S A, Blanch H W (1986) Analytical affinity chromatography: I. Local equilibrium theory and the measurement of association and inhibition constants. J. Chrom. A 355:1–12 & Arnold F H, Blanch H W (1986) Analytical affinity chromatography: II. Rate theory and the measurement of biological binding kinetics. J. Chrom. A 355:13–27
53. Cannon M J et al. (2004) Comparative analyses of a small molecule/enzyme interaction by multiple users of Biacore technology. Anal. Biochem. 330:98–113
54. Katsamba PS et al. (2006) Kinetic analysis of a high-afnity antibody/antigen interaction performed by multiple Biacore users. Anal. Biochem. 352:208–221
55. Navratilova I et al. (2007) Thermodynamic benchmark study using Biacore technology. Anal. Biochem. 364:67–77
56. Rich R L (2009) A global benchmark study using affinity-based biosensors. Anal. Biochem. 386:194–216
57. Karlsson R, Fält A (1997) Experimental design for kinetic analysis of protein-protein interactions with surface plasmon resonance biosensors. J. Immunol. Methods 200:121–133
58. Morton T A, Myszka D G, Chaiken I M (1995) Interpreting complex binding kinetics from optical biosensors: a comparison of analysis by linearization, the integrated rate equation, and numerical integration. Anal. Biochem. 227:176–185
59. Rich R L, Myszka D G (2010) Grading the commercial optical biosensor literature – class of 2008: "The Mighty Binders". J Mol. Recognit. 23:1–64
60. de Crescenzo G, Boucher C, Durocher Y, Jolicoeur M (2008) Kinetic characterization by surface plasmon resonance-based biosensors: principle and emerging trends. Cell. Mol. Bioeng. 1:204–215
61. Price N, Nairn J (2009) Exploring Proteins: A Student's Guide to Experimental Skills and Methods. Oxford University Press, Oxford
62. Sips R (1950) On the structure of a catalyst surface. J. Chem. Phys. 18:1024

63. García-Calzóna J A, Díaz-García M E (2006) Review: characterization of binding sites in molecularly imprinted polymers. Sens. Actuators B 123:1180–1194
64. Vijayendran R A, Leckband D E (2001) A quantitative assessment of heterogeneity for surface-immobilized proteins. Anal. Chem. 73:471–480
65. Selinger J V, Rabbany S Y (1997) Theory of heterogeneity in displacement reactions. Anal. Chem. 69:170–174
66. Jaroniec M, Madey R (1988) Physical Adsorption on Heterogeneous Solids. Elsevier, Amsterdam
67. Koopal L K, Vos C H W (1993) Adsorption on heterogeneous surfaces. Calculation of the adsorption energy distribution function or the affinity spectrum. Langmuir 9:2593–2605
68. Puzly A M, Matynia T, Gawdzik B, Poddubnaya O I (1999) Use of CONTIN for calculation of energy distribution. Langmuir 15:6016–6025
69. Press W H, Flannery B P, Teukolsky S A, Vetterling W T (1986) Numerical Recipes. Cambridge University Press, New York, p 502
70. Malmborg A-C, Michaëlsson A, Ohlin M, Jansson b, Borrebäck C A K (1992) Real time analysis of antibody-antigen reaction kinetics. Scand. J. Immunol. 35:643–650
71. Karlsson R, Katsamba P S, Nordin H, Pol E, Myszka D G (2006) Analyzing a kinetic titration series using affinity biosensors. Anal. Biochem. 349:136–147
72. Myszka D G, He X, Dembo M, Morton T A, Goldstein B (1998) Extending the range of rate constants available from BIACORE: interpreting mass transport-influenced binding data. Biophys. J. 75:583–594
73. Önell A, Andersson K (2005) Kinetic determinations of molecular interactions using Biacore-minimum data requirements for efficient experimental design. J. Mol. Recognit. 18:307–317
74. Svitel J, Boukari H, Van Ryk D, Willson R, Schuck P (2007) Probing the functional heterogeneity of surface binding sites by analysis of experimental binding traces and the effect of mass transport limitation. Biophys. J. 92:1742–1758
75. Myszka D A, Morton T A (1998) CLAMP: a biosensor kinetic data analysis program. Trends Biochem. Sci. 23:149–150
76. Lipschultz C A, Li Y, Smith-Gill S (2000) Experimental design for analysis of complex kinetics using surface plasmon resonance. Methods 20:310–318
77. Myszka D A (1999) Improving biosensor analysis. J Mol. Recognit. 12:279–284
78. Thevenot D R, Toth K, Durst R A, Wilson G S (1999) Pure Appl. Chem. 71:2333–2348
79. Wortberg M, Orban M, Renneberg R, Cammann K (1996) Fluorimetric immunosensors. In: Kress-Rogers E (Ed) Handbook of Biosensors and Electronic noses. CRC Press, Boca Raton, p 371
80. Eddowes M J (1987–1988) Direct immunochemical sensing: basic chemical principles and fundamental limitations. Biosensors 3:1–15
81. (2003) Biacore 3000 Instrument Handbook. GE Healthcare, Uppsala
82. Jonsson B, Löfås S, Lindquist G (1991) Immobilization of proteins to carboxy methyl dextran-modified gold surface for biospecific analysis in surface plasmon resonance sensors. Anal. Biochem. 198:268–277
83. Löfås S, Jönsson B (1992) A novel hydrogel matrix on gold surfaces in surface plasmon resonance sensors for fast and efficient covalent immobilization of ligands. J. Chem. Soc. Commun. 21:1526–1528
84. Kambhampati D (Ed) (2005) Protein Microarray Technology. VCH/Wiley, Weinheim
85. Boozer C, Kim G, Cong S, Guan H, Londergan T (2006) Looking towards label-free biomolecular interaction analysis in a high-throughput format: a review of new surface plasmon resonance technologies. Curr. Opin. Biotechnol. 17:400–405
86. Eddings M A, Eckman J W, Arana C A, Papalia G A, Connolly J E, Gale B. K, Myszka D G (2009) "Spot and hop": internal referencing for surface plasmon resonance imaging using a three-dimensional microfluidic flow cell array. Anal. Biochem. 385:309–313

87. Beusink J B, Lokate A M C, Besselink G A J, Pruijn G J M, Schasfoort R B M (2008) Angle-scanning SPR imaging for detection of biomolecular interactions on microarrays. Biosens. Bioelectron. 23:839–844
88. Albers W M, Vikholm I, Viitala T, Peltonen J (2001) Interfacial and materials aspects of the immobilisation of biomolecules onto solid surfaces. In: Nalwa HS (Ed) Handbook of Surfaces and Interfaces of Materials. Academic Press, San Diegop. p. 1–(1/N)31
89. Shankaran D R, Miura N (2007) Trends in interfacial design for surface plasmon resonance based immunoassays. J. Phys. D: Appl. Phys. 40:7187–7200
90. Gutiérrez-Gallego R, Bosch J, Such-Sanmartín G, Segura J (2009) Surface plasmon resonance immunoassays – a perspective. Growth Horm. IGF Res. 19:388–398
91. Bilitewski U (2006) Review: protein-sensing assay formats and devices. Anal. Chim. Acta 568:232–247
92. Förch R, Schönherr H, Jenkins A T A (Eds) (2009) Surface Design: Applications in Bioscience and Nanotechnology. Wiley/VCH, Weinheim
93. Lofas S, Johnsson B, Tegendal K, Ronnberg I (1993) Dextran modified gold surface plasmon resonance sensors: immunoreactivity of immobilized antibodies and antibody–surface interaction studies. Colloids Surf. B 1:83–89
94. Stigter E C A, de Jong G J, van Bennekom W P (2005) An improved coating for the isolation and quantitation of interferon-γ in spiked plasma using surface plasmon resonance (SPR). Biosens. Bioelectron. 21:474–482
95. Löfås S (1995) Dextran modified self-assembled monolayer surfaces for use in biointeraction analysis with surface plasmon resonance. Pure Appl. Chem. 67:829–834
96. Löfås S, Johnsson B, Edström Å, Hansson A, Lindqvist G, Müller-Hillgren R-M, Stigh L (1995) Methods for site controlled coupling to carboxymethyldextran surfaces in surface plasmon resonance sensors. Biosens. Bioelectron. 10:813–822
97. GE Healthcare (2010) Data sheet No. 28–9681–84 AA, Sensor Chip CM7
98. Myszka D G (2004) Analysis of small-molecule interactions using Biacore S51 technology. Anal. Biochem. 329:316–323
99. Rich R L, Day Y S N, Morton T A, Myszka D G (2001) High-resolution and high-throughput protocols for measuring drug/human serum albumin interactions using BIACORE. Anal. Biochem. 296:197–207
100. Cannon M J, Myszka D G, Bagnato J D, Alpers D H, West F G, Grissom C B (2002) Anal. Biochem. 305:1–9
101. Rich R L, Hoth L R, Geoghegan K F, Brown T A, LeMotte P K, Simons S P, Hensley P, Myszka D G (2002) Kinetic analysis of estrogen receptor-ligand interactions. Proc. Natl. Acad. Sci. U.S.A. 99:8562–8567
102. Johnson B, Löfås S, Lindquist G, Edström Å, Müller-Hillgren R-M, Hansson A (1995) Comparison of methods for immobilisation to carboxymethyl dextran sensor surfaces by analysis of the specific activity of monoclonal antibodies. J. Mol. Recognit. 8:125–131
103. Volden S, Kaizheng Z, Nystrom B, Glomm W R (2009) Use of cellulose derivatives on gold surfaces for reduced nonspecific adsorption of immunoglobulin G. Colloids Surf. B, 72:266–271
104. Kyprianou D, Guerreiro A R, Chianella I, Piletska E V, Fowler S A, Karim K, Whitcombe M J, Turner A P F, Piletsky S A (2009) New reactive polymer for protein immobilisation on sensor surfaces. Biosens. Bioelectron. 24:1365–1371
105. Iwasaki Y, Omichi Y, Iwata R (2008) Site-specific dense immobilization of antibody fragments on polymer brushes supported by silicone nanofilaments. Langmuir 24:8427–8430
106. F. Khan, M. He, M.J. Taussig, Double-hexahistidine tag with high-affinity binding for protein immobilization, purification, and detection on ninitrilotriacetic acid surfaces. Anal. Chem. 78 (2006) 3072–3079
107. Y. Huang, R. Shi, X. Zhong, D. Wang, M. Zhao, Y. Li, Enzyme-linked immunosorbent assays for insulin-like growth factor-I using six-histidine tag fused proteins. Anal. Chim. Acta 596 (2007) 116–123

108. Morgan H, Taylor D M (1992) A surface plasmon resonance immunosensor based on the streptavidin–biotin complex. Biosens. Bioelectron. 7:405–510
109. Bonroy K, Frederix F, Reekmans G, Dewolf E, De Palma R, Borghs G, Declerck P, Goddeeris B (2006) Comparison of random and oriented immobilisation of antibody fragments on mixed self-assembled monolayers. J. Immunol. Methods 312:167–181
110. Nagatomo K, Kawaguchi T, Miura N, Toko K, Matsumoto K (2009) Development of a sensitive surface plasmon resonance immunosensor for detection of 2,4-dinitrotoluene with a novel oligo (ethylene glycol)-based sensor surface. Talanta 79:1142–1148
111. Vikholm I, Viitala T, Albers W M, Peltonen J (1999) Highly efficient immobilisation of antibody fragments to functionalised lipid monolayers. Biochim. Biophys. Acta 1421:39–52
112. Goto Y, Matsuno R, Konno T, Takai M, Ishihara K (2008) Polymer nanoparticles covered with phosphorylcholine groups and immobilized with antibody for high-affinity separation of proteins. Biomacromolecules 9:828–833
113. Yuan Y, He H, Lee L J (2009) Protein A-based antibody immobilization onto polymeric microdevices for enhanced sensitivity of enzyme-linked immunosorbent assay. Biotechnol. Bioeng. 102:891–901
114. Lekkala J O, Sadowski J W (1994) Surface plasmon immunosensors. In: Aizawa M (Ed) Chemical Sensor Technology. Kodansha, Tokyo 5:199–213
115. Oh B K, Lee W, Chun B S, Bae Y M, Lee W H, Choi J W (2005) Surface plasmon resonance immunosensor for the detection of Yersinia enterocolitica. Colloids Surf. A 257–258:369–374
116. Svensson H G et al. (1998) Protein LA, a novel hybrid protein with unique single-chain Fv antibody- and Fab-binding properties. Eur. J. Biochem. 258:890–896
117. Kihlberg B M et al. (1992) Protein LG: a hybrid molecule with unique immunoglobulin binding properties. J. Biol. Chem. 267:25583–25588
118. Saerens D, Huang L, Bonroy K, Muyldermans S (2008) Review: antibody fragments as probe in biosensor development. Sensors. doi:10.3390/s8084669
119. Vareiro M M, Liu J, Knoll W, Zak K, Williams D, Jenkins A T (2005) Surface Plasmon fluorescence measurements of human chorionic gonadotropin: role of antibody orientation in obtaining enhanced sensitivity and limit of detection. Anal. Chem. 77:2426–2431
120. Jung Y, Jeong J Y, Chung B H (2008) Recent advances in immobilization methods of antibodies on solid supports. Analyst 133:697–701
121. O'Brien J C, Jones V W, Porter M D, Mosher C L, Henderson E (2000) Immunosensing platforms using spontaneously adsorbed antibody fragments on gold. Anal. Chem. 72:703–710
122. Weber J, Albers W M, Tuppurainen J, Link M, Gabl R, Wersing W, Schreiter M (2006) Shear mode FBARs as highly sensitive liquid biosensors. Sens. Actuators A 128:84–88
123. Albers W M, Auer S, Helle H, Munter T, Vikholm-Lundin I (2009) Functional characterisation of Fab'-fragments self-assembled onto hydrophilic gold surfaces. Colloids Surf. B 68:193–199
124. Vikholm I (2005) Self-assembly of antibody fragments and polymers onto gold for immunosensing. Sens. Actuators B 106:311–316
125. Vikholm-Lundin I (2005) Immunosensing based on site-directed immobilization of antibody fragments and polymers that reduce nonspecific binding. Langmuir 21:6473–6477
126. Vikholm-Lundin I, Albers W M (2006) Site-directed immobilisation of antibody fragments for detection of C-reactive protein. Biosens. Bioelectron. 21:1141–1148
127. Vikholm I. Sadowski J (2007) Method and biosensor for analysis. US Patent no. 7332327
128. Zayats M, Pogorelov S P, Kharitonov A B, Lioubashevski O (2003) Au nanoparticle-enhanced surface plasmon resonance sensing of biocatalytic transformations. Chem. Eur. J. 9:6108–6114
129. Hanning A, Roerade J, Delrow J J, Jorgenson R C (1999) Enhanced sensitivity of wavelength modulated surface plasmon resonance devices using dispersion from a dye solution. Sens. Actuators B 54:25–36

130. Wink T, Zuilen S J V, Bult A, van Bennekom W P (1998) Liposome-mediated enhancement of the sensitivity in immunoassays of proteins and peptides in surface plasmon resonance spectrometry. Anal. Chem. 70:827–832
131. Chen S-J, Chien F C, Lin G Y, Lee K C (2004) Enhancement of the resolution of surface plasmon resonance biosensors by control of the size and distribution of nanoparticles. Opt. Lett. 29:1390–1392
132. Liu X, Sun Y, Song D Q, Zhang Q L, Tian Y, Zhang H Q (2004) Sensitivity-enhancement of wavelength-modulation surface plasmon resonance biosensor for human complement factor 4. Anal. Biochem. 333:99–104
133. Tian Y, Chen Y H, Song D Q, Liu X, Zhang H Q (2005) Acousto-optic tunable filter-surface plasmon resonance immunosensor for fibronectin, Anal. Chim. Acta 551:98–104
134. Gobi K V, Sasaki M, Shoyama Y, Miura N (2003) Highly sensitive detection of polycyclic aromatic hydrocarbons (PAHs) and association constants of the interaction between PAHs and antibodies using surface plasmon resonance immunosensor. Sens. Actuators B 89:137–143
135. Aldinger U, Pfeifer P, Schwotzer G, Steinrucke P (1998) A comparative study of spectral and angle-dependent SPR devices in biological applications. Sens. Actuators B 51:298–304
136. Besselink G A J, Kooyman R P H, van Os, P J H J, Engbers G H M, Schasfoort, R B M (2004) Signal amplification on planar and gel-type sensor surfaces in surface plasmon resonance-based detection of prostate-specific antigen. Anal. Biochem. 333:165–173
137. Choi J-W, Kang D-Y, Jang Y-H, Kim H-H, Min J, Oh B-K (2008) Ultra-sensitive surface plasmon resonance based immunosensor for prostate-specific antigen using gold nanoparticle-antibody complex. Colloids Surf. B 313–314:655–659
138. Mangeney C et al. (2002) Synthesis and properties of water-soluble gold colloids covalently derivatized with neutral polymer monolayers. J. Am. Chem. Soc. 124:5811–5821
139. Albers W M, Munter T, Laaksonen P, Vikholm-Lundin I (2010) Improved functionality of antibody-colloidal gold conjugates with the aid of lipoamide-grafted N-[tris(hydroxymethyl) methyl]acrylamide polymers. J. Colloid Interface Sci. 348(1):1–8
140. Fouqu'e B, Schaack B, Obëd P, Combe S, Gétin S, Barritault P, Chaton P, Chatelein F (2005) Multiple wavelength fluorescence enhancement on glass substrates for biochip and cell analyses. Biosens. Bioelectron. 20:2335–2340
141. Liu J, Cao Z, Lu Y (2009) Functional nucleic acid sensors. Chem. Rev. 109:1948–1998
142. Lucarelli F, Tombelli S, Minunni M, Marrazza G, Mascini M (2008) Electrochemical and piezoelectric DNA biosensors for hybridisation detection. Anal. Chim. Acta 609:139–159
143. Ananthanawat C, Vilaivan T, Mekboonsonglarp W, Hoven V P (2009) Thio-lated pyrrolidinyl peptide nucleic acids for the detection of DNA hybridization using surface plasmon resonance. Biosens. Bioelectron. 24:3544–3549
144. Liu Y, Wilson W D (2010) Quantitative analysis of small molecule-nucleic acid interactions with a biosensor surface and surface plasmon resonance detection. Methods Mol. Biol. 613:1–23
145. Torres-Chavolla E, Alocilja E C (2009) Aptasensors for detection of microbial and viral pathogens. Biosens. Bioelectron. 24:3175–3182
146. Kohlhammer H et al. (2004) Genomic DNA-chip hybridisation in t(11;14)-positive mantle cell lymphomas shows a high frequency of aberrations and allows a refined characterization of consensus regions. Blood 104:795–801
147. Deng J Y, Zhang X E, Mang Y, Zhang Z P, Zhou Y F, Liu Q, Lu H B, Fu Z J (2004) Oligonucleotide ligation assay-based DNA chip for multiplex detection of single nucleotide polymorphism. Biosens. Bioelectron. 19:1277–1283
148. Mannelli I, Lecerf L, Guerrouache M, Goossens M, Millot M-C, Canva M (2007) DNA immobilisation procedures for surface plasmon resonance imaging (SPRI) based microarray systems. Biosens. Bioelectron. 22:803–809
149. Mannelli I, Courtois V, Lecaruyer P, Roger G, Millot M C, Goossens M, Canva M (2006) Surface plasmon resonance imaging (SPRI) system and real-time monitoring of DNA

biochip for human genetic mutation diagnosis of DNA amplified samples. Sens. Actuators B 119 583–591
150. Bianchi N, Rutigliano C, Tomassetti M, Feriotto G, Zorzato F, Gambari R (1997) Biosensor technology and surface plasmon resonance for real-time detection of HIV-1 genomic sequences amplified by polymerase chain reaction. Clin. Diagn. Virol. 8:199–208
151. Feriotto G, Borgatti M, Mischiati C, Bianchi N, Gambari R (2002) Biosensor technology and surface plasmon resonance for real-time detection of genetically modified roundup ready soybean gene sequences. J. Agric. Food Chem. 50:955–962
152. Silin V, Plant A (1997) Biotechnological applications of surface plasmon resonance. Tibtech 15:353–359
153. Nikiforov T T, Rogers Y H (1995) The use of 96-well polystyrene plate for DNA hybridization-based assays: an evaluation of different approaches to oligonucleotide immobilization. Anal. Biochem. 227:201–209
154. Rehman F N, Audeh M, Abrama E S, Hammond P W, Kenney M, Boles T C (1999) Immobilisation of acrylamide-modified oligonucleotides by co-polymerisation. Nucleic Acids Res. 27:649–655
155. Nimyer C M, Boldt L, Ceyhan B, Blohm D (1999) DNA-directed immobilization: efficient, reversible, and site-selective surface binding or proteins by means of covalent DNA streptavidin conjugates. Anal. Biochem. 268:54–63
156. Herne T, Tarlov M (1997) Characterization of DNA probes immobilized on gold surfaces. J. Am. Chem. Soc. 119:8916–8920
157. Kim J H, Hong J, Yoon M, Yoon M Y, Juong H-S, Hwang H (2002) Solid-phase genetic engineering with DNA immobilized on a gold surface. J. Biotechnol. 96:213–221
158. Rogers Y H., Jiang-Baucom P, Huang Z J, Bogdanov V, Anderson S, Boyce-Jacino M (1999) Immobilization of oligonucleotides onto glass support via disulfide bonds: a method for preparation of DNA microarrays. Anal. Biochem. 266:23–30
159. Peterson A, Wolf L, Georgiadis R (2002) Hybridization of mismatched or partially matched DNA at surfaces. J. Am. Chem. Soc. 124:14601–14607
160. Lucarelli F, Marrazza G, Turner A P F, Mascini M (2004) Carbon and gold electrodes as electrochemical transducers for DNA hybridisation sensors. Biosens. Bioelectron. 19:515–530
161. Dugas V, Depret G, Chevalier Y, Nesme X, Souteyrand E (2004) Immobilization of single-stranded DNA fragments to solid surfaces and their repeatable specific hybridization: covalent binding or adsorption? Sens. Actuators B 101:112–121
162. Cloarec J-P, Chevolot Y, Laurenceau E, Phaner-Goutorbe M, Souteyrand E (2008) A multidisciplinary approach for molecular diagnostics based on biosensors and microarrays. ITBM-RBM 29:105–127
163. Sandström P, Boncheva M, Åkerman B (2003) Nonspecific and thiol-specific binding of DNA to Gold nanoparticles. Langmuir 19:7537–7543
164. Steel A B, Levicky R L, Herne T M, Tarlov M J (2000) Immobilization of nucleic acids at solid surfaces: effect of oligonucleotide length on layer assembly. Biophys. J. 79:975–981
165. Steel A, Herne T, Tarlov M (1999) Electrostatic interactions of redox cations with surface-immobilized and solution DNA. Bioconjug. Chem. 10:419–423
166. Vikholm-Lundin I, Piskonen R, Albers W M (2007) Hybridisation of surface-immobilised single-stranded oligonucleotides and polymer monitored by surface plasmon resonance. Biosens. Bioelectron. 22:1323–1329
167. Vikholm-Lundin I, Piskonen R (2008) Binary monolayers of single-stranded oligonucleotides and blocking agent for hybridization. Sens. Actuators B 134:189–192
168. Vikholm-Lundin I, Auer S, Munter T, Fiegl H, Apostolidou S (2009) Hybridization of binary monolayers of single stranded oligonucleotides and short blocking molecules. Surf. Sci. 603:620–624
169. Morris V J, Kirby A R, Gunning A P (2004) Atomic Force Microscopy for Biologists. Imperial College Press, London

170. Eaton P, West P (2010) Atomic Force Microscopy. Oxford University Press, Oxford
171. Watson G S, Watson J (Eds Quantitative Measurements of Nano Forces Using Atomic Force Microscopy (AFM) – Quantifying Nano Forces in Three-Dimensions Using AFM: Applications in the Biological, Physical and Chemical Sciences. VDM Verlag, Saarbrücken
172. Braga P C, Ricci D (2003) Atomic Force Microscopy: Biomedical Methods and Applications (Methods in Molecular Biology, Vol 242). Humana Press, Totowa NY, USA
173. Morris V J, Kirby A R, Gunning A P (2010) Atomic Force Microscopy for Biologists. Imperial College Press, London
174. Zhang Y, Sheng S J, Shao Z (1996) Imaging biological structures with the cryo atomic force microscope. Biophys. J. 71:2168–2176
175. Hafner J H, Cheung C L, Woolley A T, Lieber C M (2001) Structural and functional imaging with carbon nanotube AFM probes. Prog. Biophys. Mol. Biol. 77:73–110
176. Hafner J H, Cheung C L, Lieber C M (1999) Growth of nanotubes for probe microscopy tips. Nature (London) 398:761–762
177. Cheung C L, Hafner J H, Lieber C M (2000) Carbon nanotube atomic force microscopy tips: direct growth by chemical vapour deposition and application to high-resolution imaging. Proc. Natl. Acad. Sci. U.S.A. 97:3809–3813
178. San Paulo A, Garcia R (2000) High-resolution imaging of antibodies by tapping-mode atomic force microscopy: attractive and repulsive tip-sample interaction regimes. Biophys. J. 78:1599–1605
179. San Paulo A, Garcia R (2000) High-resolution imaging of antibodies by tapping-mode atomic force microscopy: attractive and repulsive tip-sample interaction regimes. Biophys. J. 78:1599–1605
180. Thomson N H (2005) The substructure of immunoglobulin G resolved to 25 kDa using amplitude modulation AFM in air. Ultramicroscopy 105:103–110
181. Zitzler L, Herminghaus S, Mugele F (2002) Capillary forces in tapping mode atomic force microscopy. Phys. Rev. B 66:155436–155443
182. Thomson N H (2005) Imaging the substructure of antibodies with tapping mode AFM in air: the importance of a water layer on mica. J Microsc. 217:193–199
183. Lallemand D, Rouillat M H, Dugas V, Chevolot Y, Souteyrand E, Phaner-Goutorbe M (2007) AFM characterization of ss-DNA probes immobilization: a sequence effect on surface organization. J. Phys. Conf. Ser. 61:658–662
184. Ando T, Uchihashi T, Fukuma T (2008) High-speed atomic force microscopy for nanovisualisation of dynamic biomolecular processes. Prog. Surf. Sci. 83:337–437
185. Tappura K, Vikholm-Lundin I, Albers W M (2007) Lipoate-based imprinted self-assembled molecular thin films for biosensor applications. Biosens. Bioelectron. 22:912–919
186. Hoa X D, Kirk A G, Tabrizian (2007) Towards integrated and sensitive surface plasmon resonance biosensors: a review of the recent progress. Biosens. Bioelectron. 23:151–160
187. Weber J, Albers W M, Tuppurainen J, Link M, Gabl R, Wersing W, Schreiter M (2006) Shear mode FBARs as highly sensitive liquid biosensors. Sens. Actuators A 128:84–88

Chapter 5
Nanotechnology to Improve Electrochemical Bio-sensing

Sandro Carrara

5.1 Introduction

In his famous lecture on nanotechnology held at California Institute of Technology in 1959, Richard Phillip Feynman said that "Biology is not simply writing information; it is doing something about it. A biological system can be exceedingly small. Many of the cells are very tiny, but they are very active." Accordingly, nanotechnology seems to have a special relationship with biology. Modern nanotechnology applied to biology may recover a such special link. Nanotechnology plays out at the same scale as biological molecules and, thus, it provides new opportunities to operate on biological systems. This means we can improve the characteristics of materials by involving biological molecules with control at the nanoscale. Thinking about fully electronic sensing on biological systems, this opens up the new branch of electrochemical nano-biosensing.

In this chapter, different structures and systems at the nanometer scale will be considered as building blocks for improving electrochemical biosensing. The chapter initially presents the basics of electrochemistry. This is required to provide information about enzyme–substrate electrochemical interactions, which are highly useful for specificity in molecular sensing.

Then, we will introduce the role of nanotechnology in providing useful building blocks. The physics of these blocks will be discussed in detail. All possible nanostructures will be theoretically defined and their quantum physics will be discussed. In particular, nanosystems with different dimensionalities will be considered and the experimental investigations required to outline their physical properties will be summarized.

S. Carrara (✉)
Fac. Informatique et Communications, Labo. Systèmes Intégrés (LSI)
EPFL 1015, Lausanne, Switzerland
e-mail: sandro.carrara@epfl.ch

S. Carrara (ed.), *Nano-Bio-Sensing*,
DOI 10.1007/978-1-4419-6169-3_5, © Springer Science+Business Media, LLC 2011

For each proposed nanostructure, we will describe applications to electrochemical sensing and we will review the main results published recently. We will evaluate the main advantages provided by these nanoscale building blocks, taking into consideration the behavior of the bulk materials. The low dimensionality of nanosystems will be related to the enhanced performances in detection. Successful examples of increased sensitivity and decreased detection limits will be presented as case studies.

5.2 The Electrochemistry of Biosensing

Electrochemical detection is an important branch in biosensing because it enables sensing of different biomarkers with an important role for many applications in biomedical diagnostics or in monitoring of biological systems. Glucometers, which are already present on the market, are mainly based on electrochemical detection and they are so important for diabetic patients in automated monitoring with point-of-care devices as well as in continuous monitoring with implantable systems [1]. They are based on glucose oxidase, which transforms glucose into gluconic acid and hydrogen peroxide (H_2O_2). The hydrogen peroxide is oxidized and monitored by means of a current measurement because electrons are directly transferred from the peroxide to the sensor electrode. Similarly, other oxidases are usually used to detect lactate, glutamate, cholesterol, and other metabolic molecules, which are so relevant as disease biomarkers or as metabolites for monitoring cell systems [2]. Cholesterol is also detected by using the cytochromes P450 [3]. The P450 cytochromes are enzymes of a protein family with more then 3,000 different isoforms. They catalyze many different endogenous and exogenous compounds, which are highly relevant for the human metabolism. For example, isoform 11A1 (also called P450scc) catalyzes cholesterol, whereas isoforms 4A11 and 3A4 from the same family catalyze metabolites such as arachidonic acid and testosterone, respectively. The P450 proteins are also important since they are also used to develop label-free drug screening tools [4]. In the case of electrochemical detection based on P450 enzymes, the electrons are directly transferred from the electrode to the cytochrome. The 11A1 isoform needs to receive two electrons to transform cholesterol into pregnenolone and the 2B4 isoform needs two electrons to transform benzphetamine (a very well known amphetamine) into its oxidized form.

In all the above-mentioned cases, a redox reaction occurs at the interface of the sensor surface. However, the case of oxidases is slightly different from that of the cytochromes. In the case of P450 proteins, the electrons are directly transferred from the electrodes to the enzyme, whereas they are directly released by the hydrogen peroxide hydrolysis in the case of oxidases. The following chemical reactions show the details of these kinds of redox reactions.

In the case of detection based on oxidases the first reaction is

$$\mathrm{XOD} + \mathrm{substrate} + \mathrm{O_2} \rightarrow \mathrm{XOD} + \mathrm{product} + \mathrm{H_2O_2}, \tag{5.1}$$

where XOD is glucose oxidase, lactate oxidase, glutamate oxidase, cholesterol oxidase, etc. The substrate would be then glucose, lactate, glutamate, cholesterol, etc.; the product would be gluconic acid, pyruvate, oxoglutarate, cholestenone, etc. The common thing in all the cases is that the reaction also produces hydrogen peroxide. This molecule is hydrolyzed directly once it comes into contact with the polarized electrode of the sensor. The hydrogen peroxide hydrolysis follows the reaction

$$2H_2O_2 \rightarrow 2H_2O + O_2 + 4e^-. \tag{5.2}$$

This shows that four electrons for each two hydrogen peroxide molecules are released to the sensor electrode. Equations (5.1) and (5.2) show that we have two substrate molecules for each set of four electrons measured by the sensor electrode. A current measurement at the sensor electrode enables the stoichiometric measurement of the substrate related to the oxidase used for functionalizing the sensor electrode. So, the enzyme we choose for functionalizing the sensor electrode determines the substrate the sensor should sense, whereas the current we measure is directly related to the amount of that compound.

Similarly, in the case of cytochromes, the redox reaction is

$$\text{P450} + \text{substrate} + O_2 + 2H^+ + 2e^- \rightarrow \text{P450} + \text{product} + H_2O. \tag{5.3}$$

This shows that two electrons are required from the sensor electrode to enable the reaction to progress to the product. Of course, the redox reactions in (5.1)–(5.3) are shifted toward the right or left sides depending on the potential at the sensor electrode. This potential is the potential of the electrochemical interface. If the rate of the electron transfer is enough fast, then the ratio of the concentrations of the substrates and products at the electrode surface is assumed to be in equilibrium at a certain given electrode potential. This equilibrium is governed by the Nernst equation [5]:

$$E = E^0 + \frac{RT}{nF} \ln\left(\frac{C_S}{C_P}\right), \tag{5.4}$$

where E^0 is the standard potential related to the redox species and the electrode material considered, R is the gas constant, T is the temperature, F is the Faraday constant, C_s and C_p are the concentrations of the substrate and product, respectively, and n is the number of electrons involved in the reaction (four in (5.1) and two in (5.3)). The number of electrons collected by (or from) the sensor electrode is directly proportional to the amount of substrate, because each substrate molecule produces (or requires) four (or two) electrons by (5.1) (or (5.3)). If there are no reaction products at the starting time, then the semiempirical steady-state model enables us to write an equation for the current obtained by counting the electrons involved in the redox reaction [5]:

$$E = E_{1/2} + \frac{RT}{nF} \ln\left(\frac{i_L - i}{i}\right), \tag{5.5}$$

where $E_{1/2}$ is determined by the diffusion coefficients of the substrate and the product and by the thickness of the Nernst diffusion layer, and the limiting current i_L is also due to the substrate concentration,

$$i_L = nFA\frac{D_S}{\delta_S}C_S, \tag{5.6}$$

where A is the surface area of the sensor electrode, D_S is the diffusion coefficient of the substrate molecules, and δ_S is the thickness of the Nernst layer. It is easy to see from (5.5) that the current profile for potential E will be similar to that shown in Fig. 5.1a. Initially, there is no current, and the reaction proceeds and electrons are collected (or released) by the sensor electrode for increasing potential values. At a certain potential value, which depends on the diffusion properties of the substrate molecules, the current suddenly increases until a final value given by (5.6). The maximum current reached is proportional to the concentration of the substrate, as shown by (5.6). Thus, a current measurement at a high enough interface potential allows a precise estimation of the substrate concentration and, therefore, the electrochemical sensing of the biological molecules. Equations (5.1) and (5.3) provide a direct stoichiometric relationship between the substrate concentration and the number of electrons involved in the redox reaction. Therefore, (5.6) leads to the linear relationship shown in Fig. 5.1b.

5.3 From Electrochemistry to Nanotechnology

By using (5.6), we can define the detection sensitivity as the amount of current we can measure for each increment in the substrate concentration. Thus, the sensitivity of the electrochemical sensor is the slope of the linear graph shown in Fig. 5.1b.

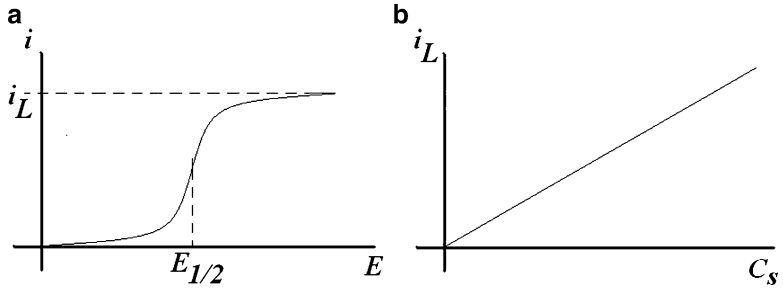

Fig. 5.1 Typical current profiles of redox reactions in Nernst conditions when the electron transfer is so fast that the redox species are at equilibrium for each potential E. (**a**) Current versus the interface potential, and (**b**) maximum current versus the substrate molecular concentration

The sensitivity of the sensor is, then, defined as the current increment divided by the concentration change per unit of electrode area:

$$S = \frac{\Delta i}{A\Delta C}, \tag{5.7}$$

which is usually measured in microampere per millimole per square millimeter. By taking into account of (5.6), we obtain

$$S = nF\frac{D_S}{\delta_S}. \tag{5.8}$$

However, (5.8) shows that we may have two different sensitivities in the case of two kinds of substrates with different diffusion coefficients and layer thicknesses (D_S and δ_S). Moreover, if more than one molecular species is involved in the redox reaction, then the measured current also depends on the rate of electron transfer between the molecules. The rate of electron transfer between two molecules is calculated with the equation [6]

$$k_{ET} = \frac{2\pi}{\hbar}V_R^2 FC, \tag{5.9}$$

where V_R^2 is the electronic coupling of the molecules and FC is the Franck–Condon weighted density of states. In other words, V_R^2 is the quantum-mechanical matrix element coupling the electronic wave functions of two molecules which exchange electrons, and FC is the integrated overlap of the nuclear wave functions of equal energy of the molecules. Both in oxidases and in cytochromes, the electron transfer efficiency and the diffusion of the redox species onto the electrode surface may be enhanced by using nanostructures. It has already been demonstrated by using carbon nanotubes that the sensitivity is improved by two orders of magnitude in hydrogen peroxide detection [7]. It is enhanced by one order of magnitude in cholesterol detection by using gold nanoparticles [8] or carbon nanotubes [9].

Gold nanoparticles and carbon nanotubes are nanostructures with quite interesting physical properties. Gold nanoparticles are produced by the aggregation of atoms in solution by using gold salts [10]. Particles with different core sizes are obtained by using different salt-to-thiol concentrations [11]. Thiols are used to stabilize the particles, once they have formed. Particle size, typically on the scale of a few nanometers, is the key parameter to achieve single-electron trapping inside the particle at room temperature [12]. The particle behaves as a quantum dot, which is a zero-dimensional quantum system. On the other hand, carbon nanotubes are fabricated by arc discharge [13] or in a controlled manner by using chemical vapor deposition [14]. It is possible to obtain single-walled or multiwalled nanotubes. The lateral sizes range from 2 nm, in the case of single-walled nanotubes, up to 70 nm, in

the case of multiwalled nanotubes. Multiwalled carbon nanotubes have both metallic and semimetallic walls. In the case of metallic walls, electrons flow in ballistic mode through the tube. In both cases, the electrons have mean free paths up to the micrometer range at room temperature, which is two orders of magnitude higher than that registered in the case of the best macroscopic conductor [15]. This means that a carbon nanotube behaves as an almost perfect one-dimensional quantum system.

Although the amazing physical properties of both gold nanoparticles and carbon nanotubes have been used to enhance the performances of electrochemical sensors, a clear theoretical framework enabling a deep understand of the physics of such enhancement is still missing [16]. Moreover, the above-mentioned improvement due to nanotechnology in biosensing seems to be a general phenomenon found in nanoscale materials. It has been shown that the detection limit decreases and the sensitivity improves whenever a sensor is developed by using nanoscale materials [17]. The detection limit is usually defined as the minimum quantity of substrate detectable by the sensor. By following the general definition of the limit of detection [18], and considering (5.7), we can write the detection limit as

$$|C_S|_{min} = \frac{i_0 + 3\sigma_0}{AS}, \tag{5.10}$$

where i_0 is the measured current for the blank (absence of substrate), σ_0 is the standard deviation of measurements on the blank, and A and S are the sensor area and its sensitivity, respectively. Equation (5.10) demonstrates that the detection limit decreases with the increase in sensitivity. An inverse relationship between the improvements in terms of sensitivity and detection limit has been shown taking into account different nanostructured materials in sensing of hydrogen peroxide, lactate, glucose, and cholesterol [17]. The typical registered curve was similar to that shown in Fig. 5.2 and is consistent with (5.10).

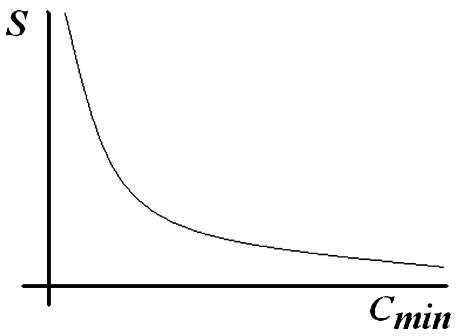

Fig. 5.2 The enhancement of sensitivity and detection limit follows an inverse curve when different nanosized materials are used to improve the biosensing performances

5.4 Zero-Dimensional Quantum Systems

5.4.1 The Physics of Quantum Dots

A zero-dimensional system is a box with negligible size. In quantum physics, it is thought of as a space region in which elementary particles are trapped inside. It is called a *quantum dot*. In a quantum dot, the wavelengths of the trapped particles, say, electrons, are on the same scale as the box size. The electron momentum is [19]

$$\vec{p} = \hbar\vec{k}. \tag{5.11}$$

From that, we can derive the wavelength as

$$\lambda = \frac{h}{p} = \frac{h}{m_0 v} = \frac{h}{\sqrt{2m_0 eU}}, \tag{5.12}$$

in case of electrons with rest mass m_0, charge e, and pushed by an electric field with potential U. In the case of a potential of 1 V, the electron wavelength is 1.2 nm. It is exactly on the nanoscale!

If electrons are trapped within the box, then they are only in steady states with quantized energy. To see that in a simple manner, we can consider the Schrödinger equation in the case of a single dimension x:

$$\mathrm{i}\hbar \frac{\mathrm{d}\psi(x,t)}{\mathrm{d}t} = -\frac{\hbar^2}{2m_0} \frac{\mathrm{d}^2\psi(x,t)}{\mathrm{d}x^2}. \tag{5.13}$$

In this simplified form, (5.13) is valid if the potential energy of the electrons is zero in all the positions x. Equation (5.13) is the typical differential equation of a

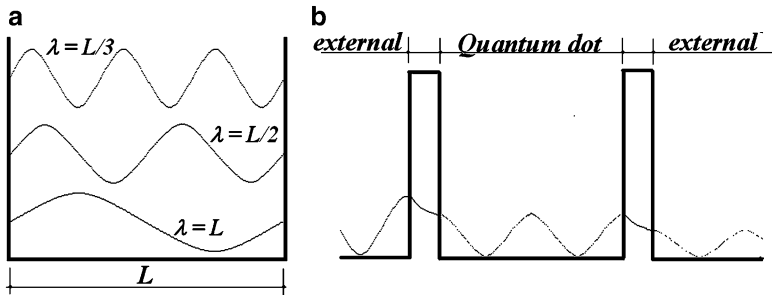

Fig. 5.3 (**a**) A theoretical quantum dot in a single dimension; (**b**) a two-barrier system in a single dimension

waveform in x for any value of time t. Therefore, the general solution of (5.13) is any function with the form

$$\psi(x,t) = A(t)\sin\left(\frac{2\pi}{\lambda}x\right) + B(t)\cos\left(\frac{2\pi}{\lambda}x\right). \tag{5.14}$$

The time-dependent coefficients $A(t)$ and $B(t)$ are calculated by considering the boundary conditions. If we search for a solution for a quantum dot, then the boundary conditions lead to steady states with zero values of $\psi(x,t)$ at the beginning and at the end of the dot, as shown in Fig. 5.3a. Then, we can calculate the energy of such states as

$$E_n = \hbar\omega_n = h\upsilon_n = \frac{hc}{\lambda_n} = n\frac{hc}{L},\ n \in \aleph. \tag{5.15}$$

Equation (5.15) and the graph in Fig. 5.3b clearly show that an electron, whose motion is governed by the Schrödinger equation in (5.13), may only be in quantized steady states when it is trapped in a one-dimensional quantum dot of size equal to L.

Equation (5.15) also shows that energy quantization of the trapped electrons only depends on the quantum dot size L, whereas (5.12) demonstrates that such a dot traps electrons within a conductive region with size of a few nanometers. Of course, a quantum dot such as that shown in Fig. 5.3a does not have any electron exchange with the external world. Thus, we need to have finite-sized barriers to trap quantized electrons in a nanometer region, as shown in Fig. 5.3b. In that case, solutions of (5.13) are still valid in the external and internal regions of the dot, whereas the Schrödinger equation is different within the two tunneling barriers:

$$\mathrm{i}\hbar\frac{\mathrm{d}\psi(x,t)}{\mathrm{d}t} = -\frac{\hbar^2}{2m_0}\frac{\mathrm{d}^2\psi(x,t)}{\mathrm{d}x^2} + (V-\varphi)\psi(x,t). \tag{5.16}$$

In (5.16), V is the external potential applied across the barriers and ϕ is the barrier height. Equation (5.16) admits solutions in the form

$$\psi(x,t) = A(t)\mathrm{e}^{\sqrt{(2m_0(V-\varphi))/\hbar^2}D} + B(t)\mathrm{e}^{-\sqrt{(2m_0(V-\varphi))/\hbar^2}D}, \tag{5.17}$$

where D is the width of the tunneling barrier. Thus, complete solutions of the Schrödinger equations shown in (5.13) and (5.16) for all the regions with a double tunneling barrier are combinations of free waves from solutions of (5.14) and exponential curves from (5.17). The boundary conditions at each interface lead to a continuous wave function $\psi(x,t)$ with shape similar to that schematically shown in Fig. 5.3b. For a certain value of the external potential V, the electron

energy will fit the values in (5.15) and the electrons will remain trapped in the dot, whereas for other values of V the electrons will simple cross the two barriers. Thus, in a quantum dot electrons can overcome the tunneling barriers and enter steady states that correspond to quantized energy levels as described by (5.15) if they are provided with enough energy.

5.4.2 *Quantum Dots as Electrochemical Enhancers*

We have seen that (5.11) provides us with an electron wavelength on the nanoscale, whereas (5.17) tells us that two-barrier systems consist of electrons of enough energy. That means modern nanotechnology may furnish us with quantum dots by providing very small conductive cores surrounded by insulating thin barriers. Such systems are produced with very simple chemical or physical procedures. The easiest way to obtain quantum dots is to grow them by atom aggregation in liquid conditions starting with metallic salts. Stabilizers in the form of organic matrices are then required to avoid degradation or fusion of the cores. Molecules with alkyl chains are usually used to create an organic shell surrounding the metallic core. The alkyl molecules are typically alkanethiols and they provide a stable coating to protect the core. After aggregation of atoms, the result is a solution of monodispersed metallic nanoparticles. Quantum dots with a metallic core made with gold [20], silver [21], rhodium [22], platinum, and ruthenium [23] were fabricated by using this method. Quantum dots are obtained with diameters ranging from 1.5 to 5.2 nm by adjusting the salt-to-thiol ratio [24]; the method is known as the "Brust method" [25].

Another easy way to obtain quantum dots is to grow them by atom aggregation in quasi-liquid conditions. In that case, a Langmuir–Blodgett film is required. An ordered Langmuir monolayer is obtained by compressing amphiphilic molecules at the air/water interface. Then, the layer is transferred onto a solid substrate by vertical dipping (Langmuir–Blodgett technique) or horizontal dipping (Langmuir–Schaeffer technique). Repetition of the transfer step results in a multilayer being formed on a solid substrate. Arachidic acid is used to obtain the semiliquid matrix to grow quantum dots with semiconducting materials. Then, an atmosphere of hydrogen sulfide is used to aggregate the atoms into the arachidic acid matrix. Quantum dots of CdS [26], PbS [27], or CuS [28] are obtained with this method depending on the kind of arachidic acid used to form the matrix.

All these kinds of nanofabricated quantum dots may be used to enhance charge storage, current transport, and electron transfer in biosensing. Figure 5.4 schematically shows that gold nanoparticles stabilized by alkanethiols are used as electrons mediators to enhance electron transfer between protein probes and electrodes during enzyme-based electrochemical detection. A gain in terms of sensitivity up to 6.5 μA/mM mm^2 in cholesterol detection has been shown by using cytochromes P450 and gold nanoparticles with a radius of 12 nm [29]. The sensitivity registered with a similar system but without gold nanoparticles was only 0.069 μA/mM mm^2 [3].

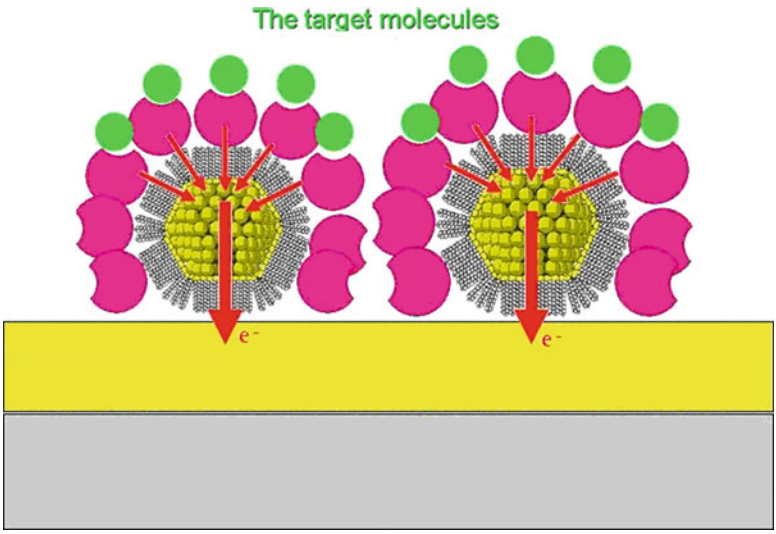

Fig. 5.4 The role of thiol-capped gold nanoparticles in electron transfer between cytochromes and an electrode

Similar improvements in sensitivity were obtained in biosensors based on oxidases: 16.5 μA/mM m^2 for glucose [30], 500 μA/mM mm^2 for lactate [31], and 70.4 μA/mM mm^2 for phenol [32].

5.5 One-Dimensional Quantum Systems

5.5.1 The Physics of Quantum Wires

A one-dimensional system is a string with negligible diameter. In quantum physics, it is thought of as a space region where quantum particles may freely move along the string but cannot leave the string. Quantum effects arise owing to the lateral confinement, and, then, the string is called a *quantum wire*.

Equation (5.15) says that energy levels are quantized considering the wave vector in the lateral dimensions of the wire, whereas (5.13) says that the particles are governed by free states in the longitudinal dimension of the wire. Figure 5.5 shows the situation considering the dimension y as being along the wire and the dimension x as being transverse to the wire as a sketch of the Schrödinger waveforms corresponding to the lower wavelengths.

Using Fig. 5.5 and (5.13) and (5.14), we can write the wave function of the electrons inside a quantum wire in the form

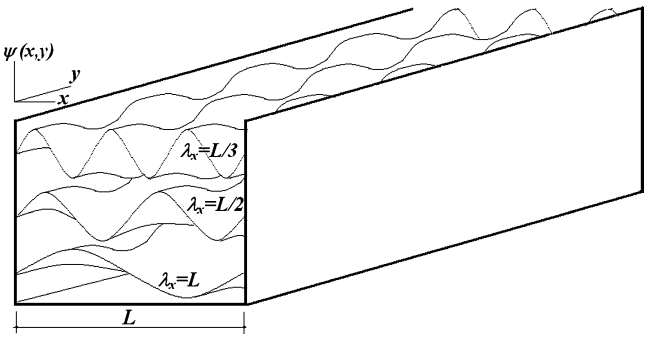

Fig. 5.5 A theoretical quantum wire has Schrödinger waves that are quantized steady states along x and free states along y

$$\psi(x,y,z,t) = A(t)\sin\left(\frac{2\pi}{\lambda_n}x + \frac{2\pi}{\lambda_m}z + \frac{2\pi}{\lambda_y}y\right) + B(t)\cos\left(\frac{2\pi}{\lambda_n}x + \frac{2\pi}{\lambda_m}z + \frac{2\pi}{\lambda_y}y\right), \tag{5.18}$$

where λ_n and λ_m are quantized wavelengths following (5.15), while λ_y assumes any real number corresponding to free states along the longitudinal dimension of the wire.

Of course, (5.12) tells us that a quantum wire is a system with two dimensions on the nanoscale. Modern nanotechnology provides us with quantum wires both in silicon [33] and in carbon [34]. Both silicon nanowires and carbon nanotubes are good examples of systems where the majority of carriers are confined in a one-dimensional space region. Carbon nanotubes are allotropes of carbon organized in cylindrical shapes with a single wall or multiple walls. Their typical lengths are on the microscale, whereas their diameters are on the nanoscale. Their lengths are usually below 5 μm, whereas their diameters are usually close to 2 nm for single-walled tubes and in the range between 10 and 100 nm for multiwalled tubes. Consequently, the huge form factor of carbon nanotubes makes them suitable for confinement of carriers in almost-one-dimensional-shaped space regions. The confinement of the carriers in a one-dimensional space region results in amazing properties of carrier transport along the tube. Among these properties, the electron field emission at the tip of individual carbon nanotubes has been intensively investigated by using density functional or Green's function theories [35, 36] or by direct solution of the Schrödinger equation by accounting for properties of symmetry in the tubes [37, 38]. On the other hand, experimental works have been performed to investigate the sidewall field emission properties of carbon nanotubes (Fig. 5.6), for which the current obeys the Fowler–Nordheim equation [39, 40]:

$$I = K_1 \sigma E_\perp^2 \exp\left(-\frac{K_2}{E_\perp}\right), \tag{5.19}$$

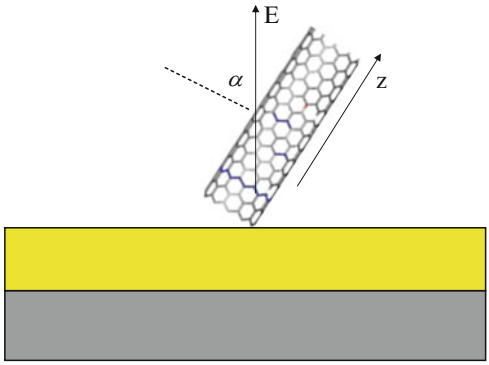

Fig. 5.6 A quantum wire made with a carbon nanotube in an electric field for the electron emission from the sidewall surface

where σ is the flat projection of the sidewall nanotube area, $E_\perp = E \sin\alpha$ is the projection of E on the normal to the sidewall area, and K_1 and K_2 are suitable constants.

For a carbon nanotube with radius ρ and length L, the total current emitted from the sidewall surface is obtained by integrating on the portion of the surface facing the anode [41]:

$$\begin{aligned} i_S(E) &= K_1 \rho E^2 \int_0^L \mathrm{d}z \int_{-\pi/2}^{+\pi/2} (\cos\vartheta \sin\alpha)^2 \exp\left(-\frac{K_2}{E\cos\vartheta \sin\alpha}\right) \mathrm{d}\vartheta, \\ &= K_1 \rho E^2 L \int_{-\pi/2}^{+\pi/2} (\cos\vartheta \sin\alpha)^2 \exp\left(-\frac{K_2}{E\cos\vartheta \sin\alpha}\right) \mathrm{d}\vartheta, \end{aligned} \tag{5.20}$$

where ϑ is the radial angle in cylindrical coordinates spanning the transverse section of the tube.

The current from the tip also obeys (5.19), and then we can also write

$$i_T(E,\alpha) = K_1' A (E\cos\alpha)^2 \exp\left(-\frac{K_2'}{E\cos\alpha}\right). \tag{5.21}$$

The total current emitted by a carbon nanotube oriented at an angle α with respect to the emitting electric field is then [41]

$$i(E,\alpha) = i_S(E,\alpha) + i_T(E,\alpha). \tag{5.22}$$

Suitable values for the constants in (5.20) and (5.21) are $K_1 = 10^{12}$, $K_2 = 35$, $K_1' = 2.5 \times 10^{12}$, and $K_2' = 20$, obtained by comparison with experiments

performed under a vacuum [40]. In the case of a water environment, like that usually considered in nano-biosensing, the emitted current is further enhanced by the presence of water molecules close to the nanotube surface [35].

5.5.2 *Quantum Wires as Electrochemical Enhancers*

Carbon nanotubes have maximum current densities greater than 10^9 A/cm^2 [42], thermal conductivities over 3,000 W/mK [43, 44], and mean free paths for charge carriers in the range 1,000–25,000 nm [45, 46]. They are used as linear field emission sources [40] and their field emission is enhanced by the adsorption of water molecules [35]. Thus, they are suitable candidates to promote electron transfer from the electrode to enzyme probes in water buffers.

As shown in Fig. 5.7, if the active redox species are in contact with all the available surface of carbon nanotubes cast onto an electrode, then they act as electron collectors, support the current transport, and then enhance the sensitivity in biosensing. In Fig. 5.7, electron emission or the injection toward/from redox species would happen both in the sidewall and in the tip. The electric field would be typically normal to the electrode baseline. The single carbon nanotube assumes a certain angle with respect to the electric field depending on the region where it is located. Thus, (5.22) and then (5.21) and (5.20) have to be integrated for all the nanotubes deposited onto the sensor electrodes taking into account all the final deposition angles of the carbon tubes.

Figure 5.7 schematically and clearly shows that both electron extraction/injection following (5.22) and ballistic conductivity due to free states along the y-axis in (5.18) are cooperative phenomena that contribute to sensitivity enhancement in nano-biosensing. We saw in Sect.5.2 that enzymes are proteins that transform biochemical molecules (usually called enzyme *substrates*) by means of redox reactions. In such reactions, electrochemical species exchange electrons with the electrode. The related current enables the biosensing. Carbon nanotubes enhance the sensing by enhancing the electron transfer between probes and the electrode.

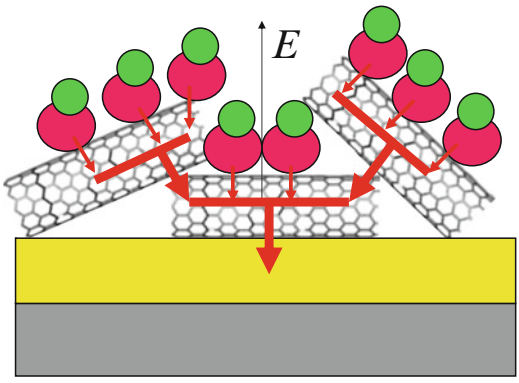

Fig. 5.7 The role of carbon nanotubes in electron transfer between cytochromes and an electrode

We can consider the case of benzphetamine, a commonly used drug, detected by the enzyme P450 2B4. The enzyme P450 2B4 transforms the reduced benzphetamine into its oxidized form by following the chemical redox reaction presented in (5.3). Equation (5.3) shows that two electrons are required to transform the reduced form of the drug (the *substrate*) into its oxidized form (the *product*). These two electrons are more easily extracted from the carbon nanotube surface than from the electrode surface. Therefore, configurations like that shown in Fig. 5.7 may be used to enhance the electron transfer in the redox reaction shown in (5.3) for benzphetamine sensing.

This is a general concept in biosensing because we have already seen that the family of P450 proteins has more than 3,000 different isoforms, which may be used for different biosensing purposes. Cytochrome P450 2B4 detects commonly used antiobesity drugs [47], whereas the 2C9 isoform detects anti-inflammatory drugs and anticoagulant drugs [48], and the 3A4 isoform detects vasodilators and sedatives [4] and anticancer agents [47]. The 11A1 isoform detects cholesterol [3], whereas the 4A11 isoform detects testosterone [49], and the 2J2 isoform detects arachidonic acid [50]. With use of this protein family, the electron-transfer improvement due to carbon nanotubes has already been proven for isoforms 11A1 [9] and 2B4 [47]. An enhanced sensitivity of 1.12 μA/mM mm^2 was registered in cholesterol sensing by using multiwalled carbon nanotubes [9], whereas only 0.069 μA/mM mm^2 was found by using electrodes with other molecular mediators [3]. Sensitivity in benzphetamine detection was enhanced up to 20.5 nA/mM mm^2 by using multiwalled carbon nanotubes, whereas only 5.1 nA/mM mm^2 was registered with bare electrodes [47].

Similarly, oxidases are also used in configurations like that shown in Fig. 5.7. They are another kind of protein family, and catalyze redox reactions involving substrates related to human metabolism. In that case, the redox reaction follows the scheme shown in (5.1) by producing hydrogen peroxide. The direct hydrolysis of hydrogen peroxide releases two electrons onto the electrode surface. In that case, electron-transfer enhancement up to two orders of magnitudes as due to carbon nanotubes was shown in hydrogen peroxide detection [7]. Glucose, lactate, glutamate, and other metabolic molecules are usually detected by choosing the appropriate oxidase for the reaction shown in (5.1) and Fig. 5.7 for improved nanobiosensing. Sensitivity in glucose detection was enhanced up to 171.2 μA/mM cm^2 [51] by using multiwalled carbon nanotubes, whereas only 15 μA/mM cm^2 was obtained by using sol–gel films [52]. Sensitivity in lactate detection was improved to 2.1 μA/mM cm^2 [53], 8.3 μA/mM cm^2 [54], and 19.7 μA/mM cm^2 [7] by using multiwalled carbon nanotubes, whereas only 0.24 μA/mM cm^2 was achieved by using titanate nanotubes [55].

The increase in terms of effective area due to nanostructured morphology of the electrodes is not the only phenomenon contributing to these sensitivity enhancements. Phenomena such as the increase of capacitive currents [56], enhancement of peaks in voltammetry [9], peak potential shifts [2], increased layering [57], and supercapacitance effects [58] take place too.

5.6 Two-Dimensional Quantum Systems

5.6.1 The Physics of Quantum Wells

A quantum well is similar to a mathematical plane. It is a system where the motion of particles is mainly allowed in two dimensions and it is almost forbidden in the third. So, the particles are free to move along directions x and y and not along z. This is quantum confinement in two dimensions. In quantum physics, we can assume that the particles are confined within a quantum region along the z direction. By following the Schrödinger equation in (5.13) and quantization of energy in (5.14), we can write a solution for the probability of the states as

$$\psi(x,y,z,t) = A(t)\sin\left(\frac{2\pi}{\lambda_x}x + \frac{2\pi}{\lambda_y}y + \frac{2\pi}{\lambda_n}z\right) + B(t) \times \cos\left(\frac{2\pi}{\lambda_x}x + \frac{2\pi}{\lambda_y}y + \frac{2\pi}{\lambda_n}z\right) \tag{5.23}$$

where only the wavelength along z assumes discrete values owing to the quantum confinement in that dimension. Once trapped, the particles can freely move only in two dimensions, x and y, by following (5.23). The trapped particles would be in steady states in the z direction and in free-motion states in the x–y plane. Nanotechnology may realize quantum wells by organizing heterostructures with sufficiently thin layers. Equation (5.12) tells us that the sizes of these thin layers have to be only a few nanometers to get quantum phenomena taking place in the heterostructure. Therefore, the simplest structure nanotechnology may provide us with for fabricating a quantum well is a heterostructure made by a very thin layer (with thickness on the scale of a few nanometers) of a narrower-gap semiconducting material between two thicker layers of wider-gap materials [59]. Modern nanotechnology can also provide us with graphene as an atomically flat two-dimensional layer [60], which acts as a quantum well.

Graphene is a one-atom-thick planar sheet of graphite. Graphite is made of many graphene sheets all stacked together to form the bulk material. When a single sheet is removed from the bulk, the single atomically flat plane of carbon atoms gives us a graphene layer. Taking into account that the carbon–carbon bond is about 0.142 nm in highly oriented pyrolytic graphite as seen with a scanning tunneling microscope [61], we can conclude that a graphene layer is a system with the z dimension smaller than 1 nm. Equations (5.15) and (5.23) tell us that quantum effects appear in such small systems. As schematically shown in Fig. 5.8, conductance measurements demonstrated the acquired ballistic conductivity due to two-dimensional gases made of electrons or holes. Figure 5.8b shows the typical shape of the plot of the acquired conductivity versus the voltage applied between the source and the gate in a field-effect transistor where the channel is made of a single graphene layer. The

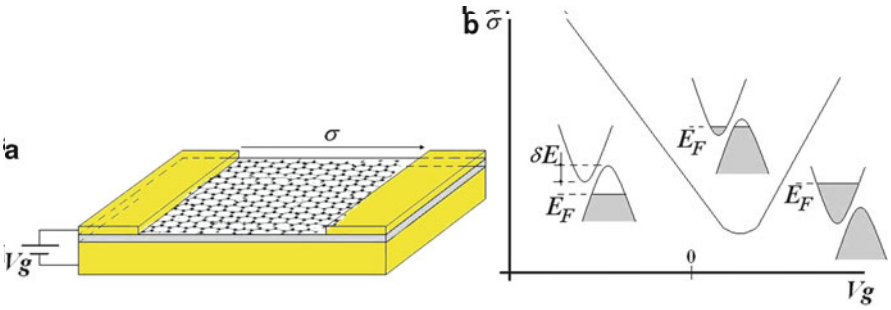

Fig. 5.8 (**a**) Conductivity measurements on a graphene layer, and (**b**) graphene conductivity versus gate voltage represented by conductance and valence bands

graph clearly shows the ambipolar nature of the conductivity. The minimum value of the conductivity is not centered at the zero value of the gate voltage, and this means that an intrinsic carrier state is present in graphene owing to both electrons and holes. In fact, annealing shifted the voltage position of such a minimum toward zero, whereas doping with water vapor or ammonia (NH_3) led to p- or n-type doping, respectively [60]. Close to this minimum, the conductivity changes slightly with the voltage owing to the mixed-carrier state. Once the conductivity becomes fully driven by electrons (right branch in Fig. 5.8b) or by holes (left branch in Fig. 5.8b), the conductivity increases in a linear manner. In the linear branches, the conductivity in the graphene sheets is related to the mobility of the carriers as

$$\sigma = ne\mu, \tag{5.24}$$

whereas in the mixed-carrier state, it is driven by the band overlap:

$$\delta E = \frac{n_0}{D} = \frac{n_0 \pi \hbar^2}{m_c}. \tag{5.25}$$

In (5.24) and (5.25), n is the number of majority carriers (electrons or holes), n_0 is the number of mixed carriers, e is the electron charge, $\hbar$ is the Planck constant, and m_c is the carrier mass, which is usually a fraction of the free electron mass. In graphene, typical values of the parameters in (5.24) and (5.25) are $\sigma = 1\ \mathrm{m}\Omega^1$, $\delta E = 4$ meV, μ in the range 3×10^3–10×10^3, with mean free paths up to 0.4 μm [60]. In some conditions, the conductivity in graphene has been pushed until charge carriers reached relativistic behavior mimicking particles with zero rest mass and effective speed close to that of light [62].

5.6.2 *Quantum Wells as Electrochemical Enhancers*

The high conductivity of graphene for electrons and holes promises practical payoffs in applications as sensors [63]. The high sensitivity of graphene to its chemical environment is well known, and then it is possible to imagine an array of graphene devices, even differently functionalized, able to react to different chemicals or biomolecules [64], like in the sketches in Fig. 5.9. Because of the ambipolar conductivity of graphene, sensing using graphene has been proposed for pH measurements by following both negatively and positively charged ions. In particular, the minimum value of the conductance in curves similar to the curve in Fig. 5.8b was found to shift toward the right side of the graphs upon increasing the pH [65]. This is possible because modulation of the channel conductance is achieved by applying a gate potential across the electrolyte from the top of the graphite layer, like in the cases of solution-gate field-effect transistors.

On the other hand, many atomically flat graphene layers may be used to improve sensitivity in enzyme-based biosensing, as schematically proposed in Fig. 5.9b. In this case, the electrons furnished in the reaction depicted in (5.2) or required in the reaction depicted in (5.3) may be collected by graphene sheets, which provide an enhanced coupling with the electrodes. Modern nanotechnology does not provide high control in fabricating nanostructures like that in Fig. 5.9a. However, graphene sheets may be drop-cast onto electrodes and then functionalized with proteins. Alternatively, they may be biofunctionalized first, and then cast onto electrodes. In both cases, nano/biostructured electrodes with behavior mimicking that suggested in Fig. 5.9b result. For example, graphene sheets dispersed in chitosan solution were cast onto glassy carbon electrodes and then functionalized with platinum nanoparticles and glucose oxidase to sense glucose down to 0.6 μM [66]. This device showed a sensitivity of 142 μA/mM cm^2 [66], which compares quite well with the value of 171.2 μA/mM cm^2 obtained by using glucose oxidase immobilized onto multiwalled carbon nanotubes [51]. In drug detection, the feasibility of paracetamol biosensing has been demonstrated by preparing graphene-modified glassy carbon electrodes in the same way [67]. Paracetamol is a widely used and well-known drug used as either a pain reliever or a fever reducer. It is an electrochemically active species and, thus, it may be detected through its direct reduction on an electrode surface. Improved sensitivity for paracetamol up to 56 μA/mM cm^2 was obtained by using graphene [67]. Similarly, dopamine was

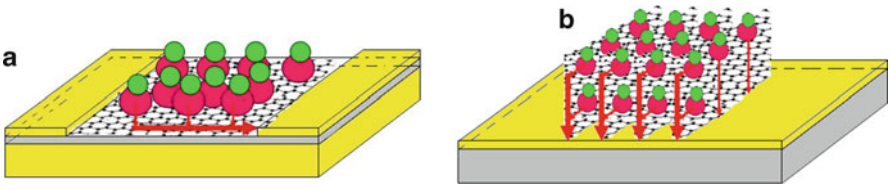

Fig. 5.9 Protein-based biosensing as improved by (**a**) a single graphene layer between two conductive electrodes and (**b**) graphene layers cast onto a conductive electrode

detected with a sensitivity of 1.03 μA/mM cm^2 [68]. Dopamine is a neurotransmitter, and is another electrochemically active biomolecule. With the use of normal glassy carbon electrodes, it is usually detected at a potential close to 200 mV (versus the Ag/AgCl reference electrode), where ascorbic acid may interfere because it is reduced at a potential close to 250 mV [69]. It was instead demonstrated that it is reduced at a potential close to 300 mV, whereas ascorbic is reduced close to 150 mV in the case of glassy carbon electrodes modified by using graphene [69]. To improve the biosensing performances of graphene layers, nanocomposites with other molecules were very recently tested. A current of 80 μA was acquired for 1 mM dopamine by using platinum nanoparticles embedded in graphene layers [69], whereas a current of 75 μA was acquired for 70 μM dopamine by preparing a mixture of graphene sheets and β-cyclodextrin, a compound made up of seven sugar ring molecules [70]. In the first case, the current peak was acquired at a potential close to 300 mV versus the Ag/AgCl reference electrode [69], whereas in the second case, it was acquired at a potential close to 170 mV versus the saturated calomel reference electrode [70]. A gain of more than one order of magnitude is obtained by using β-cyclodextrin instead of platinum nanoparticles as co-nanostructures in preparing the electrodes. This is due to an improved nanostructuring. Well-separated single sheets of graphene with uniform thickness of 1 nm were obtained in the case of β-cyclodextrin/graphene samples, whereas agglomerated multilayers of graphite with an average thickness of 4 nm were obtained with graphene sheets not treated with β-cyclodextrin [70].

So, graphene can be successfully used as a nanomaterial for sensitivity enhancement in biosensing as well as in chemical sensing. Good sensitivities greater than 100 μA/mM cm^2 were obtained for glucose detection [66] or for detection of hydrazine [71], a well-known and highly toxic pollutant. Of course, it is difficult to say if graphene will be the ultimate material in nano-biosensing. However, materials science, physics, and chemistry are crowded, highly competitive fields, and graphene will remain firmly in fashion for the next few years [63].

5.7 Conclusions

In this chapter, we have briefly summarized different nanotechnologies for building structures that have one, two, or all three physical dimensions on the nanoscale. By theory, we can refer to those structures as systems with reduced dimensionality because they offer mobility to quantum carriers only in one or two dimensions, or because they trap the carriers in a zero-dimensional space region. Modern nanotechnology offers us the possibility to develop planes that are atomically flat, wires with nanosized diameters, and small particles with radii of a few nanometers. We have seen different examples of such systems referring to single graphene sheets, to carbon nanotubes, and to metallic nanocores stabilized by alkanethiols.

These materials have altered properties and show new functionalities once they are structured at the nanoscale. Band overlap in bulk graphite is close to 40 meV,

whereas in graphene it is close to 4 meV [60]. The mean free path is larger by orders of magnitudes in carbon nanotubes with respect to bulk conductors [45, 46]. The effect of single-electron conductivity appears in metals or in semiconductors only when they are structured in nanoparticles [12, 28]. The reason for such large differences between bulk and nanostructured materials is the nanometric size of the components. The quantum nature of the electrical carriers arises at that nanoscale. The phenomenon of charge confinement appears when the Schrödinger wavelengths associated with charge carriers become of the same order of magnitude as the sizes of the systems. This confinement leads to improved properties when nanomaterials are applied to biosensing.

Nanotechnology provides new materials that help in fitting detection ranges of biomarkers in patients' serum, plasma, blood, or interstitial tissues. An example of that is the case of verapamil. Verapamil is a commonly used antihypertensive compound. Its concentration in patients' blood is in the pharmacological range below 55 nM [72]. P450-based biosensors realized with conventional methods detect verapamil in the range 0.5–3 mM [4], which is four orders of magnitude larger than that required for applications in patient's serum. P450-based biosensors realized by using carbon nanotubes recently succeeded in detecting commonly used drugs in patients' serum [73].

Nanotechnology may contribute significantly to the development of new electrochemical biosensing devices for direct, online, and continuous monitoring of patients in personalized therapy.

References

1. Klonoff, D.C.: Continuous glucose monitoring – roadmap for 21st century diabetes therapy. *Diabetes Care* 2005, 28, 1231–1239.
2. Boero, C., Carrara, S., De Micheli, G.: Sensitivity enhancement by carbon nanotubes: applications to stem cell cultures monitoring. In: Proceedings of IEEE/PRIME 2009, 5th International Conference on Ph.D. Research in Microelectronics & Electronics, Cork, Ireland, 2009.
3. Shumyantseva, V., De Luca, G., Bulko, T., Carrara, S., Nicolini, C., Usanov, S.A., Archakov, A.: Cholesterol amperometric biosensor based on cytochrome P450scc. *Biosens. Bioelectron.* 2004, 19, 971–976.
4. Joseph, S., Rusling, J.F., Lvov, Y.M., Friedberg, T., Fuhr, U.: An amperometric biosensor with human CYP3A4 as a novel drug screening tool. *Biochem. Pharmacol.* 2003, 65, 1817–1826.
5. Bard, A.J., Faulkner, L.R.: Electrochemcial methods, fundamentals and applications, Wiley, New York, 2001 (2nd edition), p. 49.
6. Moser, C.C., Keske, J.M., Warncke, K., Farid, R.S., Leslie Dutton, P.: Nature of biological electron transfer. Nature 1992, 355, 796–802.
7. Cui, X., Li, C.M., Zang, J., Yu, S.: Highly sensitive lactate biosensor by engineering chitosan/PVI-Os/CNT/LOD network nanocomposite. *Biosens. Bioelectron.* 2007, 22, 3288–3292.
8. Shumyantseva, V.V., Carrara, S., Bavastrello, V., Riley, D.J., Bulko, T.V., Skryabin, K.G., Archakov, A.I., Nicolini, C.: Direct electron transfer between cytochrome P450scc and gold

nanoparticles on screen-printed rhodium–graphite electrodes. *Biosens. Bioelectron.* 2005, 21, 217–222.
9. Carrara, S., Shumyantseva, V.V., Archakov, A.I., Samorì, B.: Screen-printed electrodes based on carbon nanotubes and cytochrome P450scc for highly sensitive cholesterol biosensors. *Biosens. Bioelectron.* 2008, 24, 148–150.
10. Brust, M., Walker, M., Bethell, D., Schiffrin, D.J., Whyman, R.: Synthesis of thiol-derivatized gold nanoparticles in a 2-phase liquid–liquid system. *J. Chem. Soc. Chem. Commun.* 1994, 7, 801–802.
11. Hostetler, M.J., Wingate, J.E., Zhong, C.J., Harris, J.E., Vachet, R.W., Clark, M.R., Londono, J.D., Green, S.J., Stokes, J.J., Wignall, G.D., Glish, G.L., Porter, M.D., Evans, N.D., Murray, R.W.: Alkanethiolate gold cluster molecules with core diameters from 1.5 to 5.2 nm: core and monolayer properties as a function of core size. *Langmuir* 1998, 14, 17–30.
12. Carrara, S., Erokhin, V., Facci, P., Nicolini, C.: On the role of nanoparticle sizes in mono-electron conductivity. In: Fendler, J., Dékány, I. (eds.) Nanoparticle in solid and solutions. NATO ASI Series 3. High Technology, vol. 18, pp. 497–503, Kluwer, Dordrecht, 1996.
13. Kim, H.H., Kim, H.J.: Preparation of carbon nanotubes by DC arc discharge process under reduced pressure in an air atmosphere. *Mater. Sci. Eng.* 2006, B133, 241–244.
14. He, C., Zhao, N., Han, Y., Li, J., Shi, C., Du, X.: Study of aluminum powder as transition metal catalyst carrier for CVD synthesis of carbon nanotubes. *Mater. Sci. Eng. A* 2006, 441, 266–270.
15. Li, H.J., Lu, W.G., Li, J.J., Bai, X.D., Gu, C.Z.: Multichannel ballistic transport in multiwall carbon nanotubes. *Phys. Rev. Lett.* 2005, 95, 086601-1–086601-4.
16. Gooding, J.J.: Nanostructuring electrodes with carbon nanotubes: a review on electrochemistry and applications for sensing. *Electrochim. Acta* 2005, 50, 3049–3060.
17. Carrara, S., Boero, C., De Micheli, G.: Quantum dots and wires to improve enzymes-based electrochemical bio-sensing. In: Proceedings of the 4th International Conference Nano-Nets 2009, Luzern, Switzerland, October 2009, LNICTS 20, pp. 189–199, Springer, Berlin, 2009.
18. MacDougall, D., and many other authors: Guidelines for data acquisition and data quality evaluation in environmental chemistry. *Anal. Chem.* 1980 52, 2242–2249.
19. Feynman, R.P., Leighton, R.B., Sands, M.: The Feynman lectures on physics, vol. I, part 2, pp. 38–42, Inter European Editions, Amsterdam, 1975.
20. Shi, W.; Lu, W.; Jiang, L.: Fabrication of amphiphilic gold nanoparticles of well-defined size, high concentration and robust colloidal stability. *J. Nanosci. Nanotechnol.* 2009, 9, 5764–5769.
21. Brust, M., Kiely, C.: Some recent advances in nanostructure preparation from gold and silver particles: a short topical review. *Colloids Surf. A* 2002, 202, 175–186.
22. Lokesh, K., Shivaraj, Y., Dayananda, B., Chandra, S.: Synthesis of phthalocyanine stabilized rhodium nanoparticles and their application in biosensing of cytochrome c. *Bioelectrochemistry* 2009, 75, 104–109.
23. Yang, J., Lee, J., Deivaraj, T., Too, H.: An improved Brust's procedure for preparing alkylamine stabilized Pt, Ru nanoparticles. *Colloids Surf. A* 2004, 240, 131–134.
24. Hostetler, M., Wingate, J., Zhong, C., Harris, J., Vachet, R., Clark, M., Londono, J., Green, S., Stokes, J., Wignall, G.: Alkanethiolate gold cluster molecules with core diameters from 1.5 to 5.2 nm: core and monolayer properties as a function of core size. *Langmuir* 1998, 14, 17–30.
25. Brust, M., Walker, M., Bethell, D., Schiffrin, D., Whyman, R.: Synthesis of thiol-derivatised gold nanoparticles in a two-phase liquid–liquid system. *J. Chem. Soc. Chem. Commun.* 1994, 7, 801–802.
26. Facci, P., Erokhin, V., Tronin, A., Nicolini, C.: Formation of ultrathin semiconductor films by CdS nanostructure aggregation. *J. Phys. Chem.* 1994, 98, 13323–13327.
27. Erokhin, V., Feigin, L., Ivakin, G., Klechkovskaya, V., Lvov, Y., Stiopina, N.: Formation and X-ray and electron diffraction study of CdS and PbS particles inside fatty acid matrix. *Macromol. Chem. Macromol. Symp.* 1991, 46, 359–363.

28. Erokhina, S., Erokhin, V., Nicolini, C., Sbrana, F., Ricci, D., di Zitti, E.: Microstructure origin of the conductivity differences in aggregated CuS films of different thickness. *Langmuir* 2003, 19, 766–771.
29. Shumyantseva, V., Carrara, S., Bavastrello, V., Jason Riley, D., Bulko, T., Skryabin, K., Archakov, A., Nicolini, C.: Direct electron transfer between cytochrome P450scc and gold nanoparticles on screen-printed rhodium-graphite electrodes. *Biosens. Bioelectron.* 2005, 21, 217–222.
30. Liu, S., Ju, H.: Reagentless glucose biosensor based on direct electron transfer of glucose oxidase immobilized on colloidal gold modified carbon paste electrode. *Biosens. Bioelectron.* 2003, 19, 177–183.
31. Cheng, J., Di, J., Hong, J., Yao, K., Sun, Y., Zhuang, J., Xu, Q., Zheng, H., Bi, S.: The promotion effect of titania nanoparticles on the direct electrochemistry of lactate dehydrogenase sol–gel modified gold electrode. *Talanta* 2008, 76, 1065–1069.
32. Njagi, J., Andreescu, S.: Stable enzyme biosensors based on chemically synthesized Au–polypyrrole nanocomposites. *Biosens. Bioelectron.* 2007, 23, 168–175.
33. Zheng, G., Patolsky, F., Cui, Y., Wang, W., Lieber, C.: Multiplexed electrical detection of cancer markers with nanowire sensor arrays. *Nat. Biotechnol.* 2005, 23, 1294–1301.
34. Iijima, S.: Helical microtubules of graphitic carbon. *Nature* 1991, 354, 56–58.
35. Qiao, I., Zheng, W.T., Wen, Q.B., Jiang, Q.: First-principles density-functional investigation of the effect of water on the field emission of carbon nanotubes. *Nanotechnology* 2007, 18, 155707.
36. Roohi, H., Bagheri, S.: Atomic and electronic structures of finite single-walled BN nanotubes: hybrid DFT calculations. *J. Mol. Struct.* THEOCHEM 856, 2008.
37. Mayer, A., Vigneron, J.P.: Real-space formulation of the quantum-mechanical elastic diffusion under n-fold axially symmetric forces. *Phys. Rev. B* 1997, 56(19), 12599–12607.
38. Mayer, A., Miskovsky, N.M., Cutler, P.H.: Theoretical comparison between field emission from single-wall and multi-wall carbon nanotubes. *Phys. Rev. B* 2002, 65, 155420.
39. McClain, D., DeRoss, M., Tavan, N., Jiao, J., McCarter, C.M., Richards, R.F., Mesarovic, S.: Effect of diameter on electron field emission of carbon nanotube bundles. *Mater. Res. Soc. Symp. Proc.* 2006, 901E.
40. Chen, Y., Shaw, D.T., Guo, L.: Field emission of different oriented carbon nanotubes. *Appl. Phys. Lett.* 2000, 76(17), 2469–2471.
41. Boero, C., Carrara, S., De Vecchio, G., Albini, G., Calza', L., De Micheli, G.: Carbon nanotubes-based electrochemical sensing for cell culture monitoring. In proceedings of the 2010 IEEE/ICME International Conference on Complex Medical Engineering, p. 288.
42. Radosavljevi, M., Lefebvre, J., Johnson, A.: High-field electrical transport and breakdown in bundles of single-wall carbon nanotubes. *Phys. Rev. B* 2001, 64, 241307.
43. Hone, J., Whitney, M., Piskoti, C., Zettl, A.: Thermal conductivity of single-walled carbon nanotubes. *Phys. Rev. B* 1999, 59, 2514–2516.
44. Kim, P., Shi, L., Majumdar, A., McEuen, P.: Thermal transport measurements of individual multiwalled nanotubes. *Phys. Rev. Lett.* 2001, 87, 215502.
45. McEuen, P., Fuhrer, M., Park, H.: Single-walled carbon nanotube electronics. *IEEE Trans. Nanotechnol.* 2002, 1, 78–85.
46. Li, X., Voss, P., Sharping, J., Kumar, P.: Optical-fiber source of polarization-entangled photons in the 1550 nm telecom band. *Phys. Rev. Lett.* 2005, 94, 53601.
47. Carrara, S., Cavallini, A., Garg, A., Micheli, G.D.: Dynamical spot queries to improve specificity in p450s based multi-drugs monitoring. In: *International Conference on Complex Medical Engineering*,Tampe, AZ, USA, April 9–11, 2009.
48. Johnson, D., Lewis, B., Elliot, D., Miners, J., Martin, L.: Electrochemical characterisation of the human cytochrome P450 CYP2C9. *Biochem. Pharmacol.* 2005, 69, 1533–1541.
49. Agematu, H., Matsumoto, N., Fujii, Y., Kabumoto, H., Doi, S., Machida, K., Ishikawa, J., Arisawa, A.: Hydroxylation of testosterone by bacterial cytochromes P450 using the Escherichia coli expression system. *Biosci. Biotechnol. Biochem.* 2006, 70, 307–311.

50. Jiang, J.G.G., Chen, C.L.L., Card, J.W., Yang, S., Chen, J.X.X., Xiang-Ning, N.F., Ning, Y.G.G., Xiao, X., Zeldin, D.C., Dao Wen, W.: Wang cytochrome P450 2J2 promotes the neoplastic phenotype of carcinoma cells and is up-regulated in human tumors. *Cancer Res.* 2005, 65, 4707–4715.
51. Rahman, M., Umar, A., Sawada, K.: Development of amperometric glucose biosensor based on glucose oxidase co-immobilized with multi-walled carbon nanotubes at low potential. *Sens. Actuators B Chem.* 2009, 137, 327–333.
52. Wang, B., Li, B., Deng, Q., Dong, S.: Amperometric glucose biosensor based on sol–gel organic inorganic hybrid material. *Anal. Chem.* 1998, 70, 3170–3174.
53. Huang, J., Song, Z., Li, J., Yang, Y., Shi, H., Wu, B., Anzai, J.I., Osa, T., Chen, Q.: A highly-sensitive L-lactate biosensor based on sol-gel film combined with multi-walled carbon nanotubes (MWCNTs) modified electrode. *Mater. Sci. Eng.* 2007, C27, 29–34.
54. Tsai, Y.C., Chen, S.Y., Liaw, H.W.: Immobilization of lactate dehydrogenase within multiwalled carbon nanotube-chitosan nanocomposite for application to lactate biosensors. *Sens. Actuators B Chem.* 2007, 125, 474–481.
55. Yang, M., Wang, J., Li, H., Zheng, J., Wu, N.: A lactate electrochemical biosensor with a titanate nanotube as direct electron transfer promoter. *Nanotechnology* 2008, 19, 75502–75502.
56. Li, J., Cassell, A., Delzeit, L., Han, J., Meyyappan, M.: Novel three-dimensional electrodes: electrochemical properties of carbon nanotube ensembles. *J. Phys. Chem. B* 2002, 106, 9299–9305.
57. Carrara, S., Bavastrello, V., Ricci, D., Stura, E., Nicolini, C.: Improved nanocomposite materials for biosensor applications investigated by electrochemical impedance spectroscopy. *Sens. Actuators B Chem.* 2005, 109, 221–226.
58. Pan, H., Poh, C., Feng, Y., Lin, J.: Supercapacitor electrodes from tubes-in-tube carbon nanostructures. *Chem. Mater.* 2007, 19, 6120–6125.
59. Dingle, R., Wiegmann, W., Henry, C.H.: Quantum states of confined carriers in very thin $Al_xGa_{1x}As$–GaAs–$Al_xGa_{1x}As$ heterostructures. *Phys. Rev. Lett.* 1974, 33, 827.
60. Novoselov, K.S., Geim, A.K., Morozov, S.V., Jiang, D., Zhang, Y., Dubonos, S.V., Grigorieva, I.V., Firsov, A.A.: Electric field effect in atomically thin carbon films. *Science* 2004, 306, 666–669.
61. Carrara, S., Facci, P., Nicolini, C.: More information on the calibration of scanning stylus microscopes by two dimensional Fourier transform analysis. *Rev. Sci. Instrum.* 1994, 65(9), 2860–2863.
62. Novoselov, K.S., Geim, A.K., Morozov, S.V., Jiang, D., Katsnelson, M.I., Grigorieva, I.V., Dubonos, S.V., Firsov, A.A.: Two-dimensional gas of massless Dirac fermions in graphene. *Nature* 2005, 438, 197–200.
63. Robert, F.: Service, carbon sheets an atom thick give rise to graphene dreams. *Science* 2009, 324, 875–877.
64. Geim, A.K.: Graphene: status and prospects. *Science* 2009, 324, 1530–1534.
65. Kailian Ang, P., Chen, W., Thye, A., Wee, S., Ping Loh, K.: Solution-gated epitaxial graphene as pH sensor. J. Am. Chem. Soc. 2008, 130, 14392–14393.
66. Wu, H., Wang, J., Kang, X., Wang, C., Wang, D., Liu, J., Aksay, I.A., Lin, Y.: Glucose biosensor based on immobilization of glucose oxidase in platinum nanoparticles/graphene/chitosan nanocomposite film. *Talanta* 2009, 80, 403–406.
67. Kang, X., Wang, J., Wu, H., Liu, J., Aksay, I.A., Lin, Y.: A graphene-based electrochemical sensor for sensitive detection of paracetamol. *Talanta* 2010, 81, 754–759.
68. Kim, Y.R., Bong, S., Kang, Y.J., Yang, Y., Kumar Mahajan, R., Kim, J.S., Kim, H.: Electrochemical detection of dopamine in the presence of ascorbic acid using graphene modified electrodes. *Biosens. Bioelectron.* 2010, 25, 2366–2369.
69. Li, F., Chai, J., Yang, H., Han, D., Niu, L.: Synthesis of Pt/ionic liquid/graphene nanocomposite and its simultaneous determination of ascorbic acid and dopamine. *Talanta* 2010, 81, 1063–1068.

70. Tan, L., Zhou, K.G., Zhang, Y.H., Wang, H.X., Wang, X.D., Guo, Y.F., Zhang, H.L.: Nanomolar detection of dopamine in the presence of ascorbic acid at (β-cyclodextrin/graphene nanocomposite platform. *Electrochem. Commun.* 2010, 12, 557–560.
71. Yi, W., Yi, W., Zhang, D.: Reduced graphene sheets modified glassy carbon electrode for electrocatalytic oxidation of hydrazine in alkaline media. *Electrochem. Commun.* 2010, 12, 187–190.
72. Eichelbaum, M., Somogyi, A., von Unruh, G.E., Dengler, H.J.: Simultaneous determination of the intravenous and oral pharmacokinetic parameters of D,L-verapamil using stable isotope-labelled verapamil. *Eur. J. Clin. Pharmacol.* 1981, 19, 133–137.
73. Carrara, S., Cavallini, A., De Micheli, G.: Multi-panel drugs detection in human serum for personalized therapy. *Biosens. Bioelectron.* 2010, submitted.

Chapter 6
Nano-Photonics and Opto-Fluidics on Bio-Sensing

Ming C. Wu and Arash Jamshidi

6.1 Optofluidics for Manipulation of Bioparticles

6.1.1 Survey of Bioparticle Manipulation Techniques

Characterization and monitoring of single cells is an important tool for quantitative biological studies. Development of various optofluidic systems has played an important role in facilitating the interaction with and handling of single cells. The ability to manipulate and trap individual cells is one of the most important functionalities that single cell platforms require. Various mechanical, electrical, optical, and magnetic forces have been used to address this challenge. Here, we will briefly review these techniques.

Mechanical manipulators [1–3] are the most intuitive method of manipulating particles. However, these techniques are inherently invasive and difficult to scale for parallel manipulation of large arrays. Fixed-electrode dielectrophoresis (DEP) is a powerful method that has been widely used to manipulate micro-scale objects such as cells [4–7] and has also been employed recently to manipulate various suspended nanostructures [8–11]. In this technique, the interaction of a nonuniform electric field with suspended particles in the solution results in attraction or repulsion of particles from areas of highest electric field intensity gradient. The nonuniform field is typically created using lithographically-defined electrodes. As a result, this method does not allow for real-time and flexible manipulation and transport of trapped particles. Other electrokinetic effects such as electrophoresis [12, 13] and electroosmosis [14, 15] have been used to address various biomaterials. However, electrophoresis requires the particles to carry charges and does not act on uncharged particles; and electroosmotic flows have fixed trapping patterns similar to that of the fixed-electrode DEP. Magnetic

M.C. Wu (✉)
University of California, Berkeley, CA, USA
e-mail: wu@eecs.berkeley.edu

S. Carrara (ed.), *Nano-Bio-Sensing*,
DOI 10.1007/978-1-4419-6169-3_6, © Springer Science+Business Media, LLC 2011

forces have also been used to address various micro and nanoparticles [16–18]. However, these methods can only address intrinsically magnetic materials or require tagging of particles with magnetic objects. Microfluidics provide a noninvasive way to manipulate [19, 20] and sort [21] a large number of particles, using hydrodynamic forces. However, these methods require complicated pump and flow control systems and are incapable of addressing single particles.

In the field of *optical* manipulation, only two technologies have emerged as most influential. The first technique, optical tweezers, invented by Ashkin et al. [22, 23], takes advantage of the optical gradient forces resulting from a tightly focused laser source to interact with the particles. Optical tweezers is a powerful tool to study biological and molecular interactions. However, it requires tight focusing and high optical power intensities to stably trap particles, which limits its effectiveness in performing high-throughput and large-scale optical manipulation functions. The high optical power can potentially damage the trapped objects, especially the biological materials [24, 25]. The second technique, called optoelectronic tweezers [26] (OET), is an optically-controlled manipulation technique based on the principle of light-induced DEP. In this technique, the optical field is not used directly to perform the manipulation; instead, the light pattern creates "virtual electrodes" on a photoconductive substrate, and the resulting DEP from the electric field gradient traps the object. OET is capable of trapping a large number of objects with optical power intensities approximately 5 orders of magnitude lesser than that of the optical tweezers. As a result, OET is more suitable for large-scale, high-throughput optical manipulation functions. In the next section, we will describe this technique in more detail and discuss some of the recent advances in this field.

6.1.2 Optoelectronic Tweezers

Figure 6.1 shows the structure of the OET device. The liquid chamber containing the sample is sandwiched between a photoconductive and a transparent electrodes. The photoconductive electrode consists of a 1-μm-thick hydrogenated amorphous silicon (a-Si:H) layer deposited on indium–tin–oxide (ITO)-coated glass substrate. The top transparent electrode is simply ITO-coated glass. The spacing between the electrodes is defined by a 100-μm-thick spacer. An AC voltage (5–20 peak-to-peak voltage at 1–100 kHz frequency) is applied between the top and bottom ITO electrodes. The inset shows the scanning electron microscopy (SEM) cross-section of the photoconductive electrode.

Once the OET device is assembled, it is placed under a microscope for observation and actuation. Various microscope observation modes such as bright-field, dark-field, fluorescent, or differential interference contrast (DIC) microscopy can be used for particle visualization. Dark-field observation is particularly suitable for observation of nanoscale objects because of the strong light scattering by nanostructures. A charge-coupled device (CCD) camera is used to record the particle manipulation and provide image feedback. Coherent light sources such as low-power laser diodes or incoherent

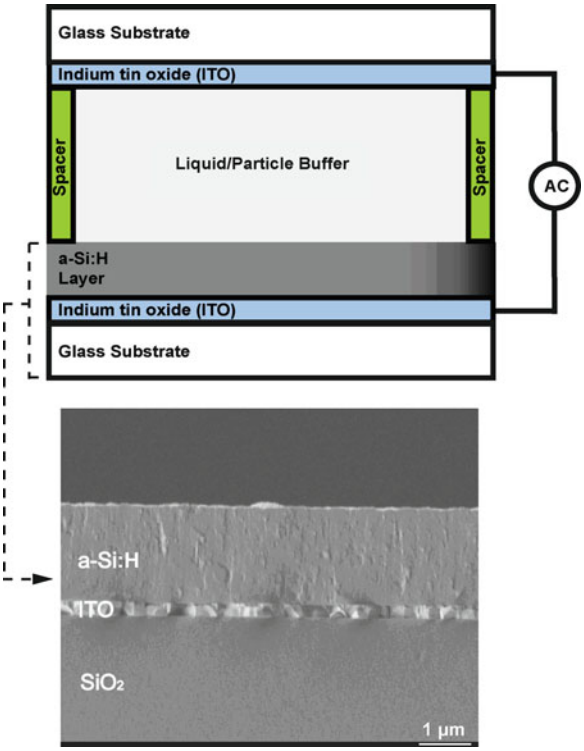

Fig. 6.1 Optoelectronic tweezers (OET) device structure. The OET device consists of a top transparent ITO electrode and a bottom ITO electrode. There is a layer of photoconductive material (hydrogenated amorphous silicon) on top of the bottom electrode. An AC voltage is applied between the two electrodes. A spacer separates the top and bottom surface to form the OET chamber. The inset is an SEM image of the OET device bottom surface cross-section

light sources such as light-emitting diodes (LEDs) can be used to actuate the OET device. Dynamic light patterns are generated using spatial light modulators such as digital micromirror devices (Texas Instruments) or liquid-crystal based spatial light modulators (Hamamatsu). Generated light patterns are then focused onto the OET device surface either through the same microscope objective used for observation or through an additional objective lens.

OET device actuation is achieved by modulating the impedance of the photoconductive layer (a-Si:H). In the absence of light, the dark conductivity of a-Si:H is approximately 10^{-5} S/m. However, in the presence of a light source, electron–hole pair carriers are generated in the photoconductive material, and the photoconductivity is increased by 3 orders of magnitude to approximately 10^{-2} S/m, using a 10–100 W/cm^2 illumination intensity. The amount of light absorbed by a-Si:H is a function of its absorption coefficient, which depends strongly on the illumination wavelength [27]. The absorption coefficient of a-Si:H is approximately 10^4 cm^{-1} in the visible region, which corresponds to 90% absorption length of ~1 μm, and is

the typical value used for a-Si:H layer thickness in the OET device. Even though a-Si:H has large absorption coefficients in the UV region (10^5–10^6 cm^{-1}), the absorption length is ~100 nm and cannot fully actuate the OET device. On the other hand, a-Si:H absorption coefficient for near infrared is approximately 10^3 cm^{-1}; therefore, larger intensity illumination is required to actuate the OET device at these wavelengths.

To better understand the operation of the OET device, we can model it as a simple lumped circuit element model. When there is no light present, the impedance of the photoconductive layer (a-Si:H) is higher than the impedance of the liquid layer; therefore, the majority of the applied AC voltage is dropped across the photoconductive layer. However, when the light source is present, the impedance of the photoconductive layer is reduced locally, creating a "virtual electrode," causing the majority of the AC voltage to drop across the liquid layer. It is important to note that the impedance of the photoconductive layer is reduced only in the area that the light source is present. This is due to a-Si:H's small ambipolar diffusion length of 115 nm [28], which confines the actuated area within the illumination region. Therefore, the resolution of the OET device virtual electrodes is fundamentally limited by the light source diffraction limit given by:

$$\text{Diffraction Limit} = 0.6\frac{\lambda}{\text{N.A.}}, \tag{6.1}$$

where λ is the wavelength of illumination and N.A. is the numerical aperture of the objective lens. Using a typical illumination wavelength of 630 nm and N.A. = 0.6, we achieve a diffraction limited spot of approximately 630 nm.

Typical liquid conductivities used for optimal OET device operation are between 1 and 10 mS/m. At liquid conductivity values higher than this range, the impedance of the liquid layer would be much lower than the a-Si:H layer even under illumination, therefore, impeding the transfer of voltage from the a-Si:H layer to the liquid layer.

Since the voltage is transferred to the liquid layer only in the illuminated area, a nonuniform electric field is created in the liquid layer. The interaction of this nonuniform field with the particles, liquid media, and the virtual electrodes creates various electrokinetic forces under different operational regimes. In the next section, we will briefly discuss and characterize these electrokinetic forces.

In the OET technique, the optical power intensity required for trapping the particles is reduced considerably relative to optical tweezers, since the optical field is not directly used to trap the particles; rather, the optical field is used to create virtual electrodes in the photoconductive layer. In addition, since the electrodes are defined optically, it is possible to create real-time flexible trapping patterns by patterning the light source using a spatial light modulator. Furthermore, due to the small optical power intensity required for trapping and relaxed optical focusing requirements, a large working area can be achieved using a spatial light modulator. These capabilities of OET have previously been demonstrated through massively parallel manipulation of 15,000 particles over a large area 1.3×1.0 mm^2, as shown in Fig. 6.2 [26].

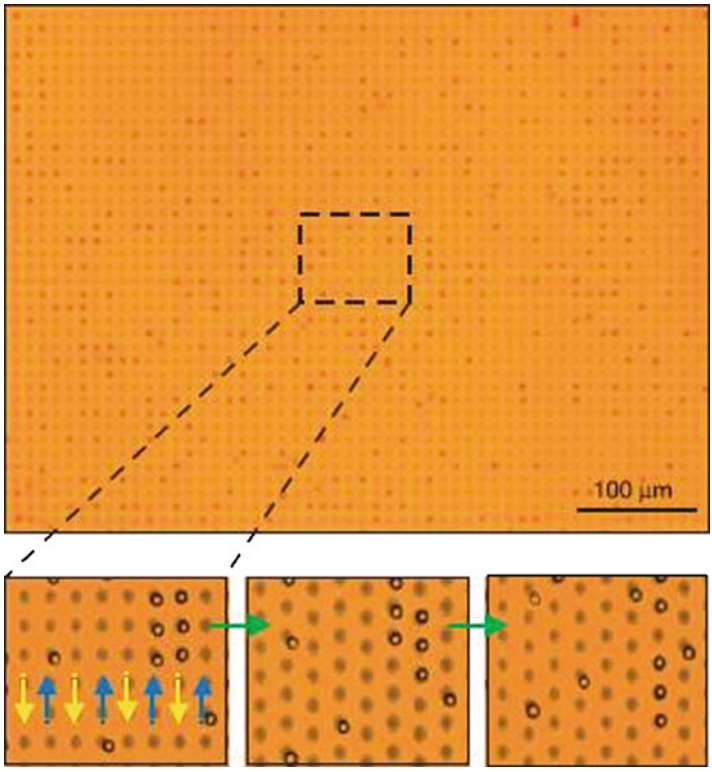

Fig. 6.2 Massively parallel manipulation of single 4.5-µm-diameter polystyrene particles over $1.3 \times 1.0\ mm^2$ area using 15,000 traps created by a digital micromirror device. The inset shows the transport of particles in the direction depicted by the *arrows*

Since the DEP force is dependant on the properties of the particles in relation to the surrounding media, OET is also capable of distinguishing between particles with differing complex permittivities such as dead and live cells [26] and semiconducting and metallic materials [29]. This ability is particularly important in cell separation and sample purification.

Since the first demonstration of OET in 2003, OET has grown to become an important optofluidic manipulation tool and is pursued around the world by various research groups, who have innovating new ideas to expand this field. To date, various photoconductive materials such as hydrogenated amorphous silicon [26], silicon phototransistor [30], CdS [31], metallic plasmonic nanoparticles [32, 33], and polymers [34] have been used to realize the OET devices. Dynamic actuation of OET has been accomplished with a variety of coherent and incoherent light sources such as scanning lasers [35], digital micromirror devices [26], and LCD flat panel displays [36, 37]. Moreover, various modes of operation such as DEP [26], light-actuated AC electroosmosis [38], and electrothermal heating [39] have been

observed and characterized in the OET optofluidic platform. Manipulation of microparticles such as polystyrene beads [26, 36, 37, 40–43], red blood cells [37, 41], *E. coli* bacteria [35], white blood cells [26, 42], Jurkat cells [42], HeLa cells [42, 44], yeast cells [43], and neuron cells [45] and nanoparticles such as semiconducting and metallic nanowires [29, 46–48], carbon nanotubes [49], metallic spherical nanoparticles [50], and DNA [51, 52] has been achieved with OET. Other functionalities such as dynamic single cell electroporation [53] and cell lysis [54], optically induced flow cytometry [55], and large-scale, dynamic patterning of nanoparticles [56] have been demonstrated using the OET platform.

In addition to the conventional OET device structure, other OET configurations have also been invented including phototransistor OET (phOET), which makes use of a phototransistor structure as the photoconductive layer to achieve higher optical gains and manipulate cells in high conductivity cell culture media [30]; lateral-field OET (LOET) and planar lateral-field OET (PLOET) [42, 46–48], which are capable of manipulating particles in a lateral fashion through the use of interdigitated photoconductive electrodes; floating electrode OET (FLOET) [57], which can manipulate aqueous droplets in oil; double-sided OET [58], which reduces the nonspecific stiction of particles by using amorphous silicon as the top and bottom surfaces; and OET integrated with electrowetting-on-dielectric [59–60] devices, which enables manipulation of particles within droplets.

6.1.2.1 Electrokinetic Forces in OET

Even though the main operational principle of OET has been the light-induced DEP principle, there are other operational regimes in the OET device that can be used [39]. A comprehensive understanding of these operational regimes is essential in using OET as an integral part of an optofluidic system.

The main electrokinetic effect in the OET device is the DEP force. DEP is a technique that uses the interaction of a nonuniform electric field with the induced dipoles in the particles to attract or repel the particles from areas of highest electric field intensity gradient. In the presence of a nonuniform electric field (E), a dipole moment (p) is induced in the particles with unequal charges on two ends. Therefore, the dipole feels a net force toward or away from areas of highest field intensity gradients depending on the AC bias frequency and properties of the particles and the liquid solution. By taking the difference between the forces experienced by the charges at the two ends of the dipole, we can approximate the DEP force as [61]:

$$F = (p \cdot \nabla)E. \tag{6.2}$$

To calculate the DEP force expression on various objects, the particles are assigned an effective dipole moment, which is the moment of a point dipole that creates an identical electrostatic potential when immersed in the imposed electric field. By comparing the electrostatic potential of the particle of interest with the electrostatic

potential of a point dipole, and by ignoring the higher order terms in the Taylor expansion of the electric field, the following formula is derived for the DEP force on a spherical particle [61]:

$$\langle F_{\mathrm{DEP}} \rangle = 2\pi r^3 \varepsilon_{\mathrm{m}} \mathrm{Re}\{K^*(\omega)\} \nabla E^2, \tag{6.3}$$

$$K^*(\omega) = \frac{\varepsilon_{\mathrm{p}}^* - \varepsilon_{\mathrm{m}}^*}{\varepsilon_{\mathrm{p}}^* + 2\varepsilon_{\mathrm{m}}^*}, \quad \varepsilon_{\mathrm{m}}^* = \varepsilon_{\mathrm{m}} - j\frac{\sigma_{\mathrm{m}}}{\omega}, \quad \varepsilon_{\mathrm{p}}^* = \varepsilon_{\mathrm{p}} - j\frac{\sigma_{\mathrm{p}}}{\omega}, \tag{6.4}$$

where r is the radius of the particle; ε_{m} and ε_{p} are the permittivities of the medium and the particle, respectively; σ_{m} and σ_{p} are the conductivities of the medium and the particle, respectively; ω is the frequency of the AC potential; $\mathrm{Re}\{K^*\}$is the real part of the Clausius-Mossotti (C.M.) factor (K^*); and ∇E^2 is the gradient of the electric field intensity. The C.M. factor is a function of the permittivity and conductivity of the particle and the medium, and in the case of spherical particles, it has a value between -0.5 and 1. For particles that are more polarizable than the surrounding medium, the C.M. factor is positive and the particles experience a positive DEP force. However, those particles that are less polarizable than the surrounding medium experience a negative DEP force and are repelled from regions of highest electric field intensity gradient.

Another effect that is observed in the OET device is the electro-thermal flow. This effect is due to a temperature gradient created in the liquid layer by absorption of the light source in the photoconductive material and is only observed at very high optical power intensities of more than 100 W/cm^2, which is much larger than typical optical power intensities used for trapping. The electro-thermal flow is mostly a parasitic effect; however, due to the very high optical powers necessary to achieve this operational regime, it does not interfere with typical OET operation. Another electrokinetic effect that has been observed in OET is the light-actuated AC electro-osmosis or LACE. At lower frequencies, the lateral component of the electric field created in the liquid layer interacts with the double-layer charges on the surface of the OET device virtual electrodes and can accelerate them laterally, creating a flow vortex centered around the light source. This effect is typically observed at frequencies lesser than 10 kHz for ~1–10 mS/m conductivities and can be used for trapping nanoscale objects such as polystyrene beads as small as 200 nm. Using this method, it has been demonstrated that 31,000 individually addressable traps can be created for particle larger than 1 μm in diameter [62]. This trapping mechanism is essentially independent of particle properties, which makes it an attractive choice for manipulation and trapping of nanoparticles.

The three main operational regimes in the OET device (DEP, electro-thermal flow, and light-actuated AC electro-osmosis) are shown in Fig. 6.3, as a function of optical power and frequency. The different operational regimes can be achieved in OET by tuning the parameters such as optical power and frequency. A figure of merit comparing the particle speed due to these various effects has been developed [39] and can be used as a guide to identify the operating conditions of the OET device.

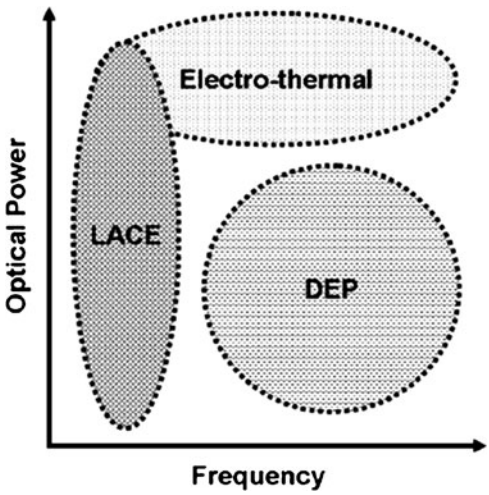

Fig. 6.3 OET operational regimes as a function of optical power and frequency

6.1.2.2 Optical Manipulation of Biological Objects in High Conductivity Cell Culture Media

The conventional OET devices with hydrogenated amorphous silicon as the photoconductive layer have been limited to manipulation of particles in liquid conductivities less than 100 mS/m. This limitation is due to the fact that conventional OET cannot switch the AC voltage effectively from the photoconductive layer to the liquid layer because of the relatively small photoconductivity of the amorphous silicon layer. However, manipulation of cells in high conductivity physiological solutions is essential to maintaining the cell viability [63–64]. One way to overcome the limitation of the conventional OET is to replace amorphous silicon as the photoconductive layer with an $N^{+}PN$ phototransistor structure, which has roughly 2–3 orders of magnitude more photoconductivity due to the higher carrier mobility in single crystalline silicon and the phototransistor current gain. This device is referred to as phOET [30]. Figure 6.4 shows the structure of the phOET device, and the phototransistor structure fabricated on a silicon substrate which replaces the amorphous silicon on the bottom surface.

It has been demonstrated [30] that phOET can transport various cell lines such as HeLa and Jurkat cells with speeds exceeding 30 μm/s in phosphate-buffered saline (PBS) solution and Dulbecco's modified eagle medium (DMEM) solutions (1.5 S/m conductivities). PhOET is typically operated at MHz frequencies, and the cells experience a negative DEP force, as shown in Fig. 6.5 for the transport of two HeLa cells in a PBS solution. The two HeLa cells are pushed away from the light pattern as it is scanned across the phOET device surface.

By retaining the many advantages of conventional OET and permitting manipulation in cell culture media, the phOET device opens up many possibilities in practical cell manipulation such as cell sorting, single cell assays for drug screening, and cell-to-cell communication studies.

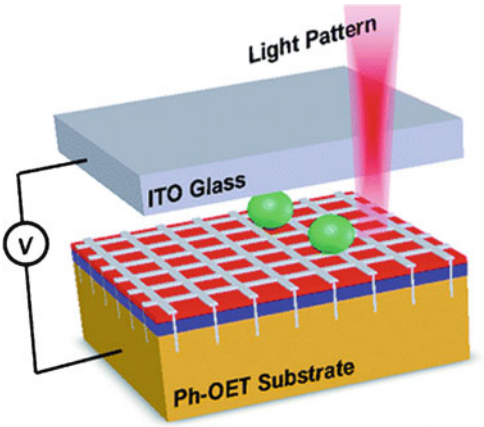

Fig. 6.4 (**a**) Phototransistor OET (phOET) device structure. The phOET device structure resembles the conventional OET structure with the exception that the photoconductive layer is replaced by an $N^{+}PN$ phototransistor structure. The larger carrier mobility and higher transistor gain of this layer enables phOET to trap cells in their high-conductivity physiological solutions (© Lab on Chip [30])

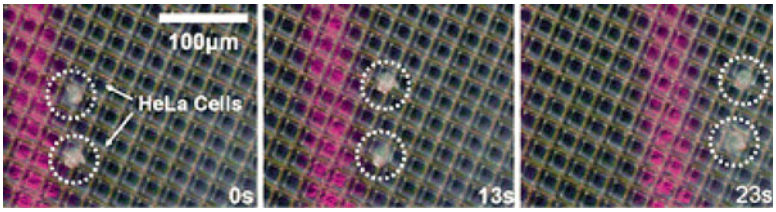

Fig. 6.5 Transport of two Hela cells in a PBS solution using the phOET (© Lab on Chip [30])

6.1.2.3 Parallel Light-Induced Single Cell Electroporation

The ability to transport external molecules across the cell membranes into the cell's intracellular matrix is an important tool for biological characterization of single cells and is essential in applications such as genetic transfection and cell-to-cell signaling studies. The external molecules are typically transported into the intracellular matrix through the formation of temporary pores in the cell membrane. Current methods that are used to achieve the poration of cells have either single cell selectivity but low throughput [65] or high throughput (many cells) but no selectivity [66]. One of the more common techniques used to achieve poration of cells is referred to as electroporation [67, 68]. In this method, temporary holes are created in the cell membrane by exposing the cell to an external electric field above a certain threshold. Once the pores are created, the molecules are transported across the membrane either through passive diffusion or field-assisted drift. Although the exact nature of pore formation in electroporation is not understood clearly, pores with nanoscale dimensions will eventually reseal [69]. Parallel light-induced electroporation of single cells has been achieved using the OET device. This method follows a similar process to conventional electroporation of cells with the difference that the electrodes are optically defined; therefore, it allows for large-scale and parallel poration of cells. Moreover, OET-assisted electroporation

of cells has single cell sensitivity since the electrodes are virtually defined using a spatial light modulator and are able to concentrate the electric field locally over individual cells while maintaining all manipulation capabilities of OET. Figure 6.6 shows selective poration of a 2 × 2 array of HeLa cells. The cells are first positioned using conventional OET method, and the applied bias (0.2 kV/cm) does not result in the poration of the cells as indicated due to the lack of signal in the fluorescent image of the PI dye in the solution. Once the cells are positioned, light patterns are placed on the two cells as indicated in the middle panel, the electroporation bias (1.5 kV/cm) is applied, and the fluorescence image confirms the poration of the two cells. Subsequently, the remaining two cells are porated with all cells fluorescing, as the PI dye enters into the cellular matrix and interacts with the cell's DNA.

6.1.2.4 Thermocapillary Movement of Air Bubbles

The ability to move air bubbles is an important functionality necessary for a versatile optofluidic system. A variety of applications such as mixers [70], valves [71], pumps [72], and performing Boolean logic [73] require manipulation of air

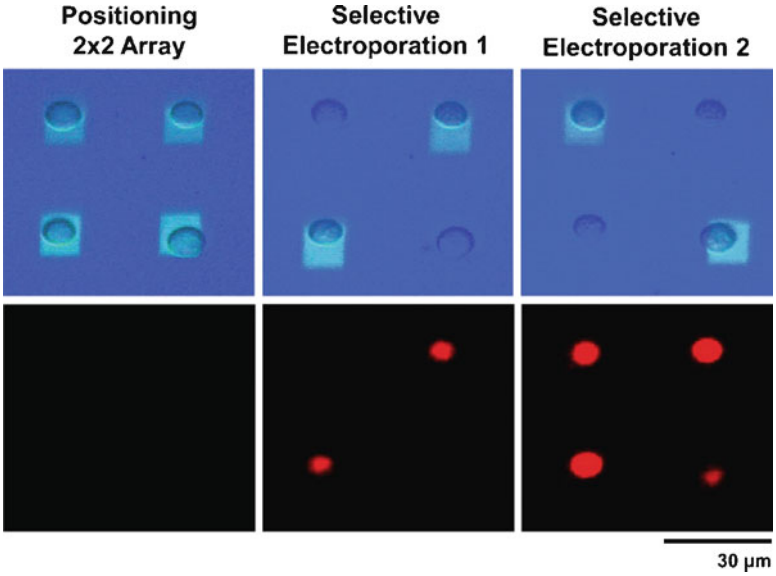

Fig. 6.6 Parallel single cell electroporation. *Top row* shows bright field image of cells and optical pattern. *Bottom row* shows corresponding PI dye fluorescence. Cells are first arrayed using OET ($0.2\,\mathrm{kVcm^{-1}}$). OET manipulation bias does not cause electroporation. Two cells on the diagonal are then subjected to the electroporation bias ($1.5\,\mathrm{kVcm^{-1}}$) and, subsequently, fluoresce (image taken 5 min following electroporation bias). Finally, the remaining two cells are porated, resulting in the fluorescence of all cells (image taken 5 min following electroporation bias) (© Lab on Chip [53])

bubbles. The active positioning of the air bubbles is achieved using various methods such as DEP [74], electrowetting [75], optoelectrowetting [76], evaporation [77], and thermal gradients [78]. Thermal gradients have been typically created using resistive heating elements. However, light actuation has also been used to create required temperature gradients [79] for thermocapillary manipulation.

Optical actuation of the thermocapillary force offers several advantages over conventional methods including massively parallel and dynamic manipulation and control of a large number of bubbles. It has been demonstrated [80] that the OET platform can be used for optical actuation of thermocapillary force. In this method, the photoconducive substrate absorbs the light energy and forms a temperature gradient in the liquid layer. The temperature gradient results in a surface tension gradient in the liquid layer, which creates a flow pattern from warm areas to cold areas to minimize the energy. This flow pattern results in movement of the bubbles toward areas with high temperature gradients and stably traps them in the illuminated areas. Figure 6.7 shows a single 109-μm-diameter air bubble in a silicone oil media trapped using the optically-induced thermocapillary force. The trapped air bubble follows the laser position as it is scanned across the stage. Bubbles with diameters ranging from 33 to 329 μm (corresponding to 19 pL–23 nL) can be transported using this technique. The translation speed of the bubbles can be tuned by varying the optical power intensity used, since the laser intensities are directly proportional to the temperature gradients. Translation speeds of 1.5 mm/s have been demonstrated for bubbles less than 0.5 nL with 2 kW/cm^2 optical intensity.

To summarize this section, we have seen that through the integration of optical and electrical forces, OET achieves a powerful optofluidic platform for manipulation and organization of bioparticles in cell culture media and is able to achieve other important functionalities such as parallel single-cell poration of cells and movement of air bubbles. In the next section, we will see how OET operation can be extended to integrate nanophotonic sensors for chemical and biological applications.

6.2 Nanophotonics for Biosensing

Nanophotonic devices and techniques such as resonant cavities [82], interferometric systems [83], photonic crystals [84], and surface plasmons [85] have been used for biosensing applications [86] with high selectivity and extreme sensitivity. These techniques typically detect the presence of objects as a change in the optical characteristics of the system such as the propagating or evanescent optical modes. In recent years, there has been much interest in metallic nanoparticles as biological nanosensors because of their interesting optical properties [87]. For metallic nanoparticles with dimensions lesser than the wavelength, the collective oscillations of the electrons leads to localized surface plasmon modes, which concentrate the

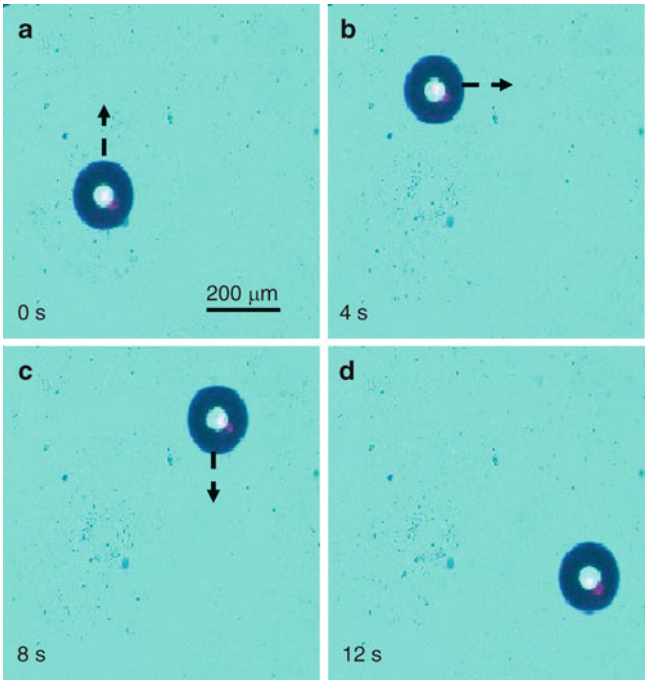

Fig. 6.7 (**a**–**d**) Optically actuated thermocapillary transport of an air bubble in silicone oil. A 109-μm-diameter bubble is trapped in the thermal trap created by a laser. The bubble follows the position of the laser spot as it is scanned across the stage (© Optical Society of America [81])

incident field in the near field of the particles. Because of this field localization, metallic nanocrystals such as gold nanoparticles have been shown to enhance the magnitude of Raman signals from molecules placed in their vicinity as much as 10^{14} times [88, 89]. This effect is referred to as surface-enhanced Raman spectroscopy (SERS) and plays an important role in sensing applications since Raman scattering is an inherently inefficient process and the enhancement of Raman signal makes it much easier to detect the "fingerprint" of molecules. Moreover, the plasmonic resonance conditions of the nanoparticles depend strongly on the surrounding environment; therefore, detecting a shift in the resonance peak is another way of sensing various molecules. The colloidal nanoparticles can also be easily integrated with microfluidic systems as practical lab-on-a-chip biosensors [90].

6.2.1 Dynamic Manipulation of Metallic Nanoparticles

Optical tweezers have been used to trap metallic nanoparticles of various sizes [91, 92]; however, the high optical intensities required for stable trapping of particles ($\sim 10^7$ W/cm^2) result in excessive heating of the metallic nanoparticles,

(with $\Delta T > 55°C$) [93]. This temperature increase hampers the application of optical tweezer-trapped particles in biological environments. DEP can also be used to trap nanoparticles using fixed electrodes [94]; however, since the trapping positions are lithographically defined, fixed-electrode DEP lacks the capability to dynamically manipulate the trapped particles. Anti-Brownian electrokinetic (ABEL) traps [95] have also been used to trap single molecules and study the particle dynamics. However, this technique requires the molecules to be fluorescent.

OET can overcome these challenges by trapping metallic nanoparticles [50] using optical intensities 100,000× lesser than optical tweezers; therefore, it significantly reduces the heating in particles due to absorption. Moreover, the optical traps can be dynamically controlled, which overcomes the challenge of fixed trapping patterns.

Figure 6.8 shows trapping and transport of a single 100-nm diameter gold nanoparticle. The trapping laser source is scanned manually across the OET device over a ∼200 μm^2 area and the nanoparticle follows the trap. Since the DEP force is proportional to the volume of the particle, the magnitude of the force drops rapidly for nanoscale objects. However, in the OET device, the strongest field intensity gradients, ∇E^2, are present near the a-Si:H surface; therefore, the metallic nanoparticles are immersed in the highest ∇E^2 region because of their small sizes. This overcomes the reduction in DEP force due to small particle volume. We have characterized the maximum translational velocities of 100-nm diameter gold nanoparticles to be ∼68 μm/s at 20Vpp, which corresponds to a DEP force of ∼0.1 pN.

The relaxed requirements on optical actuation of OET make it possible to integrate the OET optical manipulation setups with other forms of optical spectroscopy and characterization. An example of such techniques is Raman spectroscopy

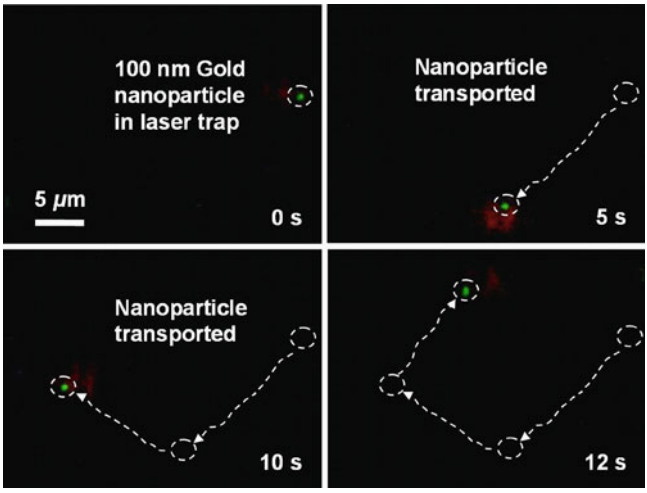

Fig. 6.8 Trapping and transport process of a single 100 nm gold nanoparticle using OET. The nanoparticle is transported over an approximately 200 μm^2 area in 12 s (© IEEE [50])

[96–97], which is an optical spectroscopic technique used to study the vibrational or rotational modes of molecules. In this technique, photons generated by a monochromatic light source (such as laser) are inelastically scattered by the molecules and collected by an objective lens. A notch or high-pass filter is typically used to remove the laser line and the remaining signal is sent to a spectrometer and detector to identify the "fingerprints" of the molecules.

The "fingerprints" of the molecules are unique since their vibrational modes are related to the chemical structure of each molecule. Therefore, Raman spectroscopy is an important technique in chemical and biological characterization and identification of various materials. Integration of OET with Raman spectroscopy opens up many possibilities for in-situ characterization and detection of trapped objects. Therefore, the OET-trapped nanoparticles can be used as a dynamic sensor in the OET chamber to sense the Raman signal from a dilute solution of molecules. To demonstrate this capability, we have mixed a 24 μM solution of trans-1,2-bis (4-pyridyl)ethane [98] (BPE) molecules with the nanoparticles solution in 1:1 ratio. A single laser source (785 nm, 30 mW) was used to collect the nanoparticles and detect the Raman signal. Figure 6.9a, b shows the collection of nanoparticles after the application of trapping laser, and the dotted line indicates the laser area.

Figure 6.9c shows the detected Raman signal from the BPE molecules in the solution as a function of time. There are nine individual spectra acquired 4 s apart from each other starting at the onset of application of the laser source. As we can see, the Raman signal grows over time and reaches a maximum, which indicates the maximum concentration of nanoparticles achieved.

Other measurement techniques such as two-photon photoluminescence (TPPL) of metallic nanostructures have also been used for in-vivo and in-vitro imaging of biological objects [99, 100] and can be combined with OET manipulation platform to allow real-time dynamic imaging and manipulation of metallic particles. Moreover, OET can potentially be used to concentrate and position nanoparticles of interest near the surface of cells. This capability combined with cell surgery techniques [101, 102] could be used for targeted delivery of sensors inside the cells to study cellular processes such as phosphorylation [103].

6.2.2 Large-Scale Patterning of SERS Sensors

Patterning of nanostructures has important applications in medical diagnosis [104, 105], sensing [106], nano- and optoelectronic device fabrication [107, 108], nanostructure synthesis [109], and photovoltaics [110]. Various methods including dip-pen nanolithography [111–116], nanofabrication [117], contact printing [118–121], self-assembly [122, 123], and Langmuir-Blodgett [124] have been used to address this challenge. However, these techniques cannot be used to create real-time reconfigurable patterns without the use of complicated instrumentation or processing steps. Optical patterning techniques [125–129] have been used previously to overcome this challenge. However, these methods are either slow [125] (several minutes to

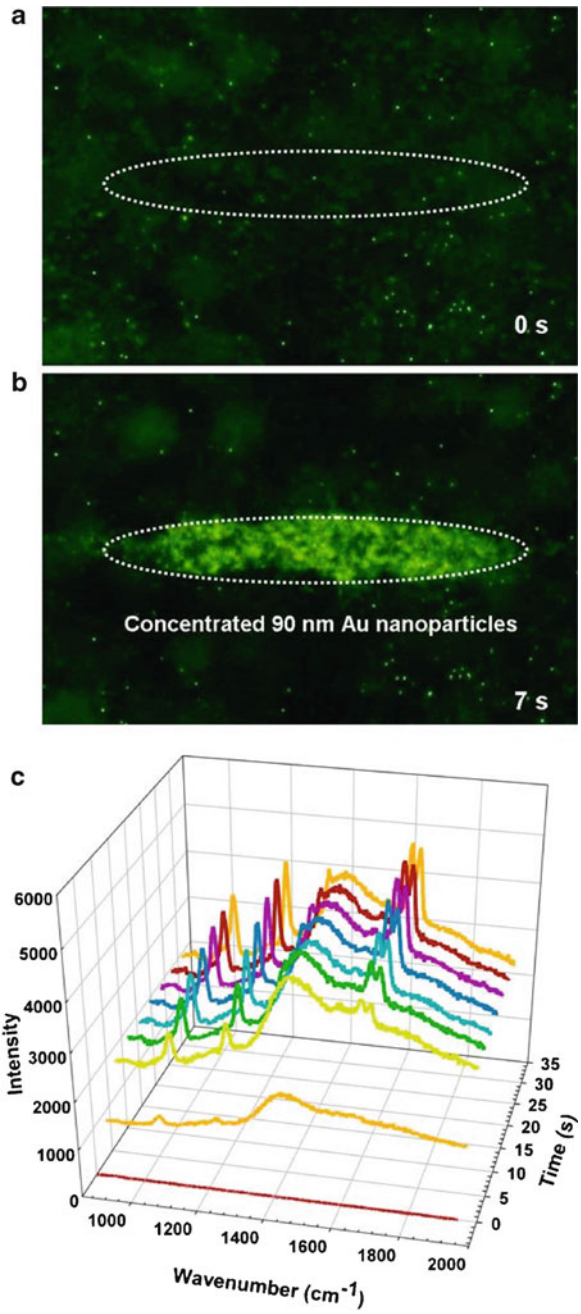

Fig. 6.9 (**a**–**b**) Collection of 90 nm gold nanoparticles in the OET chamber for enhancement of Raman signal from a dilute solution of BPE molecules. (**c**) In-situ SERS spectra of BPE molecules using OET trapped 90 nm gold nanoparticles

hours) or require very high optical intensities [126] ($\sim 10^5$ W/cm^2) to pattern the nanostructures, which prevents the widespread application of such techniques. Optical tweezers have been used to permanently assemble nanostructures on various substrate [127, 128]; however, due to very high optical intensities ($\sim 10^7$ W/cm^2) and high numerical aperture objectives required for patterning, optical tweezers are limited in the ease of operation, the available working area, and can potentially damage the nanoparticles [127].

It has been demonstrated [56] that the combination of various electrokinetic effects present in the OET device (light-induced DEP, LACE, and electrothermal flow) can be used to "directly write" patterns of nanoparticles. This novel technique is called *NanoPen*. NanoPen enables low optical power intensity, flexible, real-time reconfigurable, and large-scale *light-actuated* patterning of single or multiple nanoparticles such as metallic spherical nanocrystals, and one-dimensional nanostructures such as carbon nanotubes and nanowires.

Figure 6.10a, b depicts the schematic of the NanoPen process and finite-element simulation of various electrokinetic forces in the OET chamber for an applied voltage of 20Vpp at 10 kHz, with 1 mS/m liquid conductivity, respectively. There are two distinct forces that lead to light-actuated patterning of nanoparticles: a *collection force*, which collects the particles over a long range (over 100 μm distances) and concentrates them in the light spot, and an *immobilization force*, which strongly attracts and immobilizes the particles on the OET surface. The collection force is mainly found in LACE and electrothermal flow over the long range and DEP over the short range. The immobilization force is dominated by the light-induced DEP force but is also affected by electrophoretic forces due to the particles surface charges.

Figure 6.10c shows NanoPen immobilization and patterning of 90-nm diameter gold nanoparticles (obtained from Nanopartz Inc. [130]) dispersed in a 5 mS/m solution of KCl and DI water with $\sim 10^{11}$ particles/mL concentration. The number of immobilized particles in the laser spot is a function of the exposure time as can be seen for the 2–120 s exposure times. Figure 6.10c inset shows the SEM images of each spot; the number of particles patterned ranges from ~250 particles for a 2 s exposure to ~6,500 particles for a 120 s exposure. Figure 6.10d shows a close-up view of the spots with 20, 30, and 120-s exposure times.

Using a spatial light modulator to define the light patterns, NanoPen is capable of real-time dynamic and flexible patterning of nanoparticles. Moreover, the light patterns can be created using a commercial projector due to low required optical power intensity for actuation of NanoPen (<10 W/cm^2). Figure 6.11a–c shows patterning of 90-nm diameter gold nanoparticles in the form of a 10 × 10 array over a 150 × 140 μm^2 area, the "NIH" logo over a 160 × 140 μm^2 area, and the "CAL" logo over a 140 × 110 μm^2 area, respectively. These arbitrary patterns were created by interfacing Microsoft PowerPoint with the projector.

As mentioned in the previous section, metallic nanocrystals are ideal local, subdiffraction limited nanosensors [106] for medical and chemical diagnosis and imaging, because of their interesting plasmonic properties. Therefore, NanoPen patterned metallic nanoparticles present a method for flexible and dynamic

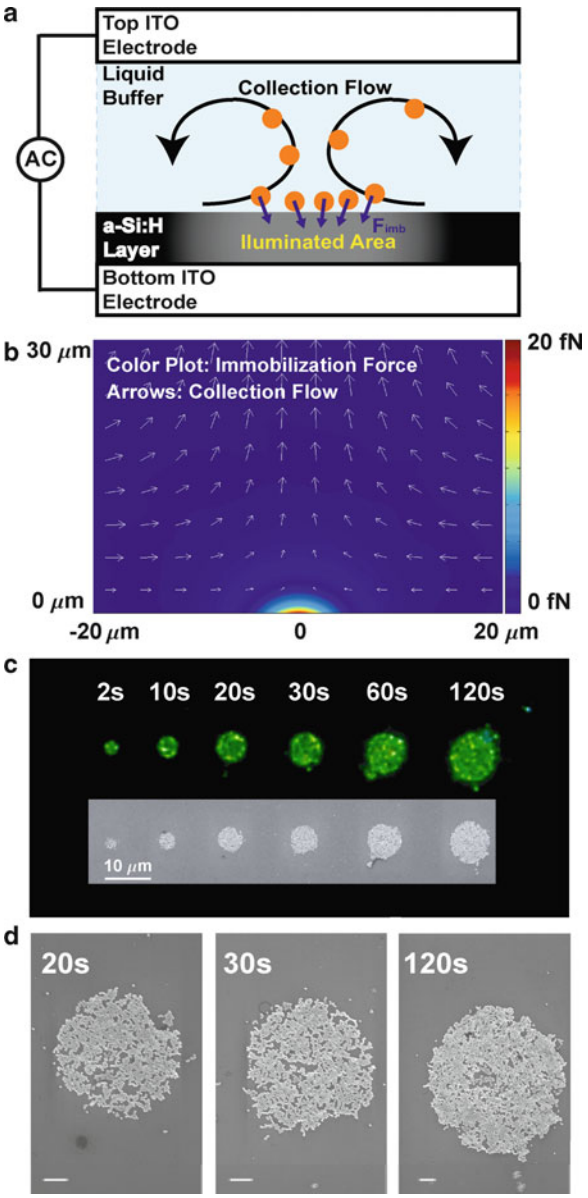

Fig. 6.10 (**a**) Optoelectronic tweezers (OET) optofluidic platform used to realize the NanoPen process. The collection flow collects the particles towards the illuminated area and the immobilization force patterns the particles on the surface. (**b**) Finite-element simulation of the NanoPen process. The *arrows* indicate the collection flow, which is a combination of the electrothermal (ET) flow and light-actuated AC electroosmosis (LACE) flow. The immobilization force consists mainly of the dielectrophoresis (DEP) force. (**c**) Increasing the exposure time expands the patterned area and density of particles within the illuminated region as indicated for 2–120-s exposure times. (**d**) Close-up view of the immobilized spots with 20, 30, and 120-s exposure times, scale bars = 1 μm (© American Chemical Society [56])

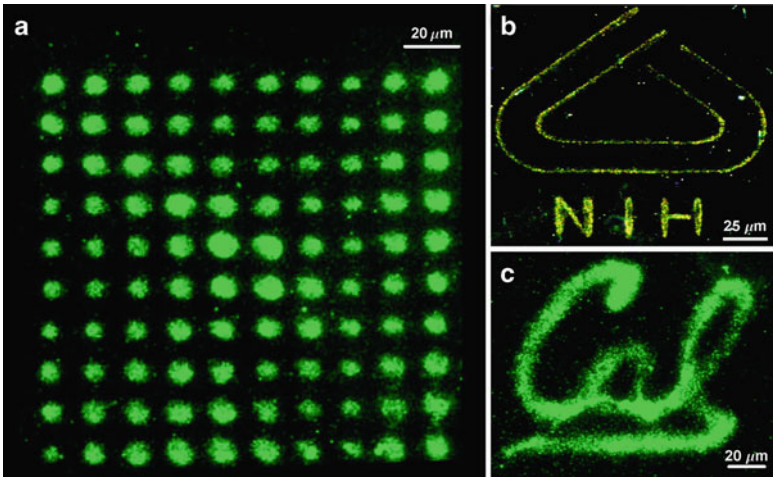

Fig. 6.11 Large area patterning of nanoparticles using NanoPen. Patterning of 90-nm diameter gold nanoparticles in the form of (**a**) a 10 × 10 array, over 150 × 140 μm^2, (**b**) "NIH" logo over 160 × 140 μm^2,and (**c**) "CAL" logo over 140 × 110 μm^2, all using a commercial light projector (<10 W/cm^2 light intensity) (© American Chemical Society [56])

patterning of SERS sensing structures. Moreover, it has been demonstrated that the field enhancement increases rapidly as the distance between nanoparticles decreases; therefore, the closely-packed structures of the NanoPen patterned gold particles provide an extremely effective SERS substrate.

Figure 6.12 a shows a two-dimensional Raman scan (at 1,570 cm^{-1} Raman shift) of a NanoPen patterned structure covered with a layer of Rhodamine 6G molecules dried on the surface. It is observed that positions with higher nanoparticle concentration display much stronger enhancements relative to areas with lower particle density. The enhancement factor of NanoPen patterned SERS substrates has been characterized to be more than 10^7 by comparing the Raman signal from a background 10 mM solution of BPE molecules to the Raman signal detected from a 100 nM solution of BPE dried on Nanopen patterned SERS substrates, as depicted in Fig. 6.12b. The BPE Raman signals were collected with 4 s integration time using a 30 mW, 785 nm laser source. Moreover, Raman signals were detected from the SERS substrates with concentrations as small as picomolars.

6.3 Conclusion

One of the main capabilities that the integration of optical and microfluidic systems enables is the ability to address micro and nanoscale particles. Here, OET was presented as an optically controlled manipulation technique for large-scale and flexible manipulation of micro and nanoscopic particles. By integrating the optical and electrical forces, OET is capable of trapping and patterning particles with

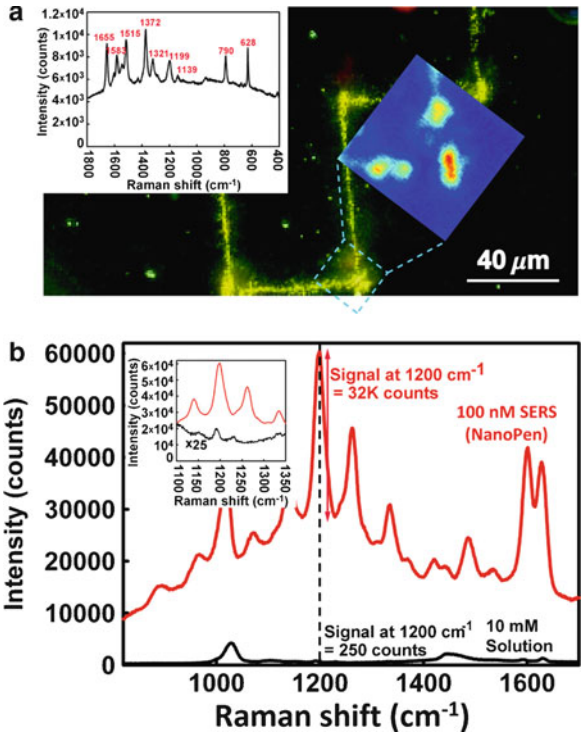

Fig. 6.12 Surface-enhanced Raman spectroscopy (SERS) using NanoPen patterned metallic nanoparticles. (**a**) Measurement of Rhodamine 6G (R6G) spectrum using the NanoPen patterned gold nanoparticle (mixture of 60 and 90 nm sizes). The two-dimensional scan of Raman signal at ~1,570 cm^{-1} Raman shift indicated a large enhancement in the areas with higher density nanoparticles. The inset shows a typical Raman spectrum of R6G achieved. (**b**) Characterization of Raman enhancement factor for the BPE molecules. The Raman signal level is compared with 100 nM BPE solution on NanoPen SERS structures (*red line*) to the Raman signal from a benchmark 10 mM solution of BPE (*black line*). The inset shows a zoom-in of 1,100–1,350 cm^{-1} Raman shift range with the benchmark 10 mM solution signal multiplied by 25 to make it more visible. The calculated enhancement factor at the 1,200 cm^{-1}Raman shift peak is ~10^7 (© American Chemical Society [56])

optical power intensities 5 orders of magnitude lesser than the optical tweezers. Moreover, by defining the light-induced virtual electrode using a spatial light modulator, OET can address various particles in a real-time reconfigurable fashion over large working areas. We also discussed some of the recent advances in this field such as manipulation of biological objects in highly conductive media using phOET, light-induced electroporation of single cells, manipulation and trapping of air bubbles, and large-scale patterning of SERS sensors for in-situ chemical and biological sensing. These advances further enhance OET's capability as a versatile optofluidic system for manipulation and monitoring of single cells and lab-on-a-chip biosensing applications.

References

1. N. Chronis and L. P. Lee, "Electrothermally activated SU-8 microgripper for single cell manipulation in solution," *IEEE Journal of Microelectromechanical Systems*, vol. 14, pp. 857–863, 2005.
2. C. G. Keller and R. T. Howe, "Hexsil tweezers for teleoperated micro-assembly," in *Tenth Annual IEEE International Workshop on Micro Electro Mechanical Systems (MEMS)*, 1997, pp. 72–77.
3. C. J. Kim, A. P. Pisano, and R. S. Muller, "Silicon-processed overhanging microgripper," *IEEE Journal of Microelectromechanical Systems*, vol. 1, pp. 31–36, 1992.
4. J. Cheng, E. L. Sheldon, L. Wu, M. J. Heller, and J. P. O'Connell, "Isolation of cultured cervical carcinoma cells mixed with peripheral blood cells on a bioelectronic chip," *Analytical Chemistry*, vol. 70, pp. 2321–2326, 1998.
5. P. R. C. Gascoyne and J. V. Vykoukal, "Dielectrophoresis-based sample handling in general-purpose programmable diagnostic instruments," *Proceedings of the IEEE*, vol. 92, pp. 22–42, 2004.
6. P. R. C. Gascoyne, X.-B. Wang, Y. Huang, and F. F. Becker, "Dielectrophoretic separation of cancer cells from blood," *IEEE Transactions on Industry Applications*, vol. 33, pp. 670–678, 1997.
7. R. Pethig, M. S. Talary, and R. S. Lee, "Enhancing traveling-wave dielectrophoresis with signal superposition," *IEEE Engineering in Medicine and Biology Magazine*, vol. 22, pp. 43–50, 2003.
8. R. Krupke, F. Hennrich, H. von Lohneysen, and M. M. Kappes, "Separation of metallic from semiconducting single-walled carbon nanotubes," *Science*, vol. 301, pp. 344–347, Jul 18 2003.
9. S. Y. Lee, T. H. Kim, D. I. Suh, J. E. Park, J. H. Kim, C. J. Youn, B. K. Ahn, and S. K. Lee, "An electrical characterization of a hetero-junction nanowire (NW) PN diode (n-GaN NW/p-Si) formed by dielectrophoresis alignment," *Physica E-Low-Dimensional Systems & Nanostructures*, vol. 36, pp. 194–198, Feb 2007.
10. P. A. Smith, C. D. Nordquist, T. N. Jackson, T. S. Mayer, B. R. Martin, J. Mbindyo, and T. E. Mallouk, "Electric-field assisted assembly and alignment of metallic nanowires," *Applied Physics Letters*, vol. 77, pp. 1399–1401, Aug 28 2000.
11. S. J. Papadakis, Z. Gu, and D. H. Gracias, "Dielectrophoretic assembly of reversible and irreversible metal nanowire networks and vertically aligned arrays," *Applied Physics Letters*, vol. 88, 2006.
12. C. R. Cabrera and P. Yager, "Continuous concentration of bacteria in a microfluidic flow cell using electrokinetic techniques," *Electrophoresis*, vol. 22, pp. 355–362, 2001.
13. C. R. Barry, J. Gu, and H. O. Jacobs, "Charging process and coulomb-force-directed printing of nanoparticles with sub-100-nm lateral resolution," *Nano Letters*, vol. 5, pp. 2078–2084, 2005.
14. N. G. Loucaides, A. Ramos, and G. E. Georghiou, "Trapping and manipulation of nanoparticles by using jointly dielectrophoresis and AC electroosmosis," *Journal of Physics: Conference Series*, vol. 100, 2008.
15. A. Y. Fu, C. Spence, A. Scherer, F. H. Arnold, and S. R. Quake, "A microfabricated fluorescence-activated cell sorter," *Nature Biotechnology*, vol. 17, pp. 1109–1111, 1999.
16. H. Lee, A. M. Purdon, V. Chu, and R. M. Westervelt, "Controlled assembly of magnetic nanoparticles from magnetotactic bacteria using microelectromagnets arrays," *Nano Letters*, vol. 4, pp. 995–998, 2004.
17. M. Tanase, L. A. Bauer, A. Hultgren, D. M. Silevitch, L. Sun, D. H. Reich, P. C. Searson, and G. J. Meyer, "Magnetic alignment of fluorescent nanowires," *Nano Letters*, vol. 1, pp. 155–158, 2001.
18. A. K. Bentley, J. S. Trethewey, A. B. Ellis, and W. C. Crone, "Magnetic manipulation of copper-tin nanowires capped with nickel ends," *Nano Letters*, vol. 4, pp. 487–490, 2004.

19. D. D. Carlo, L. Y. Wu, and L. P. Lee, "Dynamic single cell culture array," *Lab on a Chip*, vol. 6, pp. 1445–1449, 2006.
20. A. R. Wheeler, W. R. Throndset, R. J. Whelan, A. M. Leach, R. N. Zare, Y. H. Liao, K. Farrell, I. D. Manger, and A. Daridon, "Microfluidic device for single-cell analysis," *Analytical Chemistry*, vol. 75, pp. 3581–3586, 2003.
21. A. Y. Fu, H. P. Chou, C. Spence, F. H. Arnold, and S. R. Quake, "An integrated microfabricated cell sorter," *Analytical Chemistry*, vol. 74, pp. 2451–2457, 2002.
22. A. Ashkin, "Acceleration and trapping of particles by radiation pressure," *Physical Review Letters*, vol. 24, p. 156, 1970.
23. A. Ashkin, M. Dziedzic, and T. Yamane, "Optical trapping and manipulation of single cells using infrared-laser beams," *Nature*, vol. 330, pp. 769–771, 1987.
24. S. K. Mohanty, A. Rapp, S. Monajembashi, P. K. Gupta, and K. O. Greulich, "Comet assay measurements of DNA damage in cells by laser microbeams and trapping beams with wavelengths spanning a range of 308 nm to 1064 nm," *Radiation Research*, vol. 157, pp. 378–385, 2002.
25. K. C. Neuman, E. H. Chadd, G. F. Liou, K. Bergman, and S. M. Block, "Characterization of photodamage to *Escherichia coli* in optical traps," *Biophysical Journal*, vol. 77, pp. 2856–2863, 1999.
26. P. Y. Chiou, A. T. Ohta, and M. C. Wu, "Massively parallel manipulation of single cells and microparticles using optical images," *Nature*, vol. 436, pp. 370–372, Jul 21 2005.
27. S. Adachi, *Optical properties of crystalline and amorphous semiconductors: materials and fundamental principles*: Boston: Kluwer Academic Publishers, 1999.
28. R. Schwarz, F. Wang, and M. Reissner, "Fermi level dependence of the ambipolar diffusion length in silicon thin film transistors," *Applied Physics Letters*, vol. 63, pp. 1083–1085, 1993.
29. A. Jamshidi, P. J. Pauzauskie, P. J. Schuck, A. T. Ohta, P. Y. Chiou, J. Chou, P. Yang, and M. C. Wu, "Dynamic manipulation and separation of individual semiconducting and metallic nanowires," *Nature Photonics*, vol. 2, pp. 85–89, 2008.
30. H. Y. Hsu, A. T. Ohta, P. Y. Chiou, A. Jamshidi, S. L. Neale, and M. C. Wu, "Phototransistor-based optoelectronic tweezers for dynamic cell manipulation in cell culture media," *Lab on a Chip*, vol. 10, pp. 165–172, DOI 10.1039/b906593h, 2010.
31. Y. Higuchi, T. Kusakabe, T. Tanemura, K. Sugano, T. Tsuchiya, and O. Tabata, "Manipulation system for nano/micro components integration via transportation and self-assembly," in *Conference on Micro Electro Mechanical Systems*, 2008.
32. X. Miao and L. Y. Lin, "Trapping and manipulation of biological particles through a plasmonic platform," *IEEE Journal of Selected Topics in Quantum Electronics: Special Issue on Biophotonics*, vol. 13, pp. 1655–1662, 2007.
33. X. Miao, B. K. Wilson, S. H. Pun, and L. Y. Lin, "Optical manipulation of micron/submicron sized particles and biomolecules through plasmonics," *Optics Express*, vol. 16, p. 13517, 2008.
34. W. Wang, Y. H. Lin, T. F. Guo, and G. B. Lee, "Manipulation of biosamples and microparicles using optical images on polymer devices," in *IEEE 22nd International Conference on Micro Electro Mechanical Systems*, 2009.
35. P. Y. Chiou, W. Wong, J. C. Liao, and M. C. Wu, "Cell addressing and trapping using novel optoelectronic tweezers," IEEE International Conference on Micro Electro Mechanical Systems, Technical Digest, 17th, Maastricht, Netherlands, Jan. 25–29, 2004, pp. 21–24, 2004.
36. W. Choi, S. H. Kim, J. Jang, and J. K. Park, "Lab-on-a-display: a new microparticle manipulation platform using a liquid crystal display (LCD)," *Microfluidics and Nanofluidics*, vol. 3, pp. 217–225, 2007.
37. H. Hwang, Y. J. Choi, W. Choi, S. H. Kim, J. Jang, and J. K. Park, "Interactive manipulation of blood cells using a lens-integrated liquid crystal display based optoelectronic tweezers system," *Electrophoresis*, vol. 29, pp. 1203–1212, 2008.
38. P. Y. Chiou, A. T. Ohta, A. Jamshidi, H. Y. Hsu, and M. C. Wu, "Light-actuated AC electroosmosis for nanoparticle manipulation," *Journal of Microelectromechanical Systems*, vol. 17, 2008.

39. J. K. Valley, A. Jamshidi, A. T. Ohta, H. Y. Hsu, and M. C. Wu, "Operational regimes and physics present in optoelectronic tweezers," *Journal of Microelectromechanical Systems*, vol. 17, 2008.
40. S. L. Neale, M. Mazilu, J. I. B. Wilson, K. Dholakia, and T. F. Krauss, "The resolution of optical traps created by light induced dielectrophoresis (LIDEP)," *Optics Express*, vol. 15, pp. 12619–12626 2007.
41. A. T. Ohta, P. Y. Chiou, T. H. Han, J. C. Liao, U. Bhardwaj, E. R. B. McCabe, F. Q. Yu, R. Sun, and M. C. Wu, "Dynamic cell and microparticle control via optoelectronic tweezers," *Journal of Microelectromechanical Systems*, vol. 16, pp. 491–499, 2007.
42. A. T. Ohta, P. Y. Chiou, H. L. Phan, S. W. Sherwood, J. M. Yang, A. N. K. Lau, H. Y. Hsu, A. Jamshidi, and M. C. Wu, "Optically-controlled cell discrimination and trapping using optoelectronic tweezers," *IEEE Journal of Selected Topics in Quantum Electronics*, vol. 243, pp. 235–243, 2007.
43. Y.-S. Lu, Y.-P. Huang, J. A. Yeh, C. Lee, and Y.-H. Chang, "Controllability of non-contact cell manipulation by image dielectrophoresis (iDEP)," *Optical and Quantum Electronics*, vol. 37, pp. 1385–1395, 2005.
44. H. Y. Hsu, A. T. Ohta, P. Y. Chiou, A. Jamshidi, and M. C. Wu, "Phototransistor-based optoelectronic tweezers for cell manipulation in highly conductive solution," in *Solid-State Sensors, Actuators and Microsystems Conference*, 2007.
45. H. Y. Hsu, H. Lee, S. Pautot, K. Yu, S. Neale, A. T. Ohta, A. Jamshidi, J. Valley, E. Isocaff, and M. C. Wu, "Sorting of differentiated neurons using phototransistor based optoelectronic tweezers for cell replacement therapy of neurodegenerative diseases," in *The 15th International Conference on Solid-State Sensors, Actuators and Microsystems* Denver, Colorado, 2009.
46. S. L. Neale, Z. Fan, A. T. Ohta, A. Jamshidi, J. K. Valley, H. Y. Hsu, A. Javey, and M. C. Wu, "Optofluidic assembly of red/blue/green semiconductor nanowires," in *Conference on Lasers and Electro-Optics* 2009.
47. A. T. Ohta, A. Jamshidi, P. J. Pauzauskie, H. Y. Hsu, P. Yang, and M. C. Wu, "Trapping and transport of silicon nanowires using lateral-field optoelectronic tweezers," in *Conference on Lasers and Electro-Optics (CLEO)*, Baltimore, MD, 2007, pp. 828–829.
48. A. T. Ohta, S. L. Neale, H. Y. Hsu, J. K. Valley, and M. C. Wu, "Parallel assembly of nanowires using lateral-field optoelectronic tweezers," in *2008 IEEE/LEOS International Conference on Optical MEMS and Nanopotonics*, 2008.
49. P. J. Pauzauskie, A. Jamshidi, J. K. Valley, J. Satcher, J. H. and M. C. Wu, "Parallel trapping of multiwalled carbon nanotubes with optoelectronic tweezers," *Applied Physics Letters*, vol. 95, pp. 113104–1, 2009.
50. A. Jamshidi, H. Y. Hsu, J. K. Valley, A. T. Ohta, S. Neale, and M. C. Wu, "Metallic nanoparticle manipulation using optoelectronic tweezers," in *IEEE 22nd International Conference on Micro Electro Mechanical Systems*, 2009.
51. M. Hoeb, J. O. Radler, S. Klein, M. Stutzmann, and M. S. Brandt, "Light-induced dielectrophoretic manipulation of DNA," *Biophysical Journal*, vol. 93, pp. 1032–1038, 2007.
52. Y.-H. Lin, C.-M. Chang, and G.-B. Lee, "Manipulation of single DNA molecules by using optically projected images," *Optics Express*, vol. 17, pp. 15318–15329, 2009.
53. J. K. Valley, S. Neale, H. Y. Hsu, A. T. Ohta, A. Jamshidi, and M. C. Wu, "Parallel single-cell light-induced electroporation and dielectrophoretic manipulation," *Lab on a Chip*, vol. 9, pp. 1714–1720, 2009.
54. Y.-H. Lin and G. B. Lee, "An optically induced cell lysis device using dielectrophoresis," *Applied Physics Letters*, vol. 94, p. 033901, 2009.
55. Y.-H. Lin and G.-B. Lee, "Optically induced flow cytometry for continuous microparticle counting and sorting," *Biosensors and Bioelectronics*, vol. 24, pp. 572–578, 2008.
56. A. Jamshidi, S. L. Neale, K. Yu, P. J. Pauzauskie, P. J. Schuck, J. K. Valley, H. Y. Hsu, A. T. Ohta, and M. C. Wu, "NanoPen: dynamic, low-power, and light-actuated patterning of nanoparticles," *Nano Letters*, vol. 9, pp. 2921–2925, 2009.

57. S. Park, C. Pan, T.-H. Wu, C. Kloss, S. Kalim, C. E. Callahan, M. Teitell, and E. P. Y. Chiou, "Floating electrode optoelectronic tweezers: light-driven dielectrophoretic droplet manipulation in electrically insulating oil medium," *Applied Physics Letters*, vol. 92, pp. 151101–1511013, 2008.
58. H. Hwang, Y. Oh, J. J. Kim, W. Choi, J. K. Park, S. H. Kim, and J. Jang, "Reduction of nonspecific surface-particle interactions in optoelectronic tweezers," *Applied Physics Letters*, vol. 92, p. 3, 2008.
59. G. J. Shah, A. T. Ohta, P. Y. Chiou, M. C. Wu, and C.-J. Kim, "EWOD-driven droplet microfluidic device integrated with optoelectronic tweezers as an automated platform for cellular isolation and analysis," *Lab on a Chip*, vol. 9, pp. 1732–1739, 2009.
60. G. J. Shah, P. Y. Chiou, J. Gong, A. T. Ohta, J. B. Chou, M. C. Wu and C.-J. Kim, in Proc. IEEE Int. Conf. MEMS, Istanbul, Turkey, pp. 129–132, 2006.
61. T. B. Jones, *Electromechanics of Particles*: Cambridge University Press, 1995.
62. P. Y. Chiou, A. T. Ohat, A. Jamshidi, H.-Y. Hsu, and J. W. Chou, M. C., "Light-actuated AC electroosmosis for optical manipulation of nanoscale particles," in *Proceedings of Solid-State Sensor, Actuator, and Microsystems Workshop* 2006, pp. 56–59.
63. J. Voldman, "Electrical forces for microscale cell manipulation," *Annual Review of Biomedical Engineering*, vol. 8, pp. 425–454, 2006.
64. G. Fuhr, H. Glassera, T. Müllera and T. Schnellea, "Cell manipulation and cultivation under a.c. electric field influence in highly conductive culture media", vol. 1201, pp. 353–360, 1994.
65. J. A. Lundqvist, F. Sahlin, M. A. I. Aberg, A. Stromberg, P. S. Eriksson, and O. Orwar, "Altering the biochemical state of individual cultured cells and organelles with ultramicroelectrodes," *Proceedings of the National Academy of Sciences*, vol. 95, pp. 10356–10360, 1998.
66. E. Neumann, M. Schaeferridder, Y. Wang, and P. H. Hofschneider, "Gene transfer into mouse lyoma cells by electroporation in high electric fields," *EMBO Journal*, vol. 1, pp. 841–845, 1982.
67. H. Q. He, D. C. Chang, and Y. K. Lee, "Using a micro electroporation chip to determine the optimal physical parameters in the uptake of biomolecules in HeLa cells," *Bioelectrochemistry*, vol. 70, pp. 363–368, 2007.
68. L. A. MacQueen, M. D. Buschmann, and M. R. Wertheimer, "Gene delivery by electroporation after dielectrophoretic positioning of cells in a non-uniform electric field," *Bioelectrochemistry*, vol. 72, pp. 141–148, 2008.
69. J. C. Weaver, "Electroporation of cells and tissue," *IEEE Transactions on Plasma Science*, vol. 28, pp. 24–33, 2000.
70. P. Garstecki, M. J. Fuerstman, M. A. Fischbach, S. K. Sia, and G. M. Whitesides, "Mixing with bubbles: a practical technology for use with portable microfluidic devices," *Lab on a Chip*, vol. 6, pp. 207–212, 2006.
71. S. Z. Hua, F. Sachs, D. X. Yang, and H. D. Chopra, "Microfluidic actuation using electrochemically generated bubbles," *Analytical Chemistry*, vol. 74, pp. 6392–6396, 2002.
72. T. K. Jun and C. J. Kim, "Microscale pumping with traversing bubbles in microchannels," *Journal of Applied Physics*, vol. 83, 1998.
73. M. Prakash and N. Gershenfeld, "Microfluidic bubble logic," *Science*, vol. 315, pp. 832–835, 2007.
74. J. A. Schwartz, J. V. Vykoukal, and P. R. C. Gascoyne, "Droplet-based chemistry on a programmable micro-chip," *Lab on a Chip*, vol. 4, pp. 11–17, 2004.
75. M. G. Pollack, A. D. Shenderov, and R. B. Fair, "Electrowetting-based actuation of droplets for integrated microfluidics," *Lab on a Chip*, vol. 2, pp. 96–101, 2002.
76. P. Y. Chiou, H. Moon, H. Toshiyoshi, C. J. Kim, and M. C. Wu, "Light actuation of liquid by optoelectrowetting," *Sensors and Actuators A: Physical*, vol. 104, pp. 222–228, 2003.
77. G. L. Liu, J. Kim, Y. Lu, and L. P. Lee, "Optofluidic control using photothermal nanoparticles," *Nature Materials*, vol. 5, 2006.

78. D. E. Kataoka, "Patterning liquid flow on the microscopic scale," *Nature*, vol. 402, pp. 794–797, 1999.
79. K. T. Kotz, K. A. Noble, and G. W. Faris, "Optical microfluidics," *Applied Physics Letters*, vol. 85, pp. 2658–2660, 2004.
80. A. T. Ohta, A. Jamshidi, J. K. Valley, H. Y. Hsu, and M. C. Wu, "Optically actuated thermocapillary movement of gas bubbles on an absorbing substrate," *Applied Physics Letters*, vol. 91, p. 074103, 2007.
81. A. Jamshidi, A. T. Ohta, J. K. Valley, H. Y. Hsu, S. L. Neale, and M. C. Wu, "Optofluidics and optoelectronic tweezers," in *Proceedings of the SPIE*, 2008.
82. V. S. Ilchenko and A. B. Matsko, "Optical resonators with whispering-gallery modes-part II: applications," *IEEE Journal Of Selected Topics in Quantum Electronics*, vol. 12, pp. 15–32, 2006.
83. A. Ymeti, J. Greve, P. V. Lambeck, T. Wink, S. W. F. M. van Hovell, T. A. M. Beumer, R. R. Wijn, R. G. Heideman, V. Subramaniam, and J. S. Kanger, "Fast, ultrasensitive virus detection using a young interferometer sensor," *Nano Letters*, vol. 7, pp. 394–397, 2007.
84. M. Lee and P. M. Fauchet, "Two-dimensional silicon photonic crystal based biosensing platform for protein detection," *Optics Express*, vol. 15, pp. 4530–4535, 2007.
85. R. Karlsson, "SPR for molecular interaction analysis: a review of emerging application areasy," *Journal of Molecular Recognition*, vol. 17, pp. 151–161, 2004.
86. D. Erickson, S. Mandal, A. H. J. Yang, and B. Cordovez, "Nanobiosensors: optofluidic, electrical and mechanical approaches to biomolecular detection at the nanoscale," *Microfluid Nanofluid*, vol. 4, pp. 33–52, 2008.
87. K. L. Kelly, E. Coronado, L. L. Zhao, and G. C. Schatz, "The Optical Properties of Metal Nanoparticles: The Influence of Size, Shape, and Dielectric Environment", *J. Phys. Chem. B*, vol. 107, pp 668–677, 2003.
88. K. Kneipp, Y. Wang, H. Kneipp, L. T. Perelman, I. Itzkan, R. R. Dasari, and M. S. Feld, "Single molecule detection using surface-enhanced Raman scattering (SERS)," *Physical Review Letters*, vol. 78, pp. 1667–1670, 1997.
89. S. Nie and S. R. Emory, "Probing single molecules and single nanoparticles by surface-enhanced Raman scattering," *Science*, vol. 275, pp. 1102–1106, 1997.
90. L. Tong, M. Righini, M. U. Gonzalez, R. Quidantbc, and M. Kall, "Optical aggregation of metal nanoparticles in a microfluidic channel for surface-enhanced Raman scattering analysis," *Lab on a Chip*, vol. 9, pp. 193–195, 2009.
91. K. Svoboda and S. M. Block, "Optical trapping of metallic Rayleigh particles," *Optics Letters*, vol. 19, pp. 930–932, 1994.
92. P. M. Hansen, V. K. Bhatia, N. Harrit, and L. Oddershede, "Expanding the optical trapping range of gold nanoparticles," *Nano Letters*, vol. 5, pp. 1937–1942, 2005.
93. Y. Seol, A. E. Carpenter, and T. T. Perkins, "Gold nanoparticles: enhanced optical trapping and sensitivity coupled with significant heating," *Optics Letters*, vol. 31, pp. 2429–2431, 2006.
94. L. Zheng, S. Li, J. P. Brody, and P. J. Burke, "Manipulating nanoparticles in solution with electrically contacted nanotubes using dielectrophoresis," *Langmuir*, vol. 20, pp. 8612–8619, 2004.
95. A. E. Cohen and W. E. Moerner, "Method for trapping and manipulating nanoscale objects in solution", APL, vol. 86, pp. 093109, 2005.
96. E. Ewen Smith and G. Dent, *Modern Raman Spectroscopy: A Practical Approach* Wiley, 2005.
97. R. L. McCreery, *Raman Spectroscopy for Chemical Analysis* Wiley-Interscience, 2000.
98. W. Yang, J. Hulteen, G. C. Schatz, and R. P. V. Duyne, "A surface-enhanced hyper-Raman and surface-enhanced Raman scattering study of trans-1,2-bis(4-pyridyl)ethylene adsorbed onto silver film over nanosphere electrodes. Vibrational assignments: Experiment and theory," *The Journal of Chemical Physics*, vol. 104, pp. 4313–4323, 1996.

99. N. J. Durr, T. Larson, D. K. Smith, B. A. Korgel, K. Sokolov, and A. Ben-Yakar, "Two-photon luminescence imaging of cancer cells using molecularly targeted gold nanorods," *Nano Letters*, vol. 7, pp. 941–945, 2007.
100. H. Wang, T. B. Huff, D. A. Zweifel, W. He, P. S. Low, A. Wei, and J.-X. Cheng, "In vitro and in vivo two-photon luminescence imaging of single gold nanorods," *Proceedings of the National Academy of Sciences*, vol. 102, pp. 15752–15756, 2005.
101. N. Shen, D. Datta, C. B. Schaffer, P. LeDuc, D. E. Ingber, and E. Mazur, "Ablation of cytoskeletal filaments and mitochondria in live cells using a femtosecond laser nanoscissor," *Mechanics & Chemistry of Biosystems*, vol. 2, pp. 17–25, 2005.
102. A. Vogel, J. Noack, G. Hüttman, and G. Paltauf, "Mechanisms of femtosecond laser nanosurgery of cells and tissues," *Applied Physics B: Lasers and Optics*, vol. 81, pp. 1015–1047, 2005.
103. S. A. Johnson and T. Hunter, "Kinomics: methods for deciphering the kinome," *Nature Methods*, vol. 2, pp. 17–25, 2005.
104. P. O. Brown and D. Botstein, "Exploring the new world of the genome with DNA microarrays," *Nature Genetics*, vol. 21, pp. 33–37, 1999.
105. M. Schena, D. Shalon, R. W. Davis, and P. O. Brown, "Quantitative monitoring of gene expression patterns with a complementary DNA microarray," *Science*, vol. 270, pp. 467–470, 1995.
106. J. N. Anker, W. P. Hall, O. Lyandres, N. C. Shah, J. Zhao, and R. P. Van Duyne, "Biosensing with plasmonic nanosensors," *Nature Materials*, vol. 7, pp. 442–453, 2008.
107. M. H. Huang, S. Mao, H. Feick, H. Yan, Y. Wu, H. Kind, E. Weber, R. Russo, and P. Yang, "Room-temperature ultraviolet nanowire nanolasers," *Science*, vol. 292, pp. 1897–1899, 2001.
108. A. Javey, J. Guo, Q. Wang, M. Lundstrom, and H. Dai, "Ballistic carbon nanotube field-effect transistors," *Nature*, vol. 424, pp. 654–657, 2003.
109. P. Yang, "The chemistry and physics of semiconductor nanowires," *MRS Bulletin*, vol. 30, pp. 85–91, 2005.
110. B. Sun, A. T. Findikoglu, M. Sykora, D. J. Werder, and V. I. Klimov, "Hybrid photovoltaics based on semiconductor nanocrystals and amorphous silicon," *Nano Letters*, vol. 9, pp. 1235–1241, 2009.
111. R. D. Piner, J. Zhu, F. Xu, S. Hong, and C. A. Mirkin, ""Dip-Pen" nanolithography," *Science*, vol. 283, pp. 661–663, 1999.
112. K. Salaita, Y. Wang, and C. A. Mirkin, "Applications of dip-pen nanolithography," *Nature Nanotechnology*, vol. 145, pp. 145–155, 2007.
113. B. Basnar and I. Willner, "Dip-Pen-nanolithographic patterning of metallic, semiconductor, and metal oxide nanostructures on surfaces," *Small*, vol. 5, p. 28, 2009.
114. D. S. Ginger, H. Zhang, and C. A. Mirkin, "The evolution of Dip-Pen nanolithography," *Angewandte Chemie (International ed. in English)*, vol. 43, p. 30, 2004.
115. B. Li, C. F. Goh, X. Zhou, G. Lu, H. Tantang, Y. Chen, C. Xue, F. Y. C. Boey, and H. Zhang, "Patterning colloidal metal nanoparticles for controlled growth of carbon nanotubes," *Advanced Materials*, vol. 20, pp. 4873–4878, 2008.
116. H. T. Wang, O. A. Nafday, J. R. Haaheim, E. Tevaarwerk, N. A. Amro, R. G. Sanedrin, C. Y. Chang, F. Ren, and S. J. Pearton, "Toward conductive traces: Dip Pen nanolithography of silver nanoparticle-based inks," *Applied Physics Letters*, vol. 93, p. 143105, 2008.
117. J. C. Hulteen, D. A. Treichel, M. T. Smith, M. L. Duval, T. R. Jensen, and R. P. V. Duyne, "Nanosphere lithography: size-tunable silver nanoparticle and surface cluster arrays," *The Journal of Physical Chemistry. B*, vol. 103, pp. 3854–3863, 1999.
118. J. H. Ahn, H. S. Kim, K. J. Lee, S. Jeon, S. J. Kang, Y. Sun, R. G. Nuzzo, and J. A. Rogers, "Heterogeneous Three-dimensional electronics by use of printed semiconductor nanomaterials," *Science*, vol. 314, pp. 1754–1757, 2006.

119. Z. Fan, J. C. Ho, Z. A. Jacobson, R. Roie Yerushalmi, R. L. Alley, H. Razavi, and A. Ali Javey, "Wafer-scale assembly of highly ordered semiconductor nanowire arrays by contact printing," *Nano Letters*, vol. 8, pp. 20–25, 2008.
120. H. X. He, Q. G. Li, Z. Y. Zhou, H. Zhang, W. Huang, S. F. Y. Li, and Z. F. Liu, "Fabrication of microelectrode arrays using microcontact printing," *Langmuir*, vol. 16, p. 9683, 2000.
121. Y. Xia and G. M. Whitesides, "Soft lithography," *Annual Review of Material Science*, vol. 28, p. 153, 1998.
122. R. Yerushalmi, J. C. Ho, Z. A. Jacobson, and A. Javey, "Generic nanomaterial positioning by carrier and stationary phase design," *Nano Letters*, vol. 7, pp. 2764–2768, 2007.
123. E. Rabani, D. R. Reichman, P. L. Geissler, and L. E. Brus, "Drying-mediated self-assembly of nanoparticles," *Nature*, vol. 426, pp. 271–274, 2003.
124. C. P. Collier, R. J. Saykally, J. J. Shiang, S. E. Henrichs, and J. R. Heath, "Reversible tuning of silver quantum dot monolayers through the metal-insulator transition," *Science*, vol. 277, pp. 1978–1981, 1997.
125. R. C. Hayward, D. A. Saville, and I. A. Aksay, "Electrophoretic assembly of colloidal crystals with optically tunable micropatterns," *Nature*, vol. 404, pp. 56–59, 2000.
126. S. J. Williams, A. Kumar, and S. T. Wereley, "Electrokinetic patterning of colloidal particles with optical landscapes," *Lab on a Chip*, vol. 8, pp. 1879–1882, 2008.
127. P. J. Pauzauskie, A. Radenovic, E. Trepagnier, H. Shroff, P. Yang, and J. Liphardt, "Optical trapping and integration of semiconductor nanowire assemblies in water," *Nature Materials*, vol. 5, pp. 97–101, 2006.
128. S. Ito, H. Yoshikawa, and H. Masuhara, "Optical patterning and photochemical fixation of polymer nanoparticles on glass substrates," *Applied Physics Letters*, vol. 78, pp. 2566–2568, 2001.
129. B. K. Wilson, M. Hegg, X. Miao, G. Cao, and L. Y. Lin, "Scalable nano-particle assembly by efficient light-induced concentration and fusion," *Optics Express*, vol. 16, pp. 17276–17281, 2008.
130. Nanopartz, "Nanopartz accurate spherical gold nanoparticles," 2008.

Chapter 7
Nano-metric Single-Photon Detector for Biochemical Chips

Edoardo Charbon and Yuki Maruyama

7.1 CMOS SPAD: From Concept to Design

Quantitative sensing has become a necessary ingredient in many research activities and industrial design. Quantitative detection of elementary particles, including protons, electrons, positrons, and photons, is an emerging area of research in both the sensing and imaging communities. In addition to quantitative imaging, another important ingredient has been speed [1], among the reasons for this trend, the creation of new biomedical and/or improved diagnostics techniques based on optical imaging. In addition, The emergence of more powerful and faster light sources has only accelerated this trend and placed an increasing burden on conventional image sensors. As a result, researchers have turned toward sensors capable of photomultiplication.

There exist many non-solid-state implementations of such sensors, most notably photomultiplier tubes (PMTs) and microchannel or multichannel plates (MCPs) [2]. The common operating principle of a PMT is shown in Fig. 7.1. Incoming photoelectrons are accelerated and progressively multiplied by impact ionization until a detectable current is generated. Generally, voltages up to several hundred volts and a micro-pressure chamber are required.

The main limitation of PMTs is their size that prevents use in large arrays. A solution to this problem is the use of a MCP, a device in which photoelectron multiplication is achieved inside a micro-chamber. Figure 7.2 shows the principle of photoelectron multiplication in the micro-chamber, usually of micrometric size. The figure also shows the arrangement of the pixels in an array. Photoelectrons are then projected onto a phosphor screen and imaged onto a CCD (not shown in the figure).

E. Charbon (✉)
TU Delft, Delft, The Netherlands
e-mail: e.charbon@tudelft.nl

S. Carrara (ed.), *Nano-Bio-Sensing*,
DOI 10.1007/978-1-4419-6169-3_7, © Springer Science+Business Media, LLC 2011

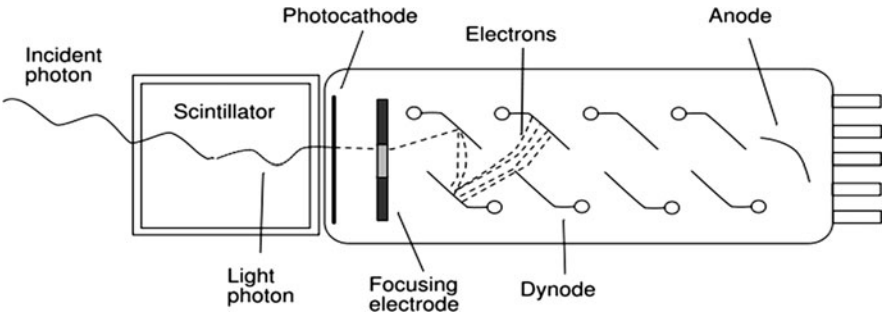

Fig. 7.1 Schematic diagram of photomultiplier tube (PMT). Incident photons may be in the visible spectrum or down converted to visible ones via, e.g., a scintillator. Photoelectrons are progressively multiplied by impact ionization. Source: Wikipedia

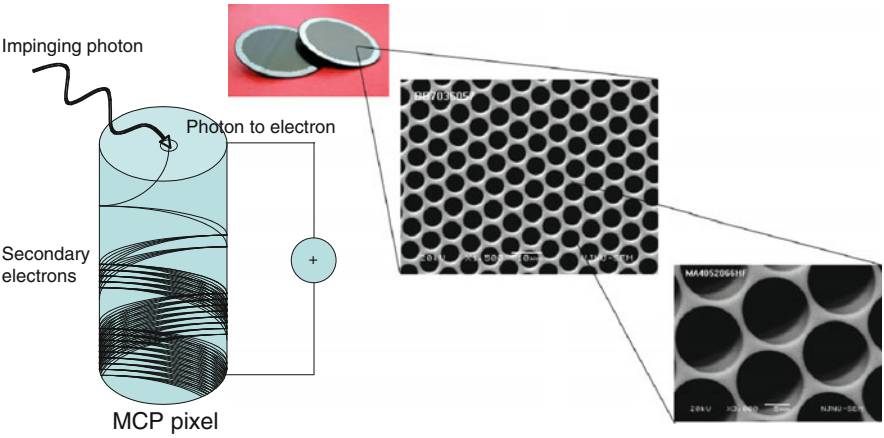

Fig. 7.2 Structure of a micro-channel plate (MCP) sensor: pixel (*left*); plate SEM micrograph (*right*). Secondary electrons are generally reconverted onto photons via a phosphor screen and imaged onto a CCD (not shown in the figure). Source: Tectra GmbH

Multiple photon and electron conversions involved in MCPs may result in a relatively low timing accuracy of the overall imager and elevated complexity, thus potentially barring these devices from mass-production.

Solid-state alternatives to these sensors have been known for some time and among them the leading device is the avalanche photodiode (APD). The basic principle of operation in these devices is also avalanching via impact ionization, whereas the atoms being ionized are not from a metal electrode but from the lattice of a semiconductor. Since the structure of the lattice is very different from that of a metallic mass, naturally, the operating conditions are also fundamentally different. The main and more evident difference is the voltage required to achieve the critical electric field necessary for a sustainable avalanche, which is generally lower in APDs, due to the smaller dimensions of the device. Known since the 1960s [3],

silicon APDs have seen a rapid growth in the last decade due to their applicability in imaging and telecommunications.

Silicon photomultipliers (SiPMs) are of particular interest due to the compatibility with PMTs in terms of format, while being significantly thinner. SiPMs are essentially arrays of APDs whose avalanche currents are collected and cumulated together onto a single output, resulting in high optical gain. The APDs are generally biased above breakdown so as to operate in so-called Geiger mode. Each APD operating in this mode is known as single-photon avalanche diode (SPAD). SiPMs, as PMTs, have optical gains in the hundreds; the main drawback of these devices, however, is a relatively complex amplification scheme and/or complex ancillary electronics. In addition, specific semiconductor technologies are often required. Nevertheless, SiPMs offer flexible, versatile, and relatively low-cost solutions to imaging where sensitivity, low noise, and high time-resolution are needed.

SPADs can also operate independently, whereby their outputs are not combined into one but independently processed. In a SPAD, the optical gain is virtually infinite; thus, it enables the detection of single photons. The time resolution is generally in excess of 100 ps, whereas the detection cycle, dominated by the dead time of the device, is generally of the order of 10–100 ns. Recently, CMOS-compatible SPADs have emerged; thanks to the high level of integration possible in CMOS, large arrays of single-photon detectors may be built and unprecedented levels of parallelism may be achieved. In this chapter, we focus on these devices and review some of the latest results achieved using SPAD arrays in deep-submicron CMOS technologies

In Geiger mode of operation, SPADs exhibit a virtually infinite optical gain; however, a mechanism must be provided to quench the avalanche. There exist several techniques to accomplish quenching, classified in active and passive quenching. The simplest approach is the use of a ballast resistance. The avalanche current causes the diode reverse bias voltage to drop below breakdown, thus pushing the junction to linear avalanching and even pure accumulation mode. After quenching, the device requires a certain recovery time, to return to the initial state. The quenching and recovery times are collectively known as *dead time*. Figure 7.3 shows a cross-section of the SPAD and a possible passive quenching scheme.

Since the first successful integration of SPADs in CMOS, large arrays of SPAD pixels have been developed [4]. Current developments in more advanced CMOS technologies have demonstrated full scalability of SPAD devices, a 25-μm pitch, and dead time as low as 32 ns [5–8]. The sensitivity, characterized in SPADs as photon detection probability (PDP), can exceed 25–60%. The noise, measured in SPADs as dark count rate (DCR), can be as low as a few Hertz [5].

Thanks to these properties, CMOS SPAD arrays have been proposed for imaging where speed and/or event timing accuracy are critical. Such applications range from fluorescence-based imaging, such as Förster Resonance Energy Transfer (FRET), fluorescence lifetime imaging microscopy (FLIM) [9], and fluorescence correlation spectroscopy (FCS) [10], to voltage-sensitive dye (VSD)-based imaging [11, 12], particle image velocimetry (PIV) [13], instantaneous gas imaging, [14], etc.

7.2 SPAD Nanodesign

The design of SPADs in view of their use in large arrays requires careful sizing of the quenching circuitry to ensure that three issues be addressed. First, in the case of passive quenching, the quenching resistor, represented in Fig. 7.3 by transistor Mq, must be sufficiently high to enable the voltage pulse caused by the avalanche to be detectable by a simple circuitry, such as a digital inverter. At the same time, the resistance of Mq must be contained during recharge to ensure that the recharge time, proportional to the RqC product, be in line with the overall frame rate requirements. Note that C is the overall capacitance at the SPAD evaluation node (the anode in this case). Second, the dead time of the SPAD (quenching + recharge time) must be long enough to respect the after-pulsing requirements of the pixel [15]. Third, the current required by the avalanche discharge and recharge should be contained so as to minimize the effects of IR drops across a SPAD array when exposed with significant light intensities. This could have the effect of locally and temporarily reducing the voltage on V_{OP}, thus interfering with other SPAD's functionality and sensitivity and generating electrical cross-talk between pixels.

Actually, if one wants to build SPAD arrays for complex operations, such as FLIM or FCS, one may consider adding integrated counters and stopwatches on chip. The additional level of complexity introduced in the sensor my be offset by the reduced data communication rate between chip and external world as well as an increased capture efficiency of the sensor system, thanks to increased parallelism. An example of this concept is the LASP sensor that includes 128 × 128 SPAD pixels and an array of 32 time-to-digital converters (TDCs) that serve 128 columns, each TDC being shared among four columns [16]. This sensor enabled to determine photon time-of-arrival upon detection at the chip level for the first time and showed to be useful in FLIM and FCS applications when combined with a microscope.

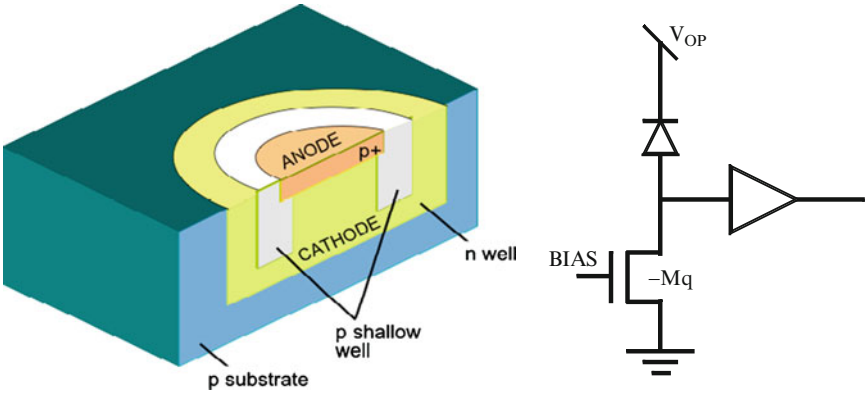

Fig. 7.3 CMOS single-photon avalanche diode (SPAD). Cross-section of the device (*left*); passive quenching is achieved by means of a ballast resistor obtained with a properly biased transistor, Mq (*right*)

More advanced levels of parallelism were achieved later in other designs, such as RADHARD2, whereby each pixel includes a dedicated 1-bit counter capable of operating at up to 833,000 frames per second [17]. Figure 7.4 shows a micrograph of the chip implemented in CMOS technology for imaging of earth's airglow in space.

The FP7 project MEGAFRAME has gone even further, creating a chip where each pixel includes a SPAD, a counter, and a TDC [18–21]. Naturally, these sensors present a challenge when it comes to designing the readout system that needs to be fast and often introduce some degree of compression. The development of architectures that support time-correlated modes with some degree of resource sharing is currently underway in many research groups. The main trade-off is at the architectural level, due to the nature of the signal generated by SPADs. Application-specific optimal architectures are possible, provided a model of the application is built to characterize the performance of the sensor a priori. The sharing of resources may involve a number of pixels, say 4 or 16, or on-demand sharing based upon the reaction of SPADs may be used. Other trade-offs may include the complexity of the time discriminator itself.

Creating a new family of SPADs implemented in 130-nm CMOS technology was a necessary condition for the implementation of large arrays of pixels implementing complex functionality, such as high resolution TDCs and counters. The detector implemented in [18] is capable of a time resolution in the excess of 125 ps while exhibiting a DCR of a few hundred to a few tens of Hertz.

The active area of the detector is less than 6 μm in diameter while the minimum pitch possible with this technology is of the order of tens of micrometers due to the fact that a guard ring must be built around the active area to prevent premature edge

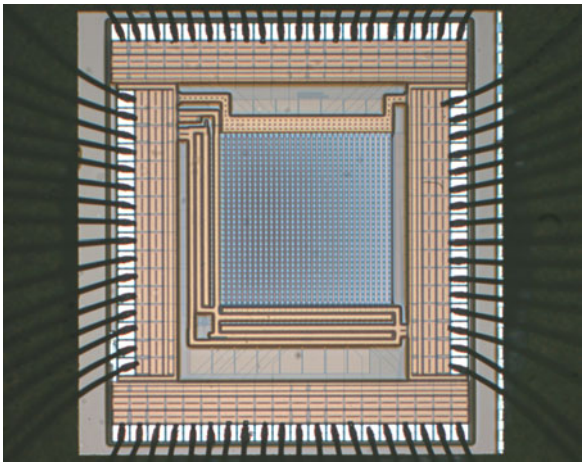

Fig. 7.4 Photomicrograph of RADHARD2, a fully parallel SPAD pixel architecture implemented in CMOS technology for space applications

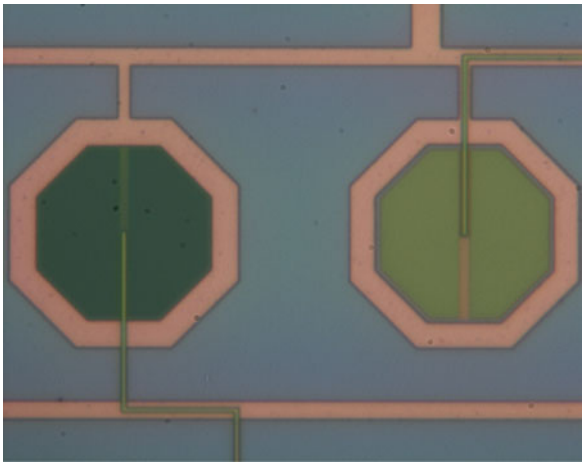

Fig. 7.5 Nanometric SPAD micrograph. The octagonal sensitive area is surrounded by a guard ring to prevent premature edge breakdown

breakdown. A micrograph of a SPAD developed in 130-nm CMOS technology is shown in Fig. 7.5. The p $\pm$ n junction is designed so as to achieve a breakdown voltage at about 10 V. Operating the device at a few volts above breakdown, Geiger mode of operation is achieved, whereby this voltage is known as excess bias voltage. In these devices, photon detection probabilities up to 50% can be reached when an appropriate excess bias voltage is used.

SPADs implemented in nanometric technologies have other advantages, besides miniaturization. Due to the small dimensions of the junction and the consequently smaller number of charges involved, the photonic emission during an avalanche is reduced. Thus, the probability of it being picked up by other nearby devices is lower. This results in smaller optical crosstalk that is a growing problem with SPAD scaling. As a side effect, electrical crosstalk is also reduced, since the same charges required by the avalanche are also reduced, thus causing smaller IR voltage drops across large arrays of switching SPADs. To quantify this effect, consider an excess bias voltage V_e and a breakdown voltage V_{bd}, then the number of charges N involved in an avalanche is approximated as

$$N = \frac{V_e C}{q},$$

where q is the charge of an electron or a hole and C the average capacitance of the junction. The avalanche current and its propagation throughout the junction is a complex function and depends on a number of factors [22, 23]. However, a rough approximation can be made with the assumption that the charges involved in the avalanche flow as a pulse of width Δt. In this case,

$$I = \frac{\mathrm{d}Q}{\mathrm{d}t} \cong \frac{\Delta Q}{\Delta t} = \frac{Nq}{\Delta t}.$$

With the same rough approximation, one can compute a bound to the overall IR voltage drop due to avalanching on an array of M SPADs as

$$V_{\mathrm{IR}} < M \cdot I \cdot R,$$

where R is the resistance of the average path from source to the SPADs in the array and it is assumed that all SPADs are triggered at the same time; this latter assumption is not realistic but it represents the worst case scenario. The main technique to reduce this parasitic effect is the use of localized capacitive buffers on pixel and large decoupling capacitances on column and chip level. These measures have the effect of storing the charge required by the avalanche upon triggering, in local capacitances that are recharged over long periods of time with much less overall current and discharged in Δt when needed. Assuming a relatively small internal resistance of the local capacitor, the average current reduction is given by the ratio

$$\frac{I}{I_{\mathrm{eff}}} \cong \frac{\langle t_{\mathrm{A}} \rangle}{\Delta t},$$

where $\langle t_{\mathrm{A}} \rangle$ is the average time between photon detections, which in turn is a function of photon flux and the DCR. Even when the overall resistance of the local system is low, it is not negligible; thus, an avalanche discharge temporarily lowers voltage V_{OP}. This temporarily reduces the PDP; however, since the avalanche is subsequently followed by a period of dead time, it has no or negligible impact on the length of the detection cycle. The impact on neighboring pixels may, however, be felt as an electrical crosstalk or cross-blanking, as the temporary reduction in PDP will act on them. Local capacitive buffering must thus be designed to make sure that the excess bias voltages in other pixels be unaffected by other pixel discharges.

Optical crosstalk, though improved by the reduced number of charges involved in each avalanche, may become more prominent and even dominant over electrical crosstalk when the distances between SPADs shrink.

Even though the main purpose of SPAD scaling is the potential increase of functionality on pixel at no cost in terms of pitch. It is conceivable that new generations of deep-submicron SPAD arrays will keep the pitch constant or slightly reduce it. In this case, due to the aforementioned capacitance reduction at the junction, optical crosstalk will be kept in check; electrical crosstalk will be controllable by means of proper power management and sufficient capacitive buffering. An effect that could be of more concern is localized heating that could in principle change the value of V_{bd} and thus artificially modify excess bias voltage V_{e}. The effect of this is a locally different PDP as well as a non-uniform DCR. An example

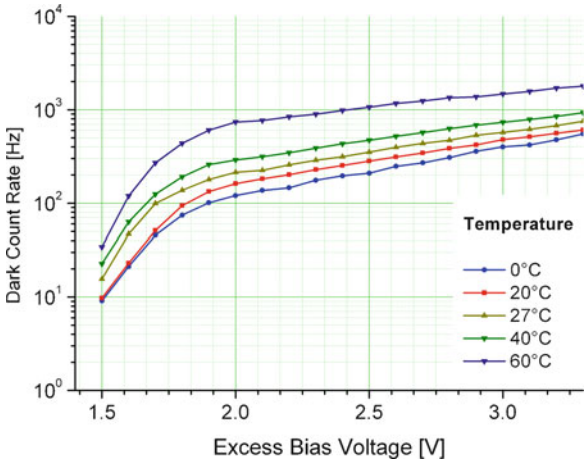

Fig. 7.6 Typical dark count rate in a SPAD as a function of temperature and excess bias voltage. The diameter of the active area of this device, implemented in 0.35-μm CMOS technology, is 10 μm

of this dependency can be seen in Fig. 7.6, where DCR is plotted as a function of temperature and excess bias voltage; the plot is derived from [15] for a SPAD with an active area of 10 μm in diameter.

The PDP uniformity has been measured to be better than 1% in sensors with up to 16-k pixels, whereby each pixel consisted of medium-complexity functionality [16]. The plot of Fig. 7.7 shows the landscape of PDP measured over an array of 1-k pixels all operating simultaneously under a blanket of uniform, collimated white light [4].

Similar results have been obtained in large-complexity pixels (up to 500 transistors per pixel) over arrays of comparable sizes.

7.3 From Single-Photon Detection to Molecular Imaging

Among time-correlated imaging methods, time-correlated single-photon counting (TCSPC) is perhaps one of the most used in bioimaging. Multiple exposures are employed to reconstruct the statistical response of matter to sharp and powerful light pulses. The study of calcium at the cellular level has made intensive use of fluorescent Ca^{2+} indicator dyes. Examples of heavily used dyes or fluorophores are Oregon Green Bapta-1 (OGB-1), Green Fluorescent Protein (GFP), and many others. Calcium concentration can be determined precisely by measuring the lifetime of the response of the corresponding fluorophore, when excited at a given wavelength. Lifetime is generally characterized using FLIM. There exist several flavors of FLIM based on how lifetime is characterized or based on the excitation mode.

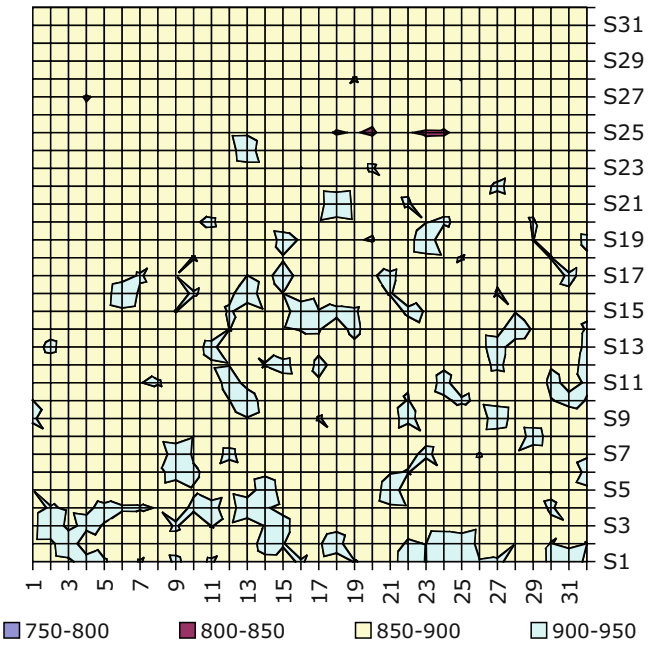

Fig. 7.7 PDP uniformity in a 1-k pixel sensor implemented in a submicron technology with minimal on-pixel functionality. The plot shows the count rate in kHz

In [24], a two-photon FLIM setup was employed based on a SPAD array capable of a time resolution of 79 ps at a system level. The sensor made it possible to fit the lifetime dependency of OGB-1 on Ca^{2+} using a triple exponential fit. Unlike previous approaches that exploit detectors with lower resolution [9], our model required neither calibration factors nor corrections of any kind, thus proving the robustness of the measurement system.

$$I_k = \frac{1}{2}\left[\frac{1+\mathrm{e}^{-T/t_k}}{1-\mathrm{e}^{-T/t_k}} - \mathrm{erf}\left(\frac{\sigma_{\mathrm{IRF}}}{\sqrt{2}\tau_k} - \frac{t}{\sqrt{2}\sigma_{\mathrm{IRF}}}\right)\right] \times \exp\left(-\frac{t}{\tau_k} + \frac{\sigma_{\mathrm{IRF}}^2}{2\tau_k^2}\right), k = \{f, i, s\},$$

where I_{k} represents the intensity of fluorescence emission, k denotes the fast "f," intermediate "i," and slow "s" components of it. Terms σ_{IRF}^2 and τ_k denote the variance of the instrument response function (IRF) and the corresponding lifetime time constants, respectively. In addition, thanks to this model and the capability of detecting photon arrival with high timing resolution, it was possible to measure free Ca^{2+} concentration and dye dissociation constant precisely [24].

As discussed earlier, the applicable fabrication technology for SPADs has reached and passed the 100-nm barrier. However, many difficulties still remain, such as leakage current and tunneling effects, due to the shallow implantation depth and its high doping concentration. How to overcome these issues will become interesting

topics for further miniaturization of SPADs. On the other hand, many researchers are investigating not only miniaturization but also diversification. These are RF devices, Power devices, Sensor/Actuator/MEMS, and Biochips. In this section, possibilities of SPAD-based devices especially for biochip will be discussed.

Generally, CCD/CMOS image sensors are combined with lenses to take an optical image. However, for on-site and point-of-care applications, miniaturized low-cost devices are suitable. Thus, expensive and relatively bulky optical components need to be removed. Contact imaging might be a solution to solve these problems. In contact imaging setup, measuring object such as living cells will be placed onto the photodetector directly or in proximity to the photodetector. Additionally, multiple sensing such as local pH value, ion concentration, and local temperature as well as high sensitive optical imaging can be performed. Using parallel information from the same position in the sample will improve measurement precision and even the description of new phenomena, thus opening the way to discoveries and new possibilities for biologists, biochemists, and medical doctors.

A DNA chip is a sensor generally used for encompassing gene expression and genetic diagnosis based on single nucleotide polymorphisms (SNP). Needless to say, fluoresce detection method is commonly used for DNA detection. However, fluorescence detection may not be the best way for on-site application due to size and cost issues.

A number of new approaches for direct label-free detection of DNA have been proposed and demonstrated. Most of them are based on electrochemical detection capacitance measurements [25], and potentiometric detection. Among them, field-effect transistor (FET)-type DNA sensors have been extensively studied. The use of FET as DNA sensors was first studied as ion-sensitive field-effect transistor (ISFET) [26]. In the case of DNA detection, the sensors detect surface potential changes induced by a DNA molecule's negative charge in aqueous solutions. The negative charge on the gate electrode/membrane induces a threshold voltage shift as a result of immobilization and hybridization [27–29]. Thus, DNA molecules are detected without using any fluorescence labels. A standard CMOS-compatible label-free DNA sensor [30, 31] is a good candidate since it can be integrated with signal processing circuitry and optical imaging devices, including SPADs. Label-free detection enables the use of inexpensive and portable genetic analysis tools instead of expensive and a bulky fluorescence detection-based systems.

Researchers have also been investigating label-free CMOS potentiometric detection-type sensors for genetic diagnosis for some time now. An example of that activity is a label-free 32×32 CMOS DNA sensor array fabricated in a 1-poly 1-metal CMOS technology by Hitachi ULSI Systems Co. In this sensor, each pixel comprises a junction and a follower similar to conventional CMOS active pixel sensors. As a result, significantly increased throughput and easy operation can be achieved. In addition, thanks to its portability, advanced DNA analysis can in principle be performed everywhere and doctors will provide the most suitable treatment tailored to each patient based on his/her genetic information.

The chip architecture is shown in Fig. 7.8. The detection system consists of electrolyte, an external reference electrode, and a CMOS DNA image sensor

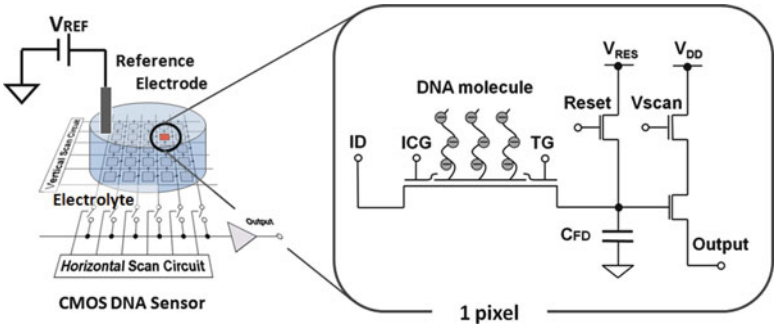

Fig. 7.8 Concept of label-free CMOS DNA sensing. The system consists of electrolyte, a reference electrode, and the sensor. The surface potential changes induced by DNA molecules are detected as a two-dimensional image

containing a scanning circuit. The DNA molecules are immobilized on top of the sensing surface and the surface potential change is transformed into an electrical charge packet by charge transfer technique [32]. The array image sensor was also applied for pH detection [33].

To immobilize DNA molecules, sensor surface functionalization is necessary before performing DNA detection. At first, the Silicon Nitrate sensor surface was silanized using 3-aminopropyltriethoxysilane to introduce an amino group. Then, amino-silanized sensor surface and amino-linked probe DNA were connected via glutaraldehyde crosslinking. The base sequence of the probe DNA was 5′-CTAGACCTTGAAGTGTCTGATC-3′ (22 bases), and an amino-base was attached at 3′-end. The base sequence of the target DNA for full mismatch was 5′-CTAGACCTTGAAGTGTCTGATC-3′ (22 bases), and full match DNA was 5′-GATCAGACACTTCAAGGTCTAG-3′ (22 bases). This surface modification and immobilization process has clearly drawn in [28].

Then, DNA immobilization and hybridization on the silanized surface are performed and detected as shown in Fig. 7.9. Figure 7.9b shows the sensor output after silanization. Then, probe DNA was immobilized on the region A, B, and C as shown in Fig. 7.9c. Finally, the fully mismatched DNA and fully matched DNA were placed on the regions B and C, and hybridized as shown in Fig. 7.9d. The detected image indicates the amount of immobilized DNA and its location. Output voltage shifts of 76.4 ± 16.5 mV and 64.5 ± 15.7 mV were detected after immobilization and hybridization of DNA molecules. The DNA densities were estimated as $6.3 \pm 1.4 \times 10^8$ cm^{-2} and $5.3 \pm 1.3 \times 10^8$ cm^{-2}, respectively. However, a similar voltage shift was observed from region B where fully mismatched DNA was placed. It is caused by the non-specific binding of mismatched DNA due to the inefficient blocking and washing. This problem will be solved by optimization or fundamental change of the surface treatment process.

Integration with microfluidics will enhance the value of the CMOS sensor for diagnosis and clinical use as shown in Fig. 7.10. The microfluidics will facilitate sample handling, purification, separation, and mixing, which are performed by highly skilled operators.

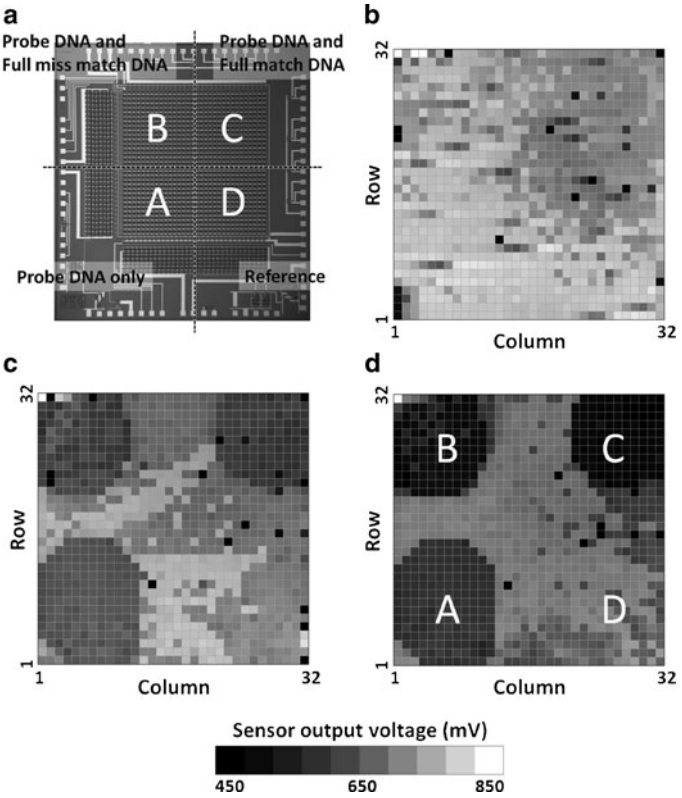

Fig. 7.9 Sensor output after each surface modification process. (**a**) Sample location. (**b**) After silanization. (**c**) After immobilization of probe DNA. (**d**) After hybridization of fully mismatched DNA and fully matched DNA. Grayscale code at the bottom

As a preliminary experiment, chemiluminescence was observed at room temperature using SPADs and a Y-shaped millimetric channel under laminar flow condition [34] as shown in Fig. 7.11. The millimetric channel was made by PDMS and PMMA expecting future integrated device. The experiment involved Enhanced Chemiluminescence (ECL) plus Western Blotting Detection Regents and a HRP-linked Anti-Mouse IgG diluted in Tris buffered saline. The reaction takes place in the laminar flow surface where the two solutions are mixed through diffusion. A portion of chemiluminescence is collected by the objective lens placed externally. Thanks to single-photon detectability of SPADs, chemiluminescence distribution in the channel was successfully observed at room temperature. This result indicates the possibility of an immune reaction-based analysis system using SPADs. In this experiment, channel and SPADs are set up separately, while microfluidics need to be integrated with CMOS circuitry and SPADs.

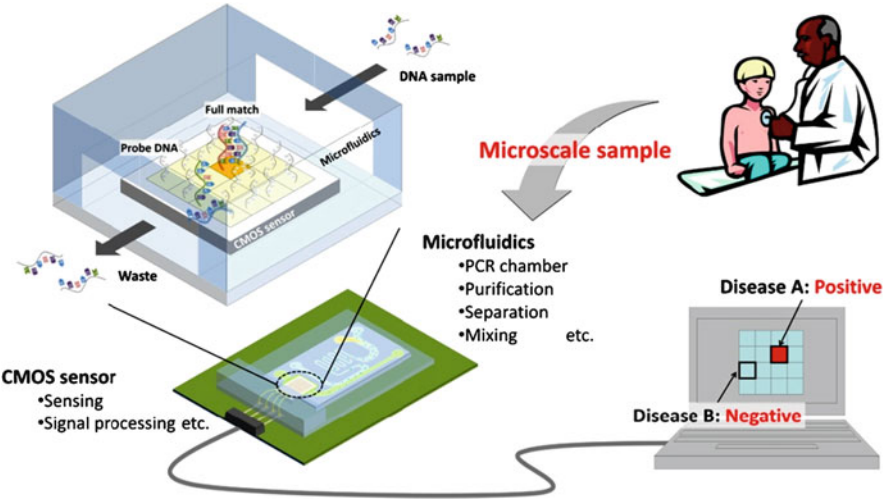

Fig. 7.10 Schematic of the CMOS sensor platform integrated with microfluidics for portable DNA diagnosis system

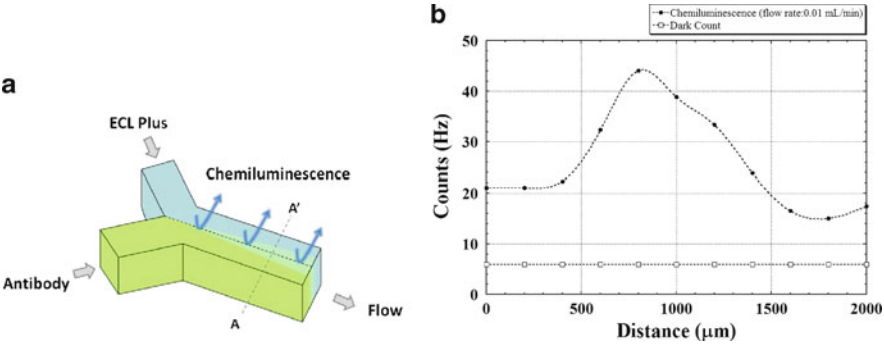

Fig. 7.11 Chemiluminescence detection using a Y-shaped millimetric channel (height: 2 mm width: 2 mm). (**a**) Image of photon distribution emission. (**b**) Photon emission distribution in a sweep perpendicular to the flow (A-A′)

Generally, bare Si wafer or glass wafers are used for microfluidics fabrication process. However, generally researchers use few mm^2 size dice since it was made by commercial foundry. Thus, a post-CMOS process needs to be modified as described in previous work [35–37]. Researchers have also used 4-.in wafer as a support wafer throughout the entire process. Then, main chip and several dummy dice were fixed onto the support wafer. Setting the same height is important for photolithography using contact aligner. The microfluidics was made by SU-8 photoresist directly onto the SPAD array as shown in Fig. 7.12.

Combining composite semiconductor with CMOS SPADs is appropriate to sense infrared as well as visible light. Recently, an impact ionization-based solid-state

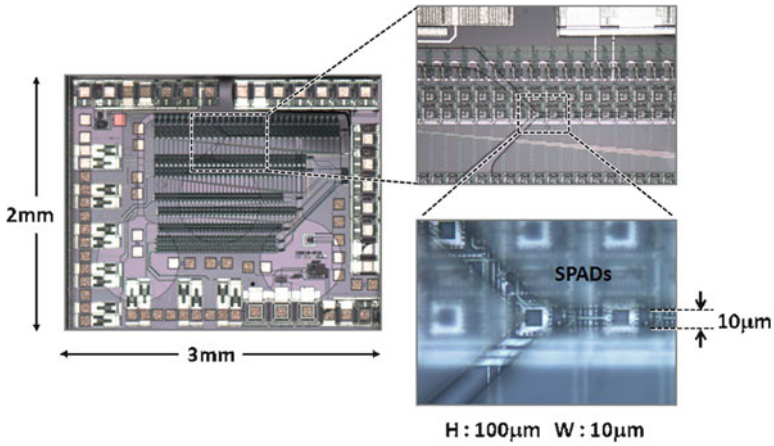

Fig. 7.12 Integrated Y-shaped microfluidics onto SPADs. The microfluidics was made by SU-8 photoresist. (This work was performed as a collaborative research with Prof. K. Sawada at Toyohashi University of Technology, Japan)

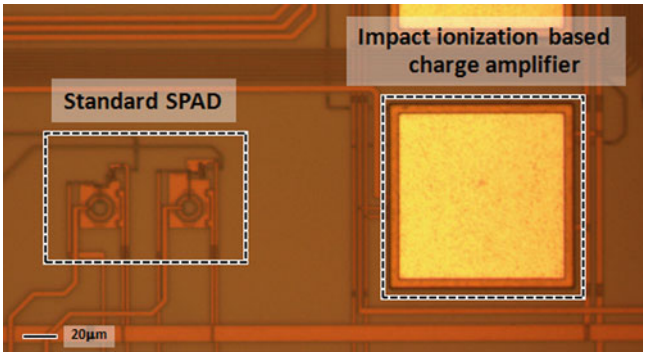

Fig. 7.13 Standard SPAD and impact ionization-based charge amplifier for biosensing applications. Charge injection part is designed by means of ISFET-type device. Charge injection, charge amplifier, and CMOS inverter are underneath the extended gate ISFET

current amplifier has been reported [38]. The device was built in silicon and involved InGaAs APDs as a current source. The impact ionization-based charge amplifier might be another future research perspective of SPADs. For example, the signal charge due to the biomolecule binding might be injected by means of ISFET to the amplification region. Amplified current is converted to digital pulse and it is readout through an implemented counter such as CMOS SPADs. One of the test devices for the proposed biosensor is shown in Fig. 7.13, which was fabricated in standard CMOS technology. Standard SPADs are implemented on same chip; however, further work is currently being completed and will be reported in the near future.

7.4 Conclusions

With the creation of CMOS SPADs, it is possible today to achieve great levels of miniaturization without compromising time resolution and overall speed. Not only are large arrays of photon counters now possible but very high dynamic range and timing accuracy have become feasible as well. Thanks to these advances, applications requiring time-resolved single-photon detection are now possible using low-cost CMOS detectors. We have outlined some of these applications and discussed system issues related to these and novel applications in the field of bio-medical imaging.

Acknowledgments The authors are grateful to the AQUA group's graduate students and alumni, Dmitri L. Boiko, Lucio Carrara, Matt Fishburn, Marek Gersbach, Mohammad A. Karami, Estelle Labonne, Cristiano Niclass, Maximilian Sergio, as well as Emile Dupont, Ulrike Lehmann, Martin Lanz, and Giovanni Nicoletti, and to the members of the MEGAFRAME consortium.

References

1. E. Charbon, "Will CMOS Imagers Ever Need Ultra-High Speed?", *IEEE Int. Conf. Solid-State Integrated-Circuit Technol.*, pp. 1975–1980, Oct. 2004.
2. J. McPhate, J. Vallerga, A. Tremsin, O. Siegmund, B. Mikulec, A. Clark, "Noiseless Kilo-hertz-Frame-Rate Imaging Detector Based on Microchannel Plates Readout with Medipix2 CMOS Pixel Chip", *Proc. SPIE*, Vol. 5881, pp. 88–97, 2004.
3. R. H. Haitz, "Studies on Optical Coupling between Silicon p-n Junctions", *Solid-State Electron.*, Vol. 8, pp. 417–425, 1965.
4. C. Niclass, A. Rochas, P. A. Besse, E. Charbon, "Design and Characterization of a CMOS 3-D Image Sensor Based on Single Photon Avalanche Diodes", *IEEE J. Solid-State Circuits*, Vol. 40, N. 9, pp 1847–1854, Sept. 2005.
5. C. Niclass, M. Sergio, E. Charbon, "A Single Photon Avalanche Diode Array Fabricated on Deep-Submicron CMOS Technology", *Design Test Europe (DATE)*, Mar. 2006.
6. D. Mosconi, D. Stoppa, L. Pacheri, L. Gonzo, A. Simoni, "CMOS Single-Photon Avalanche Diode Array for Time-Resolved Fluorescence Detection", *Proc. ESSCIRC*, Oct. 2006.
7. C. Niclass, M. Sergio, E. Charbon, "A CMOS 64x48 Single Photon Avalanche Diode Array with Event-Driven Readout", *Proc. ESSCIRC*, Oct. 2006.
8. M. Sergio, C. Niclass, E. Charbon, "A 128x2 CMOS Single-Photon Streak Camera with Timing-Preserving Latchless Pipeline Readout", *Proc. ISSCC*, pp. 120–121, Feb. 2007.
9. A. V. Agronskaia, L. Tertoolen, H. C. Gerritsen, "Fast Fluorescence Lifetime Imaging of Calcium in Living Cells", *J. Biomed. Optics*, Vol. 9, N. 6, pp. 1230–1237, Nov./Dec. 2004.
10. P. Schwille, U. Haupts, S. Maiti, W. W. Webb, "Molecular Dynamics in Living Cells Observed by Fluorescence Correlation Spectroscopy with One- and Two-Photon Excitation", *Biophys. J.*, Vol. 77(4), pp. 2251–2265, 1999.
11. A. Grinvald, D. Shoham, A. Shmuel, D. Glaser, I. Vanzetta, E. Shtoyerman, H. Slovin, A. Sterkin, C. Wijnbergen, R. Hildesheim and A. Arieli, "*In-Vivo* Optical Imaging of Cortical Architecture and Dynamics", *Modern Techniques in Neuroscience Research*, U. Windhorst and H. Johansson (Eds), Springer, 2001 pp. 893–969. New York.
12. Jonathan A. N. Fisher, Eugene F. Civillico, Diego Contreras, and Arjun G. Yodh, "In Vivo Fluorescence Microscopy of Neuronal Activity in Three Dimensions by Use of Voltage-Sensitive Dyes", *Optics Lett.*, Vol. 29, N. 1, pp 71–73, Jan. 2004.

13. S. Eisenberg, W. Reckers, B. Wieneke, "Visualization and PIV Measurements of High-Speed Flows and Other Phenomena with Novel Ultra-High-Speed CCD Camera", *Proc. SPIE*, Vol. 4948, pp. 671–676, 2002.
14. Reckers W., Schwab H, Weiten C, Befrui B, Kneer R, "Investigation of Flame Propagation and Cyclic Combustion Variations in a DISI Engine Using Synchronous High-Speed Visualization and Cylinder Pressure Analysis", *Proc. Intl. Symposium für Verbrennungdiagnostik*, pp. 27–32, 2002.
15. C. Niclass, M. Sergio, E. Charbon, "A Single Photon Avalanche Diode Array Fabricated in 0.35um CMOS and Based on an Event-Driven Readout for TCSPC Experiments", *SPIE Optics East, Boston*, Oct. 2006
16. C. Niclass, C. Favi, T. Kluter, M. Gersbach, E. Charbon, "A 128×128 Single-Photon Imager with on-Chip Column-Level 10-bit Time-to-Digital Converter Array", *IEEE J. Solid-State Circuits*, Vol. 43, N. 12, pp. 2977–2989, Dec. 2008.
17. L. Carrara, C. Niclass, N. Scheidegger, H. Shea, E. Charbon, "A Gamma, X-Ray and High Energy Proton Radiation-Tolerant CMOS Image Sensor for Space Applications", *IEEE Intl. Solid-State Circuits Conference (ISSCC)*, pp. 40–41, Feb. 2009.
18. M. Gersbach, J. Richardson, C. Niclass, L. Grant, R. Henderson, E. Charbon, "A Low-Noise Single-Photon Detector Implemented in a 130nm CMOS Imaging Process", *Solid-State Electron.*, Vol. 53, N. 7, pp. 803–808, July 2009.
19. J. Richardson, R. Walker, L. Grant, D. Stoppa, F. Borghetti, E. Charbon, M. Gersbach, R. K. Henderson, "A 32x32 50ps Resolution 10 Bit Time to Digital Converter Array in 130nm CMOS for Time Correlated Imaging", *Custom Integrated Circuits Conference*, pp. 77–80, Sep. 2009.
20. M. Gersbach, Y. Maruyama, E. Labonne, J. Richardson, R. Walker, L. Grant, R. K. Henderson, F. Borghetti, D. Stoppa, E. Charbon, "A Parallel 32x32 Time-to-Digital Converter Array Fabricated in a 130nm Imaging CMOS Technology", *IEEE European Solid-State Circuits Conference (ESSCIRC)*, pp. 196–199, Sep 2009.
21. D. Stoppa, F. Borghetti, J. Richardson, R. Walker, L. Grant, R. K. Henderson, M. Gersbach, E. Charbon, "A 32x32-Pixel Array with In-Pixel Photon Counting and Arrival Time Measurement in the Analog Domain", *IEEE European Solid-State Circuits Conference (ESSCIRC)*, pp. 204–207, Sep. 2009.
22. A. Rochas, "Single photon avalanche diodes in CMOS technology," Ph.D. Thesis, EPF-Lausanne, 2003.
23. A. Spinelli, A. L. Lacaita, "Physics and Numerical Simulation of Single Photon Avalanche Diodes", *Trans. Electron. Devices*, Vol. 44, N. 11, Nov. 1997.
24. M. Gersbach, D. L. Boiko, C. Niclass, C. Petersen, E. Charbon, "Fast Fluorescence Dynamics in Nonratiometric Calcium Indicators", *Optics Lett.*, Vol. 34, N. 3, pp. 362–364, Feb. 2009.
25. C. Stagni, C. Guiducci, L. Benini, B. Ricco, S. Carrara, B. Samori, C. Paulus, M. Schienle, M. Augustyniak, R. Thewes, "CMOS DNA Sensor Array With Integrated A/D Conversion Based on Label-Free Capacitance Measurement", *IEEE J. Solid-State Circuit*, Vol. 41, pp. 2956–2964, 2006.
26. P. Bergveld, *Sens. Actuator B Chem*, "Thirty years of ISFETOLOGY. What Happened in the Past 30 Years and What May Happen in the Next 30 Years", Vol. 88, pp. 1–20, 2003.
27. F. Uslu, S. Ingebrandt, D. Mayer, S. Bocker-Meffert, M. Odenthal, A. Offenhausser, *Biosens. Bioelectron*, "Labelfree Fully Electronic Nucleic Acid Detection System based on a Field-effect Transistor Device", Vol. 19, pp. 1723–1731, 2004.
28. T. Sakata, M. Kamahori, Y. Miyahara, "DNA Analysis Chip Based on Field-Effect Transistors" *Jpn. J. Appl. Phys.*, Vol. 44, pp. 2854–2859, 2005.
29. D. Goncalves, D. M. F. Frazeres, V. Chu, J. P. Conde, "Detection of DNA and Proteins using Amorphous Silicon Ion-sensitive Thin-film Field Effect Transistors", *Biosens. Bioelectron.*, Vol. 24, pp. 545–551, 2008.

30. D. S. Kim, Y. T. Jeong, H. J. Park, J. K. Shin, P. Choi, J. H. Lee, G. Lim, "An FET-type Charge Sensor for Highly Sensitive Detection of DNA Sequence", *Biosens. Bioelectron.*, Vol. 20, pp. 69–74, 2004.
31. M. Barbaro, A. Bonfiglio, L. Raffo, A. Alessandrini, P. Facci, I. Barak, "A CMOS, Fully Integrated Sensor for Electronic Detection of DNA Hybridization", *IEEE Electron Device Lett.*, Vol. 27, pp. 595–597, 2006.
32. K. Sawada, S. Miura, K. Tomita, T. Nakanishi, H. Tanabe, M. Ishida, T. Ando, "Novel CCD-Based pH Imaging Sensor", *IEEE Electron. Device.*, Vol. 46, pp.1846–1849, 1999.
33. T. Hizawa, K. Sawada, H. Takao, M. Ishida, *Sens. Actuator B Chem.*, "Fabrication of a Two-dimensional pH Image Sensor using a Charge Transfer Technique",Vol. 117, pp. 509–515, 2006.
34. M. Gersbach, Y. Maruyama, C. Niclass, K. Sawada, E. Charbon, "A Room Temperature CMOS Single Photon Sensor for Chemiluminescence Detection",*Proc. TAS*, pp. 744–746, 2006.
35. M. J. Milgrew, P. A. Hammond, D. R. S. Cumming, "The Development of Scalable Sensor Arrays Using Standard CMOS Technology", *Sens. Actuator B Chem.*, Vol. 103, pp. 34–42, 2004.
36. H. Lee, Y. Liu, R. M. Westervelt, D. Ham, "IC/Microfluidic Hybrid System for Magnetic Manipulation of Biological Cells", *IEEE J. Solid-State Circuit*, Vol. 41, pp. 1471–1479, 2006.
37. R. Pal, M. Yang, R. Lin, B. N. Johnson, N. Srivastava, S. Z. Razzacki, K. J. Chomistek, D. C. Heldsinger, R. M. Haque, V. M. Ugaz, P. K. Thwar, Z. Chen, K. Alfano, M. B. Yim, M. Krishnan, A. O. Fuller, R. G. Larson, D. T. Burked, M. A. Burns, "An Integrated Microfluidic Device for Influenza and Other Genetic Analyses", *Lab Chip*, Vol. 5, pp.1024–1032, 2005.
38. H-W. Lee, A. R. Hawkins, "Solid-state Current Amplifier based on Impact Ionization", *Appl. Phys. Lett.*, Vol. 87, 2005.

Chapter 8
Energy Harvesting for Bio-sensing by Using Carbon Nanotubes

Koushik Maharatna, Karim El Shabrawy, and Bashir Al-Hashimi

8.1 Introduction

Wireless systems are becoming pervasive, for example, wireless networking based upon the IEEE 802.11 standards and the wireless connectivity between the body-worn devices for different purposes. One such purpose is remote telecare, where a number of devices measuring electrophysiological signals distributed over the body automatically transmit the data to primary/secondary care unit facility [1, 2]. Such a typical application comprises of sensing devices for measuring electrocardiogram (ECG), electroencephalogram (EEG), blood pressure monitoring, body/ambient temperature sensing, breathing rate variability estimation, etc. Each of these devices uses a front-end radio transmitter to facilitate data transfer to the intended care unit. Typically in a wireless system, the analog radio front-end consumes most of the power. In addition, the digital baseband part of each of these devices require significant amount of signal processing to estimate the desired signal in the presence of noise and artifacts apart from regulatory signal processing jobs required to present the data to the analog front-end for communication. Overall, the energy requirement for sustained operation is quite high and depends on the number of sensors in the system being deployed. Typically, the devices are charged through batteries that are quite bulky in size and are not really suitable for body-worn devices. Alternative is to convert ambient energy into electrical energy from different sources like ambient/body temperature, kinetic motion, chemical energy, and solar radiation in the form of micro fuel cells [3], micro turbine generator [4], or wearable micro solar cells [5]. Such systems are capable of high levels of energy and power density and show good potential for recharging of, or even replacing, mobile phone or laptop batteries [6]. Thus, they can be used either as direct replacement or to augment a battery, thereby increasing the systems' operation

K. Maharatna (✉)
University of Southampton, Southampton, Hampshire, UK
e-mail: km3@ecs.soton.ac.uk

S. Carrara (ed.), *Nano-Bio-Sensing*,
DOI 10.1007/978-1-4419-6169-3_8, © Springer Science+Business Media, LLC 2011

lifetime [7–10]. A comprehensive review of energy harvesting from different sources is outlined in [11].

In recent years, carbon nanotubes (CNTs) have emerged as a material of interest mainly due to their mechanical strength and versatile electrical properties. However, their application in energy generation has been relatively unexplored compared with other application areas. Recently in [12], it is suggested that CNTs could be formed into tiny springs capable of storing as much energy as the state-of-the-art lithium ion batteries – and more than 1,000 times as much as steel springs with potentially more durability and reliability. This approach has the potential to be used for body-worn sensors, where energy can be harvested from kinetic motion of a person. Also a macroscopic fiber composite of CNT and ionically conducting matrix has been developed [13] recently, which shows promise of storing electrochemical energy. However, most application for CNT in energy harvesting has so far concentrated on how to harvest solar energy. Thus, in this chapter, we will concentrate on harvesting solar energy with CNT for powering body-worn nanosensors.

8.2 CNT-Based Photovoltaic (PV) Device

CNTs have been regarded as promising building blocks in a variety of nano-optoelectronic applications due to their distinctive electrical and optical properties [14–17]. Owing to their direct band-gap characteristics, superior carrier mobility, high surface-to-volume ratio, and low scattering and recombination losses, CNTs have been proposed as a potential active material in photovoltaic (PV) devices [16, 18, 19].

Two different approaches are mainly adopted for using CNT for developing PV devices [5]:

1. Direct band-gap excitation of semiconducting CNTs.
2. The use of conduction tubes as conduits to improve the charge transport from light-harvesting assemblies.

A comprehensive review of these methods and their state-of-the-art has been described in [5].

The PV effect of an individual *p-n* junction CNT was first studied experimentally in [16], and due to its almost defect-free 1D structure, an ideal diode behavior was observed [14, 16, 18]. However, the process by which the CNT *p-n* junction diode was formed involved the intricate use of electrostatic doping from a split gate [16]. In addition, it was found that defect states in the single-wall carbon nanotube (SWCNT) band gap emerged from the interaction of the CNT with the surface it laid upon, leading to nonideal behavior [16]. Later, a microcell consisting of a network of SWCNTs was theoretically [18] and experimentally [19] studied, where efficiencies were investigated with respect to the electromagnetic coupling and scattering between CNTs. By nanowelding the SWCNTs across two asymmetric

metal electrodes with high- and low-work functions, respectively, this established a strong built-in electric field along the entire length of the tubes [19]. As a result, efficient separation and collection of electron–hole pairs proceeded once generated by an absorbed photon. Despite the substantial gains in conversion efficiency compared with the first experimental device, performance was undermined by the thin monolayer of widely spaced CNTs used, which scarcely absorb a small fraction of the incident power [19]. Also, the introduction of undesirable defect states from interactions with the substrate surface produced high recombination losses. Most importantly, it was found that major improvements to efficiency could ensue with the selection of SWCNTs having band gaps appropriately matched with the solar spectrum [19].

However, apart from the approaches mentioned in [16–18], there is another approach that has been overlooked currently where the geometric variability of SWCNT produced in a particular process can be used for absorbing a wide range of solar spectrum, which we will describe in this chapter. The material presented here is based on our recent work on this approach, which utilizes the fact that a leading property that makes SWCNTs very attractive for PV applications is their dependence on their geometrical structure, which consists of the diameter (d) and chirality (θ); they can remarkably exhibit a tunable band gap [16, 18, 20]. By exploiting this unique trait, more photons of various wavelengths may be absorbed from the solar spectrum compared with a single band-gap material, and hence device conversion efficiencies may be enhanced. Currently, available CNT synthesis techniques show a wide range of variation of d and θ. In particular, chemical vapor deposition (CVD) synthesis process, which is the most common practice for CNT synthesis till date, introduces approximately $\pm 15\%$ [21] variability in d. Thus, the property of tunable band gap can be readily used for developing a PV cell. In this chapter, after a short review of electronic property of CNT in Sect. 8.3, we will describe a step-by-step approach to model the band-gap variation of SWCNT due to its geometric structural variation in Sects. 8.4 and 8.5 and then compare the resulting band-gap tunability with the solar spectrum in Sect. 8.6. Finally, in Sect. 8.7, we will show how this tunable property can be exploited for developing an efficient solar cell.

8.3 Review of SWCNT Electronic Properties

A SWCNT is a self-assembled hollow cylinder constructed from a rolled-up sheet of graphene [22] that can be uniquely defined by a roll-up vector called the chiral vector, $\mathbf{C_h}$. $\mathbf{C_h}$ can be expressed in terms of two primitive unit vectors $\mathbf{a}_1$ and $\mathbf{a}_2$ of the graphene lattice [23]:

$$\mathbf{C_h} = m\mathrm{a}_1 + n\mathrm{a}_2, \tag{8.1}$$

where m and n are integers that are specific to a particular CNT [23]. The magnitude of $\mathbf{C_h}$ corresponds to the circumference around the CNT. The diameter (d) of the CNT can be expressed in terms of indices (m, n) as follows:

$$d = \frac{\sqrt{3}}{\pi} a_{cc} \sqrt{m^2 + nm + n^2}. \tag{8.2}$$

In (8.2), the constant a_{cc} (0.142nm) represents the nearest-neighbor C–C distance [24]. The chiral angle (θ) is defined as the angle between $\mathbf{C_h}$ and $\mathbf{a}_1$, which can be expressed as [25] follows:

$$\theta = \tan^{-1}\left(\frac{\sqrt{3}n}{2m+n}\right). \tag{8.3}$$

Previous studies have confirmed the sensitivity of the CNT's band gap to both d and θ,where several theoretical and analytical models have been established to simulate their electronic band structure [22, 23, 25–29]. Among the commonly used band models are the nearest-neighbor tight-binding (TB) approach with zone folding [22, 23, 25–27], the extended Hückel theoretical (EHT) technique [28], and First-principle ab initio calculations [22, 29]. Although accurate, these models are computationally intensive and possess a time complexity that increases with the size of the CNT. For applications that require simultaneous simulation of millions of distinct CNT devices, these models would be difficult to utilize in a timely manner.

Analytical models such as those mentioned in [24, 30] were formed by experimentally probing a small number of semiconducting CNTs in order to measure their geometric structure and corresponding electrical output characteristics. In turn, results were plotted and curves were extrapolated to acquire the CNT band-gap [29]. Not only were these results based on undersized samples of CNTs but the measurements were also found to be strongly dependent upon the characterization of the technique employed [31–33]. Moreover, it has been argued that there is a lack of statistical validity of measurements made using bulk sensitive probes due to the lack of sensitivity in the characterization of individual CNTs present within a given sample [31, 34].

8.4 Modeling Band Gap of Isolated SWCNT

Normally, the electronic properties of a SWCNT are obtained by first computing the dispersion relation of graphene using a TB approach and subsequently imposing the Born-von Karman periodic boundary conditions along the circumferential direction slicing the 2D band structure of graphene into 1D subbands [22]. If one

of these slices intersects with a high-symmetry K point in the Brillouin zone of graphene (where conduction and valence band touch at the Fermi level), the CNT can be considered metallic [35] (zero band gap). Otherwise, the CNT is semiconducting with a finite band-gap energy Eg. According to the choice of n and m, each CNT will have a different electronic band structure. This is known as the zone-folding technique and is sufficient in approximating the CNT band gap.

However, in [27, 32], it was shown that the nearest-neighbor TB approximation does not accurately reproduce the graphene band structure when compared with ab initio calculations. Instead, it was demonstrated that the third-nearest-neighbor TB approach exhibits better fitting results along the high-symmetry points of the Brillouin zone and that CNT band-structure models were improved by the inclusion of more distant neighbors [27]. To compute the band-gap energy Eg of an isolated SWCNT, we can adopt a simulation-based approach described in [36]. In this approach, first the third-nearest-neighbor TB approach is used to simulate a set of 286 SWCNTs. The CNTs are characterized by all possible chiralities (0–30°) and diameters ranging between 0.45 and 2.55nm. The result of this simulation is depicted in Fig. 8.1.

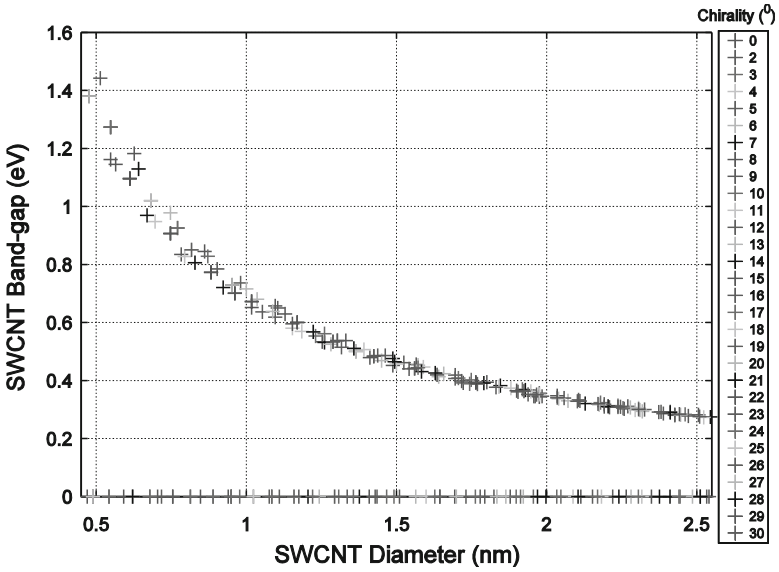

Fig. 8.1 SWCNT band-gap (Eg) for different geometrical properties, d, and θ. CNTs with different chirality are illustrated by separate color shading

8.4.1 Distinguishing Semiconducting and Metallic SWCNTs

The geometric variables (θ, d) that produced a zero band gap and nonzero band-gap were separately plotted as data points, indicated by symbols *plus sign* and *open circle*, respectively, in the structural parameter space shown in Fig. 8.2.

Rearranging (8.3) and substituting in (8.2) we get

$$d = \frac{3a_{cc}}{2\pi}\frac{n}{\sin\theta}. \tag{8.4}$$

Assuming that the sine function of (8.4) can be approximated by a first-degree polynomial ($b\theta$+c) over the interval $0° \leq \theta \leq 30°$, it becomes apparent that the diameter d is inversely proportional to $b\theta$+c. This approximation results in a normalized root mean square (NRMS) error of 0.6%, which is well within the limit. With this approximation when looking at the zero band-gap data points in Fig. 8.2, it could be seen that if several distinct curves were to be fitted over the points describing zero band-gap CNT, then they would all share the same asymptote at θ=30°. Thus, b can be expressed in terms of c as b=–c/30. The only unknown factor here is c. Upon close inspection of the zigzag tubes (θ=0°), a pattern in the tube diameters in the form of third multiple of the smallest possible diameter can be found that offer a zero band gap. The smallest possible SWCNT diameter can be determined from (8.2) given a tube's indices of (1, 0), provided $d_{\min}=\sqrt{3a_{cc}/\pi}$. Therefore, the value of c can be expressed as a reciprocal of

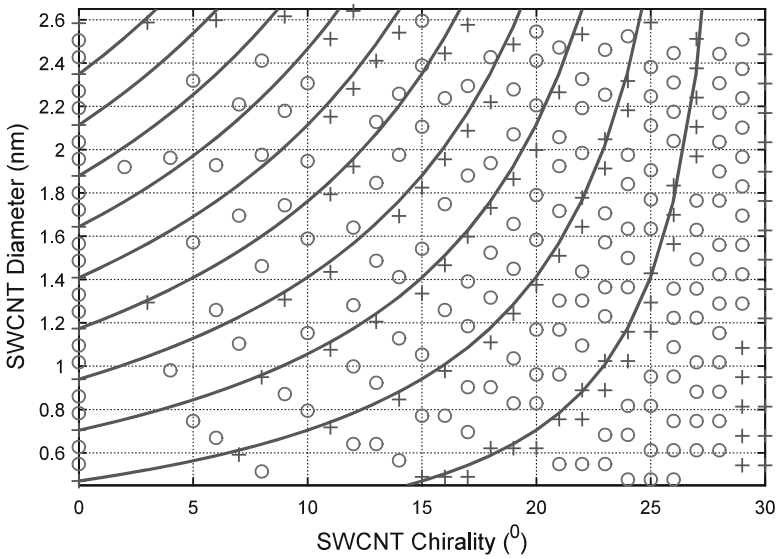

Fig. 8.2 CNT structural parameter space indicating data points (θ, d) for metallic and semiconducting tubes. Curves represent (8.5) for p = 1–10

$3pd_{\min}$, where p is a positive integer. Combining the above-mentioned results, the zero band-gap data points can be given as follows:

$$D(\theta, p) = \left(\frac{\pi}{3p\sqrt{3}a_{cc}} \left(1 - \frac{\theta}{30} \right) \right)^{-1}. \tag{8.5}$$

Equation (8.5) represents the zero band-gap curves shown in Fig. 8.2, where p selects the curve of interest. However, using (8.5), it is not possible to predict the band gap of Armchair tubes (θ=30°) as well as zero-diameter tubes. Thus, to cover all zero band-gap data points in Fig. 8.2, a function can be formulated that assumes a value of zero only when:

- the diameter d lies on a curve approximated by (8.5) for a given geometry
- the SWCNT is an Armchair (θ=30°) tube, or
- the SWCNT has a null diameter (d=0 nm).

Quantitatively, this function can be expressed as:

$$f(\theta, d) = d(30 - \theta) \prod_{p=1}^{N} (D(\theta, p) - d), \tag{8.6}$$

where N represents the total number of curves taken into consideration and $f(\theta, d)$ can be rearranged giving

$$f(\theta, d) = d(30 - \theta) \prod_{p=1}^{N} \left(1 - \frac{\alpha}{p} \right) \frac{pd}{\alpha}, \tag{8.7}$$

where

$$\alpha = \frac{d\pi}{90\sqrt{3}a_{cc}} (30 - \theta). \tag{8.8}$$

To solve (8.7), N iterations are required, where each product term is evaluated individually and then multiplied by the rest of the function. This process is time consuming for simulating a design with multiple CNT devices, and hence there is a need to reduce the product term to a noniterative form. Moreover, the accuracy of (8.7) is limited by the number of curves chosen when defining N, since the more the number of curves considered, the higher the number of zero band-gap data points covered. One way of resolving these issues is to consider a large number of curves and taking the limit as N tends toward a finitely large value. To do this, multiplying and dividing (8.7) by the conjugate of the product term and subsequently rearranging $f(\theta, d)$ we get

$$f(\theta,d)=\frac{\alpha 90\sqrt{3}a_{cc}}{\pi}\prod_{p=1}^{N}\left(1-\frac{\alpha^2}{p^2}\right)\prod_{p=1}^{N}\left(\frac{p^2 d}{\alpha(p+\alpha)}\right). \tag{8.9}$$

As N tends toward a finitely large value (practically infinite), the first product term of (8.9) could be approximated by a $\sin(\pi\alpha)$ function and the second product term tends toward a high value. Since only the roots of $f(\theta, d)$ are of interest, we can approximate (8.9) as

$$f(\theta,d)=|\Re(\sin(\pi\alpha))|, \tag{8.10}$$

where $\Re$ is a function that rounds values to the nearest integer, giving $f(\theta, d)$=0 for metallic CNTs and $f(\theta, d)$=1 for semiconducting tubes.

In [36], (8.10) was evaluated by sourcing the geometrical properties of all 286 randomly distinct metallic and semiconducting CNTs. The results for $f(\theta, d)$ are depicted in the structural parameter space of Fig. 8.3, where it can be seen that 266 out of 286 CNTs are correctly distinguished, which corresponds to a detection accuracy of 93% when compared with the third-nearest-neighbor TB approach with zone folding. This value offers an 11% improvement over the accuracy obtained in [37].

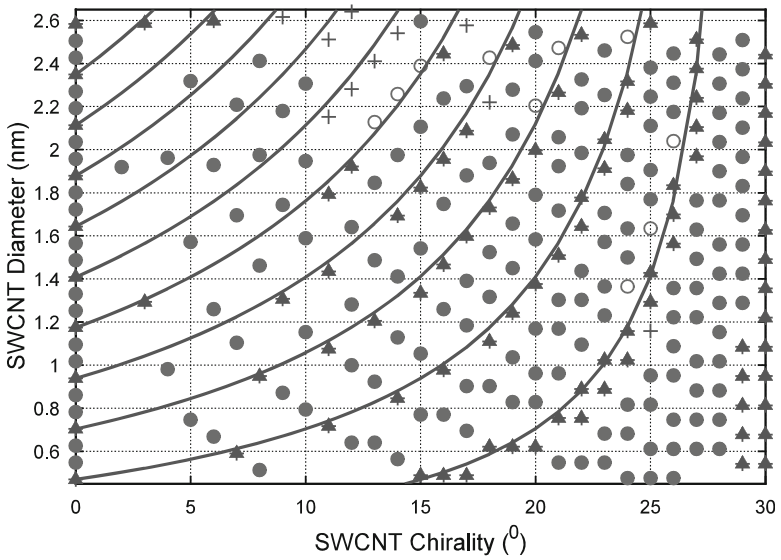

Fig. 8.3 CNT structural parameter space indicating data points (θ, d) for metallic and semiconducting tubes. *Plus sign* (*open circle*) represents metallic (semiconducting) results obtained using the third-nearest-neighbor TB approach with the zone-folding technique. *Closed triangle* (*closed circle*) represents metallic (semiconducting) tubes identified correctly by (8.10)

8.4.2 Calculating Band Gap of Semiconducting SWCNTs

From Fig. 8.1, it could be seen that for all semiconducting SWCNTs, the dependence of Eg on diameter is inversely proportional. This fact is in agreement with the $1/d$ relationship derived in [22, 24, 26, 29, 30, 38–40]. However, all these sources differ on an additional factor that is used during the calculation of a semiconducting CNT band gap: the overlap energy γ_0. γ_0 is a constant that has been debated to be in the range 2.45–2.90eV. Unfortunately, no agreed value of γ_0 has ever emerged [39]. In [39], it was mentioned that the reason for the resulting discrepancy in γ_0 is due to the fact that chirality is neglected when interpreting the band gap for different diameters. Thus, here we have plotted Eg with respect to d and θ for semiconducting CNTs only. Subsequently, a curve-fitting technique (shown in Fig. 8.4) was used to establish the following relationship among Eg, d, and θ:

$$\text{Eg} = 10.2\frac{3a_{cc}}{2\pi d} = \frac{0.692}{d}. \tag{8.11}$$

Equation (8.11) confirms that Eg is proportional to $1/d$, and the constant of proportionality is independent of θ. Moreover, a value of 2.44eV is calculated from (8.11) for γ_0, which is in close agreement with that derived using First principles (2.5eV) in [22]. When the semiconducting CNT band-gap values were

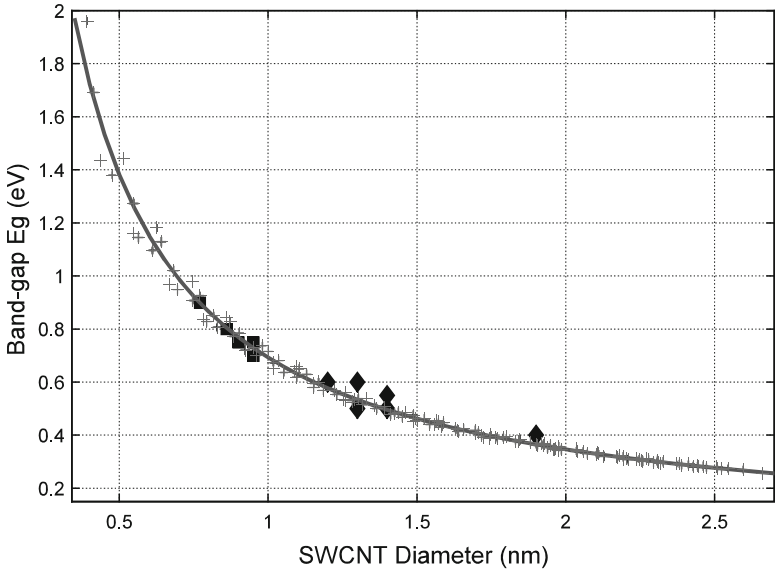

Fig. 8.4 Semiconducting band-gap vs. diameter for all θ. *Plus sign* represents results obtained using the third-nearest-neighbor TB approach with the zone-folding technique. — is the fitting curve given by (8.11). *Closed diamond* and *closed square* depict experimental measurements made in [25] and [31], respectively

generated using (8.11) and compared against the third-nearest-neighbor TB approach with zone folding, this yielded a NRMS error of 1.75% only.

To further verify (8.11), comparisons were made with respect to two references that experimentally analyzed semiconducting SWCNTs using different techniques. In [24], scanning tunneling spectroscopy (STS) was used to examine the electronic properties as a function of d and θ for a set of SWCNTs. The measurements obtained are clearly indicated in Fig. 8.4. In [30], scanning tunneling microscopy (STM) characterization of the SWCNTs was undertaken and the band gap of five nanotubes was extracted and recorded as shown in Fig. 8.4. Through inspecting the experimental data points, we can validate that the measured band-gap values lie very close to the curve proposed by (8.11).

Combining all the key expressions derived until now, a simplistic model can be established, which is depicted in (8.12). Given any SWCNT diameter (n, m) and chirality ($^{\circ}$), (8.12) computes the SWCNT band gap with a runtime independent of tube size and the value of N. This is more simulation efficient than the model proposed in [37], which possesses a time complexity of the order of $O(N)$.

$$\mathrm{Eg} = |\Re(\sin(\pi\alpha))|\frac{0.692}{d}. \tag{8.12}$$

8.5 Simulation and Modeling SWCNT Band-Gap Variation

In this section, we first discuss the probability functions appropriate to replicate a realistic spread in SWCNT diameter and chirality. By varying the distribution properties and running a set of Monte Carlo simulations, the corresponding band-gap dispersion relations can be derived, which are subsequently compared and statistically analyzed. This approach results in simplistic yet accurate models providing a relationship between the semiconducting CNT diameter distribution properties and the resulting band-gap variation characteristics, Eg_{μ} and Eg_{σ}. Since the SWCNT structural distribution differs considerably in different synthesis process, throughout the following discussion we assume the most commonly utilized method, i.e., CVD is adopted for synthesis.

In any given CVD process condition so long as the carbon feeding rate is constant, there is an optimal diameter of nanoparticles that nucleates CNTs. Thus, assuming that the process of defining the catalyst particle size can be optimized to give a narrow distribution around a specified d_{μ}, we can expect that as the number of fabricated SWCNTs increases for a given batch, the spread in diameter will converge toward a Gaussian distribution. Furthermore, having synthesized and measured the diameter distribution in a sizable mixture of CNTs, it has been found that most groups use a Gaussian fit for their diameter profiles [31, 41–43].

Unlike the CNT diameter, controlling the chiral angle can be more intricate [44]. Regulating the CNT chiral angle entails the manipulation of the molecular assembly

of the CNT [45]. This level of manipulation is unattainable using conventional CVD processes and consequently a homogeneous spread in chirality is commonly observed within a collection of synthesized CNTs [33, 46]. Hence, here we consider a uniform random distribution in the CNT chiral angle.

8.5.1 Semiconducting SWCNT Band-Gap Distribution

The variation in CNT band gap can be determined by executing expression (8.12) over a large number of samples that are randomly generated from the selected structural distributions outlined above. To carry out this in [36], a sample size of 1.5×10^5 CNTs was chosen to gain adequate accuracy for the output variables Eg_μ and Eg_σ. This value was attained by progressively simulating larger sample sets and identifying the cut-off at which the output converges. For each run of Monte Carlo simulation, the diameter distribution properties d_μ and d_σ were varied between the ranges 1.01–1.71 and 0.04–0.2nm, respectively. Figure 8.5 shows a density estimation of a subset (d_μ=1.01nm and d_σ=0.04–0.2nm) of semiconducting CNT band-gap results for a Gaussian spread in diameter.

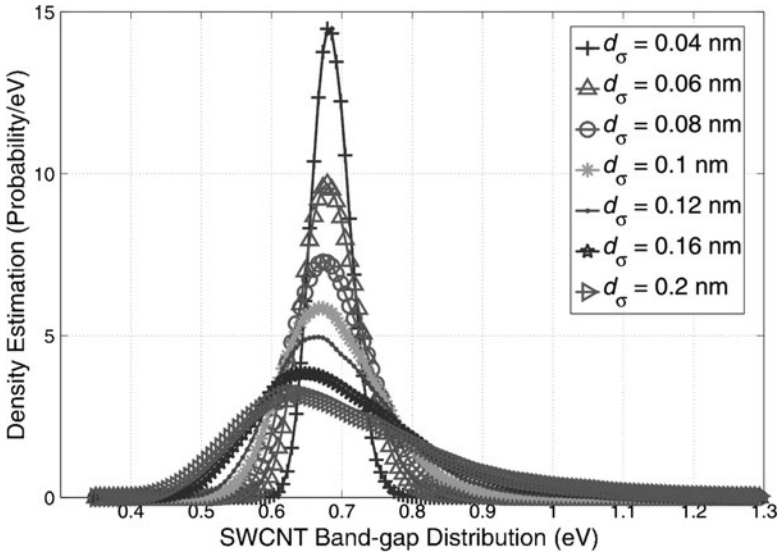

Fig. 8.5 Density estimation of semiconducting band-gap obtained from Monte Carlo simulations for a Gaussian spread in diameter with d_μ= 1.01 nm and d_σ= 0.04–0.2 nm

8.5.2 *Modeling SWCNT Band-Gap Variation for Normally Distributed Diameters*

In realizing the mean (Eg_μ) and variability (Eg_σ) of the produced band-gap dispersions, here we consider the sample mean and standard deviation as unbiased estimators owing to the large sample size taken. When Eg_μ was plotted against d_μ as depicted by Fig. 8.6, it is apparent that the mean band-gap shifted upward with higher d_σ and even more so for smaller d_μ. RSM regression technique of second order in (8.13) is used to create the optimal curves illustrated in Fig. 8.6.

$$\begin{aligned} \mathrm{Log}(Eg_\mu) =& \beta_0 + \beta_1 \log(d_\mu) + \beta_2 d_\sigma + \ldots \\ & \beta_{12} d_\sigma \log(d_\mu) + \ldots \\ & \beta_{11} \left(\log(d_\mu)\right)^2 + \beta_{22} d_\sigma^2. \end{aligned} \tag{8.13}$$

The regression coefficients of (8.13) are β_0=−0.3727, β_1=−0.9939, β_2=0.0852, β_{12}=−0.3456, β_{11}=0.0229, and β_{22}=0.7070. Although (8.13) is highly accurate (NRMS error of 0.19%) within the mean diameter range specified in our simulation, (8.14) can also provide a reasonable approximation to (8.13), especially for large mean diameters.

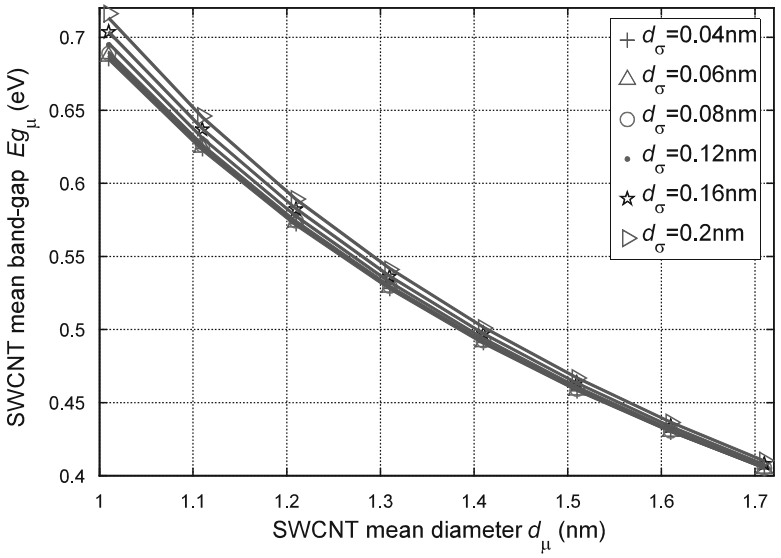

Fig. 8.6 SWCNT band-gap distribution mean (Eg_μ) vs. mean diameter (d_μ). Datasets with different diameter standard deviation (d_σ) have been marked by a distinct symbol. — represents the fitted curve given by (8.13)

$$\mathrm{Eg}_{\mu} = \frac{0.692}{d_{\mu}}. \tag{8.14}$$

For $1.01\text{nm} \leq d_{\mu} \leq 1.71\text{nm}$, the NRMS error of (8.14) in predicting the actual mean band-gap is 2.7%.

A more complete statistical analysis of band-gap distribution can be achieved by plotting the data points of the band-gap standard deviation (Eg_{σ}) that were plotted against the diameter standard deviation (d_{σ}) for different sets of d_{μ} as shown in Fig. 8.7. Again the curves of best fit can be generated by using RSM method giving the following expression:

$$\begin{aligned}\mathrm{Log}(\mathrm{Eg}_{\sigma}) =& \gamma_0 + \gamma_1 \log(d_{\sigma}) + \gamma_2 \log(d_{\mu}) + \ldots \\ & \gamma_{12} \log(d_{\sigma}) \log(d_{\mu}) + \ldots \\ & \gamma_{11} (\log(d_{\sigma}))^2 + \gamma_{22} \left(\log(d_{\mu})\right)^2,\end{aligned} \tag{8.15}$$

where the regression coefficients are γ_0=0.2883, γ_1=1.4036, γ_2=−2.5146, γ_{12}=−0.1460, γ_{11}=0.0624, and γ_{22}=0.1515.

The NRMS error of (8.15) in predicting the data points was evaluated as 0.66%. A more simplified approximation of (8.15) can be given by (8.16) that possesses a NRMS error of 2% within the ranges specified for d_{μ} and d_{σ}:

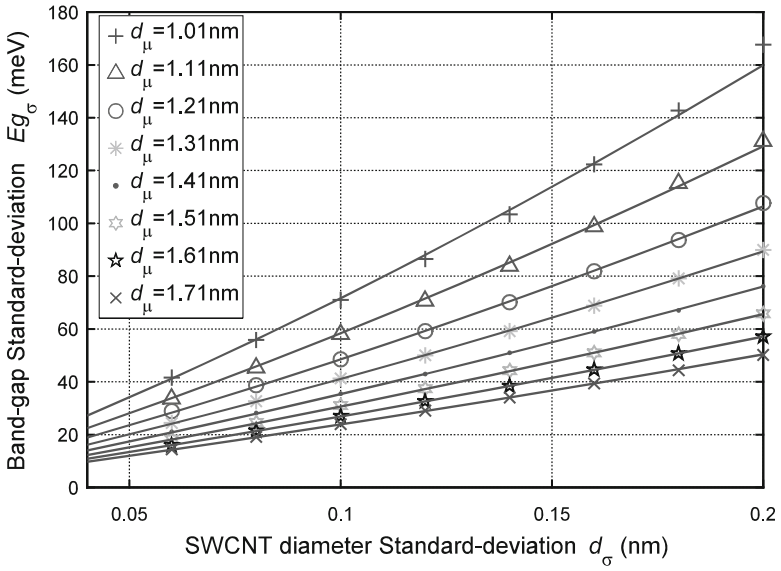

Fig. 8.7 Band-gap standard deviation (Eg_{σ}) vs. diameter standard deviation (d_{σ}). Datasets with different mean diameter (d_{μ}) have been marked by a distinct symbol. — represents the fitted curve given by (8.15) for each d_{μ}

$$\mathrm{Eg}_{\sigma} = \frac{0.8}{d_{\mu}^{2.2}} d_{\sigma}. \tag{8.16}$$

Equation (8.16) reinforces the linear relationship between Eg_{σ} and d_{σ}. More interestingly, it indicates that the band-gap variation can be significantly reduced by defining nanoparticle sizes with a higher mean diameter.

8.6 Analytical Model for Isolated SWCNT Optical Band-Gap Energies

When a semiconducting SWCNT is optically excited, a band-to-band transition (i.e., the resonant excitation of an electron from the valence band to the conduction band) occurs, which in turn generates photocurrent and a photovoltage [14, 47]. In this section, we will look at the analytical models proposed in [48] that describe the SWCNT transition energies (E_{ii}) as a function of the tube geometry. In order to do that, we will utilize the results derived in the foregoing sections describing the band-gap variability with respect to the geometric structure of CNT.

Using third-nearest-neighbor TB approach once again, the SWCNT transition energy can be simulated for a set of CNTs. Fig. 8.8 shows such simulation for a set

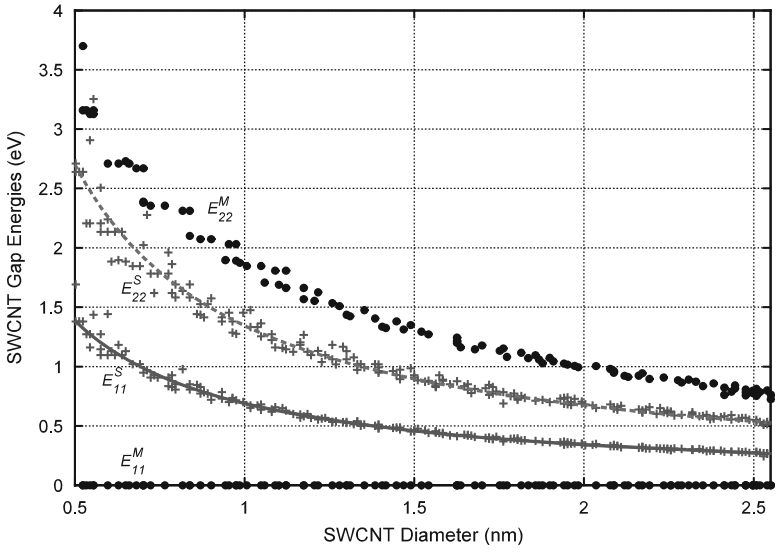

Fig. 8.8 SWCNT transition energies vs. tube diameter for chiralities in the range 0°–30°. *Plus sign* (*closed circle*) represents semiconducting (metallic) tubes. (—) and (—) correspond to (8.17) and (8.18), respectively, obtained using regression analysis

of 286 SWCNTs, where the tubes are characterized by all possible chiralities, θ=0–30°, and diameters (d) ranging between 0.5 and 2.55nm.

From Fig. 8.8, it could be seen that the data points are very much similar to the optical transition curves outlined by the Kataura plot in [49], although in this case the values have an additional accuracy for the smaller tube diameters and certain chiralities as more distant neighbors are considered in the TB model employed [46, 50]. Since we are concerned with the semiconducting CNTs only, the first and second excitation transition energies (denoted as $[E_{11}^S$ and E_{22}^S) are of interest. Once again a curve-fitting and regression technique can be utilized to model the corresponding data points in Fig. 8.8 and generate the following relationships:

$$E_{11}^S = \frac{0.692}{d}, \tag{8.17}$$

$$E_{22}^S = \frac{1.356}{d}. \tag{8.18}$$

Equations (8.17) and (8.18) predict the semiconducting transition energies with a NRMS error of 1.75 and 3.8%, respectively, when compared with the third-nearest-neighbor TB with zone-folding results. More interestingly, the E_{22}^S /E_{11}^S ratio yields 1.96, which is slightly lower than that measured experimentally (2.00) in [51].

The variation of optical band gap can be determined by first executing analytical expressions derived in Sect. 8.4.2 to distinguish whether a CNT is metallic or semiconducting over a large number of samples (1.5×10^5) that are randomly generated from the selected structural distributions outlined in Sect. 8.4. If the tube is found to be semiconducting only, then the optical transition energies of (8.17) and (8.18) are computed. For each run of the Monte Carlo simulation, the diameter distribution properties d_μ and d_σ were varied between the ranges 1.01–1.71 and 0.04–0.2nm, respectively, as in [36]. Fig. 8.9 depicts a density estimation of a subset (d_μ=1.01nm and d_σ=0.04–0.2nm) of semiconducting CNT optical band-gap results and Fig. 8.10 shows a histogram comparing the optical band-gap distribution generated for the Gaussian spread in diameter (d_μ=1.01nm and d_σ=0.2nm) with the standard AM1.5 Solar Irradiance Spectrum given in [52]. Qualitatively, it could be observed that the CNTs optical band-gap energies are well matched with the IR and lower visible regions (∼0.6–2.6μm) of the solar energy spectra.

Figure 8.11 illustrates a set of curves that generally show an increasing mismatch between the solar spectra and the CNT optical band-gap distributions with higher mean diameters (d_μ). Further, as expected, the spectral mismatch is intensified with lower variations in CNT diameter (d_σ). The lowest mis-match recorded is just under 50% for d_μ=1nm, which is in good agreement with recommendations made in [16], where it was claimed that SWCNTs having diameters around 0.8nm would offer significant improvements in PV conversion efficiency.

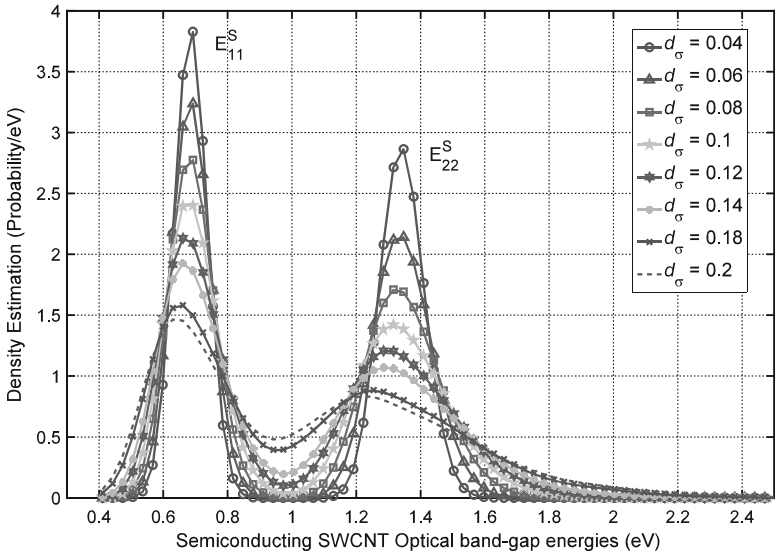

Fig. 8.9 Density estimation of semiconducting SWCNT optical band-gap energies obtained from Monte Carlo simulations for a Gaussian spread in diameter with d_μ= 1.01 nm and d_σ= 0.04–0.2 nm

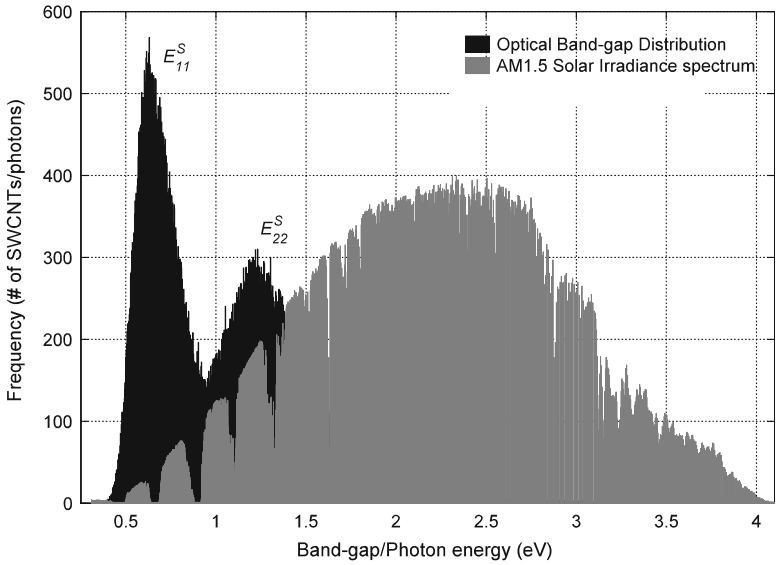

Fig. 8.10 Histogram comparing semiconducting SWCNT optical band-gap distribution (for d_μ= 1.01 nm and d_σ= 0.2 nm) with AM1.5 solar energy spectra

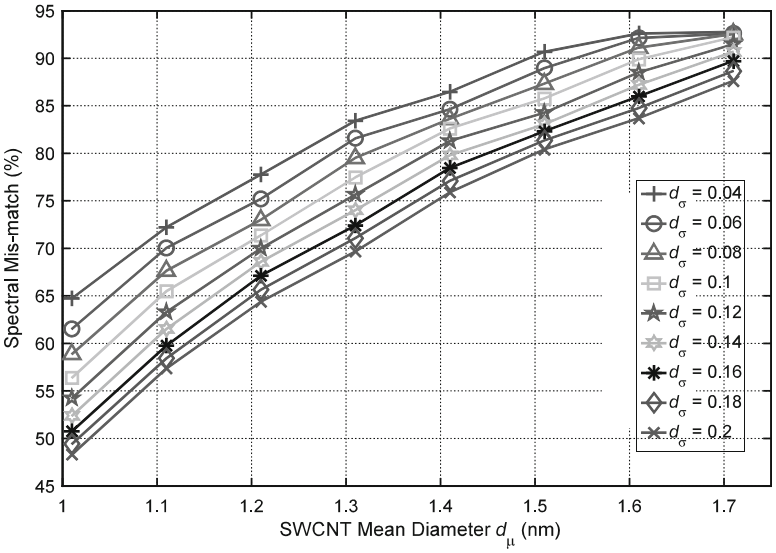

Fig. 8.11 Graph representing the mismatch as a percentage between the solar spectra and CNT optical band-gap distributions. Mis-match is given with respect to different d_μ and d_σ

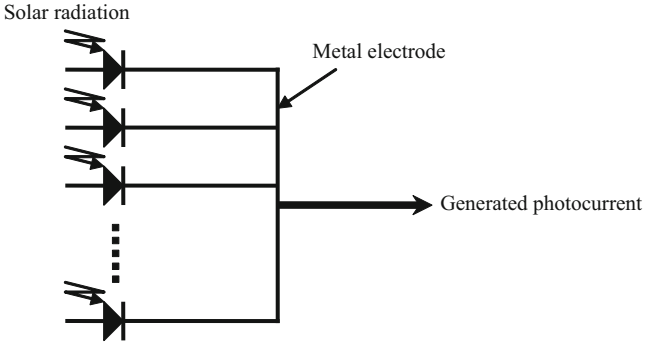

Fig. 8.12 Conceptual representation of CNT-based PV cell utilizing diameter variability

8.7 A Conceptual Photovoltaic Device

Armed with the above results, now we are ready to propose a PV device based on SWCNTs. As mentioned earlier, typical CNT production by CVD shows about $\pm 15\%$ variation in its geometrical property. Note that by geometrical property, we mean variation of diameter here. The basic concept of such a PV device can be depicted by Fig. 8.12,where n number of CNTs are arranged in such a way that they are all connected to a metal electrode on one side. Each of such CNTs can be viewed as a diode operating in a wide area of solar spectrum as shown in Fig. 8.10. Due to the

diameter variation, each of these CNTs absorbs a small portion of the solar spectrum to generate photocurrent. Since Fig. 8.10 shows that the majority of the overlap between the band-gap of CNTs and solar spectrum occurs at the "red end" and "lower visible end" of the solar spectrum, it is conceivable that, in isolation, each CNT contributes small amount of photocurrent. However, since such small contribution is integrated over a large number of CNTs, the overall photocurrent is quite substantial and may surpass any of the currently existing solar cells.

The device level view of such a cell is shown in Fig. 8.13,where a large number of vertically aligned semiconducting SWCNTs with a mean diameter d_μ and diameter variation d_σ contacted between different type Drain and Source metal electrodes. The vertical alignment can be achieved using a standard catalytic-assisted CVD technique or a low-cost postsynthesis deposition method [53].

Recent experimental results indicate that vertically aligned SWCNTs possess robust photoabsorption properties within a very wide spectral range (0.3–2.6μm) [54]. This is because when a photon is not absorbed by a tube, it is likely to be either reflected or transmitted toward another nearby tube possibly retaining an alternative band gap to the first. This "photon recycling" process may proceed from one layer of tubes to another, until the photon ultimately interacts with a CNT having a corresponding band-gap energy or lower. As an outcome, the reflectance of a sample of vertically aligned SWCNTs was measured to be 0.01–0.02 only across the entire spectral range [54]. However, it was reported that the photoresponsitivity and carrier collection can be significantly reduced with the entanglement of tubes [18]. Therefore, it would be necessary to ensure sufficient separation and adequate alignment among SWCNTs when used for the conceptual PV device. It has also been experimentally and theoretically confirmed that CNT photoabsorption could be maximized when the electric field of the incident light is polarized parallel to the tube axis as indicated in Fig. 8.13 [18, 54].

A potential improvement to the device depicted in Fig. 8.13 can include the combination of CNT samples with descending d_μ facing the incoming light first, so as to have higher band-gap tubes absorbing the shorter wavelength photons. However, an obvious question is whether there exists any upper cut-off of d_μ while developing the device shown in Fig. 8.13. Referring to the discussion presented in

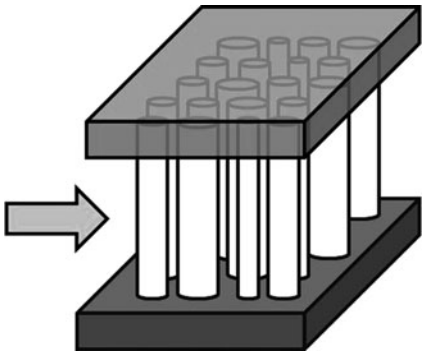

Fig. 8.13 Conceptual PV device with vertically aligned SWCNTs as a photoactive material having diameters represented by d_μ and d_σ. The tubes are contacted between two different type metal electrodes. Electric field of incident light is polarized parallel to nanotube axis

Sect. 5 and Fig. 8.11, one can conclude that in order to utilize band-gap variability resulting from the structural variation, one should use $d_\mu \leq 1$nm and a high diameter variation. The device can be potentially improved by employing standard techniques that are adopted now-a-days for increasing conversion efficiency of conventional solar cells. These techniques include applying antireflection coating for increasing photon trapping within the structure itself and implanting nanoparticles for frequency down-conversion of a portion of the solar spectrum that lies outside the zone of solar spectrum and CNT band-gap overlap. However, detailed analysis of these factors and their impact on the conversion efficiency is currently underway by the authors and thus are not provided here.

8.8 Conclusion and Outlook

In this chapter, how the geometrical variability of CNT can be used for harvesting solar energy is outlined. Although a conceptual device is shown, there is still a need for analyzing its conversion efficiency subject to the process/geometrical imperfection. The challenge in such device is to ensure the strictly vertical alignment of the nanotubes and their proper connections to the metals on both sides. It is necessary to run experiments corresponding to a particular process to see how much mismatch in vertical alignment can be achieved that is reproducible. As mentioned earlier, entanglement of the tubes may reduce conversion efficiency significantly. These imperfections need to be incorporated in a circuit model in order to compute conversion efficiency. To increase the "hit-rate" of the photons to CNTs, appropriate antireflection coating needs to be applied. Also an open area of research is what type of nanoparticle can be implanted within the CNTs for frequency down-conversion, which enables absorption of higher wavelength photons.

As the remote telecare system depends more and more on utilizing nanosensors and as a significant number of nanosensors can be made from CNTs, it would be beneficial to integrate SWCNT-based nanosolar cells as the back-plane of such sensors under one fabrication cycle. This will not only make the wearable nanosensors pervasive but is also deemed to satisfy the energy requirement of such sensors and eventually of the whole system.

References

1. Biomedical Wireless Sensor Network. NORDIC Innovation Centre. Report available at www.bwsn.net/tiki-download_file.php?fileId=74.
2. A. Triantafyllidis et al., "An Open and Reconfigurable Wireless Sensor Network for Pervasive Health Monitoring," *Methods Inf Med*., vol. 47, pp. 229–234, 2008.
3. B. Banazwski, and R. K. Shah, "The Role of Fuel Cells for Consumer Electronic Products and Toys," *Proceedings of the 1st International Conference on Fuel Cell Science, Engineering and Technology*, Rochester, NY, USA, pp. 149–155, 2003.

4. A. H. Epstein, "Millimeter-Scale, Micro-Electro-Mechanical Systems Gas Turbine Engines," *J. Eng. Gas Turbines Power*, vol. 126, pp. 205–226, 2004.
5. P. V. Kamat, "Harvesting Photons with Carbon Nanotubes," *Nanoday*, vol. 1, No. 4, pp. 20–27, 2006.
6. S. Tanaka, K.-S. Changa, K.-B. Mina, D. Satoh, K. Yoshida, and M. Esashi, "MEMS-based Components of a Miniature Fuel Cell/Fuel Reformer System," *J. Chem. Eng.*, vol. 101, pp. 143–149, 2004.
7. P. B. Koeneman, I. J. Busche-Vishniac, and K. L. Wood, "Feasibility of Micro Power Supplies for MEMS," *IEEE J. Microelectomech. Syst.*, vol. 6, pp. 355–362, 1997.
8. G. Görge, M. Kirstein, and R. Erbel, "Microgenerators for Energy Autarkic Pacemakers and Defibrillators: Fact or Fiction," *Herz*, vol. 26, pp. 64–68, 2001.
9. R. Amirtharajah, and A. P. Chandrakasan, "Self-powered Signal Processing Using Vibration-based Power Generation," *IEEE J. Solid-State Circuits*, vol. 33, pp. 687–695, 1998.
10. S. A. Jacobson, and A. H. Epstein, "An Informal Survey of Power MEMS," *Proceedings of the International Symposium on Micro-Mechanical Engineering ISMME (Japan)*, p. K18, 2003.
11. S. P. Beeby, M. J. Tudor, and N. M. White, "Energy Harvesting Vibration Sources for Microsystems Applications," *Meas. Sci. Technol.*, vol. 17, pp. R175–R195, 2006.
12. "Spring Shaped Carbon Nanotubes," *Energy Harvest. J.*, 29 September 2009, available at http://www.energyharvestingjournal.com/pages/printarticles.asp?articleids=1715.
13. Available at:http://adsabs.harvard.edu/abs/2002APS..MARQ25004D.
14. P. Avouris, M. Freitag, and V. Perebeinos, "Carbon-Nanotube Photonics and Optoelectronics," *Nat. Photonics*, vol. 2, pp. 341–350, 2008.
15. D. A. Stewart, F. Léonard, "Energy Conversion Efficiency in Nanotube Optoelectronics," *Nano Lett.*, vol. 5, pp. 219–222, 2005.
16. J. U. Lee, P. P. Gipp, and C. M. Heller, "Carbon Nanotube *p-n* Junction Diodes," *Appl. Phys. Lett.*, vol. 85, pp. 145–147, 2004.
17. M. Freitag, Y. Martin, J. A. Misewich, R. Martel, and P. Avouris, "Photoconductivity of Single Carbon Nanotubes," *Nano Lett.*, vol. 3, pp. 1067–1071, 2003.
18. C. Chen, L. Yang, Y. Lu, G. Xiao, and Y. Zhang, "Assessment of Optical Absorption in Carbon Nanotube Photovoltaic Device by Electromagnetic Theory," *IEEE Trans. Nanotechnol.*, vol. 8, pp. 303–314, 2009.
19. C. Chen, Y. Lu, E. S. Kong, Y. Zhang, and S. Lee, "Nanowelded Carbon-Nanotube-based Solar Microcells," *Small*, vol. 4, pp. 1313–1318, 2008.
20. W. J. Blau, and J. Wang, "Optical Materials: Variety Pays off for Nanotubes," *Nat. Nanotechnol.*, vol. 3, pp. 705–706, 2008.
21. Available at http://www.nano-lab.com/single-walled-carbon-nanotubes.html.
22. J. W. Mintmire, and C. T. White, "Electronic and Structural properties of Carbon Nanotubes," *Carbon*, vol. 33, pp. 893–902, 1995.
23. R. Saito, M. Fujita, G. Dresselhaus, and M. S. Dresselhaus, "Electronic Structure of Chiral Graphene Tubules," *Appl. Phys. Lett.*, vol. 60, pp. 2204–2206, 1992.
24. J. W. G. Wildoer, L. C. Venema, A. G. Rinzler, R. E. Smalley, and C. Dekker, "Electronic Structure of Atomically Resolved Carbon Nanotubes," *Nature*, vol. 391, pp. 59–62, 1998.
25. N. Hamada, S. Sawada, and A. Oshiyama, "New One-dimensional Conductors: Graphitic Microtubules," *Phys. Rev. Lett.*, vol. 68, pp. 1579–1581, 1992.
26. R. Saito, M. S. Dresselhaus, and G. Dresselhaus, *Physical Properties of Carbon Nanotubes*. Imperial College Press, 1998.
27. S. Reich, J. Maultzsch, C. Thomsen, and P. Ordejón, "Tight-binding Description of Graphene," *Phys. Rev. B*, vol. 66, p. 035412, 2002.
28. D. Kienle, J. I. Cerda, and A. W. Ghosh, "Extended Hückel Theory for Bandstructure, Chemistry and Transport: I. Carbon Nanotubes," *J. Appl. Phys.*, vol. 100, p. 043714, 2006.
29. O. Gülseren, T. Yildirim, and S. Ciraci, "Systematic Ab Initio Study of Curvature Effects in Carbon Nanotubes," *Phys. Rev. B*, vol. 65, p. 153405, 2002.

30. T. W. Odom, J. Huang, P. Kim, and C. M. Lieber, "Atomic Structure and Electronic Properties of Single-walled Carbon Nanotubes," *Nature*, vol. 391, pp. 62–64, 1998.
31. X. Liu, T. Pichler, M. Knupfer, M. S. Golden, J. Fink, H. Kataura, and Y. Achiba, "Detailed Analysis of the Mean Diameter and Diameter Distribution of Single-wall Carbon Nanotubes from Their Optical Response," *Phys. Rev. B*, vol. 66, 2002.
32. S. Reich, C. Thomsen, and P. Ordejon, "Electronic Band Structure of Isolated and Bundled Carbon Nanotubes," *Phys. Rev. B*, vol. 65, p. 155411, 2002.
33. Y. Sato, K. Yanagi, Y. Miyata, K. Suenaga, H. Kataura, and S. Iijima, "Chiral-Angle Distribution for Separated Single-Walled Carbon Nanotubes," *Nano Lett.*, vol. 8, pp. 3151–3154, 2008.
34. A. G. Nasibulin, P. V. Pikhitsa, H. Jiang, and E. I. Kauppinen, "Correlation Between Catalyst Particle and Single-walled Carbon Nanotube Diameters," *Carbon*, vol. 43, pp. 2251–2257, 2005.
35. J. R. Hauptmann, "Spin-Transport in Carbon Nanotubes," Faculty of Science, Master of Science, University of Copenhagen, 2003.
36. K. El-Shabrawy, K. Maharatna, D. Bagnall, and B. Al-Hashimi, "Modeling SWCNT Band-gap and Effective Mass Variation Using a Monte Carlo Approach," *IEEE Trans. Nanotechnol.*, available at http://ieeexplore.ieee.org/stamp/stamp.jsp?tp=. . .arnumber=5175416. . .isnumber=4359107.
37. K. El Shabrawy, K. Maharatna, D. M. Bagnall, and B. M. Al-Hashimi, "A New Analytical Model for Predicting SWCNT Band-gap from Geometrical Properties," *ICICDT*, Grenoble, France, 2008.
38. M. S. Dresselhaus, R. Saito, and A. Jorio, "Semiconducting Carbon Nanotubes," *International Conference on the Physics of Semiconductors – ICPS-27*, pp. 25–31, 2005.
39. J. W. Ding, X. H. Yan, and J. X. Cao, "Analytical Relation of Band Gaps to Both Chirality and Diameter of Single-wall Carbon Nanotubes," *Phys. Rev. B*, vol. 66, p. 073401, 2002.
40. C. L. Kane, and E. J. Mele, "Size, Shape, and Low Energy Electronic Structure of Carbon Nanotubes," *Phys. Rev. Lett.*, vol. 78, pp. 1932–1935, 1997.
41. T. Hiraoka, S. Bandow, H. Shinohara, and S. Iijima, "Control on the Diameter of Single-walled Carbon Nanotubes by Changing the Pressure in Floating Catalyst CVD," *Carbon*, vol. 44, pp. 1853–1859, 2006.
42. C. Lu, and J. Liu, "Controlling the Diameter of Carbon Nanotubes in Chemical Vapor Deposition Method by Carbon Feeding," *J. Phys. Chem. B*, vol. 110, pp. 20254–20257, 2006.
43. C. L. Cheung, A. Kurtz, H. Park, and C. M. Lieber, "Diameter-controlled Synthesis of Carbon Nanotubes," *J. Phys. Chem. B*, vol. 106, pp. 2429–2433, 2002.
44. A. Hazeghi, T. Krishnamohan, and H-S. P. Wong, "Schottky-Barrier Carbon Nanotube Field-effect Transistor Modeling," *IEEE Trans. Electron Devices*, vol. 54, pp. 439–445, 2007.
45. O. Zhou, H. Shimoda, B. Gao, S. Oh, L. Fleming, and G. Yue, "Materials Science of Carbon Nanotubes: Fabrication, Integration, and Properties of Macroscopic Structures of Carbon Nanotubes," *Acc. Chem. Res.*, vol. 35, pp. 1045–1053, 2002.
46. C. Thomsen, S. Reich, and J. Maultzsch, *Carbon Nanotubes: Basic Concepts and Physical Properties*. Wiley-VCH, 2004.
47. E. Malic, M. Hirtschulz, F. Milde, A. Knorr, and S. Reich, "Analytical Approach to Optical Absorption in Carbon Nanotubes," *Phys. Rev. B (Condens. Matter Mater. Phy.)*, vol. 74, p. 195431, 2006.
48. K. El-Shabrawy, K. Maharatna, and B. Al-Hashimi, "Exploiting SWCNT Structural Variability Towards the Development of a Photovoltaic Device," *Accepted in 12th International Symposium on Integrated Circuit*, 14–16 December 2009.
49. H. Kataura, Y. Kumazawa, Y. Maniwa, I. Umezu, S. Suzuki, Y. Ohtsuka, and Y. Achiba, "Optical Properties of Single-wall Carbon Nanotubes," *Synth. Met.*, vol. 103, pp. 2555–2558, 1999.
50. D. Chowdhary, and N. A. Kouklin, "dc Photoconduction Studies of Single-walled Carbon Nanotube Bundles," *Phys. Rev. B*, vol. 76, p. 035416, 2007.

51. S. M. Bachilo, M. S. Strano, C. Kittrell, R. H. Hauge, R. E. Smalley, and R. B. Weisman, "Structure-Assigned Optical Spectra of Single-Walled Carbon Nanotubes," *Science*, vol. 298, pp. 2361–2365, 2002.
52. "Standard G173–03 Tables for Reference Solar spectral Irradiances: Terrestrial Global 37 degree South Facing Tilt & Direct Normal + Circumsolar," available at http://rredc.nrel.gov/solar/spectra/am1.5/. American Society for Testing and Materials (ASTM) International, 1999.
53. S. Kim, H. Lee, H. Tanaka, and P. S. Weiss, "Vertical Alignment of Single-Walled Carbon Nanotube Films Formed by Electrophoretic Deposition," *Langmuir*, vol. 24, pp. 12936–12942, 2008.
54. K. Mizunoa, J. Ishiib, H. Kishidac, Y. Hayamizua, S. Yasuda, D. N. Futaba, M. Yumura, and K. Hata, "A Black Body Absorber from Vertically Aligned Single-walled Carbon Nanotubes," *PNAS*, vol. 106, pp. 6044–6047, 2009.

Chapter 9
Integrated Nano-Bio-VLSI Approach for Designing Error-Free Biosensors

Shantanu Chakrabartty, Evangelyn C. Alocilja, and Yang Liu

Reliability is a field of research that has largely been overlooked in the area of biosensing. As a result, rapid-response biosensors which have been shown to work remarkably well under controlled laboratory conditions, fail to reproduce similar results when deployed in the field [1, 2, 3, 4, 5, 6]. This degradation in reliability can be attributed to several factors which include device level artifacts, variations in experimental protocols, transducer and measurement noises, and stochastic interaction between biomolecules and background interference [5, 7]. Most of the reported methods in biosensing aim to reduce the effect of these artifacts by either improving the physical properties of the biosensor device [8, 9] or by using prefiltering techniques [10], preconcentration [11], or target-amplification (e.g., polymerase chain reaction or PCR) [12, 13] to boost the signal-to-noise ratio. However, with advances in micro-nano-fabrication, the emerging biosensors can integrate an ever increasing number of detection elements on the same device [14, 15, 16, 17, 18, 19]. This has opened the possibility that perhaps exploiting spatial redundancies across multiple detection experiments could be used to alleviate the effects of biosensor artifacts. This system level approach, also known as "forward error correction (FEC)" has been extensively used for designing ultra-reliable communication and storage systems [20]. However, its application in the area of biosensing is relatively new and is the main focus of this chapter. A generic architecture of an FEC biosensor is shown in Fig. 9.1 which comprises biomolecules as a reactive surface in close proximity to a transducer that converts the binding of the analyte with the biomolecule into a measurable signal [21]. The uniqueness of FEC biosensors compared with conventional architecture lies in the integration of the biomolecular encoding layer as shown in Fig. 9.1. This encoding could be achieved by spatially patterning biomolecular entities (e.g., antibodies, aptamers, or DNA) to form logic circuits – an antibody-based example is illustrated

S. Chakrabartty (✉)
Michigan State University, East Lansing, MI, USA
e-mail: shantanu@egr.msu.edu

S. Carrara (ed.), *Nano-Bio-Sensing*,
DOI 10.1007/978-1-4419-6169-3_9, © Springer Science+Business Media, LLC 2011

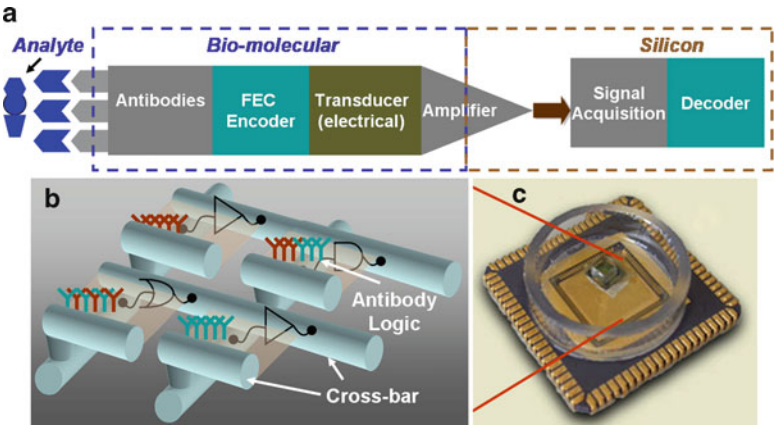

Fig. 9.1 Architecture of an FEC biosensor which comprises a biomolecular encoder that interfaces with a silicon decoder

in Fig. 9.1b. Also required for an FEC biosensor is a decoder which can then suitably correct for errors. Typically, the decoder could be implemented on silicon circuits and could be integrated in proximity with the biomolecular encoder as illustrated by an example in Fig. 9.1.

9.1 Reliability of Nano-Biosensors

The Webster's dictionary defines *reliability as the extent to which a device, experiment, or test yields the same results on repeated trials*. For biosensors, an effective measure of reliability is the total detection error rate (DER) which is the sum of two types of errors: (a) false-positive error rate or the probability that the biosensor incorrectly detects the pathogens when it is actually absent in the sample; and (b) false-negative error rate or the probability that the biosensor fails to detect the pathogen when it is actually present in the sample [22]. Several experimental and device level artifacts affect the DER of a biosensor and are illustrated in Fig. 9.2. These artifacts or sources of noise can be broadly classified into two categories: (a) systematic noise which occurs due to variations in experimental protocols (pH changes, use of low-affinity antibodies, thermal variations, and variations in the reagents used) and (b) inherent noise which occur due to the stochastic nature of the biomolecular interactions (e.g., antigen–antibody interactions) and due to the thermal and shot noise at the electrode–electrolyte interface or the measurement circuitry [7]. The errors in each stage of the biosensing process accumulate (as shown in Fig. 9.2) and finally manifests itself as a system noise which affects the overall DER. While systematic errors in biosensors could potentially be compensated either by improving the manufacturing process, maintaining strict control over experimental protocols, or using normalization

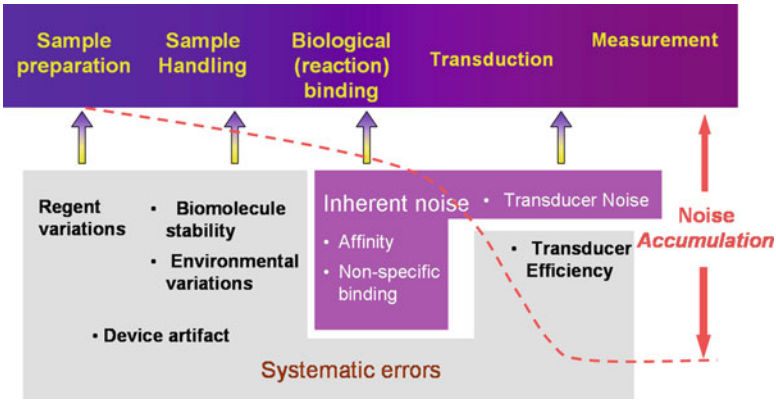

Fig. 9.2 Sources of errors that result in noise accumulation and affects the reliability of biosensors

techniques [23, 24, 25], the inherent noise can never be eliminated and has to be reduced using some form of averaging or FEC techniques.

Conventional techniques for improving the reliability of biosensors are either based on increasing the signal-to-noise ratio by amplifying the analyte concentration (e.g., PCR technique for DNA) [9] or by averaging the detection results over multiple experimental trials [23, 24]. In this regard, high-density biosensor arrays offer a unique opportunity not only because of their high-sensitivity at low-pathogen concentration [26, 27], but also as parallel detectors that can screen for multiple pathogens in a sample simultaneously [28, 29, 30]. Unfortunately, high-sensitivity comes at the price of large variance in measurements and reduced reliability [7, 31, 32]. Figure 9.3 summarizes the domain of DNA-based micro-nano-arrays in terms of their integration density, sensitivity, and reliability [33, 34]. Also, a study conducted in [1] reported that gene-chip arrays from different manufacturers showed only 5% agreement for identical experiments. For antibody-based immunoassays, the degradation is even worse [3, 35], and most of the efforts in the past have been focused either on improving the physical properties of immunoassays or enhancing the desired signal through preconcentration, prefiltering, or preamplification techniques. An alternate approach which is at the core of the proposed research is to exploit synthetic redundancies across multiple "noisy" biosensing elements to significantly improve the reliability of detection and possibly achieve error-free detection.

The advantage of using a system level approach over a traditional biosensor signal enhancement can be understood based on the celebrated *noisy-channel coding theorem* by Claude Shannon [36]. The theorem adapted for a biosensing application states that error-free detection using a "noisy" biosensor is possible as long as the rate of detection R is less than a statistical measure called the biosensor channel capacity $C > 0$. For the biosensor channel (shown in Fig. 9.1a), the rate of detection is given by $R = K/B$, where K is the number of different types pathogens

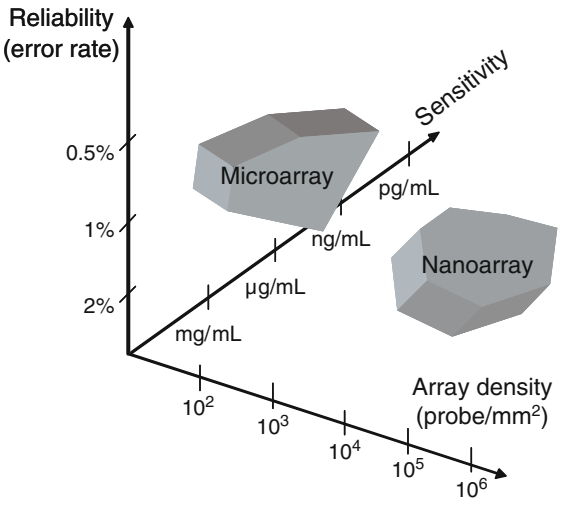

Fig. 9.3 Trends in DNA-based nano-biosensors illustrating the trade-off among integration density, sensitivity, and reliability

(*Escherichia coli*, *Salmonella*, etc.) and B is the number of elements in a biosensor array. Based on information theoretic arguments [36], the channel capacity C quantifies the theoretical limits of biosensor reliability where lowering C results in larger DER. If the "noise" or sources of errors across different biosensor elements are independent and obey Gaussian statistics (a worst case assumption), biosensor channel capacity C can be expressed as:

$$C = B \log(1 + \text{SNR}), \tag{9.1}$$

where SNR is the signal-to-noise ratio (dynamic range) of the biosensor array. Equation (9.1) illustrates the following key points with regard to achieving error-free detection:

(a) Increasing the signal-to-noise ratio using amplification techniques like the PCR in DNA biosensors or preconcentration in affinity-based biosensors increases the capacity C or the reliability of the biosensor array only logarithmically.
(b) Increasing the number of elements B in the array while maintaining a constant SNR increases the capacity and hence the reliability linearly.

Thus (9.1) shows that significant improvement in reliability of detection is possible when appropriate redundancy is introduced in a biosensor channel as opposed to just enhancing the biomolecular signal. However, (9.1) only provides an upper-bound on the capacity and does not prescribe a specific FEC approach for achieving error-free detection. Therefore, a systematic approach is required for designing a FEC biosensor which can achieve the limits of reliability dictated by the upper-bound in (9.1) given the constraints on size and fabrication accuracy.

9.2 Design Flow for a FEC Bio-Silicon Integration

Similar to an integrated circuit design flow, the design of a FEC nano-biosensor entails iterative fabrication, modeling, and simulation steps as illustrated in Fig. 9.4. The first step in the design flow is the fabrication of fundamental device and logic circuits (e.g., soft-AND and soft-OR logic gates). The responses of the fabricated devices and logic circuits are first measured, and the experimental data are used to generate equivalent circuit models and the nature and magnitude of biosensor noise. These circuit and noise models are then used to simulate the response of different biosensor topologies without resorting to painstaking fabrication and experimental procedures. The simulation framework can also incorporate practical constraints imposed by the size of the biosensor elements, element cross-talk, analyte propagation, and transducer artifacts. The performance of different biosensor FEC topologies obtained using Monte-Carlo studies and the results are compared against the target DER. The last step in the design flow involves fabricating prototypes of the FEC biosensor and validating its performance using a limited number of experiments. In the following sections, we illustrate some of the key concepts of this design flow using a specific case study.

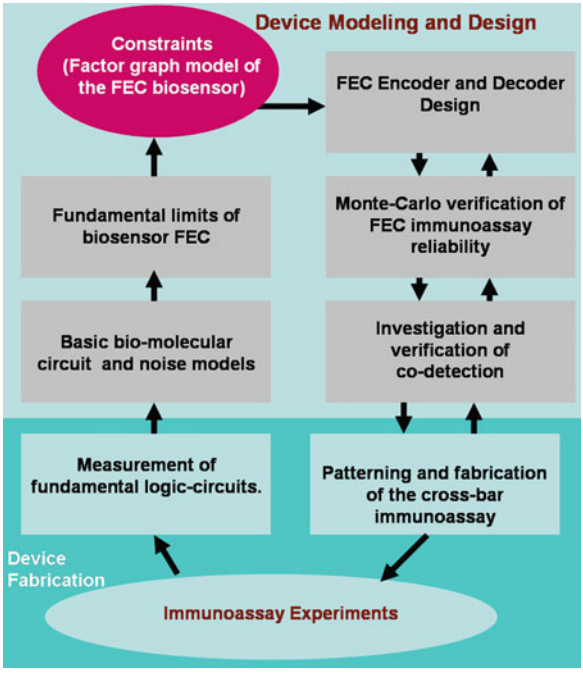

Fig. 9.4 Flow-chart describing the design flow of an FEC bio-silicon integration

9.2.1 Model Biosensor: Principle of Operation

For all our case studies in this chapter, we use a polyaniline nanowire-based immunosensor as our physical platform. Immunosensors (biosensors that use antibodies as the biomolecule) are of great interest recently because of their applicability (any compound can be analyzed as long as specific antibodies are available) and high selectivity. In particular, immunosensors with electrical readouts offer several advantages over their optical counterparts due to their reduced cost, reduced form factor and ease of signal acquisition. One such immunosensor, which is used in this chapter was introduced by Muhammad-Tahir and Alocilja [37, 38, 39], and can achieve a detection limit of 80 colony forming units CFU / mL for bacteria and 103 cell culture infective dose per milliliter (CCID / mL) for bovine viral diarrhea virus (BVDV) antigens in approximately 6 min. The immunosensor uses conductive polyaniline as a transducer and as a molecular switch that is triggered by the presence of target pathogen in the analyte. The use of polyaniline as a switch (yielding "on" and "off" responses) has been previously demonstrated using dual gold film electrodes [40]. In some biosensor configurations, polyaniline has also been used as an amplifier to improve the detection process [41, 42].

Conductive polyaniline nanowires-based immunosensors are relatively inexpensive to fabricate and easy to operate which makes it an ideal candidate for multiarray architecture. Previously, a machine learning approach was used to improve the detection rate of multiple pathogens at low concentration levels [43]. High detection rate at low pathogen concentrations is especially important for zero-tolerance pathogens for which ingesting even a small amount can prove dangerous. For instance, the US Food Safety Inspection Service has established a zero-tolerance threshold for *E. coli* O157:H7 contamination in raw meat products [44]. The infectious dosage of *E. coli* O157:H7 is 10 cells; the Environmental Protection Agency (EPA) standard in water is 40 cells per liter [45]. The US Food Safety Inspection Service also has a zero-tolerance rule for *Salmonella*, *Listeria monacytogenes* [45, 46]. In the study conducted [43], error rates less than 2% for concentration ranging from 10^0 to 10^7 CFU / mL have been reported. However, a major disadvantage of that approach is the requirement of a large calibration dataset for reliable training of a machine learning model.

9.2.2 Biosensor Structure and Principle

The architecture of a nanowire-based lateral flow immunosensor is shown in Fig. 9.5a. It is composed of four different pads: sample pad, conjugate pad, capture pad, and absorption pad. The antibody region (capture pad) constitutes a biomolecular switch triggered by specific antigens present in the analyte. The principle of operation of a single biomolecular switch is illustrated in Fig. 9.5b, which shows a cross-sectional view of the immunosensor. Before the sample solution is applied,

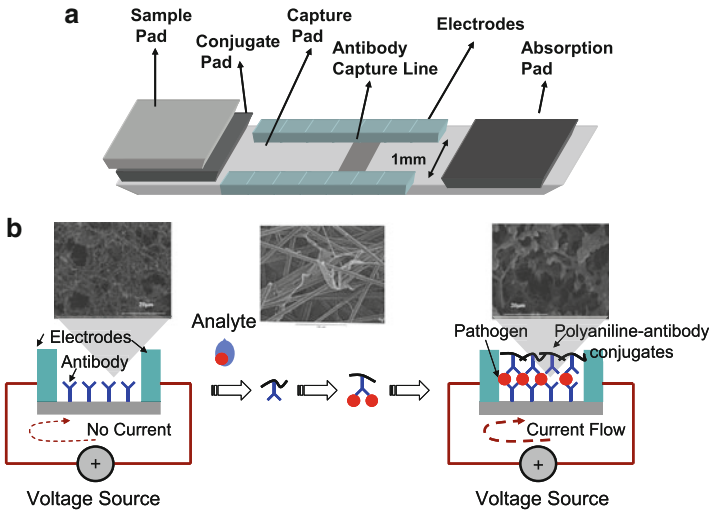

Fig. 9.5 The structure and operating principle of a nanowire-based lateral flow immunosensor

the gap between the electrodes in the capture pad is open. Immediately after the sample solution is applied to the sample pad, the solution containing the antigen flows to the conjugate pad, dissolves with the polyaniline-labeled antibody (Ab-P), and forms an antigen–antibody–polyaniline complex. The complex is transported using capillary action into the capture pad containing the immobilized antibodies. A second antibody–antigen reaction occurs and forms a sandwich. Polyaniline in the sandwich then forms a molecular wire and bridges two electrodes. The polymer structures extend out to bridge adjacent cells and leads to conductance change between the electrodes. The conductance change is determined by the number of antigen–antibody bindings, which is related to the antigen concentration in the sample. The unbound non-target organisms are subsequently separated by capillary flow to the absorption membrane. The conductance change is sensed as an electrical signal (current) across the electrodes. In Fig. 9.5b, we also show SEM images of the capture pad before and after the analyte with pathogen has been applied. The change in material texture can be observed in Fig. 9.5b, which is attributed to the formation of the antibody–antigen–antibody–polyaniline complex connecting the electrodes.

9.2.3 Fabrication and Characterization of Fundamental Logic Units

Purified rabbit polyclonal antibodies against *Bacillus cereus* and *E. coli* were obtained from Meridian Life Science (Saco, ME, USA). The antibodies were suspended in phosphate buffer solution (pH 7.4) and stored at 4 °C. *Bacillus cereus*

and *E. coli* strains were obtained from the National Food Safety and Toxicology Center (Michigan State University) and the Michigan Department of Community Health (East Lansing, MI, USA). A 10 μL loop of each isolate was cultured in 10 mL of nutrient broth and incubated for 24 h at 37 °C to prepare stock cultures. The stock cultures were serially diluted with 0.1% peptone water to obtain varying concentrations of each micro-organism. Polyaniline was purchased from Sigma–Aldrich (St. Louis, MO, USA). All experiments were carried out in a certified Biological Safety Label II laboratory. The sample pads (size: 15 ×5 mm) and absorption pads (size: 20 ×5 mm) were made of nitrocellulose membrane (flow rate: 135 s/4 cm), and the conjugate pads (size: 10 ×5 mm) were made of fiberglass membrane (grade G6). The porous nitrocellulose substrate ensures good adsorption properties for immobilized antibodies and allows nontarget antigens to flow through. The electrodes were patterned using aluminum paste and provided electrical connection between the nitrocellulose membrane and a data acquisition system. The conjugate pad was designed to allow maximal adsorption and flow of polyaniline-conjugated antibodies. Antibody concentration used for conjugate pad was 150 μg/mL and for the capture pad was 500 μg/mL. The polyaniline concentration in the conjugate pad was 1 mg/mL. All these values were found to be optimal, resulting in the highest ratio between the number of captured cells and the actual cell concentration tested. The immunosensors were then attached to an etched copper printed circuit board (PCB) which was used to connect to the multichannel potentiostat array.

The polyaniline–multivariate antibodies (PMA) conjugates were prepared by suspending 800 μL of polyclonal antibodies against *B. cereus* and *E. coli* (concentration 150 μg/mL) in a 4 mL of polyaniline solution in phosphate buffer (pH 7.4) containing 10% dimethylformamide (DMF) (v/v) and 1% LiCl (w/v). The solution was incubated at room temperature for 1 h to allow binding of the antibodies with polyaniline and then treated with a blocking reagent (Tris buffer containing 0.1% casein). The polyaniline–multivariate antibody conjugates were then precipitated by centrifugation at 12,000 rpm for 5 min. These are the settings from the centrifuge. To get the g-force number we would need to measure the distance from the center of rotation. The supernatant fluid was discarded, and the pellets were mixed with the blocking reagent and centrifuged again. The centrifugation step was repeated three times. The conjugates were finally suspended in phosphate buffer solution containing 0.1% LiCl (w/v) and 10% DMF (v/v) and stored at 4 °C until use. The conjugate pads were prepared by soaking the fiberglass strip into the PMA solution until a homogenous dispersion is achieved. Extensive characterization of a single strip, single pathogen biosensor has been performed elsewhere [37, 47]. From now on, we refer to this particular immunosensor as a biomolecular transistor because of its transistor-like responses.

We have fabricated and characterized the response of a single biomolecular transistor using *B. cereus* antibody with respect to different pathogen concentrations. Figure 9.6a shows the measured conductance across the biosensor electrodes as the concentration of pathogen (*B. cereus*) in the sample is varied. The measured conductance is normalized with respect to the "control" conductance (measured

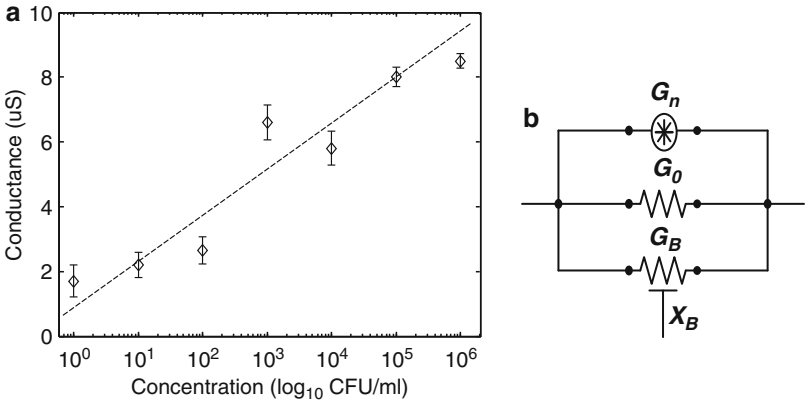

Fig. 9.6 Conductance measurement of *Bacillus cereus* single biomolecular transistor

when a sample containing no pathogens is applied) and shows a clear discrimination between pathogenic and nonpathogenic cases. The plot in Fig. 9.6a also shows a monotonic increase in conductance with an increase in pathogen concentration (given in colony forming units per milliliter – CFU/mL). This response can be approximated using a log–linear model (shown by a dotted line in Fig. 9.6), and the regression error is used to approximate the systematic error. Fig. 9.6a also shows error bars computed using multiple experimental runs and they are used for estimating the random errors. A log–linear model is given by

$$G(X_B) = G_0 + \kappa \log \frac{X_B}{X_0} + G_n \,, \tag{9.2}$$

where X_{B} represents the concentration of the pathogen *B. cereus* in CFU/mL, G_0 represents the "control" transconductance, κ represents sensitivity factor, and X_0 is a detection constant. Note that (9.2) is valid only for $X_{\mathrm{B}} \geq X_0$, which is a reasonable assumption. The systematic and random errors are included as the additive noise component G_{n} in the equivalent circuit model of the biomolecular transistor (shown in Fig. 9.6b). Based on this large signal model, it can be shown that a single biosensor acts like a "pathogen concentration" controlled resistor that is similar to an operation of a MOSFET transistor biased in weak inversion [48].

Limitations of the log–linear model in (9.2) in predicting the pathogen concentration will arise due the "hook effect," a common phenomenon observed in most biosensors where the conductance decreases with an increase in pathogen concentration. The "hook effect" is typically attributed to the presence of large concentration of pathogens, leading to saturation of binding sites and obstructing charge transfer within the conductive polyaniline structure. For instance, in [38] the "hook effect" was observed at concentrations above 10^4 CFU/mL for biosensor electrode spacing of approximately 0.5 mm. In our experiments, the electrodes are spaced approximately at 1 mm which therefore the "hook effect" was not observed, possibly at the expense of reduced sensitivity factor.

9.2.4 Biomolecular Logic Gates

The biosensor principle was extended to implement two variants of logical operations (AND and OR) in [47]. Figure 9.7a shows the structure of an AND gate (marked by 1) and OR gate (marked by 2) constructed using the antigen–antibody–polyaniline complex. An AND operation is achieved by cascading two different antibodies in-between the biosensor electrodes. Thus, in an ideal condition, conduction between the electrodes occurs only when both the pathogens are present in the sample (for completing the polyaniline bridge as shown in Fig. 9.7a (1)). An OR operation is achieved by immobilizing a mixture of antibodies between the electrodes. Thus, in an ideal condition, a polyaniline nanowire bridge is formed when either one of the antigen is present. We have successfully fabricated and characterized biomolecular logic gates based on the principles described above [47].

Figure 9.7b, c shows the transient responses measured using the fabricated AND and OR logic gates. They measure four different states when only *E. coli*, only *B. cereus*, both pathogens, and no pathogens (control) exist. The calibrated concentration of *E. coli* and *B. cereus* are 6.3×10^7 and 5.03×10^7 CFU / mL, respectively. The conductance measured across the electrodes stabilizes around 100 s after the application of analyte and it constitutes the steady state of the biosensor logic gate. The transient behavior is attributed to the dynamics of the polyaniline sandwich in the presence of analyte flow, adhesion, and capillary force. However, in this study, only the steady-state conductance will be used for modeling, and the derivation of transient models is deferred for future publications.

Figure 9.8a shows the response of an AND gate corresponding to different pathogen concentrations, where E represents *E. coli* and B represents *B. cereus*. The conductance of biosensor is measured for two sets of pathogen concentration and for four possible logic conditions ($E = 0, 1$ and $B = 0, 1$) where a binary state represents the absence or presence of a pathogen. The measured conductance are compared against a "control" response that represents the logic condition $E = 0$, $B = 0$. It can be seen from Fig. 9.8a that the measured conductance for logical condition ($E = 1$, $B = 1$) is higher than all other cases (irrespective of pathogen concentration) which corresponds to a soft-AND operation. However, Fig. 9.8a also shows that the measured conductance, when only *B. cereus* is present, is close to the condition when both *B. cereus* and *E. coli* are present. This artifact could be attributed to the imperfect antibody masking in the fabrication procedure which led to signal leakage across the electrodes. Figure 9.8b shows the measured conductance for a biosensor acting as an OR logic gate. The plot shows that for both pathogen concentration levels, the "control" condition ($E = 0$, $B = 0$) leads to a lower conductance as compared to other logical states. Therefore, the response of the biosensor "is equivalent to the response of an OR logic". Also note that OR logic is easy to pattern (no masking

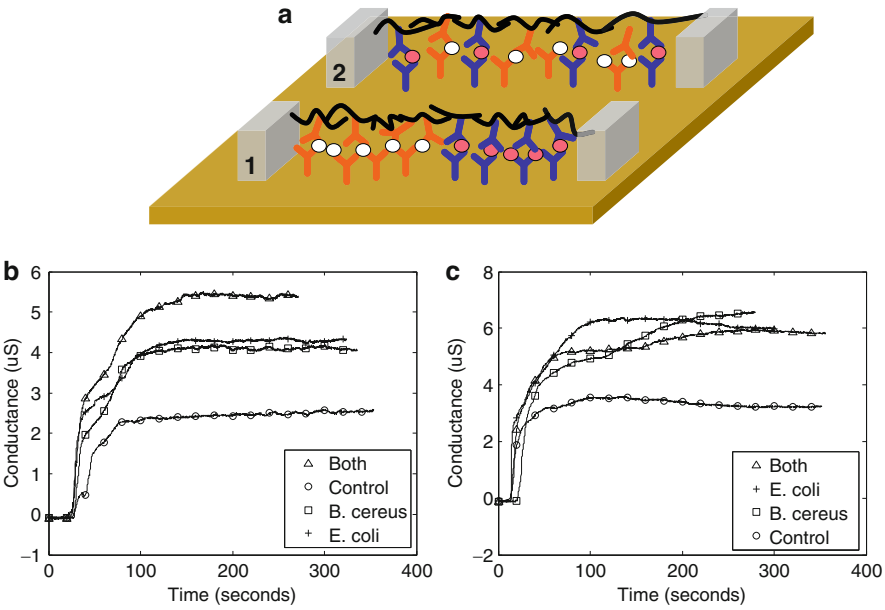

Fig. 9.7 (**a**) Schematic illustration of biomolecular logic gates. (**b**) Typical transient response of AND gate. (**c**) Typical transient response of OR gate (AND gate (marked by 1), OR gate (2))

required), therefore leading to near ideal operation as compared to an equivalent AND gate. The response of the logic gates for different concentration of pathogens is shown in Fig. 9.8a, b have been used to derive their equivalent circuit models that incorporate the inherent noise sources.

The corresponding circuit models for OR and AND gates are shown in Fig. 9.8c, d and their respective mathematical responses are provided below.

$$G(X_B, X_E) = G_{OR} + \kappa_B^{OR} \log \frac{X_B}{X_{0B}^{OR}} + \kappa_E^{OR} \log \frac{X_E}{X_{0E}^{OR}} + G_n \,, \tag{9.3}$$

$$G(X_B, X_E) = G_{AND} + \kappa_B^{AND} \log \frac{X_B}{X_{0B}^{AND}} + \kappa_E^{AND} \log \frac{X_E}{X_{0E}^{AND}} + \kappa_{EB}^{AND} \log \frac{X_E + X_B}{X_{0EB}^{AND}} + G_n \,, \tag{9.4}$$

Table 9.1 summarizes the meaning and typical values of the model parameters that have been extracted using the measured results and have been used for simulations presented in the next following chapters.

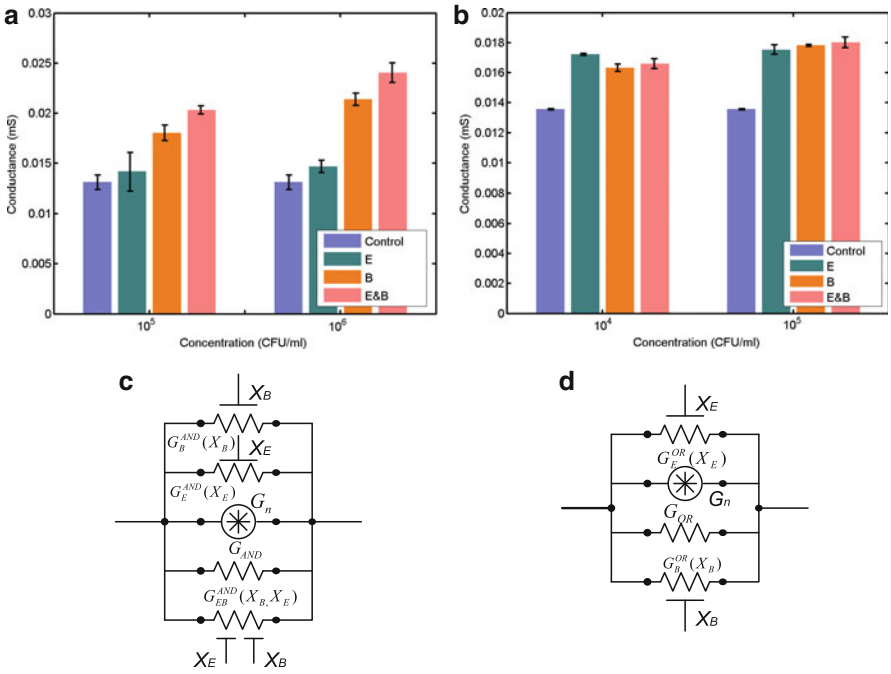

Fig.9.8 (**a**) Conductance measurement of AND biomolecular logic gate. (**b**) Conductance measurement of OR biomolecular logic gate. (**c** and **d**) The circuit model of AND and OR biomolecular logic gates

9.3 Design of Biomolecular Encoder and Silicon Decoder

9.3.1 The Framework of FEC Biosensors

As we mentioned, the similarity among the reliable communication, storage systems, and biosensor systems motivates to apply similar encoding/decoding schemes in the biosensor systems. Encoding and decoding concepts and algorithms are fairly straightforward in communication systems. While in biosensor systems, the corresponding concepts, such as codewords, are not so obvious. Also constructing a biomolecular encoder is limited by biosensor structures and principles. For example, XOR logic may be difficult to achieve in biosensor structure. If the encoder logic functions are very limited, how would one design an efficient encoder and decoding algorithm for the reliable biological information transmission? Those problems are uncommon in the communication systems, but are immediate challenges for engineered biosensor systems.

Table 9.1 Parameter meaning and typical values of formula (2)–(4)

Parameter	Meaning	Value
G_0	"Control" transconductance	1.24 μS
κ	Sensitivity factor	1.2 μS
X_0	Detection constant	0.1 CFU/mL
G_{OR}	"Control" transconductance	13.6 μS
κ_B^{OR}	Sensitivity factor of *B. cereus*	0.15 μS
X_{0B}^{OR}	Detection constant for *B. cereus*	0.76 μS
κ_E^{OR}	Sensitivity factor of *E. coli*	0.09 μS
X_{0E}^{OR}	Detection constant for *E. coli*	8.5×10^{-4} CFU/mL
G_{AND}	"Control" transconductance	13.1 μS
κ_B^{AND}	Sensitivity factor of *B. cereus*	3.4 μS
X_{0B}^{AND}	Detection constant for *B. cereus*	10^3CFU/mL
κ_E^{AND}	Sensitivity factor of *E. coli*	0.45 μS
X_{0E}^{AND}	Detection constant for *E. coli*	4.6×10^2 CFU/mL
κ_{EB}^{AND}	Sensitivity factor of coupling effect	0.4 μS
X_{0EB}^{AND}	Detection constant of coupling effect	1.2×10^3 CFU/mL
G_n	Conductance induced by noise	Variable

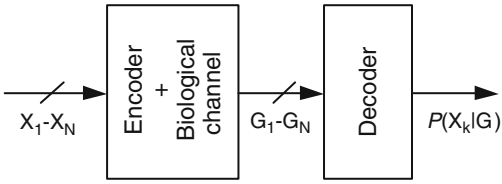

Fig. 9.9 The Framework of FEC biosensor

In this section, we utilize the biomolecular circuit models to evaluate different FEC topologies that can improve the reliability of the model biosensor. A system level architecture of a proposed FEC biosensor is shown in Fig. 9.9, which consists of an encoder that is an ensemble of N biomolecular circuits that convert the biological binding into a change in conductance, a channel that introduces random and systematic errors, and a decoder that uses the noisy measurements to produce probability estimates indicating the presence or absence of pathogens in a sample. The decoder processes the noisy measured conductances $G_i, i = 1, \ldots, N$ and produces posteriori probability estimates $P(X_k \mid G_1, \ldots, G_N), k = 1, \ldots, N$, where $X_k \in \{0, 1\}$ is a Boolean variable corresponding to the logical operation of the kth biomolecular circuit. In the mathematical treatment that follows, it will be assumed that the channel is the only source of randomness and the encoding/decoding operation is perfectly reliable.

The posteriori estimate $P(X_k \mid G_1, \ldots, G_N)$ can be simplified according to

$$
\begin{aligned}
P(X_k|G_1,\ldots,G_N) &= \propto \sum\nolimits_{\sim X_k} P(X_1,\ldots,X_N,G_1,\ldots,G_N)\,, \\
&= \sum\nolimits_{\sim X_k} \prod\nolimits_{j=1}^{N} P(G_j|X_k) P(X_1,\ldots,X_N)\,, \\
&= \sum\nolimits_{\sim X_k} f(X_1,\ldots,X_N) \prod\nolimits_{j=1}^{N} P(G_j|X_k)\,,
\end{aligned}
\tag{9.5}
$$

where $_{j=1}{}^{N}P(G_j \mid X_k)$ models the response of the biomolecular circuit elements and $f(X_1,\ldots,X_N)$ represents a Boolean function that captures the logical dependency among the variables $X_k, k = 1,\ldots,N$ and hence models the structure of the encoder. The encoder function $f(.)$ can be represented in a tabular form where each table entry represents a state of the variables $X_1,\ldots,X_N$ for which $f(X_1,\ldots,X_N) = 1$ and 0 otherwise. We will provide some specific examples of the encoder function in next section. Equation (9.5) also describes the decoding algorithm used for computing the a-posteriori probability estimates.

9.3.2 Biosensor Encoder

As Fig. 9.9 shows, the biomolecular encoder has to be constructed in the biosensor structure, being able to provide redundant information. However, it depends on the types of logic functions that can be achieved by bimolecular logic gates. We will first discuss possible encoding methods that can be applied in biosensors. The simplest encoding method is the "repetition" code where biomolecular transistors that detect single pathogen are replicated multiple times. One could get more accurate estimation when using majority voting rule. For example, biomolecular transistors specific to two model pathogens *B. cereus* and *E. coli* are replicated three times, respectively. In this case, $X_1,\ldots,X_6$ will be used to represent the Boolean variables corresponding to the output of each of the biomolecular transistor. The resulting encoder function $f(X_1, X_2,\ldots,X_6)$ is summarized in Table 9.2. This encoder is denoted as a (6,2) repetition code which implies that six measurements are independently performed (sequentially or in parallel) to detect two possible pathogens.

Another form of the encoding function that will be the focus of this study uses the biomolecular OR and AND logic circuits. In conventional FEC codes used in communications and storage systems, a XOR operation is utilized to obtain linear

Table 9.2 (6,2) Repetition code

X_1	X_2	X_3	X_4	X_5	X_6
0	0	0	0	0	0
0	1	0	1	0	1
1	0	1	0	1	0
1	1	1	1	1	1

Table 9.3 (6,2) Asymmetric code

X_1	X_2	X_3	X_4	X_5	X_6
0	0	0	0	0	0
0	1	1	0	0	1
1	0	1	0	1	0
1	1	1	1	1	1

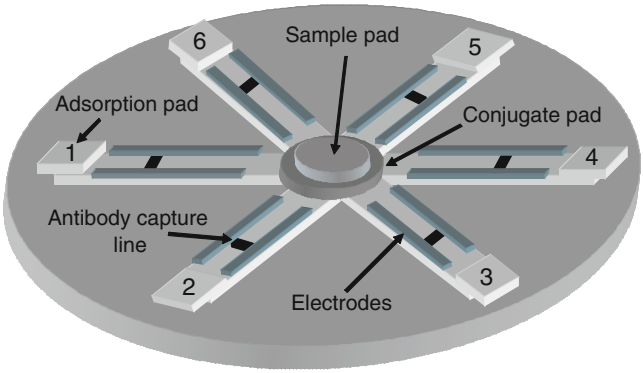

Fig. 9.10 A visualization of multipathogen biosensor CD that could implement the encoding methods

codes which by construction are symmetric. Unfortunately, XOR logic using the proposed biosensor principle is unrealizable and hence our encoding (also referred to as an asymmetric code) function will only be based on OR and AND biomolecular circuits. One specific instance of a (6,2) encoder function is summarized in Table 9.3, where X_1 and X_2 are Boolean variables corresponding to the absence or presence of *B. cereus* and *E. coli*. The variable X_3 represents a logical OR operation between X_1 and X_2, and variable X_4 corresponds to a logical AND operation. The variables X_5 and X_6 are repetition of variables X_1 and X_2.

For the lateral flow immunoassay which was taken as a model biosensor in this study, the encoder can be realized by adding redundant paths for the flow of analyte toward the biomolecular logic gates. One possible realization is illustrated in Fig. 9.10, where the sample is first applied to a sample pad and a conjugate pad where the pathogen–antibody–polyaniline complex is formed. The complex then splits into parallel flow paths and propagates to different antibody capture lines where the biomolecular logic gates/transistors are immobilized. Conductometric potentiostats [49, 50] are then used to measure the conductance across the electrodes of the biomolecular circuits. The measured conductance is then processed by a digital signal processor or analog decoder chip, which implements the factor graph decoding algorithm and flags the presence or absence of target pathogens.

9.3.3 *Factor Graph Model and Soft Decoding Algorithm*

When the encoded information of biomolecular circuits is available, appropriate and efficient decoding algorithm will be applied to decipher the original biological information. Unfortunately, some popular codes in communication systems such as Hamming code and LDPC code cannot be directly applied because of the uniqueness of biomolecular logic functions. The factor graph representations are used for efficient computation of the a-posteriori probabilities by marginalizing variables according to (9.5). Computation on factor graphs proceeds using distributed algorithms which in literature are known as the "sum-product" algorithms [51]. The structure of different biosensor codes can be conveniently represented as a factor graph (shown in Fig. 9.11). In this section, we describe the "sum-product" message passing algorithm for factor graphs corresponding to the biomolecular circuits. For a general treatment of message passing algorithms, the readers are requested to refer [52].

A Forney-style factor graph [53] corresponding to an uncoded biosensor is shown in Fig. 9.11a, a (6,2) repetition code biosensor is shown in Fig. 9.11b, and a (6,2) asymmetric code biosensor is shown in Fig. 9.11c. For the uncoded case, the factor graph in Fig. 9.11a consists of two transducer nodes (T) whose inputs are the conductance measured from two biosensors specific to *E. coli* and *B. cereus*. The transducer node captures the relationship between the measured conductances $G_1, \ldots, G_N$ and the indicator variables $X_1, \ldots, X_N$. Because estimations of the presence of pathogens are directly based on the measurement, so there is no coupling between the two transducer nodes implying that the detection of pathogens (*E. coli* and *B. cereus*) is performed independently of each other. For the (6,2) repetition code factor graph shown in Fig. 9.11b, the transducer nodes corresponding to each of the two pathogens are repeated twice. In this case, however, the measurements are coupled and the dependency is depicted in the factor graph using Equality nodes (=). In an (6,2) asymmetric code factor graph shown in Fig. 9.11c, some of the transducer nodes also models the biomolecular OR and AND circuits. Therefore, the edges in the factor graph which represent the functional dependencies between the nodes connect the pathogen indicator variables $(X_1, \ldots, X_6)$ using the AND, OR, and

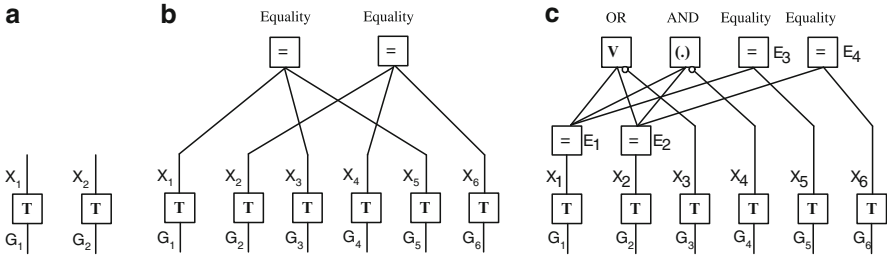

Fig. 9.11 Forney-style factor graph models of the FEC biosensor. (**a**) Uncoded biosensor; (**b**) (6,2) biosensor repetition code; (**c**) (6,2) biosensor asymmetric code

Equality nodes. Note that the AND and OR nodes are connected to exactly three edges, where as the Equality nodes are connected to at least two edges.

In the biomolecular factor graph decoding algorithm, each of the nodes propagates messages along the edges to each of its immediate neighbors. These messages take the form of probability estimates that the node to which the message is being sent to is in state 0 or 1. For example, consider an Equality node E that is connected to three adjacent nodes x, y, z (shown in Fig. 9.12). The node E receives messages from nodes x and y denoted by $(\mu_{x\to E}(0), \mu_{x\to E}(1))^T$ and $(\mu_{y\to E}(0), \mu_{y\to E}(1))^T$. It then computes the message sent to node z, denoted by $(\mu_{E\to z}(0), \mu_{E\to z}(1))^T$ according to the equality constraints which ensures that there are only two valid states $(x, y, z) = (0, 0, 0), (1, 1, 1)$. The corresponding message passing rules for the Equality node is summarized in Fig. 9.12. Also summarized in Fig. 9.12 are message passing rules corresponding to OR and AND node. Because OR and AND operations are asymmetric (as opposed to an XOR operation which is symmetric) with respective to their inputs, the figure describes two sets of rules based on the direction of the message flow. The asymmetric message schedule is unique to the proposed FEC biosensor as it only uses AND, OR, and Equality logic functions for computation.

Decoding using the factor graph model in Fig. 9.11 begins by initializing the transducer nodes using the conductance measurements obtained from the biomolecular circuits. The transducer nodes first normalize the measurements according to:

$$\mu_{G_k\to X_k}(1) = \frac{e^{\beta_k(G_k-G_0)}}{1+e^{\beta_k(G_k-G_0)}}, \tag{9.6}$$

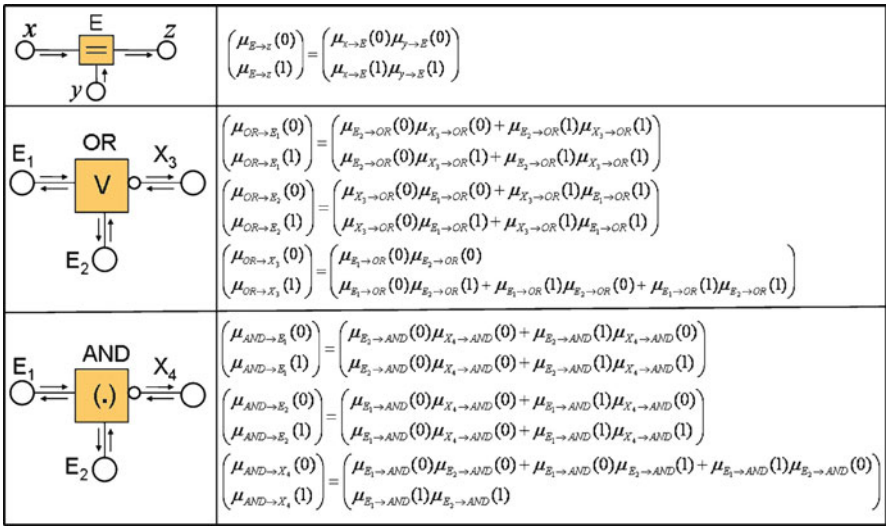
x
E
z
y
$\begin{pmatrix}\mu_{E\to z}(0)\\ \mu_{E\to z}(1)\end{pmatrix} = \begin{pmatrix}\mu_{x\to E}(0)\mu_{y\to E}(0)\\ \mu_{x\to E}(1)\mu_{y\to E}(1)\end{pmatrix}$
E1
OR
X3
V
E2
$\begin{pmatrix}\mu_{OR\to E_1}(0)\\ \mu_{OR\to E_1}(1)\end{pmatrix} = \begin{pmatrix}\mu_{E_2\to OR}(0)\mu_{X_3\to OR}(0)+\mu_{E_2\to OR}(1)\mu_{X_3\to OR}(1)\\ \mu_{E_2\to OR}(0)\mu_{X_3\to OR}(1)+\mu_{E_2\to OR}(1)\mu_{X_3\to OR}(1)\end{pmatrix}$
$\begin{pmatrix}\mu_{OR\to E_2}(0)\\ \mu_{OR\to E_2}(1)\end{pmatrix} = \begin{pmatrix}\mu_{X_3\to OR}(0)\mu_{E_1\to OR}(0)+\mu_{X_3\to OR}(1)\mu_{E_1\to OR}(1)\\ \mu_{X_3\to OR}(0)\mu_{E_1\to OR}(1)+\mu_{X_3\to OR}(1)\mu_{E_1\to OR}(1)\end{pmatrix}$
$\begin{pmatrix}\mu_{OR\to X_3}(0)\\ \mu_{OR\to X_3}(1)\end{pmatrix} = \begin{pmatrix}\mu_{E_1\to OR}(0)\mu_{E_2\to OR}(0)\\ \mu_{E_1\to OR}(0)\mu_{E_2\to OR}(1)+\mu_{E_1\to OR}(1)\mu_{E_2\to OR}(0)+\mu_{E_1\to OR}(1)\mu_{E_2\to OR}(1)\end{pmatrix}$
E1
AND
X4
(.)
E2
$\begin{pmatrix}\mu_{AND\to E_1}(0)\\ \mu_{AND\to E_1}(1)\end{pmatrix} = \begin{pmatrix}\mu_{E_2\to AND}(0)\mu_{X_4\to AND}(0)+\mu_{E_2\to AND}(1)\mu_{X_4\to AND}(0)\\ \mu_{E_2\to AND}(0)\mu_{X_4\to AND}(0)+\mu_{E_2\to AND}(1)\mu_{X_4\to AND}(1)\end{pmatrix}$
$\begin{pmatrix}\mu_{AND\to E_2}(0)\\ \mu_{AND\to E_2}(1)\end{pmatrix} = \begin{pmatrix}\mu_{E_1\to AND}(0)\mu_{X_4\to AND}(0)+\mu_{E_1\to AND}(1)\mu_{X_4\to AND}(0)\\ \mu_{E_1\to AND}(0)\mu_{X_4\to AND}(0)+\mu_{E_1\to AND}(1)\mu_{X_4\to AND}(1)\end{pmatrix}$
$\begin{pmatrix}\mu_{AND\to X_4}(0)\\ \mu_{AND\to X_4}(1)\end{pmatrix} = \begin{pmatrix}\mu_{E_1\to AND}(0)\mu_{E_2\to AND}(0)+\mu_{E_1\to AND}(0)\mu_{E_2\to AND}(1)+\mu_{E_1\to AND}(1)\mu_{E_2\to AND}(0)\\ \mu_{E_1\to AND}(1)\mu_{E_2\to AND}(1)\end{pmatrix}$

Fig. 9.12 Sum-product message updated rules of three function nodes (Equality, OR, and AND)

where $\beta_k \in [0, 1]$ is a scaling factor that is heuristically chosen for the transducer element k. These normalized measurements are used as messages that are sent to the neighboring Equality, AND, and OR nodes. The Equality, AND, and OR nodes also compute messages locally and transmit it to their neighbors. Messages are propagated back and forth between the nodes for a predetermined number of iterations before a decision on the Boolean variables $X_1, \ldots, X_6$ is made [52]. In algorithm 1. we summarize the complete message passing algorithm which is specific to the factor graph model in Fig. 9.11c.

9.4 Results and Discussions

9.4.1 Behaviorial Simulation of FEC Biosensors

In this section, we present results that were obtained using algorithm ?? when applied to the factor graphs in Fig. 9.11. The biosensor encoder was simulated using the biomolecular circuit models summarized in Sect. 9.2. For different concentration of pathogens (*B. cereus* and *E. coli*), these models produced conductance parameters that were then corrupted by measurement noise. The noise was modeled as a zero-mean additive white Gaussian noise (AWGN) whose variance was experimentally determined according to the procedure described before. The noisy conductance parameters $G_1, \ldots, G_k$ were then presented as an input to the factor graph model, and the probability of the presence of *B. cereus* and *E. coli* was estimated using the message passing algorithm 1. The estimated probability was compared against a predetermined threshold (0.5) to obtain a yes/no answer, indicating the presence or absence of pathogens in the sample. The simulation experiment was repeated 1,000 times for each pathogen concentration level and the DER was determined by the occurrence of false rejection and false acceptance.

Figure 9.13a shows two-dimensional DER (error rate for *E. coli* + error rate for *B. cereus*) curves obtained for a (6,2) biosensor repetition code (represented by the factor graph model in Fig. 9.11b) and compares it against the DER curves obtained for the uncoded case (represented by the factor graph model in Fig. 9.11a). As expected, the DER reduces when the concentration of pathogen (represented in CFU/mL) increases. Also as expected, the DER for the repetition code (due to larger redundancy) is lower than that of uncoded case. Similar improvement is also obtained when a (6,2) biosensor asymmetric code (represented by the factor graph model in Fig. 9.11c is compared against the uncoded case and is shown in Fig. 9.13b. Figure 9.13c compares the ratio of the DER corresponding to the asymmetric code with the repetition code and demonstrates that except for ultra-low pathogen concentration levels, the performance of the asymmetric code biosensor is superior to that of the repetition code biosensor by a factor of 5.

Moreover, compared with the repetition code, asymmetric code exhibits a novel detection principle which we label as “co-detection.” The principle can be clearly

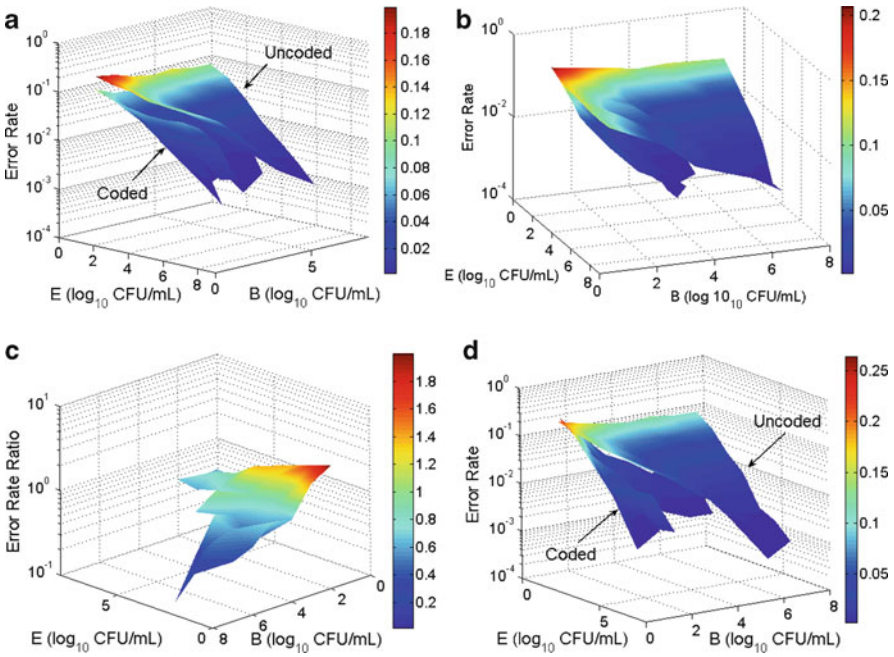

Fig. 9.13 (**a**) DER curve of (6,2) repetition code. Each point in the error curve is based on multiple biosensor experiments for a given pathogen (*B. cereus* and *E. coli*) concentration. (**b**) DER curve of (6,2) asymmetric code. (**c**) The comparison of (6,2) asymmetric code and (6,2) repetition code. The error curve compares the ratio of the DER corresponding to the asymmetric code with the repetition code. (**d**) DER curve of (10,2) extended asymmetric code

seen if the DER for each of the pathogens (instead of total DER) is separately projected on a 2D plot. This is shown in Fig. 9.14a, b for a repetition code and in Fig. 9.14c, d for the asymmetric code. Figure 9.14a shows the colormap of the DER corresponding to *B. cereus* illustrating that the DER is independent of the *E. coli* concentration which is expected Since there is no coupling between the two detection mechanisms. Similar DER plot for the *E. coli* is shown in Fig. 9.14b. However, equivalent plots for the asymmetric code shown in Fig. 9.14c, d demonstrate a strong coupling between the concentration of *E. coli*/*B. cereus* in the input sample and the DER corresponding to *B. cereus*/*E. coli*. This suggests that for the asymmetric code, large concentration of one pathogen could in fact improve the detection performance of trace quantities of another pathogen. We refer to this mutual coupling as the "co-detection" principle and represents one of the benefits of developed simulation environment where the different encoding–decoding techniques could yield novel methods of improving reliability of biosensors.

We have also conducted experiments with different sizes of asymmetric code and demonstrated that the DER will consistently improve with the size of the code. This is illustrated in Fig. 9.13d which shows the DER obtained for a (10,2) extended asymmetric code with the structure shown in Table 9.4 and compares it

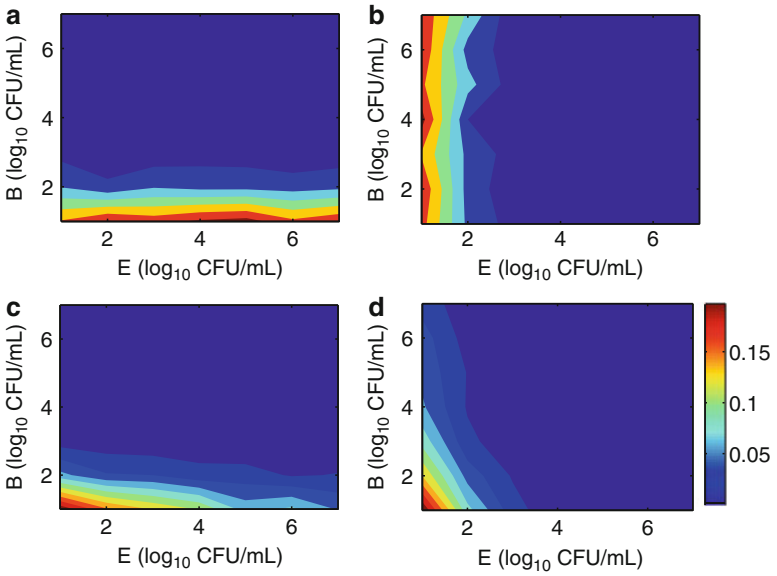

Fig. 9.14 Two-dimensional projection of DER curve. (**a**, **b**) Repetition code; (**c**, **d**) asymmetric code. Panels (a) and (c) represent the detection error rate of pathogen *B. cereus* where nonlinear detection relationship between two pathogens is revealed in (c). Panels (b) and (d) represent the DER of pathogen *E. coli* where nonlinear detection relationship between two pathogens is revealed in (d)

Table 9.4 (10,2) Asymmetric code

X_1	X_2	X_3	X_4	X_5	X_6	X_7	X_8	X_9	X_{10}
0	0	0	0	0	0	0	0	0	0
0	1	1	0	0	1	1	0	0	1
1	0	1	0	1	0	1	0	1	0
1	1	1	1	1	1	1	1	1	1

with an uncoded case. This illustrates that consistent improvement could be obtained if the asymmetric code is applied to large-scale immunoassays similar to DNA microarrays.

9.4.2 Analysis and Discussions

Several conclusions can be drawn from the simulation results presented above. First, embedding an encoding scheme like a repetition code on the biosensor

improves its reliability (given by DER) compared with the case when no encoding is used. However, an equivalent asymmetric code offers a better performance in terms of DER as shown in Fig. 9.13c. The error rate of repetition code is higher than that of asymmetric code except for low concentration of both pathogens. The deviation can be attributed to imperfect modeling of the logic gates (AND and OR) due to limited experimental data, especially at low pathogen concentration levels. We also believe that improving the response of logic gates (AND and OR) would improve the performance of the asymmetric code.

The use of logic gates in biosensor encoder synthetically introduces coupling between multiple conductance measurements. This is in contrast to most biosensor designs where the objective is to obtain independent measurements and in the process suppress any cross-reactive phenomena. In our prior work, we demonstrated that a nonlinear classifier (support vector machine) can exploit the nonlinear interaction between pathogens and their target/nontarget antibodies to improve the detection performance. However, the training complexity significantly increases when the classifier has to model the side-information present at the output of the biosensor logic gates. We believe that incorporating cross-reactive principles in the FEC encoder would enhance the side-information available to the decoder to improve the detection reliability. The nonlinear side information also leads to the previously referred principle called "co-detection." In the "co-detection" principle, a large concentration of known pathogen improves the detection of trace quantities of unknown pathogens. We attribute this effect to the nonlinear properties of the AND/OR gate formed using antibodies corresponding to the known and unknown pathogens. When large quantity of known pathogens is added, the conductive polyaniline bridge between the electrodes is partially formed. Thus, completion of the bridge could be achieved even when trace quantities of unknown pathogen are present. Also, the occurrence of false positive can be suppressed due to the principle of embedded encoding/decoding scheme. An experimental protocol that uses "co-detection" would therefore: (a) first identify easy-to-detect pathogens (pathogens which have high concentration levels in the sample); (b) then intentionally add large quantities of the identified pathogen into the sample which will enable trace detection of other pathogens using co-detection; (c) repeat the procedure until all the pathogens of interest have been screened.

The simulation study also show that the reliability of FEC biosensors improves when the size of the asymmetric code is increased. Thus, a trade-off exists between the reliability of the biosensor and redundant biomolecular circuit elements added, which is also related to biosensor area (cost). Future research will focus on optimizing the biosensor codes for achieving the optimal reliability, which is equivalent to deriving information theoretic bounds used in communication and storage systems. In this regard, the nature of biological channel needs to be investigated further to model and understand the stochastic protein–protein interaction and how it contributes to the biosensor noise.

9.5 Summary

In this study, we show how to create a symbiotic relationship between nano-bio and VLSI techniques to achieve "biological level" performance while ensuring "synthetic level" reliability of biosensors. The objective of this research is to replicate the success of FEC principles in designing reliable computing and storage systems toward designing reliable biosensors. In this regard, the study addresses some of the key challenges in this long-term goal. The first step involves mathematical abstraction where simulation models are developed which capture the experimentally measured response of the biomolecular circuits. These simulation models are then used to: (a) understand the nature of the biosensor channel and in the process which derive fundamental limits of biosensor FEC; (b) rapid design and evaluation of different FEC encoding and decoding algorithms without resorting to painstaking experimental procedures. We then have presented an analytic framework of FEC biosensors that have different encoder topologies. Reliability analysis is performed by exploiting probabilistic dependencies between the circuit elements using a factor graph-based decoding technique. Using the simulation framework, we demonstrated the efficacy of an asymmetric biosensor code as a potential candidate for improving the reliability of the FEC biosensor. We also reported a novel "co-detection" principle based on the property of the asymmetric code. The principle exploits the nonlinear coupling between different biomolecular circuits and prescribes an experimental protocol that could be used for trace detection of pathogens in a given sample. We believe that the analytical framework proposed in this study will serve as an important design tool for circuit designers and information theorists for evaluating the performance of different encoding and decoding principles in biosensor systems.

References

1. E. Marshall, "Getting the Noise Out of Gene Arrays," Science, news, vol. 306, 22 October, 2004.
2. Y. Tu, G. Stolovitzky, U. Klein, "Quantitative Noise Analysis for Gene Expression Microarray Experiments," Proceedings of the National Academy of Sciences, pp. 14031–14036, 2002.
3. L. J. Kricka, "Interferences in Immunoassay – Still a Threat," Clinical Chemistry, vol. 46, pp. 1037–1038, 2000.
4. W. Preiser, N. S. Brink, A. Hayman, J. Waite, P. Balfe, R. S. Tedder, "False-Negative HIV Antibody Test Results," Journal of Medical Virology, vol. 600, pp. 43–47, 2000.
5. C. Selby, "Interference in Immunoassay," Annals of Clinical Biochemistry, vol. 36, pp. 704–721, 1999.
6. S. Rotmensch, L. A. Cole, "False Diagnosis and Needless Therapy of Presumed Malignant Disease in Women with False-Positive Human Chorionic Gonadotropin Concentrations". Lancet, vol. 355, pp. 712–715, 2000.

7.. A. Hassibi, H. Vikalo, A. Hajimiri, "On Noise Processes and Limits of Performance in Biosensors," Journal of Applied Physics, vol. 102, no. 1, pp. 014909(12pp), 2007.
8. R. L.Stears, T. Martinsky, M. Schena, "Trends in Microarray Analysis," Nature Medicine,vol. 9, pp. 140–145, 2003.
9. S. P. Mohanty, E. Kougianos, "Biosensors: A Tutorial Review," IEEE Potentials, vol. 25, no. 2, pp. 35–40, 2006.
10. Y. Wang, F. S. Makedon, J. C. Ford, J. Pearlman, "HykGene: a hybrid approach for selecting marker genes for phenotype classification using microarray gene expression data". Bioinformatics, vol. 21, 2005.
11. J. P. Fitch, E. Raber, D. R. Imbro, "Technology Challenges in Responding to Biological or Chemical Attacks in the Civilian Sector" Science, vol. 21, 2003.
12. S. M. Huse, J. A. Huber, H. G. Morrison, M. L. Sogin, D. M. Welch, "Accuracy and quality of massively parallel DNA pyrosequencing" Genome Biology, vol. 8, 2007.
13. J. P. Noonan, G. Coop, S. Kudaravalli, D. Smith, J. Krause, J. Alessi, F. Chen, D. Platt, S. Paabo, J. K. Pritchard, E. M. Rubin, Science, "Sequencing and analysis of Neanderthal genomic DNA" vol. 17, 2006.
14. C. Wingren, A. K. Borrebaeck, "Progress in Miniaturization of Protein Arrays – A Step Closer to High-density Nanoarrays," Drug Discov Today, vol. 12, no. 19–20, pp. 813–819, 2007.
15. M. Schena, Microarray Analysis, Wiley, New York, 2003.
16. R. Wiese, Y. Belosludtsev, T. Powdrill, P. Thompson, M. Hogan, "Simultaneous Multianalyte ELISA Performed on a Microarray Platform," Clinical Chemistry, vol. 47, pp. 1451–1457, 2001.
17. C. R. Taitt, J. P. Golden, Y. S. Shubin, L. C. Shriver-Lake, K. E. Sapsford, A. Rasooly, F. S. Ligler, "A Portable Array Biosensor for Detecting Multiple Analytes in Complex Samples," Microbial Ecology, vol. 47, no. 2, pp. 175–185, 2004.
18. G. J. Zhang et al, "Production of Nanopatterns by a Combination of Electron Beam Lithography and a Self-assembled Monolayer for an Antibody Nanoarray," Journal of Nanoscience and Nanotechnology, vol. 7, pp. 410–417, 2007.
19. S. J. Park, T. A. Taton, C. A. Mirkindagger, "Array-Based Electrical Detection of DNA with Nanoparticle Probes," Science, vol. 295, no. 5559, pp. 1503–1506, 2002.
20. T. K. Moon, Error Correction Coding, John Wiley and Sons, New Jersey, 2005.
21. W. R. Heineman, W. B. Jensen, "Leland C. Clark Jr. (1918C2005)," Biosensors and Bioelectronics, vol. 21, no. 8, pp. 1403–1404, 2006.
22. D. R. Thevenot, K. Toth, R. A. Durst, G. S. Wilsond, "Electrochemical Biosensors: Recommended Definitions and Classification," Biosensors and Bioelectronics, vol. 16, no. 1, pp. 121–131, January 2001.
23. S. Draghici, Data Analysis Tools for DNA Microarrays, Chapman and Hall/CRC Press, 2003.
24. M. L. Lee, F. C. Kuo, G. A. Whitmore, J. Sklar, "Importance of Replication in Microarray Gene Expression Studies: Statistical Methods and Evidence from Repetitive cDNA Hybridizations," Proceedings of the National Academy of Sciences of the United States of America, vol. 97, no. 18, pp. 9834–9839, August 2000.
25. W. Zhang, I. Shmulevich (editors), Computational and Statistical Approaches to Genomics (Kluwer Academic Publishers, New York, 2002).
26. F. Patolsky, G. Zheng, O. Hayden, M. Lakadamyali, X. Zhuang, C. M. Lieber, "Electrical Detection of Single Viruses," Proceedings of the National Academy of Sciences, vol. 101, no. 39, pp. 14017–14022, 2004.
27. G. Zheng, F. Patolsky, Y. Cui, W. U. Wang, C. M. Lieber, "Multiplexed Electrical Detection of Cancer Markers with Nanowire Sensor Arrays," Nature Biotechnology, vol. 23, pp. 1294–1301, 2005.
28. D. Janasek, J. Franzke, A. Manz, "Scaling and the Design of Miniaturized Chemical-Analysis Systems," Nature, vol. 442, pp. 19–27, July 2006.
29. Lin-Li Lv1 et al., "Construction of an Antibody Microarray Based on Agarose-Coated Slides," Electrophoresis, vol. 28, pp. 406–413, 2007.

30. F. Vinet, P. Chaton, Y. Fouillet, "Microarrays and Microfluidic Devices: Miniaturized Systems for Biological Analysis," Microelectronic Engineering, vol. 61–62, pp. 41–47, July 2002.
31. A. Hassibi, "Integrated Microarrays," Ph.D. Thesis, Stanford University, 2006.
32. J. Madou, R. Cubicciotti, "Scaling Issues on Chemical and Biological Sensors," Proceedings of IEEE, vol. 91–830, 2003.
33. Y. Liu, E. C. Alocilja, S. Chakrabartty, "Forward Error Correcting Biosensors: Modeling, Algorithm, and Fabrication, IEEE Biomedical Circuits and Systems Conference, Baltimore, USA, 2008.
34. S. Chakrabartty, Y. Liu, "Towards Reliable Multi-Pathogen Biosensors Using High-Dimensional Encoding and Decoding Techniques, SPIE Symposium on NanoScience+Engineering, San Diego, CA, 2008.
35. Y. Gao, G. Hu, Y. H. Lin, P. M. Sherman, D. Li, "An Electrokinetically-Controlled Immunoassay for Simultaneous Detection of Multiple Microbial Antigens," Biomedical Microdevices, vol 7, no. 4, pp. 301–312, 2005.
36. C. E. Shannon, A Mathematical Theory of Communication, University of Illinois Press, 1949 (reprinted 1998).
37. Z. Muhammad-Tahir, E. C. Alocilja, "A Conductimetric Biosensor for Biosecurity," Biosensors and Bioelectronics, vol. 18, pp. 813–819, 2003.
38. Z. Muhammad-Tahir, E. C. Alocilja, "Fabrication of a Disposable Biosensor for *Escherichia coli* o157:H7 Detection, " IEEE Sensors Journal, vol. 3, pp. 345–351, 2003.
39. Z. Muhammad-Tahir, E. C. Alocilja, "Rapid Detection of Bovine Viral Diarrhea Virus as Surrogate of Bioterrorism Agents," EEE Sensors Journal, vol. 4, pp. 757–762, 2005.
40. Y. Iribe, M. Suzuki, "Integrated Enzyme Switch as a Novel Biosensing Device," Biosensors and Bioelectronics, The 7th world congress of biosensors, Japan, 2002.
41. T. A. Sergeyeva, S. A. Piletskii, A. E. Rachkov, A. V. El'Skaya, N. V. Lavrik, "Polyaniline Label-Based Conductometric Sensor for IgG Detection," Sensors and Actuators B: Chemical, vol. 34, no. 1, pp. 283–288, 1996.
42. J. H. Kim, J. H. Cho, G. S. Cha, C. -W. Lee, H. -B. Kim, S. -H. Paek, "Conductimetric Membrane Strip Immunosensor with Polyaniline Bound Gold Colloids as Signal Generator," Biosensors and Bioelectronics, vol. 14, no. 12, pp. 907–915, 2000.
43. Y. Zuo, S. Chakrabartty, Z. Muhammad-Tahir, S. Pal, E. C. Alocilja, "Spatio-Temporal Processing for Multichannel Biosensors Using Support Vector Machines," IEEE Sensors Journal, vol. 6, no. 6, pp. 1644–1651, 2006.
44. J. M. Jay, Modern Food Microbiology, Aspen Publishers, Inc., Gaithersburg, MD, 2000.
45. E. J. Dubovi, "The Diagnosis of Bovine Viral Diarrhea Virus – A Laboratory View," Veterinary Medicine, vol. 85, pp. 1133–1139, 1990.
46. E. T. Ryser, Public Health Concerns. E. H. Marth, J. L. Steele (editors), Applied Dairy Microbiology, Marcel Dekker, Inc., NY, pp. 263–404, 1998.
47. Y. Liu, S. Chakrabartty, E. C. Alcilja, "Fundamental Building Blocks for Molecular Bio-Wire Based Forward-Error Correcting Biosensors," Nanotechnology, vol. 18, no. 42, pp. 424017 (6pp), October 24, 2007.
48. Y. P. Tsividis, Operation and Modeling of the MOS Transistor, McGraw-Hill, New York, 1988.
49. A. Gore, S. Chakrabartty, S. Pal, E. C. Alocilja, "A Multichannel Femtoampere-Sensitivity Potentiostat Array for Biosensing Applications," IEEE Transactions on Circuits and Systems I, vol. 53, no. 11, pp. 2357–2363, November 2006.
50. Y. Liu, A. Gore, S. Chakrabartty, E. C. Alcilja, "Characterization of Sub-Systems of a Molecular Bio-Wire Based Biosensor Device," Microchimica Acta, vol. 163, no. 1–2, pp. 49–56, 2008.
51. R. G. Gallager, Low-Density Parity-Check Codes, MIT Press, Cambridge, MA, 1963.
52. Hans-Andrea Loeliger, "An Introduction to Factor Graphs," IEEE Signal Processing Magazine, vol. 21, pp:28–41, Jan.2004.
53. G. D. Forney, Jr., "Codes on Graphs: Normal Realizations," IEEE Transactions on Information Theory, vol. 47, no. 2, pp. 520–548, 2001.

Index

A
ABEL. *See* Electrokinetic anti-Brownian
Absorbance (E), 83, 84, 86, 91
Absorption maximum (λ_{max}), 91–93
Acoustic wave, 55–56
Acrylamide polymer, 102
Actin filaments, 113
Activation energy (E^*), 98
Active pixel sensor, 186
Affinity chromatography, 93
Affinity constant (K_A), 94, 100–104
Affinity distribution, 95
Affymetrix, 11
AFM. *See* Atomic force microscopy
Alkanethiols, 9, 135, 144
Ammonia, 142
Amplicon, 109, 110, 113
Amplification, in immunoassay, 220
Analyte, 46, 49–52, 55–58, 60, 65, 67, 70, 72, 75–77, 93, 94, 99, 100, 116, 217, 219, 222, 223, 226
AND logic, 221, 226–228, 232–234, 237
Angular sensitivity, 87
Anisotropy, 86
Antibodies, 3, 7, 46, 47, 60, 61, 72, 93, 101–107, 111–113, 217–219, 222–224, 226, 231
Antigen-antibody interaction, 101
anti-TNT antibody, 103
APD. *See* Avalanche photodiode
Apparent affinity constant (K_A'), 94
Aptamer, 108, 217
Arachidonic acid, 128, 140
Arc discharge, 8, 131
ARQ. *See* Automatic repeat request
Arrhenius equation, 98
Ascorbate, 90, 91
Association rate, 97
Asymmetric code, 231, 232, 234–238
Atomic force microscopy (AFM), 2, 3, 23–31, 34–41, 58, 61–63, 65, 66, 68, 69, 74, 75, 90, 110–114
Attenuation index (k), 84
Automatic repeat request (ARQ), 14
Avalanche photodiode (APD), 178, 179, 190
Avidin, 102

B
B-DNA, 17
Bell's model, 32
Benzphetamine, 140
Biacore, 7, 93, 99, 101, 110
Bi-dimensional, 114, 141–142, 234, 236
Bilirubin, 73–74
Binding capacity (Q/Rmax/Gmax), 66, 72, 94, 101
Binding constants, 93–97
Binding exponent (η), in Sips equation, 94, 102, 103
Binning, Gerd, 1
Biochromatography, 102
Biomolecular encoder, 218, 228–234
Biomolecular redundancy, 220
Biomolecular switch, 222
Biosensor
  channel capacity, 219, 220
  circuit models, 222, 229, 231
  LDPC code, 232
  noise, 221, 237
  signal-to-noise ratio, 30, 217, 219, 220
Biotin, 102, 103, 109
Biotinylated DNA probes, 109
BK-7 glass, 85, 87
Blocking agent, 104, 108
Blodgett Katherine, 4

S. Carrara (ed.), *Nano-Bio-Sensing*,
DOI 10.1007/_978-1-4419-6169-3,

© Springer Science+Business Media, LLC 2011

Blood, 13, 57, 62, 68, 75, 93, 145
Blue-shift, 91
Boolean logic, 160
Bovine leukemia virus (BLV), 65
Bovine serum albumin (BSA), 66
Brust method, 135
Bulk effect, 100

C
Cadmium arachidate (CdS), 227
Cadmium lead (PdS), 227
Cadmium sulfide, 135, 155
Calibration curve, 91
Calixarenes, 52
Cantilever, 24–26, 29, 30, 33, 34, 39, 40, 111
Capping agent, 90
Carbohydrate group, in the Fc-domain of antibody, 102
Carbon nanotubes, 8, 9, 14, 110, 131, 132, 137–140, 143–145, 156, 195–213
Carbon nanotubes multi-walled, 9, 131, 132, 140, 143
Carbon nanotubes single-walled, 9, 110, 131
Carboxylated dextran, 109
CCD. *See* Charge coupled device
CdS, 135, 155
Cellulose, 102, 224
Ceramic, 53
Charge confinement, 8–9, 145
Charge coupled device (CCD), 152, 177, 178, 186
Charge quantization, 5, 8
Chemical deposition, 5, 8, 48, 49, 53, 131, 139, 197
Chemiluminescence, 59, 188, 189
Chip, 12, 15, 16, 64, 100, 102, 159, 160, 162, 169, 180, 181, 186, 189, 219, 231
chi-square fitting, 95
Cholestenone, 129
Cholesterol, 40, 112, 113, 128, 129, 132, 135, 140
Citrate, 90, 91
CLAMP-routine, 100
Clinical analyzer, 93
CMOS. *See* Complementary metal oxide semiconductor
Coagulation, 93
Co-detection, 234, 235, 237
Colloidal gold, 75, 83
Colloidal particles, 9, 10, 83, 162
Complementary metal oxide semiconductor (CMOS), 12, 177–181, 186, 188–191
Complementary ssDNA, binding of, 109
Complement, part of the innate immune system, 101
Conductivity, 8, 9, 65, 84, 139, 142, 143, 145, 153, 154, 156, 158, 159, 166
CONTIN, fitting method, 95
Control transconductance, 225, 229
Cooperativity (of binding), 94, 97
Covalent binding, 102, 109
C-reactive protein (CRP), 104
Cross linker, 50, 51, 57, 74–76
Cross-talk, 180, 221
CRP. *See* C-reactive protein
Cryogenic samples, use in AFM, 110
Crystal structure, 3, 8
Current, 1, 2, 8, 13, 25, 54, 128–131, 135, 137–139, 144, 158, 177, 179, 180, 182, 183, 185, 190, 223
Current peak, 144
CuS, 135
Cytochromes, 3, 67, 68, 128, 129, 131, 135, 136, 140

D
Damping factor, imaginary part of the refractive index (k), 84, 86
Dark count rate (DCR), 179, 184
DCR. *See* Dark count rate
de Feiter-equation, 88
Degrees of freedom, of a data set, 95
Denaturation, 104
DEP. *See* Dielectrophoresis
Desiccation, of samples, in AFM, 111
Detection constant, 225, 229
Detection error rate (DER), 218, 220, 221, 234–238
Detection limit, 60, 67, 72, 101, 106, 132, 222
Dextran, 38, 101, 102, 109
Diaminopropane linker, 104
Dielectric constant (e), 84, 91
Dielectrophoresis (DEP), 11, 152, 155–158, 161, 163, 166, 167
Diffusion
  coefficient, 130, 131
  rate constant, 97–100
Digoxin, 93
Dimension, 8, 9, 25, 26, 53, 57, 58, 69, 76, 83, 114, 133, 136, 137, 144, 159
Dimethoxytrityl group, 109
Dissociation constant (KD), 94, 185
Dissociation rate, 97, 100, 101

Disulfide-modified single-stranded DNA probes (DMT-S-S-ssDNA), 109
DMT-S-S-ssDNA. *See* Disulfide-modified single-stranded DNA probes
DNA, 3, 11, 12, 27, 28, 46, 48, 59, 75, 108–110, 112, 113, 160, 186, 187, 189, 217, 219, 220
DNA detection, 11, 12, 186, 187
Dopamine, 72, 143, 144

E
Electrochemical current, 212
Electrochemical detection, 11
Electrochemical interface, 129
Electrochemical potential, 130
Electrochemistry, 128–130
Electrokinetic anti-Brownian (ABEL), 163
Electrokinetic forces, 154, 156–158, 166
Electro-magnetic multipole oscillations, 91
Electrons, 1, 5–11, 65, 84, 91, 129–131, 133–135, 137, 139, 140, 142, 145, 152, 153, 178, 182, 197, 208
Electron transfer, 129–131, 135, 139, 140
Electrophoresis, 11, 102, 151
ELISA test, 12
Ellipsometry, 86, 87
Energy barrier, 1, 35, 36
Energy scavenging, 12–14
Entrapment, 102
Enzyme, 5, 47, 66, 67, 76, 127–129, 135, 139, 140
Epitope, 65, 104
Equilibrium, 35, 93, 98, 99, 102, 105, 129, 130
Erasable programmable read-only memory (EPROM), 12, 15
Error-free, 14–16, 217–238
Erythrocytes, 40, 68–70, 76
Escherichia coli (E.coli), 59–61, 156, 222, 224, 226, 227, 230–232, 234–236
Ethylene-glycol, 7
Evanescent field, 85
Extinction coefficient (c), 84
Extinction cross-section (σext), 91
Extraction of surface molecules, 38–39
Extravidin, 109

F
Fab-fragment, 103
Factor-graph, 231–234, 238
Faraday, M., 83
Fault-tolerant, 14, 15
Fc-receptor, 102
FCS. *See* Fluorescence correlation spectroscopy
FEC. *See* Forward error-correction
Fendler, Jonas, 9
Fermi energy, 1
Fermi level, 1
Fermi sea, 5
Feynman, Richard, 1, 127
Field emission, 137, 139
Film
  Langmuir, 4
  Langmuir-Blodgett, 4, 5, 103, 135, 164
  Langmuir-Schaeffer, 4, 5, 135
  layer, 7
  layer-by-layer, 5, 47, 48
  sol-gel, 65
First order reaction, 98
Fixed-electrode dielectrophoresis, 151
FLIM. *See* Fluorescence lifetime imaging microscopy
Fluorescence correlation spectroscopy (FCS), 179, 180
Fluorescence lifetime imaging microscopy (FLIM), 179
Foot and mouth disease viruses (FMDV), 64, 65
Force clamp, 33–34
Force distance curves, 26, 27, 39
Force ramp, 33–34
Forces on the molecular scale, 24
Force spectroscopy, 3, 15, 23–41
Force volume (FV) imaging, 26
Förster resonance energy transfer (FRET), 179
Forward error-correction (FEC), 14, 217
Fourier transform, 95
Fractional surface coverage (θ), 94, 97
Free-waves, 134
Fresnell coefficients, 115
FRET. *See* Förster resonance energy transfer
Fully-electronic, 11, 12, 16, 127

G
Gaussian, 36, 95, 97, 204, 209, 210, 220, 234
Gene mutation, 108
Gibbs surface excess, 88
Gluconic acid, 128–129
Glucose, 11, 13, 14, 38, 70, 128, 129, 136, 140, 143, 144
Glutamate, 128, 129
Gold, 2, 5, 6, 9, 12, 60, 61, 65, 74, 75, 83, 86, 87, 89–93, 103, 104, 106–110, 131, 135, 136, 162, 163, 165, 166, 168, 169
Gold colloid. *See* Colloidal gold

Gold film, 85, 87, 89, 222
Gold nanoparticles (AuNPs), 9, 61, 75, 91, 93, 104, 131, 132, 135, 136, 162, 163, 165, 166, 168, 169. *See also* Colloidal gold
Goodness of fit, 89, 90
Gradient forces, 10, 11, 152
Graphene, 8, 9, 141–144, 194, 198, 199
Graphite, 2, 3, 8, 141, 143, 144
GroES, binding to GroEL, 113

H
HAuCl4, 90
hCG. *See* Human chorionic gonadotropin
HEPES (=4-(2-hydroxyethyl)piperazine-1-ethanesulfonic acid), 88
Hermann, Gaub, 3
Hertz model, 26
Heterogeneity (of binding), 94, 95, 97
Heterogeneous affinity constant (K_A'), 94
High performance liquid chromatorgraphy (HPLC), 72
High-speed atomic force microscopy, 25, 113
Histidine tag, 102
HIV, 62
Holes, 8, 9, 113, 153, 159, 182, 197
Homogeneous immunoassay, 93
Hormones, 70–73
Human chorionic gonadotropin (hCG), 93
Human rhinovirus (HRV), 63, 64
Hybridisation, 108–110, 113
Hydration, 89
Hydrogel, 93, 94
Hydrogen peroxide, 128, 129, 131, 132, 140
Hydrogen sulfide, 135
Hydrophilic gold, 104
Hydroxy-alkyl-substituted lipoamides, 109

I
Immunoassay, 93, 219, 231, 236
Immunochromatography, 93
Immunoglobulin G (IgG), 88, 95, 96, 104–107, 110–113, 188
Immunoprobe, 101
Immunosensor, 5, 101, 222–224
Imprinting bulk, 51, 65
Imprinting covalent molecular, 51–53
Imprinting molecular, 47, 49–53, 57, 62, 64, 65, 68–70, 72–76
Imprinting non-covalent, 51–53
Imprinting surface, 51–52, 56, 57, 59, 61–63, 65–66, 68–69, 71, 76, 114
Incident angle (θ), 5–6, 84–86
Indentation, 26
Indium-tin-oxide (ITO), 152–153
Initiator, 74, 75, 104
Insulator, 8, 9, 135
Intercalation, 8, 104, 106, 114
Interference, 10, 46, 51, 90, 93, 101, 109, 114, 144, 152, 157, 180, 216
Ion sensitive field-effect transistor (ISFET), 186, 190
Isoform, 128, 140
Isotherm
  Langmuir-Freundlich, 94
  Sips, 94–95, 97, 102, 105
ITO. *See* Indium-tin-oxide

J
Jones matrix, 86, 115

K
Kinetics, 13, 35–36, 41, 93, 97–101, 195, 196
Kretschmann configuration, 7, 85

L
Label, 93, 106, 107, 224, 234
Labeling, 46, 57, 108
Lactate, 128, 129, 132, 136, 140
Laminar flow, 188
Langmuir–Blodgett (LB) film, 4, 5, 103, 135, 164
Langmuir-Freundlich isotherm, 94
Langmuir Irvin, 3–4
Langmuir–Schaeffer (LS) film, 4–5, 135
Lateral-flow immunoassay, 231
Latex particles, 104, 106
LB-film. *See* Langmuir–Blodgett film
LEDs. *See* Light-emitting diodes
Ligand, 24, 26, 35–37, 41, 93–94, 99–101, 109
Light-emitting diodes, 153
Lipid, 112–113
Lipid bilayer, 102
Lipoate, 104, 110, 114
α-Lipoic acid, 104
Liposomes, 75, 104
Loading rate, 32, 35–37, 39
Localised surface plasmon resonance (LSPR), 83
LS-film. *See* Langmuir–Schaeffer film
Lysozyme, 66–68, 88

M
Magnetic tweezers, 23, 29
Mapping of surface moleculles, 39–40
Mass action, 97, 99
Mass sensitive devices, 46, 47, 53, 59, 60, 65, 70, 73, 75, 76
Mass transport, 93, 100, 101
Maxwell, 84
MCP. *See* Microchannel/Multichannel plate
Mean free-paths, 9, 132, 139, 142, 145
Mercaptohexanol, 109
11-Mercaptoundecanoic acid, 109
11-Mercaptoundecanol, 109
Message-passing algorithms, 232, 234
Metal, 5–10, 13, 14, 62, 83–85, 90, 91, 132, 135, 144–145, 155, 156, 161–164, 166, 169, 178, 186, 197, 199–202, 208, 209, 211–213
Mica surface, 63, 110–111
Micelle, 112. *See also* Liposomes; Vesicles
Microarrays, 108, 236
Microbalances crystal, 57
Microchannel/Multichannel plate (MCP), 177–178
Microchannel plate, 117
Microfluidic, 7, 10, 101, 152, 162, 168, 187–190
Mie equation, 92
Mie theory, 91
Molecular imprinted, 46
Molecules, 3–5, 7, 8, 10–12, 23, 26–29, 34, 35, 37–40, 46, 48–52, 65, 67, 68, 74–76, 83, 84, 88, 93, 102, 104, 108, 110–114, 127–131, 135, 139, 140, 143, 144, 159, 162–165, 168, 169, 186–187, 217
Monoclonal antibody, 7, 100
Mono-dimensional, 8, 9, 36, 132, 134, 136–140, 166
Monte-Carlo simulation, 32, 204, 205, 209, 210, 221
Müller matrix, 86
Multi-pathogen detection, 59, 65, 218, 219, 222, 230–232, 236–238
Multi-walled carbon nanotubes (SWCNT), 132, 140, 143
Myosin V, 113

N
$NaBH_4$, 90
Nano-biosensors, 7, 218–221
Nano-bio-VLSI, 217–238
Nano meter, 1, 3, 5, 6, 24, 47, 48, 52, 63, 76, 114, 127, 131, 134, 141, 144
Nano-particles, 9–11, 14, 48, 61, 74, 75, 83, 90, 91, 93, 104, 108, 131, 132, 135, 136, 143–145, 151, 155–157, 161–166, 168–169, 204, 208, 213
NanoPen technology, 11, 166–169
Nano-photonics, 151–169
Near-IR, 86, 87
Nernst equation, 129
Nernstian diffusion layer, 99
Network on chip, 15
Newton, 2
Nitrocellulose, 102, 224
N-methyl-aminoethanol linker, 104
Non-contact mode, in AFM, 111, 113
Non-specific binding, 63, 65, 95, 101, 107, 109, 110, 113
Non-specific interactions, 93, 105
Number density of particles (N), 91

O
Oligonucleotides, 28, 75, 102, 108–109, 113
Optical tweezers, 10, 11, 27, 29, 152, 154, 162, 163, 166, 169
Optoelectronic tweezers (OETs), 152–161, 163–169
Opto-fluidics, 10, 151–169
Orientation, effect of (in immunoassay), 102
OR logic, 221, 226
Otto configuration, 85
Ovalbumin, 88
Oxidases, 3, 128–129, 131, 136, 140, 143
Oxidized form, 90, 128, 140
Oxoglutarate, 129
Oxynitride, 89–90

P
P450, 128, 129, 135, 140, 145
Paracyclophanes, 52
Pathogen detection, 59, 65, 218, 219, 222, 224–226, 229–232, 234–238
PBS. *See* Phosphate buffered saline
PbS, 135
PCR. *See* Polymerase chain reaction
Penetration depth (of a sensor), 104, 114
Permeability (m), 84
Phosphate buffered saline (PBS), 88, 158–159
Photo-multiplier tube, 177–179
Photomultiplier tubes (PMT), 177–179
Physical adsorption, 5, 102

Pico meter, 2, 15
Pico Newton, 15
Plasmon, 155, 161, 166
Plasmonics, 155, 162, 166
Plasmon resonance, 5–8, 10, 11, 15, 46, 59, 83–117, 162
Platinum, 135, 143, 144
Point-of-care, 186
Point-of-care devices, 106
Polyaniline, 222–226, 231, 237
Polyclonal antibody, 95, 100, 104, 223, 224
Polymerase chain reaction (PCR), 46, 59, 62, 64, 108, 109, 217, 219, 220
Polymer matrix, use in immunoassay, 49–51, 76, 95
Polymers, 3, 5, 11, 24, 27, 28, 45–77, 95, 102, 104–110, 114, 155, 217, 223
Polyproteins, 30–34
Polysaccharides, 3, 37–38
Polystyrene, 102, 155–157
Poly[tris-(hydroxymethyl)methyl-acrylamide] (pTHMMAA), 104–109
Polyurethane, 57–58, 61, 62, 64, 68–69, 71
Potentiometric detection, 186
Prostate specific antigen (PSA), 106
Protein, 3, 5, 7, 11, 12, 15, 23, 24, 26–41, 46, 48, 60, 65–68, 75, 76, 88, 89, 93, 101–104, 108, 109, 111, 128, 135, 139, 140, 143, 184, 237
Protein A, 102
Protein antibody, 7, 65, 102
Protein cytochrome, 3, 67–68, 128–129, 131, 135, 136, 139, 140
Protein data bank, 111
Protein enzyme, 5, 45–47, 62, 66, 67, 76, 127–129, 135, 139, 140, 143
Protein G, 102–103
Protein LA, 102
Protein LG, 102
Protein-ligand interactions, 35–37, 101
Protein oxidase, 3, 45, 128–129, 131, 136, 140, 143
Proteins
PSA. *See* Prostate specific antigen
pTHMMAA. *See* Poly[tris-(hydroxymethyl) methyl-acrylamide]
Pyruvate, 129

Q
QCM. *See* Quartz crystal microbalance
Quality factor, 54
Quantitative imaging, 177
Quantum dot, 9, 131, 133–136, 141
Quantum well, 8, 9, 141–144
Quantum wire, 136–141
Quartz, 13, 46, 53–55, 57, 60, 65, 66, 68, 71, 72, 74, 75, 77
Quartz crystal microbalance (QCM), 46, 55, 57, 59–63, 66–67, 69–77, 89, 104
Quenching, 34, 179, 180

R
Raman, 162–165, 168, 169
Raman spectroscopy, 162–164, 169
Redox reaction, 13, 128–131, 139, 140
Reduced form, 140, 222
Reducing agent, 90–91
Reference surface, subtraction of, 100
Referencing, in immunosensing, 101
Reflectance (R), 69, 85, 86, 212
Refolding, 34
Refractive index (n), 6, 7, 84–90
Refractive index increment (dn/dc), 88, 104
Regeneration (in immunoassay), 99–101, 104
Reliability, 46, 86, 196, 217–220, 229, 235, 237, 238
Remote powering, 13
Repetition code, 230, 232, 234–237
Reproducibility, 57, 71, 73, 111, 199, 213, 217
Reversibility, 47, 49, 51, 52, 61, 71, 76, 77, 97, 101
Rhodium, 135
Rockchille salt, 53
Rorer Heinrich, 1
Ruthenium, 135

S
Sandwich assay, 104, 106, 107
Sauerbrey, 53–54, 61
SAW, 46, 55–56, 76
Scanning probe microscopy, 2–3
Scanning tunneling microscopy (STM), 1–3, 141, 204
Scattering, 83, 91, 152, 162, 196
Scattering matrix, 86
Schaeffer Vincent, 4
Schrödinger equation, 8, 133, 134, 137, 141
ss-DNA, 75, 109–110, 113
Second order reaction, 98
Seebeck effect, 13
Seed particles, 91
Self-assembled, 5, 65, 103–104, 109, 197
Self-assembled monolayer (SAM), 12, 46
Self-assembly, 5, 11, 27, 109, 114, 164

Semiconducting, 8, 9, 13, 135, 141, 145, 155–156, 178–179, 189, 195, 197–205, 208–210, 212
Sensitivity, 9, 14, 15, 24, 46, 47, 51, 58, 60–64, 66, 67, 74–77, 86–87, 93, 101, 104–108, 114, 128, 130–132, 135–136, 139–140, 143–145, 160, 161, 179, 180, 198, 219–220
Sensitivity factor, 225, 229
Sensor, 46, 55, 57, 60–65, 67, 69–77, 100, 108, 114, 128–132, 139, 164, 178, 180–181, 185–189
Sephacryl, 102
Sephadex, 102
Sequencing DNA, 14, 28
Serum, 45, 65, 66, 93, 104, 145
Shannon theorem, 219
Silanes, 5, 65, 102, 114
Silanisation, 109
Silicon, 5, 11, 12, 14, 16, 89, 111–113, 137, 152, 153, 155, 156, 158, 187, 190, 221–227
Silicon decoders, 218, 228–234
Silicon dioxide (SiO_2), 90
Silicon nitride (Si_3N_4), 24, 90
Silicon photomultipliers (SiPMs), 179
Silver, 135
Simulations, 6, 31, 32, 166, 167, 198, 199, 204–210, 221, 227, 234–238
Si_3N_4. *See* Silicon nitride
Single nucleotide polymorphism (SNP), 186
Single-photon avalanche diode (SPAD), 12, 177–186, 188–191
Single-stranded DNA oligonucleotide probes (biotin-ssDNA), 109
Single-walled carbon nanotubes (SWCNT), 110, 196–213
SiO_2. *See* Silicon dioxide
SiPMs. *See* Silicon photomultipliers
Sips isotherm, 94, 95, 97, 102, 105
Site-directed immobilization, 103
Size distribution, 90, 91
SNARE complex, 37
Sol-gel matrices, 102
SPAD. *See* Single-photon avalanche diode
Specific activity (of antibody), 103
Spectrometric ellipsometry, 86–87
SPR. *See* Surface plasmon resonance
SPREETA™ sensor, 108
Staphylococcus aureus, 60
Steady-states, 9, 99, 129, 133–135, 137, 141, 226
Steric hindrance, 102, 109
Stimuli-responsive polymer brushes, 114
STM. *See* Scanning tunneling microscopy
Streptavidin, 102–103, 109, 114
Stretching, 23, 24, 29, 31–33, 35, 37–38
Stretching DNA, 3, 27–28
Sum-product decoding, 232–233
Surface density (G), 70, 88, 100, 103, 109, 113
Surface-enhanced Raman spectroscopy (SERS), 162, 164–169
Surface imprinting, 51–52, 56, 57, 59, 61–63, 65–66, 68–69, 71, 76, 114
Surface plasmon, 161
Surface plasmon resonance (SPR), 6, 7, 15, 46, 59, 83–117
Surface recognition, 49–53
Surface roughness, 87

T
Tapping mode, in AFM, 111–112
Technology node, 12, 14, 16
TE mode, 89
Theophiline, 93
Thermal conductivity, 139
Thermal polymerisation, 104
Thin film, 4–5, 12, 47–48, 65, 84, 88–90, 102
Thiol-modified single-stranded DNA probes (SH-ssDNA), 109–110
Thiols, 3, 5, 74, 90, 131
Three-dimensional, 24, 28
Time-of-flight
Titin, 30, 34–35
TM mode, 89
Tobacco mosaic virus (TMV), 46, 62–64
Topography, in AFM, 24–26, 39–40, 110
Trace pathogen detection, 235, 237, 238
Transmission electron microscopy (TEM), 91
Transmittance (T), 84–86
Tunneling barrier, 1, 134–135
Tunneling distance
Tunneling effect, 1, 141, 185
Tweezers, 10, 11, 16, 23, 27, 29, 152–154, 162–163, 166, 167, 169

U
Unbinding, 26, 35–37, 40
Unfolding, 28–35, 38
Unfolding proteins, 34
Unzipping, 27–28
USB, 15
UV/VIS spectra, 91

V
Vesicles, 37
Virus
  foot and mouth disease viruses, 45, 64
  hepatitis C, 62
  HIV, 62
  human rhinovirus, 45, 63
  tobacco mosaic, 46, 62
VLSI, 11, 12, 15–16, 217–238
Voltage sensitive dye (VSD), 179

W
Waveforms, 134, 136
Wavelengths, 5, 8–9, 55, 83–89, 91, 93, 133, 135–137, 141, 145, 153–154, 161, 184, 196, 211, 212
Wave-matching, 84
Worm-like chain model, 31

X
X-ray crystallography, 90, 111

Y
Yeast cells, 40, 57–59, 156